The University Of Sheffield.

Rosetrees Trust
Supporting the best in medical research

The Development of Photodynamic Therapy using Transition Metal Complexes

Callum Jones

Department of Oncology and Metabolism

Department of Chemistry

August 2021

Acknowledgements

I would first and foremost like to thank my supervisors Dr. Helen Bryant and Prof. Julia Weinstein who supported and founded this fascinating project through their collaboration. Additionally, their tutelage, both personally and professionally, has been detrimental to my work progression, engagement, and overall enjoyment on this project.

An acknowledgement to all my peers with who it's been a great pleasure to work alongside for the past 4 years. This includes but isn't limited to Dr. Emma Grant, Rachel Gatenby, Leona Fields, Dr. Ola Rominiyi, Dr. Polly Gravells, Dr. Katie Myers, Dr. Tom Jones, Dan Harrison, Hannah Gagg, Aurelie Vanderlinden Dibekeme, Connor McGarrity, Kathryn Egerton, Steven Watson, Patricia Bellver, Dr. Ruth Thompson, Dr. David King, Dr. Spencer Collis, Dr. Saskia Roetschke. Additionally, to my colleagues in the Department of Chemistry, James Shipp, Samantha Peralta Arriaga, Dr. Marta Martinez Alonso, Ryan Bell, Liam Kirby, Catherine Royle, Dr. Alex Auty, Dr. Andy Sadler, Martin Appleby, Isuru Muthukudaarachi, Dr. Tao Cheng, Gwuanzhi Wu and Rory Cowin. This list is by no means exhaustive.

A special thank you to Dr. Luke McKenzie who guided me at the very start of the project and was a great support to my transition from a chemistry background into a biology lab which presented unfamiliar yet exciting new techniques. As a fellow Chemist, he provided the ideal teacher through his similar perspective and experience.

Finally, a thank you to the University of Sheffield and the Rosetrees Trust for funding and believing in the power of this project.

Abstract

Background: cancer remains to be a leading cause of death worldwide with 19.3 million estimated diagnoses in 2020. Photodynamic therapy (PDT) operates through a light-activated photosensister (PS) causing neoplasm death through ROS generation which concomitantly reduces treatment invasion and limits off-targeted damage. Despite being currently approved for some cancers, problems in PDT exist such as poor tissue penetration and undesirable pharmacokinetic/dynamic properties. **Aims and Methods:** This thesis aims to improve upon previously identified Ir(III) (IrNew) and Pt(II) (Porphyrin Plus) based PS through structural modifications and combination with upconverting lanthanide nanoparticles (UCNPs). IrTHPyBenz, IrTHPyMes and IrPPyMes, sister complexes of IrNew, were synthesised and tested for PDT activity retention alongside additional cellular behaviour. Secondly, PtCNNH was isolated from its parent compound and re-investigated. Finally, UCNPs were produced and combined with IrTHPyBenz with their ability to facilitate highly tissue penetrating near infra-red (NIR) PDT scrutinised. **Results:** IrTHPyBenz had strong PDT activity measured in both 2D cultured cancer cells (PI > 100 - 378) and 3D spheroid models after irradiation at 405 nm and 455 nm, previously not possible and unexplored with IrNew. Conversely, IrPPyMes and IrTHPyMes's PDT ability was vastly reduced due to very large increases in their dark toxicities and null phototoxicities. Similarly, PtCNNH had diminished PDT activity (PI = 4.1) again rationalised by an increase in dark toxicity and a reduction in phototoxicity. UCNPs were synthesised, biologically appropriated, and measured to emit blue light following NIR irradiation and then combined with IrTHPyBenz and tested for NIR PDT as a multi modal vehicle **Conclusions:** IrNew can be improved for PDT through structural modifications which permits a red-shift in the photoactivation wavelength into a more tissue penetrating light region. Similarly, the importance of the Benz ligand was evidenced in rationalising its strong PDT activity. The reduction in PtCNNH's PDT activity evidenced the importance of the porphyrin fragment in PorphyrinPlus's mechanism of action. Finally, despite the ultimate lack of NIR PDT, UCNPs could be suitable to permit this in the future after as discussed improvements to their light upconverting dynamics.

Table of Contents

1. Introduction

1.1 – Photodynamic Therapy

1.1.1 – The Premise

Photodynamic therapy (PDT) is used to treat a variety of diseases. It is facilitated through the light induced activation of a drug which in turn leads to cell death. Such photo-induced cell killing, or photosensitisation is caused through the cross interaction between three important components, namely a photosensitiser (PS), oxygen (O_2) and light. Firstly, a photon is absorbed (hν) by the PS which generates a singlet electronic excited state, $^1PS^*$ (Figure 1.1 and Figure 1.2). This is a reversible process and $^1PS^*$ can decay and reform the ground state, ^1PS, through both radiative (photon emission - fluorescence) or by non-radiative pathways (internal conversion – heat). However, an alternative excited state process known as intersystem crossing (ISC) can also occur which leads to the generation of singlet oxygen, $^1O_2$ (Lamola and Hammond, 1965). ISC causes an electronic re-arrangement of $^1PS^*$ thereby turning a singlet excited state (electron spin-paired) to a triplet excited state (electron spin-unpaired), $^1PS^*$ to $^3PS^*$. $^3PS^*$ is also subjected to decay and reformation of ^1PS through photon emission and vibrational cooling.

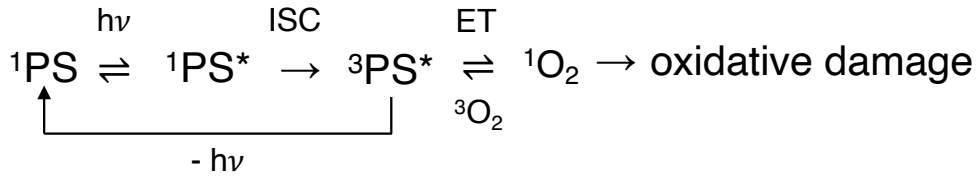

Figure 1.1 a simplistic overview of PS mediated photosensitisation through singlet oxygen generation which causes oxidative damage.

However, $^3PS^*$ decay is slow, because it involves a change of spin-state (an electron “flip”) which is a forbidden process. Therefore, the lifetime of $^3PS^*$ becomes longer due to the low probability of deactivation pathways (Baryshnikov, Minaev et al., 2017). Due to oxygen unusually possessing an electronic triplet ground state, $^3O_2$, $^3PS^*$ can undergo non-radiative energy transfer (ET) as a way of decay. This causes $^3O_2$ to undergo a spin state rearrangement to generate $^1O_2$ (Li, Lin et al., 2016). $^1O_2$ is a member of a biologically damaging group of compounds called

reactive oxygen species, ROS (Jiang, Carroll et al., 2021, Michaeli and Feitelson, 1994). The oxidative ability of such species is high, which causes oxidation of nearby molecules and/or further generation of other damaging ROS species such as peroxide and hydroxide amongst others (Lan, Zhao et al., 2019). Therefore, following irradiation of a PS, the death of diseased tissue occurs by $^1O_2$ and ROS production due to irreparable oxidative damage (Jori, Fabris et al., 2006, van Straten, Mashayekhi et al., 2017). PDT therefore utilises photosensitisation to kill tissue through the light activated generation of singlet oxygen by a PS at the site of disease.

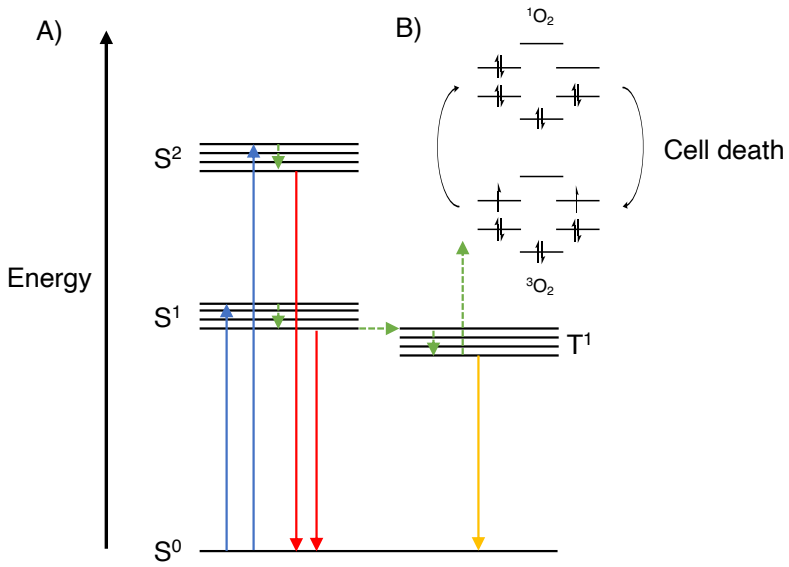

Figure 1.2: A) The photophysical and photochemical processes governing PDT; blue arrows ($S^0 \rightarrow S^n$, photon absorption), red arrows ($S^n \rightarrow S^0$, fluorescence), green arrows, non-radiative processes ($S^n \rightarrow S^n$ internal conversion, $S^1 \rightarrow T^1$ intersystem crossing, $T^1 \rightarrow {}^3O_2$ energy transfer), orange arrow ($T^1 \rightarrow S^0$, phosphorescence). B) A molecular orbital diagram of $^3O_2$ (bottom), and $^1O_2$ (top).

This project focuses solely on PDT for cancer treatment. However, PDT is additionally approved to treat a wide range of illnesses: actinic keratosis (Liu, Zhao et al.), acne (Babilas, Schreml et al., 2010), age-related macular degeneration (Wormald, Evans et al., 2007), Barretts oesophagus (Foroulis and Thorpe, 2006), viral warts (Fuchs, Fluhr et al., 2004), periodontal disease (Meisel and Kocher, 2005), antimicrobial diseases (Hamblin and Hasan, 2004) amongst others.

1.1.2 – Type I vs Type II PDT

PS can be categorised by their mechanism of action into either type I or type II. A type I PDT mechanism is characterised through the chemical reaction of $^3PS^*$ by processes such as electron transfer or hydrogen abstraction which degrades the PS and leads to radical generation (Li, Kwon et al., 2018). In contrast, a type II PDT mechanism is a catalytic cycle which produces singlet oxygen through energy transfer (Castano, Demidova et al., 2004)(Figure 1.3). Both pathways, especially type II mechanisms, are oxygen-dependent and hence oxygenated (normoxic) tissue is prone to the treatment (Ding, Yu et al., 2011). Furthermore, these two pathways can occur simultaneously upon irradiation with the tissue microenvironment determining their exact ratios (Huang, Xuan et al., 2012).

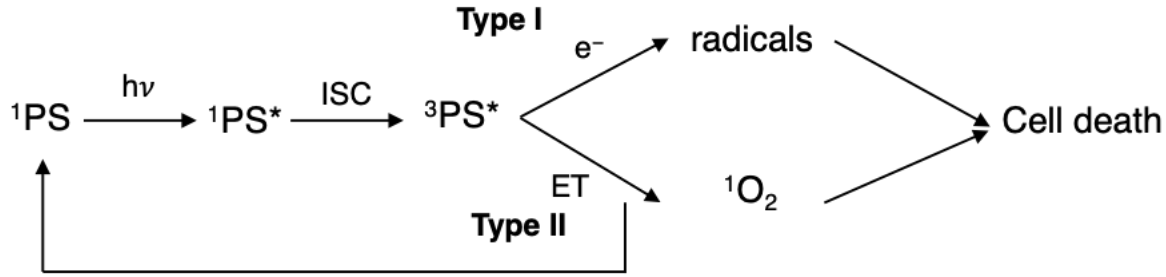

Figure 1.3 Type I and Type II oxygen-dependent PDT. Type II pathways behave as a catalytic cycle through energy transfer (ET) from $^3PS^*$ to generate $^1O_2$ whereas Type I pathways are irreversible and generate radicals via electron transfer.

1.1.3 – PACT

A third photosensitisation mechanism exists which is referred to as photoactivated chemotherapy (PACT) due to fundamental differences to PDT (Farrer, Salassa et al., 2009). These mechanisms are sometimes referred to as type III pathways and are oxygen independent (McKenzie, Bryant et al., 2019). In addition, PACT differs from PDT in not always having to rely on $^3PS^*$ population (Bonnet, 2018). Transition metal complexes in particular have been identified as excellent PACT candidates due to their light absorbing properties, excited state dynamics and their ability to complex with ligands – which can be de-bound upon light activation. PACT mechanisms can be broadly divided into three categories (Bonnet, 2018).

1. Irradiation reduces the metal centre to generate cytotoxic species. This is particularly the case for cobalt- and platinum- based compounds (Figure 1.4)(Shi, Imberti et al., 2019).
2. Irradiation produces $^3PS^*$ which populates a dissociative excited state leading to the formation of a labile aqua-metal complex (typically seen in d^6 metals). Cytotoxicity arises from either the dissociated ligand or the metal centre (Pierri, Pallaoro et al., 2012).
3. Irradiation causes C-C bond breakage which is often seen in photocaged systems, whereby the destruction of the cage releases cytotoxic cargo.

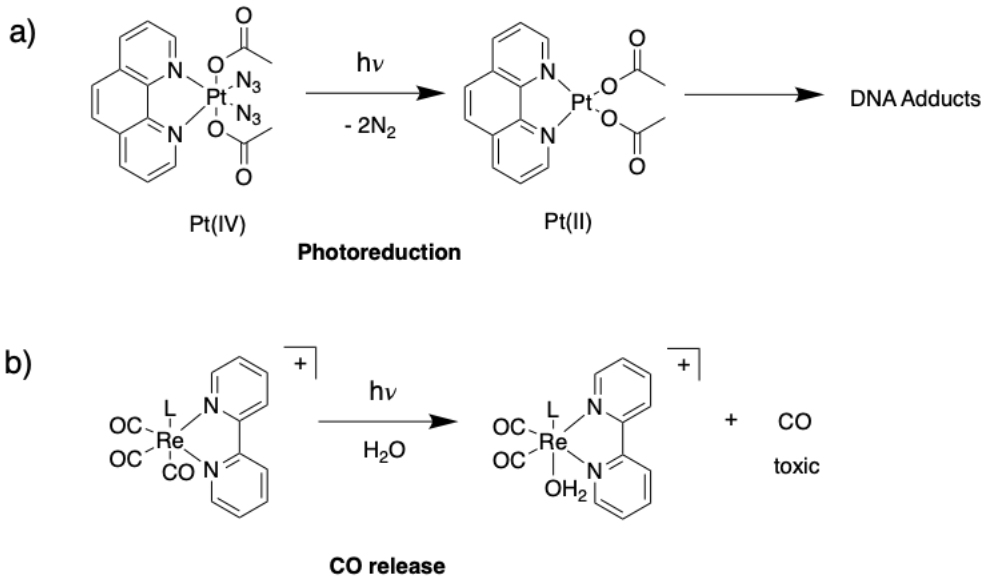

Figure 1.4 Examples of PACT drugs through a) Pt(IV) photoreduction and b) Re(I) CO photodissociation

1.1.4 – From Antiquity to the 20th Century Clinic

Photodynamic therapy was first documented in 1400 BC in the ancient Indian book, *Artharva Veda*, as a treatment for vitiligo and psoriasis (Fitzpatrick and Pathak, 1959). Subsequently, the Greeks and the Egyptians began experimenting with the healing powers of The Sun to treat the same two diseases, which became known as 'heliotherapy' (Alexiades-Armenakas, 2006). Upon the translation of *Artharva Veda*, the active ingredient of 'crushed black seeds' was deciphered as originating from the

locally available Bavachee plant (Fitzpatrick and Pathak, 1959). This plant is now known to naturally contain psoralen, a compound belonging to the coumarin family (Fitzpatrick and Pathak, 1959, Wyss, 2000). In the present day, these compounds are known for their UV activated anaerobic phototoxic effects and are presently used to treat psoriasis and vitiligo as a topical cream (Pathak and Fitzpatrick, 1959)(Figure 1.5)

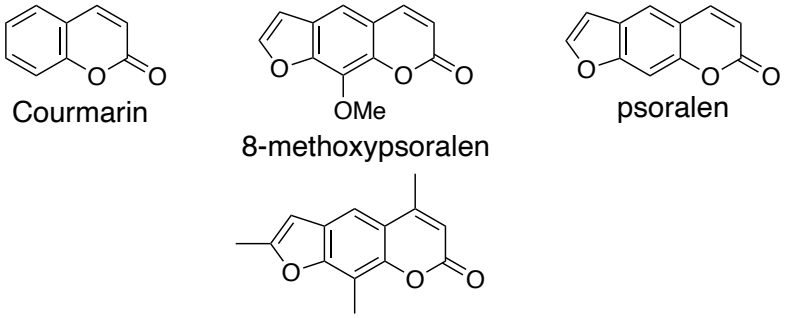

Figure 1.5 A group of natural anaerobic photosensitisers belonging to the coumarin family used since antiquity as a treatment for vitiligo, psoriasis and eczema.

A renewed interest in phototherapy emerged at the beginning of the 20th century. Finsen, who was awarded the Nobel Prize in 1903 for his work, discovered that cutaneous tuberculosis could be treated by UV irradiation. The mode of action at the time was unknown but was later rationalised as photosensitisation caused by coproporphyrin III found at elevated levels in the pathogenic bacteria (Møller, Kongshoj et al., 2005). Concurrently, Oscar Raab noticed that prokaryotic infusoria were killed upon light exposure in the presence of acridine orange dye and proposed that energy transfer from the dye was responsible (Raab, 1900). In 1907, Von Tappenheimer coined the term 'photodynamics' based on the observed disruption to the movement (-dynamics) of bacteria caused by light (photo-) and also highlighted an oxygen dependency (Dolmans, Fukumura et al., 2003, Von Tappeiner and Jodlbauer, 1907). In 1913, Meyer-Betz documented the effects of applying hematoporphyrin, Hp, followed by light exposure to his own hand, noticing that exposed regions became swollen (Dolmans, Fukumura et al., 2003).

1.1.5 – Development of the 1st Generation PS

A few decades later, PDT was used to treat cancer through intratumoral injection of murine tumours with Hp mixtures which were found to be preferentially uptaken by diseased tissue. This led to the proposal for Hp's use as a cancer-specific diagnostic tool owing to Hp's fluorescence (Figge, Weiland et al., 1948). An attempt to improve the efficacy of Hp through reaction with sulphuric and acetic acid followed by filtration and neutralisation with sodium acetate was made (Dolmans, Fukumura et al., 2003). The resulting crude product became known as HpD (hematoporphyrin derivative) which contained a mixture of PS products (LIPSON and BALDES, 1960). HpD was applied to mouse-grown, human-derived tumours and upon irradiation had a curative effect (Kelly, Snell et al., 1975). Dougherty conducted the first human clinical study, whereby HpD injection to 113 tumours of the breast, colon, SCC, chondrosarcoma and prostate followed by irradiation found 111 were cured. Additionally, an increase in dosage was required to treat low lying, highly pigmented tumours (Dougherty, Kaufman et al., 1978). Concurrently, patients with advanced stage lung cancer were exposed to HpD and subsequently irradiated using a bronchoscope fitted with a quartz fibre argon laser. However, only 2 out of 14 patients were completely cured whilst the others were minimally effected (Hayata, Kato et al., 1982). The advanced late-staged nature of these 12 tumours were found to resist PDT, thereby imposing a limitation. This conclusion was supported by additional findings of HpD in both superficial and non-superficial oesophageal and gastric cancers which found only early stage inoperable cancers were treatable (Hayata, Kato et al., 1985, Juzeniene, Peng et al., 2007). Dougherty further studied HpD through the isolation of particularly PDT effective factions of the mixture (Dougherty, Potter et al., 1984). Using HPLC, HpD was found to contain up to 50% of an unknown oligomeric Hp component which when enriched, was responsible for the major part of HpD's measured PDT activity (Dougherty, 1987). Using a further combination of HPLC and ^{1}H NMR, the identity of the component was characterised and became known as Porfimer Sodium, an oligomeric ester-linked Hp product (Figure 1.6)(Byrne, Marshallsay et al., 1990). This oligomeric mixture was commercialised, produced and branded as Photofrin® by Axcan Pharma and became the first PDT agent to be approved in Canada (1993) followed by USA, EU and Japan for cancer treatment (Baskaran, Lee et al., 2018,

Dolmans, Fukumura et al., 2003).

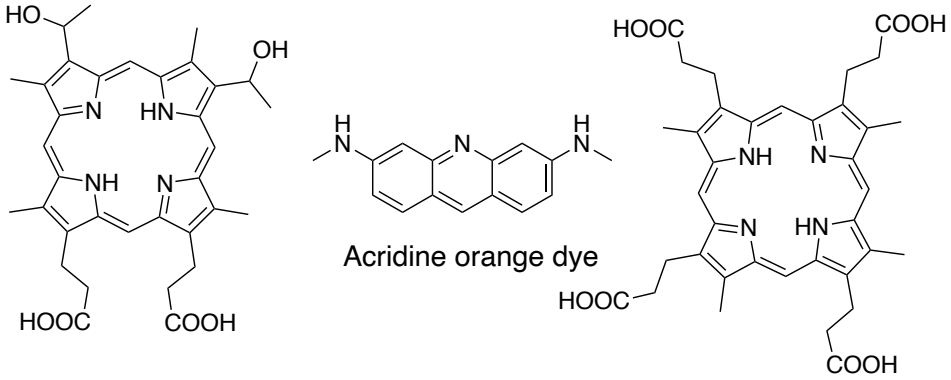

Figure 1.6 A series of photoactivate compounds used in the historical development of PDT.

1.1.6 – Drawbacks of the 1st Generation

Despite impressive initial results in cancer treatment, Photofrin® and other analogues suffered from several drawbacks.

- The clearance from the body is long, leaving patients photosensitive for up to 30 days post-treatment (Baran, 2018).
- Generally good tumour selectivity but poor retention compared to normal tissue (Hahn, Putt et al., 2006, Korbelik, 1992, Pahernik, Dellian et al., 1998).
- Poor water solubility results in aggregates in solution and strong adherence to lipophilic biomolecules such as low-density lipoproteins, LDL (Candide, Morliere et al., 1986).
- Poor efficacy against metastases and advanced tumours (Sheleg, Zhavrid et al., 2004)
- Poor tissue penetration, especially in pigmented tumours such as melanoma (Menezes, Bagnato et al., 2007).
- Small light absorption under irradiation at its highest tissue penetrating wavelength, 630 nm (Mitra and Foster, 2005)
- High rates of photobleaching due to reaction with self-produced $^1O_2$ (Georgakoudi, Nichols et al., 1997).

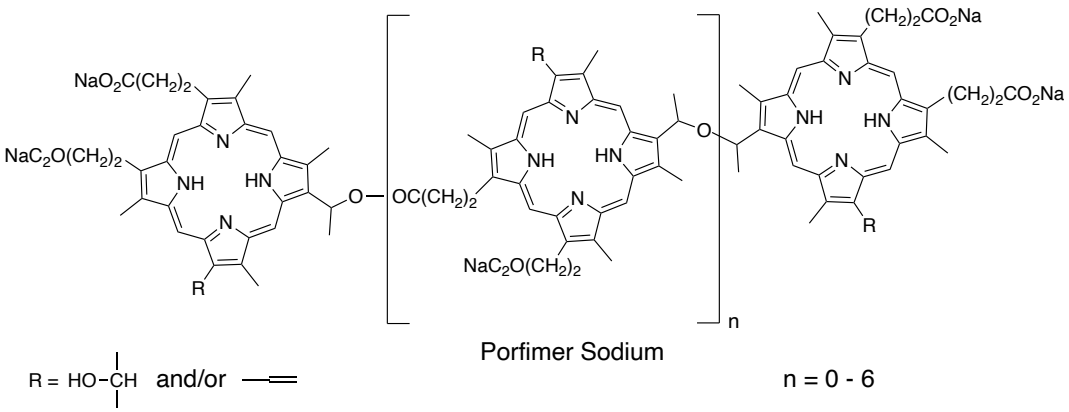

Figure 1.6 Porfimer sodium 'Photofrin®' the most famous of the first generation of photosensitisers.

1.1.7 – 2nd Generation PS

The main design aims of 2nd generation PS were to improve several disadvantages found with Photofrin® treatment. Such emerged compounds can be divided into three categories namely porphyrins, chlorophylls (chlorins) and dyes (phthalocyanines)(Allison, Downie et al., 2004).

(A) Porphyrins

A porphyrin-based 2nd generation PS uses a pro-drug called 5-aminolevulinic acid (5-ALA) which forms protoporphyrin IX, PpIX in cells (Figure 1.7). 5-ALA can be topically applied to tumorous regions whereby its uptake and biosynthesis produces naturally photoactive PpIX (Kennedy, Pottier et al., 1990). In the haem biosynthetic pathway, PpIX directly precedes non-photoactive haem with such transformation being slow. Conversely, 5-ALA's transformation into PpIX is rapid therefore causing an overall build-up of PpIX (Sassa and Kappas, 1981). Alongside this, PpIX levels can be further selectively elevated in some cancer cells which have mutated and disrupted haem pathways (Kennedy, Pottier et al., 1990, Malik, 2020). However, photoactivation of PpIX is at 630 nm giving the same low tissue penetration as Photofrin® (Gold and Goldman, 2004). Nonetheless, the approval of 5-ALA to treat skin and bladder cancers as well as actinic keratosis was announced (Hexvix®, Metvix®, Levulan®)(Freeman, Vinciullo et al., 2003, Jeffes, 2002, Martoccia, Zellweger et al., 2014).

(B) Chlorins

Chlorins also form the core structure of other approved 2nd generation PS. Chlorins are related to chlorophylls and were therefore predicted to be more red-light absorbing than porphyrins, which is generally true (chlorin e6 λ 660 nm)(Kurakina, Khilov et al., 2019). Foscan® (or Temoporfin) is a chlorin based PS which is effective at treating oesophageal, gastrointestinal, skin and head and neck cancers (Ell, Gossner et al., 1998, Fan, Hopper et al., 1997, Kübler, Haase et al., 1999, Savary, Grosjean et al., 1998). Such positive tumour shrinking effects led to the approval of Foscan® as well as NPe6 for cancer whilst Verteporfin is approved for the treatment of macular degeneration (Babu, Sindelo et al., 2021, Mae, Kanda et al., 2020, Shi and Sadler, 2020). Although chlorin-based PS are more potent than Photofrin®, problems in poor tumour selectivity, poor clearance times, poor solubility and the onset of pain during treatment were noted (Allison, Downie et al., 2004).

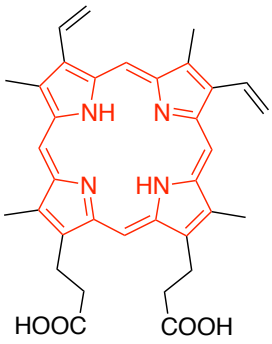

Protoporphyrin IX

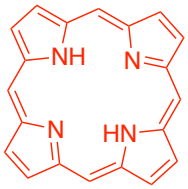

Porphyrin

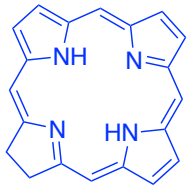

Chlorin

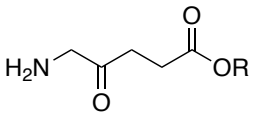

R = H Aminolevulinic acid, Levulan®
R = CH_3 Metvix®
R = C_6H_{13} Hexvix®

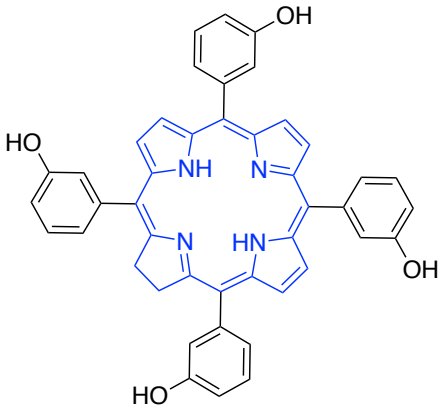

Foscan®/Temoporfin

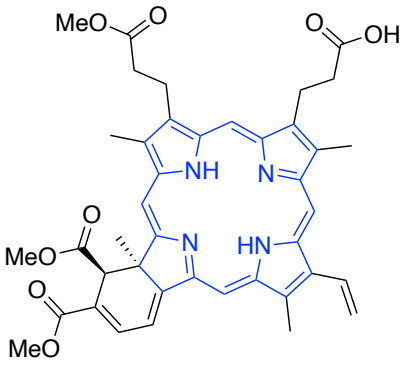

Verteporfin/Visudyne®

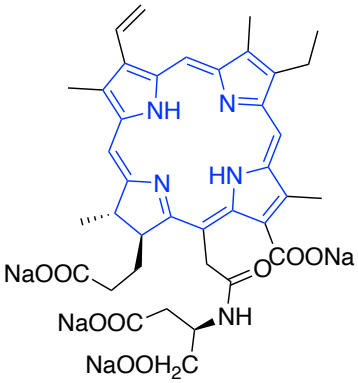

Telaporfin sodium/NPe6

Figure 1.7 A panel of second-generation PS based on porphyrins (red) and chlorins (blue). All have received approval in at least one country for use as cancer PDT treatment.

Despite multiple 2nd generation PS being approved for cancer PDT, the same drawbacks still existed as with Photofrin®. Some improvements were made in terms of tumour selectivity (Levulan®, Hexvix®, Metvix®) as well as slightly red-shifting the absorption (Verteporfin, Foscan®). However, problems due to poor solubility/cellular

uptake, long clearance times, poor tissue penetration and tumour selectivity still existed.

1.1.8 – Emergence of the 3rd Generation

Presently, a new batch of PS are being developed which build upon and aim to improve the aforementioned drawbacks of the 1st and 2nd generation. These 3rd generation PS are widely categorised by their conjugation and/or as multi-modal systems which improve/add a PDT beneficial property. Examples amongst the literature include conjugation to antibodies for tumour selectivity, multi-model nanoparticles for enhanced delivery and red-light absorbing moieties for tissue penetration (Dave, Desai et al., 2012, Gualdesi, Vara et al., 2021, Park, Cho et al., 2018).

1.1.9 – Combination PDT

PDT is an effective standalone cancer treatment but can also be used in combination with other cancer therapies. PDT has been shown to be effective upon partnering with conventional chemotherapy, immunotherapy and surgical abstraction. For example, 5-ALA combined with doxorubicin, a common chemotherapeutic, greatly inhibited tumour growth compared to each therapy alone (Casas, Fukuda et al., 1997). Similar results have been reported using a combination with other chemotherapeutics such as gemcitabine, methotrexate, mitomycin C amongst many others (Crescenzi, Chiaviello et al., 2006, Hatse, De Clercq et al., 1999, Hu, Wang et al., 2021a, Ma, Steen et al., 1992). Surgical tumour abstraction can proceed multiple rounds of PDT to cause tumour shrinkage which permits the extraction of a more manageable mass (Salvio, Stringasci et al., 2020). Alternatively, PDT can follow surgical abstraction by treatment of the post-operative site to kill any residual cancer cells. This method is successful in both treating skin cancer and preventing recurrence (Gao, Zhang et al., 2015, Lu, Wang et al., 2014).

1.1.10 – The Role of the PS

Dosage and Administration

The first step in PDT is PS administration through a pre-determined suitable route which is dictated by PS properties and targeting effects (Figure 1.8; step 1). Such routes are categorised as enteral (e.g. oral), parenteral (e.g. intravascular or intratumoral) or topical (e.g. patches or cream)(Cheng, Xu et al., 2008). In terms of administration ease and patient comfort, enteral and topical routes are superior but are often difficult to achieve in drug design (Drugs, 1997). Through the consideration of PS properties, a route which gives optimum PS biodistribution and bioavailability is selected (Mignani, El Kazzouli et al., 2013). Most 1st and 2nd generation PS are parenterally administered (intravenously and intratumorally) such as Photofrin®, Foscan®, Visudyne®, NPe6 and Levulan® (the latter of which can also be topically administered)(Bellnier and Dougherty, 1996, Chen, Yu et al., 2005, Ichikawa, Takeuchi et al., 2004, Kobayashi, Liu et al., 2006, Kübler, Haase et al., 1999). This is due to a favourable rapid increase in both bioavailability and biodistribution upon PS deposition into the bloodstream (Cheng, Xu et al., 2008, Stoner, Harder et al., 2015). Parenteral administration can be problematic for hydrophobic PS which have to be solubilised with a vehicle. Without this, many current PS are found to cause phlebitis and/or hemolysis due to their hydrophobicity (Lamch, Bazylińska et al., 2014, van Duijnhoven, Rovers et al., 2005)

Drug – Light interval

Following administration, an allotted time interval is allowed for adequate PS biodistribution into the tumorous region. In the bloodstream, hydrophobic PS adhere to lipoproteins such as high density lipoproteins, HDL, whilst hydrophilic PS tend to adhere to albumin which are then transported around the body (Castano, Demidova et al., 2004). In the short term, PS enrichment of the blood is favoured whilst longer intervals favour PS cellular uptake (Li and Luo, 2009). This time-dependent localisation forms the basis of the drug-light interval which is defined as the time between PS administration and irradiation (Figure 1.8, steps 2 – 3)(Chen, Pogue et al., 2006). Due to short term blood enrichment, short drug-light intervals majorly damage the tumour vasculature (Sheng, Ong et al., 2020). This can be beneficial in

starving and killing the tumour but can conversely promote angiogenesis and/or metastasis of surviving hypoxic cells (Chen, Roskams et al., 2002, Gomer, Ferrario et al., 2006). In contrast, long drug-light intervals promote tumour death due to adequate PS uptake occurring from the bloodstream which minimises off-target toxicity (Li and Luo, 2009). Furthermore, through the manipulation of the drug-light interval, the benefits of both vascular and cell targeted PDT can be achieved through staggered PS administration and irradiation (Lupu, Thomas et al., 2009).

Cell death and clearance

Following the irradiation of the tumorous site with a suitable light source, photosensitisation causes tissue death (Dougherty, Kaufman et al., 1978). Through tumour-specific localised irradiation, PDT effects should be restricted thereby reducing healthy cell death which offers an advantage over conventional chemotherapies (Pei, Sun et al., 2019). This forms the basis of PDT whereby all tissues not subjected to irradiation will not undergo cell death due to no production of $^1O_2$. Following PDT, an adequate and rapid PS clearance should occur which prevents healthy tissue damage from prolonged exposure or PS accumulation, problematic for 1st and 2nd generation PS (Bellnier, Ho et al., 1989, Kostron, Fiegele et al., 2006). An improvement to PS clearance is one of the developmental aims of 3rd generation PS. For example, nanoparticle-PS conjugates are currently in development to favour rapid renal clearance, an excretion route which is desirable but normally difficult to achieve (do Reis, Helal-Neto et al., 2021, Guo, Wu et al., 2018, Hu, Wang et al., 2021b).

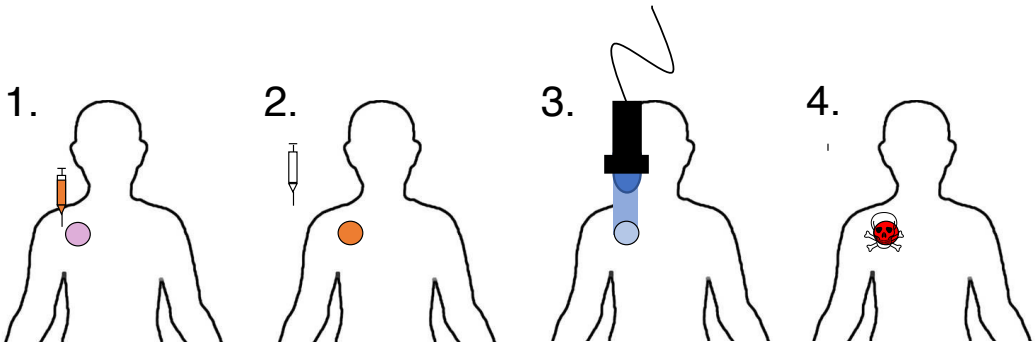

Figure 1.8 The process of PDT in cancer treatment; 1) PS is administered to cancerous region 2) PS distributes and accumulates in cancerous area 3) The PS uptaken cancerous area is irradiated by light 4) $^1O_2$ and ROS generation leads to localised cell death.

1.1.11 – The Role of Light

Light dose

The Beer-Lambert Law is used to measure the absorbing ability of a PS at a particular wavelength (Swinehart, 1962). There, A is equal to absorbance, c is PS concentration (usually in mol/litre, M), l is the path-length of the solution cell (in cm) and ε the molar absorptivity coefficient ($M^{-1}cm^{-1}$) which is proportional to the electronic transition probability (Calloway, 1997).

$$A = \varepsilon c l$$

To optimise PDT activity, a wavelength of light should be selected where the PS absorbs well which is then followed by irradiation using a light source capable of producing appreciable levels of light in said region. The number of absorbed photons, N_{ph}, can be modelled over the entire spectrum of the light source (Schaberle, 2018).

$$N_{ph} = \Delta t \sum \frac{P}{h\upsilon}(1 - 10^{-A})$$

This model introduces several important parameters, namely the time of irradiation Δt, light power P, frequency υ, and absorbance A. However, this is a purely solution devised model and any *in vivo* effects such as tissue light penetration (which will reduce N_{ph}) are ignored. Generally, PS light absorption is modelled by 3 different methods; direct, implicit and explicit prior to clinical exposure (James, Cheruku et al., 2018). Direct methods are very rudimentary and involve the direct measure of singlet oxygen via its emission decay in solution (Zhu and Finlay, 2008). Explicit dosimetry uses methods which ties together but separately treats the effect of light with PS and oxygen in a biological setting and thus includes tissue effects (Wilson, Patterson et al., 1997). Implicit dosimetry employs similar methods to explicit but instead combines PS, light and oxygen into one unifying parameter (Wilson, Patterson et al., 1997).

Power

One such variable is the power of the light source which should be sufficiently high enough to photoactivate PS, leading to $^1O_2$ generation (particularly at low N_{ph}). However, high powers can invoke adverse effects at sublethal doses leading to undesirable, non-specific necrosis and heating (Kessel and Oleinick, 2018, Shafirstein, Bellnier et al., 2018). In addition, an increase to the light source power can increase the rate of PS photobleaching which is particularly problematic for Photofrin® (Georgakoudi, Nichols et al., 1997).

Fluence rate

The fluence rate is also an important parameter which is the measure of light energy delivered per unit area of tumour (Pandey, Dougherty et al., 2016). High fluence rates drastically increase rates of photobleaching and hence depletes $^1O_2$ generation of cyanine dyes (James, Cheruku et al., 2018). Furthermore, high fluence rates can deplete cell oxygen levels causing an overtake of PS photoactivation which invokes temporary hypoxia (James, Cheruku et al., 2018). Therefore, fluence rates should be tightly controlled particularly in regions of tumour hypoxia (Sitnik, Hampton et al., 1998). Finally, an appropriate light source should be selected to uniformly treat the tumour through an optimum homogenous fluence rate on a heterogenous tumour which can be difficult (Hu, Wang et al., 2021a).

Tissue Penetration

One of the major drawbacks of PDT is the limited tissue penetration of photoactivation wavelengths. Short wave visible light (400 – 650 nm) is poorly transparent to tissue which leads to treatment difficulties on tumours below 3 mm (Li, Chen et al., 2020)(Figure 1.9). Incidence light is reduced through its absorption by tissue-present haemoglobin and/or porphyrin components which increases opacity in the short wave region (Weissleder, 2001). The optimum tissue transparency region is near infra-red (NIR) light which is split into NIR I (700 – 1000 nm) and NIR II (1000 – 1700 nm)(Zhao, Zhong et al., 2018). NIR I is more suitable for PDT when compared to NIR II, due to the latter converging into the water absorbing region which leads to heating (Dang, He et al., 2017). Photoactivation of PS in NIR I (700 -

1000 nm) is therefore highly desired due to enhanced tissue penetration and lower scattering effects which culminates in fewer off-target effects (Zhao, Xu et al., 2021). Unfortunately, all 1st and 2nd generation PS are photoactivated outside of this range and cannot be used to treat deep lying tumours. The mitigation of this issue remains a top priority in the design of emerging 3rd generation PS (Sarcan, Silindir-Gunay et al., 2018).

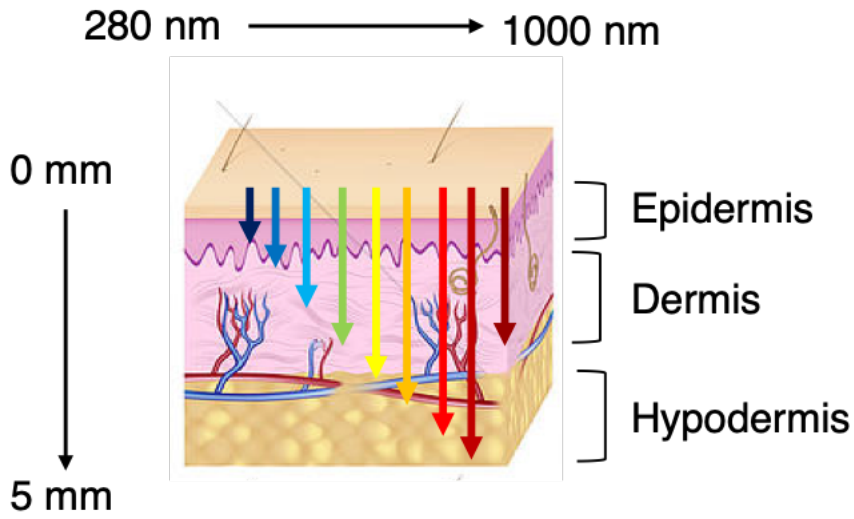

Figure 1.9 Tissue penetration varies across the visible light spectrum. The optimum window exists in the NIR I region (700 – 900 nm) whereby absorption of water and porphyrins are minimal.

1.1.12 – The Role of Oxygen

Reactive Oxygen Species (ROS)

Reactive oxygen species (ROS) broadly defines a multitude of bio-damaging oxygen-based species which includes radicals, excited molecules, ions and oxidising agents (Bayr, 2005)(Figure 1.10). ROS species are largely categorised into radicals (superoxide $O_2^{\bullet -}$, hydroxyl $OH^{\bullet}$, peroxyl $ROO^{\bullet}$) and longer living non-radical (singlet oxygen $^1O_2$, hydrogen peroxide H_2O_2, hydroperoxides ROOH)(Liou and Storz, 2010). ROS are enzymatically produced and regulated within biology and elicit both beneficial and harmful effects depending on their endogenous levels (Yu and Zhao, 2021). Both the mitochondria and peroxisomes are major cellular sites with endogenously high levels of ROS, primarily superoxide and peroxides (Liou and Storz, 2010). Although $^1O_2$ is categorised as a non-radical ROS, its short lifetime and

high reactivity is more comparable to a radical (Ogilby, 2010, Yu and Zhao, 2021). The nature of ROS makes them difficult to separate owing to their rapid interconversion whereby radical ROS species generate non-radical ROS (Yu and Zhao, 2021). Despite this, an overwhelming production of any type of ROS can kill cells through reaction with proteins, lipids and/or nucleic acids (Ogilby, 2010, Zhang, Wang et al., 2016).

Photophysics of $^1O_2$

O_2 effectively behaves as an energy relay through the quenching of ^{3}PS* by energy transfer which then extends onto biomolecules through oxidation. The quenching ability of O_2 on ^{3}PS* can be measured by the Stern-Volmer equation (Hall and Chignell, 1987).

$$\frac{\tau_0}{\tau} = 1 + k_q \tau_0 [Q]$$

The higher the ratio of the lifetime of ^{3}PS* (τ_0/τ) determined with (τ) and without (τ_0) quencher [Q] (such as O_2), the higher the quenching constant (k_q), which thereby measures quencher strength. Upon the energy transfer from ^{3}PS* onto ground state oxygen, $^3O_2$ ($X^3\Sigma_g^-$), two singlet excited states can be formed which are spin-paired $^1O_2$* ($a^1\Delta_g$) and spin unpaired $^1O_2$* ($b^1\Sigma_g^+$)(Figure 1.10)(Khan, 1976). Although higher in energy, the b1 state's reactivity remains low in water and it instead majorly decays into the a1 state which possesses reactive chemistry due to an empty molecular orbital (Scurlock, Wang et al., 1996). The diffusion distance, d, models the reactivity of the a1 species in a cellular environment through the equation below.

$$d = \sqrt{6tD} \qquad t = 5\tau$$

$^1O_2$ in water has a measured lifetime, τ, of 2 – 3.5 μs and a measured diffusion coefficient, D, of 4 x 10^{-6} cm^2s^{-1} which gives a diffusion distance of 155 nm (Mehraban and Freeman, 2015). By translating this value into cellular dimensions, $^1O_2$ would cause localised damage to the site of PS accumulation which could be

organelle specific (Skovsen, Snyder et al., 2005). Furthermore, $^1O_2$ is sufficiently long-lived to be able to survive multiple diffusive collision targets before finally reacting with a selected entity (Ogilby, 2010).

A)

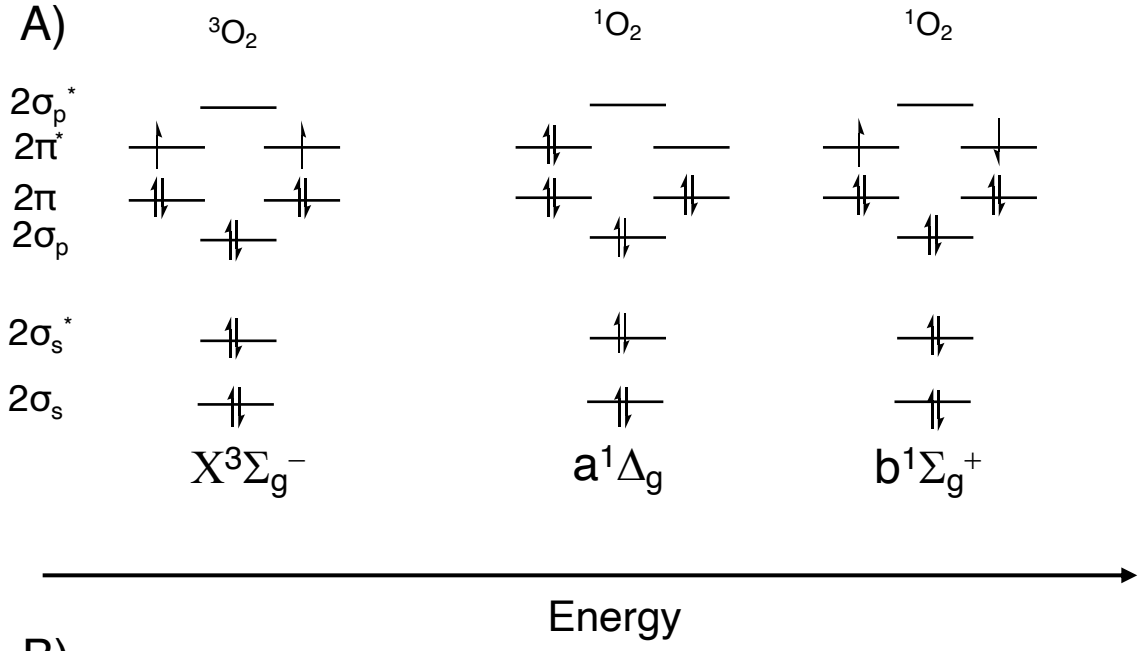

B)

Type of ROS	Examples
Radical-based	$OH^{\bullet}$ $ROO^{\bullet}$ $HOO^{\bullet}$ $O_2^{-\bullet}$
Non-radical based	$^1O_2$ H_2O_2 ROOH

Figure 1.10 A) The molecular orbital diagrams of three electronic states of O_2 B) A summary of non-radical and radical ROS important for photosensitisation in PDT.

1.1.13 – Designing Photosensitisers

Quantifying and Comparing PS agents

Newer PS are designed with several desirable properties which aim to mitigate the limitations of the 1st and 2nd generation agents. This is quantified based on PS ability to induce high phototoxicity whilst remaining poorly cytotoxic in the dark. This requirement is measured by the 'phototoxic index', PI, which is calculated as shown below (Naik, Rubbiani et al., 2014).

$$PI = \frac{LD_{50}(dark)}{LD_{50}(light)}$$

The PI is superficially beneficial to researchers for PS comparison owing to the measure of the PI magnitude with a PS's phototoxic increase factor. However, additional factors can affect the PI without necessarily being too impactful on PDT efficiency. PS water solubility can limit the LD_{50}(dark) through vehicular toxicity effects (e.g. DMSO). Therefore, poorly water-soluble PS have a capped upper limit to their PIs but could themselves remain non-toxic beyond this vehicle limit. Conversely, powerful PS with small LD_{50}(light) differences produce fluctuating PI values that are sensitive to sub μM doses. For example, two hypothetical PS with the same LD_{50}(dark) (100 μM) but different LD_{50}(light) values (0.1 vs 0.3 μM) will have PI values of 1000 vs 333. This implies that the PS are markedly different but are in fact very similar. Therefore, an analysis of multiple PS properties should be considered upon a comparison such as photoactivation, conjugation compatibility, clearance times, toxicity effects, laser power and solubility.

Desirable PS Qualities

Under the aforementioned pre-requisites, several desirable design qualities can be highlighted for targeted improvement in PS development.

1. Singlet oxygen generation (particularly type II)
2. Low dark toxicity
3. High light toxicity
4. High light absorption
5. Photoactivation in the optimum tissue penetration window
6. Selective tumour targeting
7. Good water solubility for administration
8. Good lipophilicity for cellular uptake and biodistribution
9. Resistance to photobleaching
10. Short tissue clearance times

1.2 – Transition Metals as Photosensitisers

1.2.1 – Transition Metals

Recently, an increased interest in developing transition metal PS has emerged. A transition metal is any element whose ions have partially occupied d orbitals. They are grouped together in the Periodic Table in 3 rows which constitute the 3rd, 4th and 5th rows and are termed 1st, 2nd, and 3rd row transition metals, respectively (Griffith, 1964). Transition metals form a wide variety of compounds, most notably co-ordination complexes with organic-based ligands. These ligands donate electrons to the metal atom/ion and exist as either neutral or charged species (Irving and Williams, 1953). The ligands and/or metal's molecular orbitals can then interact in the following ways by the movement of an electron through photon absorption;

1. Metal centred (MC): d-d orbital transitions between the t2g and eg* orbitals.
2. Ligand centred (LC) transitions, most often $\pi - \pi^*$ transitions located on aromatic ligands.
3. Charge transfer (CT) transitions which involve a shift of electron density from ground state orbitals based on one "part" of the complex to another. CT transitions can be of ligand-to-ligand (LLCT), metal-to-ligand (MLCT), ligand-to-metal (LMCT) and metal-to-metal (MMCT) types (Vogler and Kunkely, 2001).

CT transitions are often the most suitable for PDT as they have moderately high extinction coefficient ($\varepsilon \sim 10^3 - 10^4$ $M^{-1}cm^{-1}$) and are relatively low in energy which often results in intense absorption of visible light (Lever, 1974). In contrast, MC transitions are often favourably low in energy but poorly absorbing owing to selection rules forbidding d-d transitions (Farrer, Salassa et al., 2009, Nolet, Beaulac et al., 2004). Conversely, LCs are more highly absorbing ($\varepsilon > 10^5$ $M^{-1}cm^{-1}$) but usually lie within the higher energy, poorly penetrating and mutagenic UV region (Ma, Zhang et al., 1998).

1.2.2 – Spin Orbit Coupling

During PDT, $^1O_2$ is generated via a non-radiative energy transfer from ^{3}PS* that is rapidly populated through ISC from ^{1}PS* (Beljonne, Shuai et al., 2001). The rate of ISC can be increased by a process called spin orbit coupling, which in turn is increased by the 'heavy atom effect' which increases in proportion to the atomic number (Pomarico, Pospíšil et al., 2018). Spin orbit coupling is a phenomenon which permits normally forbidden singlet-triplet transitions to occur by quantum mechanically distorting the purity of the electronic spin-multiplicity states (Koziar and Cowan, 1978). This causes the potential energy surfaces of ^{1}PS* and ^{3}PS* to overlap creating an interface leading to ISC (Stone, 1976). The proportional strength of spin orbit coupling relates to the nuclear charge of the species, Z, and is derived from a relativistic parameter, Z/r^3, whereby r is the radial distance (Marian, 2012). An increase of Z therefore leads to an increase in spin orbit coupling which accelerates ISC leading to the population of long-lived ^{3}PS* capable of oxygen interaction (Marian, 2012). However, spin orbit coupling must be tightly controlled for PDT as it can also increase ^{3}PS* - ^{1}PS decay alongside ^{1}PS* - ^{3}PS* thereby shortening ^{3}PS* lifetime and limiting $^1O_2$ generation (Zhang, Hou et al., 2020). Transition metal complexes, in particular those in the 'Platinum Group', have a suitable heavy atom effect leading to long lived ^{3}PS* beneficial for PDT (Chou, Chi et al., 2011, Higgins and Brewer, 2012).

1.2.3 – Tuneability

In addition to desirable photophysical properties, transition metal complexes benefit from high tuneability through ligand-based exchanges/modifications and metal-based oxidation state changes. These can be incorporated into complex design to elicit a particular effect, such as organelle targeting. It has been shown that intrinsically regulated cell death pathways can be activated through targeting the mitochondria, the endoplasmic reticulum (ER), the lysosomes, DNA and other specific proteins during PDT (Huang, Banerjee et al., 2018). For example, transition metal complexes tend to passively associate with the mitochondria owing to their often charged nature, but enhanced targeting can complement this through the

addition of PEG chains (Li, Liu et al., 2010). Alongside boosting passive targeting effects, modifications can be made through active targeting of a specifically unique feature of an organelle. For example, a near complete mitochondrial localisation of a transition metal complex can be achieved through the conjugation of mitochondrial-DNA binding metallohelices to the complex's ligands (Li, Wu et al., 2020). The photophysical properties of transition metal complexes can also be modified through ligand-based exchanges and/or addition. A measured red-shift in the light absorption of a manganese phthalocyanine complex facilitated an improvement to its tissue penetration upon the exchange of more sterically hindered and electron poor axial ligands (McKearney, Zhou et al., 2019). Similarly, often simple ligand modifications can vastly affect cell toxicity. An Ir(III) PS complex displayed a drastic increase in dark toxicity upon the simple addition of a methyl group thus rendering it unsuitable for PDT. Upon methyl removal, the complex became 15 x less dark toxic which increased its PI by a factor of 25 and thus became highly effective for PDT (McKenzie, Sazanovich et al., 2017). The physical properties of transition metal PS can also be tuned to increase administration and biodistribution. This includes inclusion/removal of hydrophilic/hydrophobic moieties which balances water solubility and DNA interaction in Cu(II) porphyrin compounds and thereby induces cancer cell cycle arrest (Zhang, Zhang et al., 2020). Transition metal complexes offer promising opportunities in tailoring to a particular PDT enhancing need via ligand-based alterations which can alter organelle targeting, light absorption and solubility.

1.2.4 – Transition Metal PS

Solutions to PDT problems

As discussed above, transition metal complexes can help to alleviate a multitude of problems associated with 1st and 2nd generation PS. These can be summarised as followed (Baggaley, Weinstein et al., 2012, McKenzie, Bryant et al., 2019).

Problem	Solution inherent to transition metal complexes
Small light absorption coefficients	Generally larger through a variety of transitions.
High photobleaching rates	Smaller photobleaching rates and higher photostability than organic-based PS.
Solubility	Tuneable via ligand modifications (e.g. sulphonate groups) and/or metal oxidation state changes.
Red-shift absorption	Tuneable via ligand modifications (e.g. dyes) and/or oxidation state changes.
Tumour selectivity	Tuneable via ligand modifications (e.g. PEG) and/or oxidation state changes.
Singlet oxygen generation	Fast rates of $^3PS^*$ population due to the heavy atom effect leading to $^1O_2$ generation.
Poor cellular uptake	Tuneable via ligand modifications and/or oxidation state changes.

Considering this, several labs have developed pre-clinical transition metal PS with one agent currently undergoing clinical trials. Much work has focused on ruthenium complexes while the focus of this thesis is on iridium and platinum. Landmark developments in PS development with Ru(II) and Ir(III) are therefore presented below. However other metals such as Os have also received attention for their PDT effects.

Ru(II) complexes

Arguably the most popular transition metal employed for PDT is Ru(II). This interest originated upon the characterisation of a photoactive complex, $[Ru(bpy)_3]^{2+}$, along with its derivatives which are used in catalysis, solar energy harvesting and sensing (Bedoya, Díez et al., 2006, Foley, Lee et al., 2009, Morseth, Wang et al., 2015). Ru(II) forms octahedral complexes with d^6 high-field fully occupied electronic orbitals. Furthermore, Ru(II) complexes generally have low cytotoxicity due to their mimicry of biologically abundant Fe(II) (Clarke, Zhu et al., 1999, Kanaoujiya, Singh et al., 2020). This makes Ru(II) complexes efficient light harvesters, singlet oxygen

generators and sufficiently modifiable PS (Liu, Zhang et al., 2018). Over the past decade, a multitude of Ru(II) PS have been identified with remarkable biological chemistry (Liu, Zhang et al., 2018, Monro, Colón et al., 2018, Poynton, Bright et al., 2017). This culminated in a Ru(II) complex, termed TLD1433, entering into clinical trials for its anticancer properties (Figure 1.11)(Monro, Colón et al., 2018).

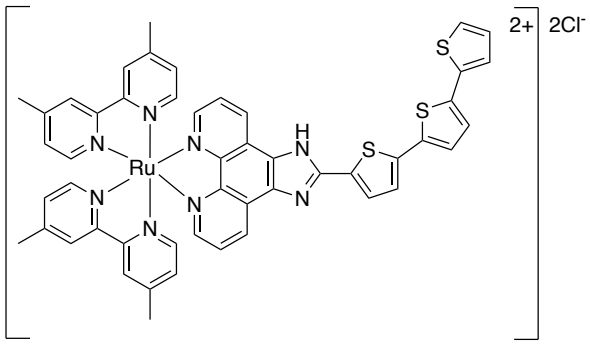

TLD1433

Figure 1.11 TLD1433, a Ru(II) complex currently in clinical trials as a PDT treatment for non-muscle invasive bladder cancer .

As of 2020, TLD 1433 has entered Phase II clinical trials for specifically treating high-risk non-muscle invasive bladder cancer through PDT (Chamberlain, Cole et al., 2020). TLD1433 is administered by bladder instillation before a drug-light interval of 1 hour is followed by green light irradiation (500 – 520 nm), resulting in cancer necrosis (Lilge, Roufaiel et al., 2020). Preliminary results have suggested TLD1433 is both an effective and safe PS with high tumour regression (McFarland, Mandel et al., 2020). As of February 2021, the recruitment for a phase II study is ongoing to recruit 100-125 bladder cancer patients for 1 round of TLD1433 PDT treatment on day 0 and again at day 180 (www.clinicaltrials.gov, identifier NCT03945162). In addition, the rate of remission will be tracked 360 days post treatment and will hence take 3 years to complete upon trial commencement. The promising and positive TLD1433 preliminary results paves the road for future transition metal PS development.

Ir(III) complexes

Within the past few years, Ir(III) has received widespread attention for its ability to facilitate PDT. Ir(III), like Ru(II), is a d^6 metal ion which has fully occupied t2g orbitals and also forms octahedral complexes with ligands. However, Ir(III) ions are more cationic than Ru(II) and are more likely to form charged complexes which benefits their water solubility (Huang, Banerjee et al., 2018). Simultaneously, their cellular uptake can be increased through ligand-based modifications leading to increases in lipophilicity which enhances their administration and uptake (McKenzie, Bryant et al., 2019). Furthermore, iridium is a 3rd row transition metal and therefore has a higher atomic number, Z, than 2nd row transition metals such as ruthenium. An increased Z value leads to an increased heavy atom effect which results in faster rates of ISC favouring $^1O_2$ generation (Bi, Yang et al., 2020). These advantages over ruthenium have contributed to a rapid increase in Ir(III) PS development (Figure 1.12)(Appendix 1). All these complexes have exhibited increased phototoxicities in comparison to their cytotoxicities which is an essential condition for PDT. Additionally, they have been tuned in their designs to increase their PDT effects. These include specific organelle targeting (**1, 5, 7, 11, 12**) and red-shifted absorptions (**4, 6**) through employment of active targeting and complexation with dyes. Due to their high organelle affinity, regulated cell death pathways become activated upon irradiation (**1, 2, 3, 4, 5, 7, 8, 9, 10, 11, 12**). This benefits the clearance of cellular debris by the immune system which reduces healthy cell damage and aids wound healing (Majno, La Gattuta et al., 1960, Rock and Kono, 2008).

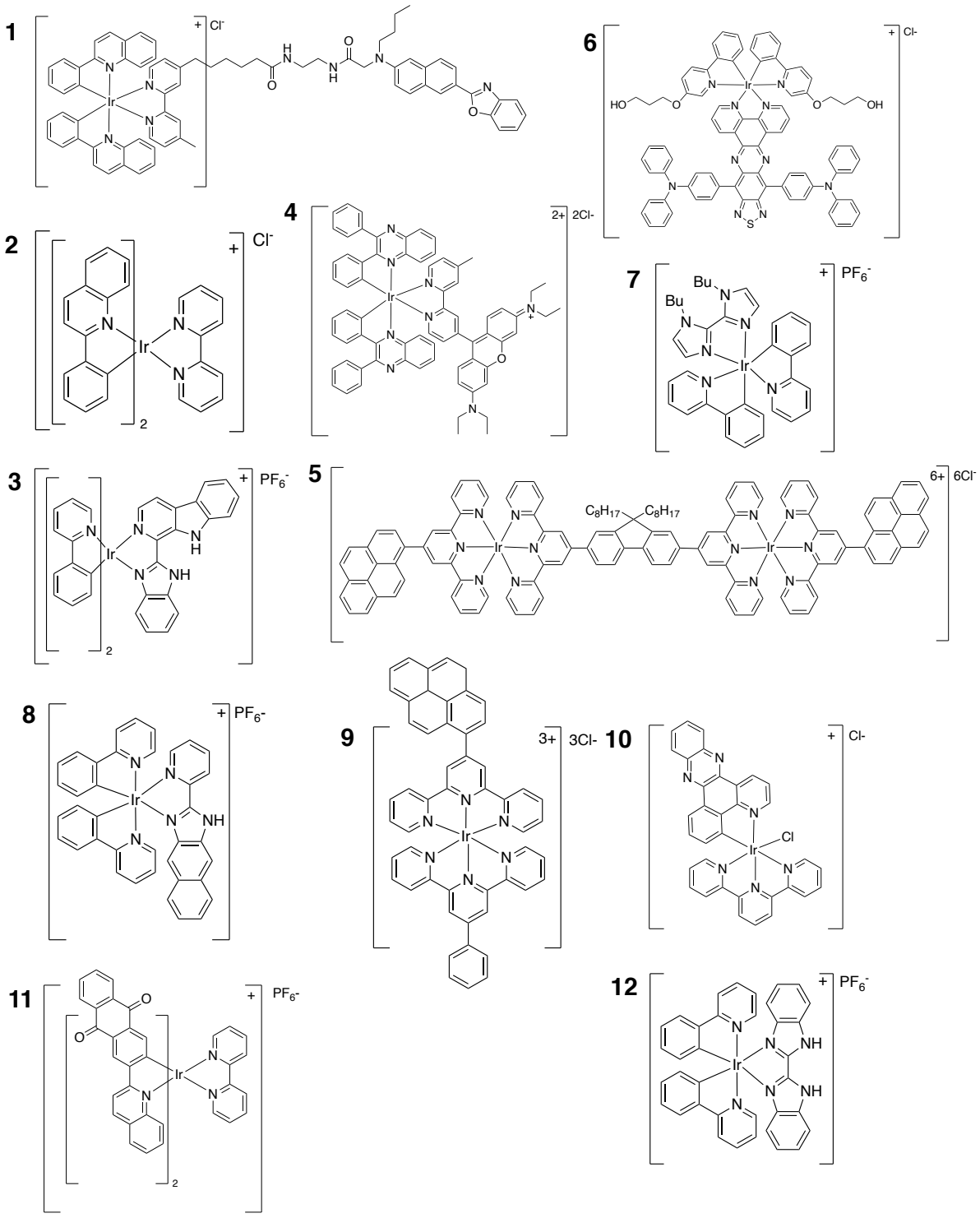

Figure 1.12 A panel of Ir(III) compounds which have been investigated for their use as PS for PDT. Accompanying information of each compound's LD_{50}(dark), PD_{50}(light), photoactivation range, localisation and cell death mechanism are detailed in Appendix 1.

1.3 – Tumour Biology and its Influence Over PDT Success

1.3.1 – Tumour Architecture

The tumour microenvironment (TME) is defined and characterised by the collection of cancer cells inside an abnormally constructed stromal network (Sorrin, Kemal Ruhi et al., 2020). In healthy tissue, the stromal network is highly organised which facilitates the delivery of nutrients and the removal of waste as opposed to the tumorous stroma which is disorganised, unregulated and hyper permeable (Siemann, 2011). Through the promotion of angiogenesis, cancer cells create a vascular system to feed their hyperplastic needs leading to an over demanding energy requirement (Folkman, 1995). This creates a mismatch between cancer cell proliferation, pro-vascular signalling and vessel growth leading to an irregular, dilated and maligned vascular network (Iyer, Khaled et al., 2006). This in turn gives rise to a passive tumour selective uptake mechanism known as the enhanced permeability and retention (EPR) effect (Figure 1.13). Upon the TME inflow of PS-containing blood, the poorly constructed vasculature leads to a trapping effect which is particularly pronounced for macromolecules which causes an enhanced retention in comparison to normal tissue (Maeda, 2001). This is accompanied by poor TME lymphatic drainage which further adds to PS retention and causes a build-up of interstitial fluid (Ngoune, Peters et al., 2016). Poor vascularisation also contributes to the formation of tumour heterogeneity which causes a gradient of hypoxia and acidosis in the TME (Ward, Langdon et al., 2013). Increases in both hypoxia and acidosis is attributed to poor vascularisation which causes a shift in growth fuelled by glycolysis whose by-products lower pH (Stylianopoulos, Martin et al., 2012).

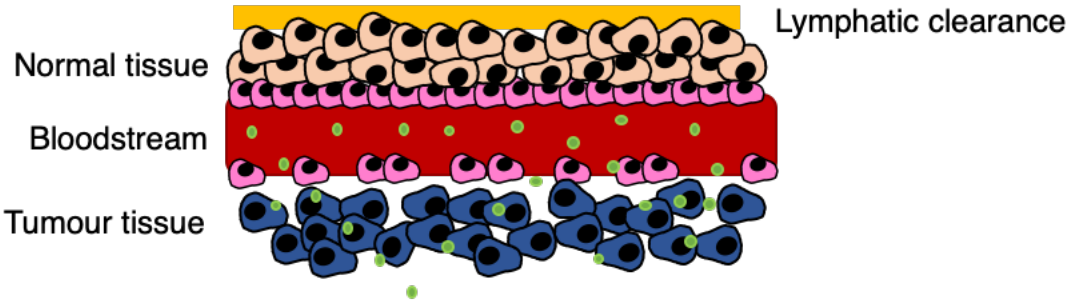

Figure 1.13 The EPR effect is facilitated through preferential drug uptake (small green circles) in tumourous tissue vs normal tissue through a mixture of leaky vasculature and poor lympathic clearance.

1.3.2 – Hypoxia

Both type I and type II PDT mechanisms are oxygen dependent and therefore critically rely on the oxygenation of tumorous tissue in order to produce photosensitisation (Du, Shi et al., 2021). Fast-growing tumours and tumours in advanced stages have an insufficient blood vessel network which inhibits both their oxygenation and nutrition in their innermost dense regions. O_2 has a measured tissue diffusion limit of ~ 150 μm which causes a rapid decrease to cell oxygen levels at those with increased distances to blood vessels (Brahimi-Horn, Chiche et al., 2007). This leads to the centremost region of the tumour being highly dense, necrotic and de-oxygenated (hypoxic)(Wilson and Hay, 2011). Due to inherent hypoxia, these deprived cells have high levels of cytoplasmic HIF-1 which leads to the genomic expression of proteins which increase angiogenesis (VEGF) and glycolysis (GLUTI) (Figure 1.14)(Dang, He et al., 2017). Additionally, HIF-1 activates cancer cell metastasis promoting pathways (CXCR4, CA IX, LOX) which increases their rate of migration and re-establishment to form metastatic secondary tumours (Bennewith and Dedhar, 2011). This can be problematic for PDT whose mechanisms cause a further expenditure of oxygen alongside the destruction of the outermost cells which can liberate metastatic cancer cells. This implies that post PDT treatment, central hypoxic cells which survive become even more hypoxic, metastatic and resistant to treatment (Jin, Lovell et al., 2013). The oxygen requirements for PDT have been modelled in animals which found that treatment was nullified in anoxic conditions,

was half effective at 0.5 - 1 % saturated O_2 levels and unaffected at 5 % levels (Chapman, Stobbe et al., 1991, Henderson and Fingar, 1987). Additionally hypoxic tumours are also resistant to other chemotherapeutics and radiotherapy which highlights the importance to their treatment (Dang, He et al., 2017, Vaupel, Thews et al., 2001). The 3rd generation of PS focus on the mitigation of hypoxia which includes nanoparticle induced tissue re-oxygenation, conjugation with catalases, and hyperbaric oxygen therapy (Cheng, Cheng et al., 2015, Maier, Anegg et al., 2000, Phua, Yang et al., 2019).

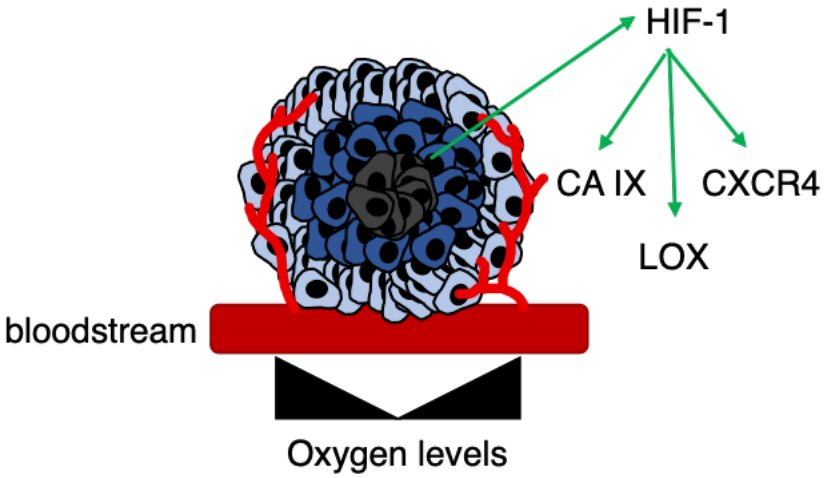

Figure 1.14 Solid state tumors can exhibit hypoxia due to poor vascularisation of the tumor microenvironment (TME) alongside the limited diffusion distance of oxygen. This establishes a gradient of increasing hypoxia upon core penetration.

1.3.3 – Mechanisms of Cell Death Induced by PDT

Apoptosis

PDT can cause cancer cell death through the activation of apoptosis which is a genetically encoded pathway (Lawen, 2003). A set of responsive and regulated pathways trigger apoptosis which culminates in the activation of caspases. Caspases are responsible for the initiation, propagation and the organised dismantling of cellular structures (Reed, 2000). Intrinsic apoptosis is activated through organelle damage which causes a disruption to the mitochondrial membrane leading to the leakage of cytochrome c oxidase (CytoC) (Jiang and Wang, 2004). Upon CytoC leakage into the cytosol, an association with Apaf-1 forms an apoptosome which cleaves and activates caspase 9, the activator caspase (Figure

1.15)(Cai, Yang et al., 1998). Caspase 9 further activates the 'executioner caspases' (caspase 3, 6 and 7) who cause morphology changes, DNA fragmentation and cellular condensation which results in membrane blebbing (Jänicke, Sprengart et al., 1998). This is accompanied by ROCK-1 cleavage which activates, modifies and packages fragmented DNA into smaller bodies which migrate to the membrane (Coleman, Sahai et al., 2001). Macrophagic recruitment and engulfment is then triggered by these apoptotic bodies which express 'eat me' signals on their membranes (Nagata, 2018). Furthermore, a well-monitored and dynamic cellular equilibrium constantly exists between pro-apoptotic factors (e.g. p53 and Bax) and anti-apoptotic factors (e.g. Bcl-2 and its relatives) whose endogenous levels causes/prevents apoptosis (Lawen, 2003, Meier, Finch et al., 2000). Photodamage to the endoplasmic reticulum (ER), lysosomes and the mitochondria have been specifically identified to trigger apoptosis. Through ER photodamage, Ca^{2+} leaks into the intracellular space which leads to apoptosis through the swelling and bursting of the mitochondria (Oleinick, Morris et al., 2002, Rizzuto, Giorgi et al., 2008). Additionally, lysosomal photodamage leads to the spillage of proteases into the cytoplasm which then activates the intrinsic apoptosis pathway (Oleinick, Morris et al., 2002). Cathepsin leakage, a lysosomal component, was found to be particularly effective at cleaving a Bcl-2 protein, Bid, which is a pro-apoptotic factor owing to its disruption of the mitochondria membrane (Stoka, Turk et al., 2001).

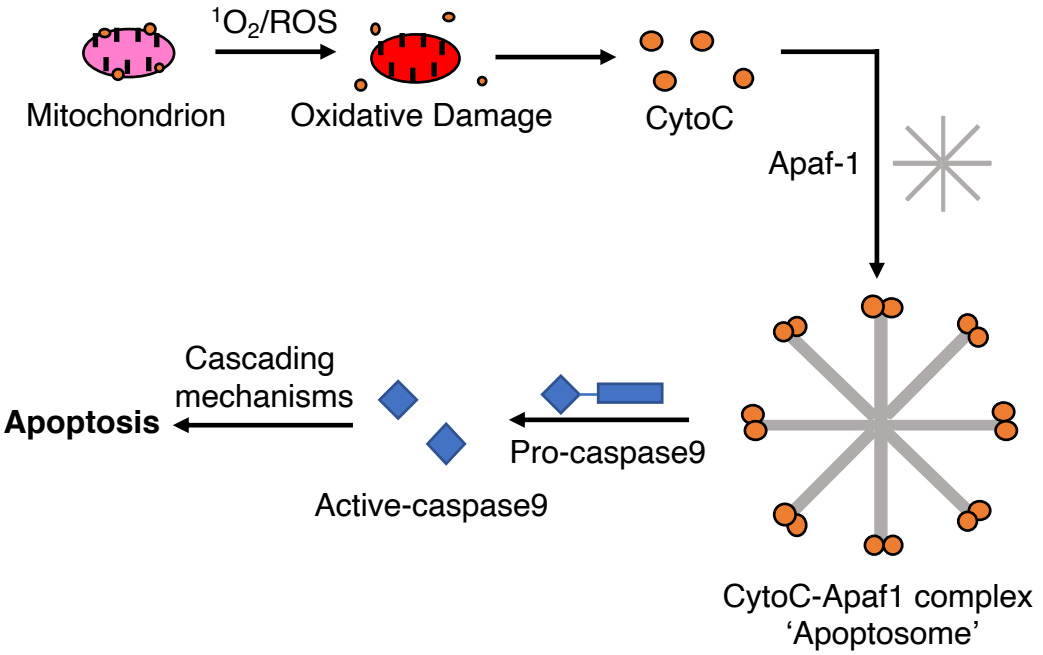

Figure 1.15 PDT activates apoptosis through oxidative damage to the mitochondrial membrane. This leads to the formation of an apoptosome which causes a destructive cascading mechanism.

Necrosis

Necrosis is a type of cell death which is passive, unregulated, and common to all cell types. The onset of necrosis can therefore be beneficial in causing cell death in cancer cells which have oncogenetically acquired an immunity to regulated cell death (Hersey and Zhang, 2003). Necrosis is induced by a cell death event which causes the plasma membrane to rupture leading to the spillage of cytoplasmic material into the exocellular space (Proskuryakov and Gabai, 2010). This spillage activates the immune system which floods the localised area with neutrophils and macrophages leading to inflammation (Majno, La Gattuta et al., 1960). The onset of inflammation along with the leakage of degrading cytoplasmic materials causes damage to healthy tissue in the inflamed region which hinders healing (Rock and Kono, 2008). The rupturing of the plasma membrane plays a critical role in necrosis and therefore PS at this locus often triggers this type of cell death (Thompson, Aggarwal et al., 2018). In addition, high laser power and high light fluence can non-specifically overwhelm cancer cells causing them to rupture (Bown, Tralau et al., 1986). Concurrently, necrosis and apoptosis can occur together based on PS dose

type which can influence their exact ratio. High doses of 5-ALA tend to favour necrosis whilst lower doses favour apoptosis. This is thought to be due to the extent of oxidative damage (Wyld, Reed et al., 2001).

Autophagy

Autophagy is derived from self (auto-) and eating (-phagy) and describes the regulated degradation of cytoplasmic material governed by the lysosomes which activate under cellular stress (Tanida, 2011). Initiation leads to the formation of a double membrane vesicle which encapsulates cellular components/organelles in the cytoplasm (Xie and Klionsky, 2007). This vesicle is known as an autophagosome whose formation is regulated through autophagy related genes (ATG) such as Atg1 kinase, a PI3K complex and mTOR which are nutrient level sensors (Sengupta, Peterson et al., 2010). The autophagosome then matures through endosome fusion which culminates in lysosome fusion to create an autolysosome (Doherty and Baehrecke, 2018). The encapsulated material is then broken down into simple molecules such as amino acids, lipids and sugars by lysosomal proteases which nourishes a nutrient deprived cell (Mizushima, Yoshimori et al., 2011). Autophagy was thought to have originally evolved as a process to promote survival in times of nutrient deprivation (Yu, Chen et al., 2018). However, extensive autophagy leads to an irreversible recovery which causes death through widespread autophagosome formation and vacuolisation (Galluzzi, Vitale et al., 2018). ATGs also functionalise to cause an inflammatory effect through their exocellular release of ATP which recruits dendritic and T cells which aids clearance (Ko, Kanehisa et al., 2014). However, it can be argued that autophagy is not an independently recognised cell death pathway and is instead a preface to apoptosis or necrosis owing to its pro-survival origins (Doherty and Baehrecke, 2018). Despite this, PS have been identified which activate autophagy through lysosomal targeting leading to ROS induced stress (Chen, Tao et al., 2020, Song, Xu et al., 2020).

Ferroptosis

Cancer cells can be sensitive to ferroptosis which is a regulated cell death pathway caused by excess iron (Cao and Dixon, 2016, Xu, Ding et al., 2019). Ferroptosis is identified by several observable markers such as mitochondrial shrinkage which leads to membrane rupture, density changes, cristae changes but no nuclear fragmentation (Dolma, Lessnick et al., 2003, Xie, Hou et al., 2016). This is accompanied by DAMP release (damage associated molecular patterns e.g. HMGB1) which leads to macrophage recruitment and inflammation (Xie, Hou et al., 2016). Ferroptosis is activated through the accumulation of iron and lipid peroxidases, the latter being increased by GPX4 deactivation which leads to lipid alcohol regeneration (Kagan, Mao et al., 2017). The excess of iron increases ferroptosis through the generation of ROS by the Fenton reaction leading to lipid peroxidation (Xie, Hou et al., 2016). Cancer cells with acquired mutations in iron accumulation, cysteine uptake reduction, GPX4 inactivation and Ras hyperactivation can lead to sensitisation to ferroptosis (Tang and Kroemer, 2020). PDT operates through ROS generation and hence several PS have been found to work hand-in-hand in killing cancer cells pre-disposed to ferroptosis (Homma, Kobayashi et al., 2019, Turubanova, Balalaeva et al., 2019, Zhu and Finlay, 2008).

Paraptosis

Paraptosis is another form of regulated cell death which involves ER and/or mitochondria swelling followed by widespread cytoplasmic vacuolisation (Sperandio, de Belle et al., 2000). Unlike apoptosis, paraptosis is independent of caspase activation and does not involve chromatin condensation, blebbing or nuclear fragmentation (Bredesen, Rao et al., 2006). Upon the onset of damage, cytoplasmic vacuolisation leads to the swallowing of the entire cytoplasmic region without the formation of an autophagosome (Sperandio, de Belle et al., 2000). Photodamage to the ER is associated with the activation of paraptosis which is particularly pronounced in both apoptosis and autophagy resistant cells (Kessel, Cho et al., 2020). Additionally, photodamage to both the lysosomes and mitochondria triggers paraptosis through Ca^{2+} leakage. Due to the morphological similarity and eventual

convergence of apoptosis, it has been recently postulated that paraptosis could be a misidentified widespread form of PDT cell death (Kessel and Reiners Jr, 2017).

Immunogenic cell death (ICD)

Cancer cells can also be killed through the triggering of exocellular immune cells caused by excretion of DAMPs (Krysko, Garg et al., 2012). This includes calreticulin (CRT, located in the ER), heat shock proteins 70 (HSP70) and high mobility group box 1 (HMGB1) which are 'eat me' signals to activate the immune system (Chaput, De Botton et al., 2007, Garg, Krysko et al., 2012). These DAMPs are also involved in apoptosis through triggering immune clearance by activation of dendritic cells, T cells, NK cells and macrophages (Michalak, Groenendyk et al., 2009). CRT in particular is linked to ER stress and Ca^{2+} release whereas HMGB1 is found to cause inflammation through macrophage recruitment by ferroptosis (Rui, Yang et al., 2020, Xie, Hou et al., 2016). In addition to DAMPs, the immune activation and clearance of cancer cells can be facilitated through T cell recognition of tumour antigens known as major histocompatibility complex (MHC) class 1 molecules (van der Bruggen and Van den Eynde, 2006). Additionally, T cells can recognise mutant surface peptides which are inherent to cancer formation through oncogenesis (Coulie, Lehmann et al., 1995). After the immune recognition of cancer cells post PS treatment, the binding of exocellular cytokines (e.g. TNF, TNFα and IFNγ) to tumour cells can occur which results in cell death (Mroz, Szokalska et al., 2010). Through the stimulated release of DAMPs, ICD is facilitated by immune cell infiltration into the TME which increases cytokine mediated death through the recognition of antigen positive cancer cells (Gollnick, Evans et al., 2003, Mroz, Szokalska et al., 2010). Therefore, PDT can cause an additional immune response through the introduction of immune stimulating cytokines and DAMPs into the TME (Li, Ou et al., 2021, Sharma and Hamblin, 2021).

1.3.4 – PS Localisation and its Effect on PDT

Vasculature

PDT performed with short drug-light intervals mainly cause vasculature-based damage which leads to tumour cell death through starvation (Chen, Pogue et al., 2003). However, upon the destruction of the TME vasculature, the oxygen levels in the remaining tumour decrease which invokes hypoxia. This is not beneficial due to the liberation of pre-existing hypoxic cells which are highly programmed to metastasise. Secondly, any surviving tumour would be difficult to treat with a second round of PDT due to the severance of blood vessels and the reduction of oxygen thereby imposing a self-impacting limit (Chapman, Stobbe et al., 1991).

Mitochondria

PDT targeting the mitochondria is one of the most powerful and common treatments elicited by specific PS localisation. The mitochondrial membrane is hydrophobic with a high negative charge potential, imposed due to their role in ATP production, which makes them attractive for cationic transition metal PS adherence (Asin-Cayuela, Manas et al., 2004). Furthermore, the critical role played by the integrity of the mitochondrial membrane in apoptosis induction makes them popular organelle targets for PS (Kessel, Luo et al., 1997). The mitochondria membrane becomes ruptured in PDT which leads to CytoC cytosol leakage causing rapid induction of intrinsic apoptosis (Figure 1.15). The rapid induction of apoptosis has led to a number of PS which both localise to the mitochondria through passive and active targeting (Figure 1.16)(Bi, Yang et al., 2020, McKenzie, Sazanovich et al., 2017). Additional targeting strategies for the mitochondria involve PS conjugation with adhering moieties including peptides (mitochondrial-targeting sequence), triphenyl phosphonium (TPO^{+}) and cationic heterocycles (rhodamine, indolium etc.) (Lu, Bruno et al., 2016, Murphy, 1997, Sun, Du et al., 2020).

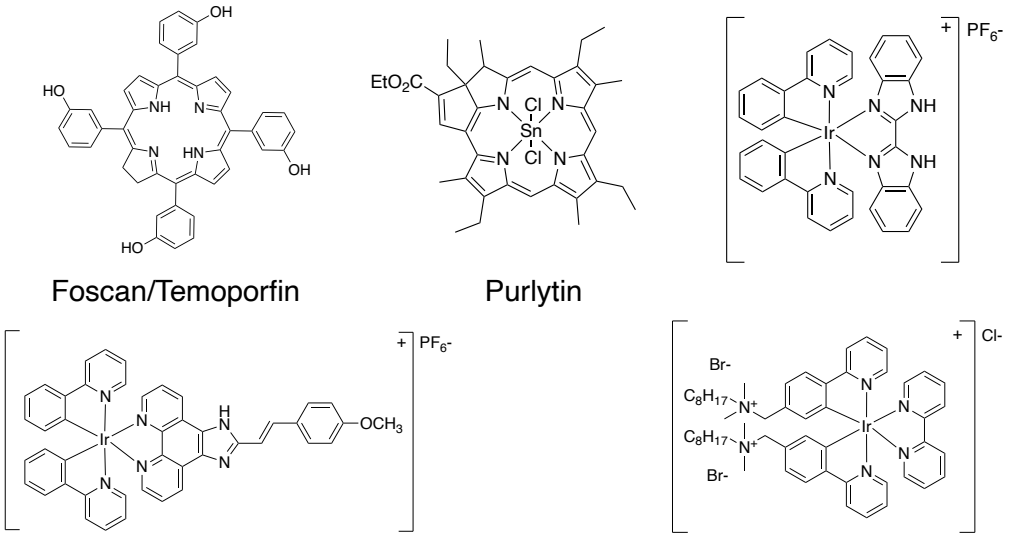

Figure 1.16 A selection of potent PS which localise to and cause damage to the mitochondria upon irradiation. Purlytin is currently in clinical trials, Foscan is a 2nd generation PS whilst the remaining Ir(III) complexes have been discussed in the literature (Bi, Yang et al., 2020, McKenzie, Sazanovich et al., 2017)

Lysosome

Lysosomes are organelles involved in the degradation of trafficked proteins and pathogenic destruction (Luzio, Pryor et al., 2007). Lysosomes are lower in pH than the rest of the cell (pH ~ 5.2) due to the production and containment of degrading proteases, making them ideal targets for pH responsive PS (Moriyama, Maeda et al., 1992, Weber, Yen et al., 2020). Lysosomal localisation and sequestration is a natural cell response allowing drug excretion and hence many PS will be passively transported there (Appelqvist, Wäster et al., 2013). Localised damage to the lysosomes is attributed to autophagy owing to the generation of a autolysosome which mediates the autophagic response and apoptosis through cathepsin release (Di, Han et al., 2020, Yim and Mizushima, 2020). Known PS which have been extensively studied and which target the lysosome include Purlytin and LuTex which are currently in clinical trials (Felder, Keller et al., 2020). Within the literature there are a multitude of transition metal PS, which have been found to localise to the lysosomes with powerful PDT effects (Figure 1.17)(Huang, Yu et al., 2015, Qiao, Liu et al., 2021, Wang, Chen et al., 2017).

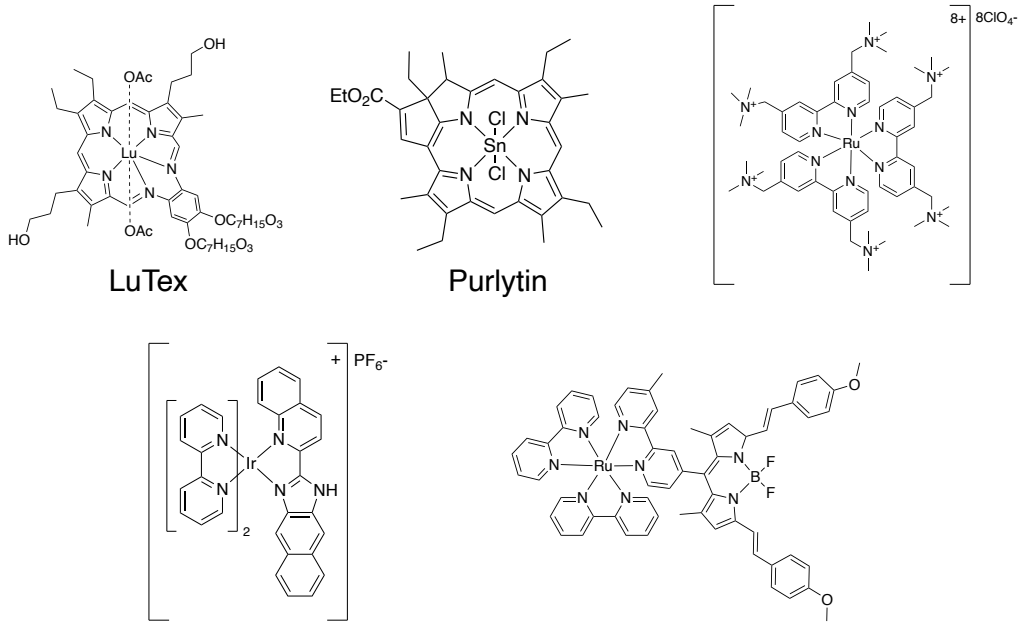

Figure 1.17 A selection of potent PS which localise to and cause damage to the lysosomes upon irradiation. LuTex and Purlytin are currently in clinical trials whilst the Ru(II) and Ir(III) complexes have been explored in the literature (Huang, Yu et al., 2015, Qiao, Liu et al., 2021, Wang, Chen et al., 2017).

Golgi Apparatus

Upon the development and study of Photofrin®, the Golgi apparatus was identified as one of its key targeted organelles (Hsieh, Wu et al., 2003). The Golgi apparatus functions as a trafficking organelle which packages and transports synthesised biomolecules to the plasma membrane (Rohn, Rouillé et al., 2000). Direct photodamage to the Golgi apparatus identified the translocation of LC3, a protein involved in autophagosome formation, to the Golgi post irradiation (Gomes-da-Silva, Jimenez et al., 2019). Additionally, photodamage to the Golgi regulates the transport and formation of autophagosomes through ATG9 release and becomes fragmented upon initiation (Deng, Liu et al., 2020). Apoptosis induction has also been linked to Golgi photodamage through the release of caspase 2, an initiator caspase, which is cleaved and released from the Golgi membrane (Mancini, Machamer et al., 2000). A visible marker of Golgi damage is its irreversible fragmentation throughout the entire cell which is observed upon photodamage and

autophagy/apoptosis which also reversibly and naturally acts in mitosis (Sütterlin, Hsu et al., 2002). A variety of effective PS have been found to localise to and cause damage to the Golgi apparatus (Figure 1.18) (Gomes-da-Silva, Zhao et al., 2018, Ho, Wong et al., 2012, Teiten, Bezdetnaya et al., 2003, Zhao, Wang et al., 2021).

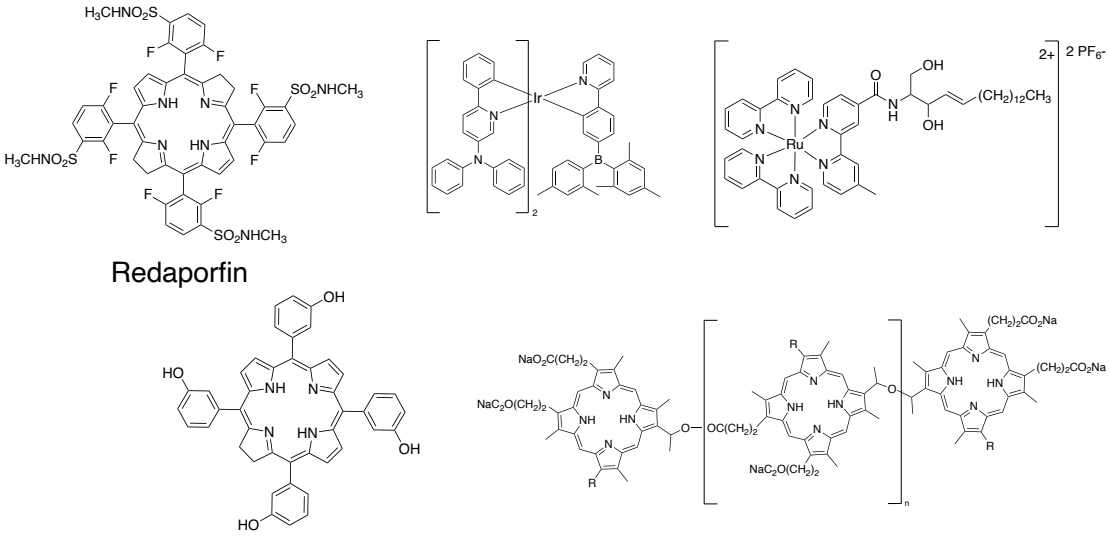

Figure 1.18 A selection of potent PS which localise to and cause damage to the Golgi apparatus upon irradiation. Photofrin is an approved 1st generation PS, Redaporfin and Foscan approved 2nd generation PS while the Ru(II) and Ir(III) complexes are explored in the literature (Gomes-da-Silva, Zhao et al., 2018, Ho, Wong et al., 2012, Teiten, Bezdetnaya et al., 2003, Zhao, Wang et al., 2021).

ER

Photodamage to the endoplasmic reticulum (ER) has also been highly targeted in PDT. The ER has multiple cellular functions including hosting protein synthesis, lipid biosynthesis and calcium storage (Schwarz and Blower, 2016). Hypericin, an ER localised PS, is found to trigger apoptosis through the disruption of calcium homeostasis. This causes an influx of Ca^{2+} into the cytoplasm which triggers the release of proapoptotic factors leading to CytoC leakage (Buytaert, Callewaert et al., 2006). Furthermore, photodamage to the ER increases ICD through the release of CRT, an 'eat me' signal, which migrates to the exocellular environment leading to dendritic and T cell recruitment (Li, Yang et al., 2019). In addition, autophagy and paraptosis are activated through ER photodamage with autophagy occurring

concurrently with apoptosis (Kessel, 2019, Zhuang, Dai et al., 2020). Several regulated cell death pathways can be activated through PS targeting of the ER which has led to the accumulation of potent PS (Figure 1.19)(Nam, Kang et al., 2016, Pracharova, Vigueras et al., 2018, Teiten, Bezdetnaya et al., 2003, Yuan, Liu et al., 2019, Zhou, Wei et al., 2020).

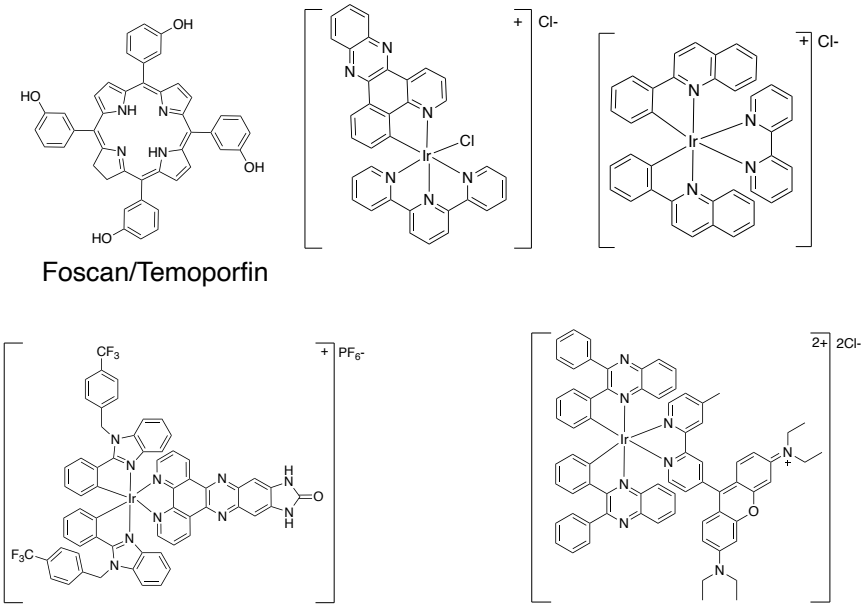

Figure 1.19 A selection of potent PS which localise to and cause damage to the ER upon irradiation. Foscan is a clinically approved 2nd generation PS whilst the Ru(II) and Ir(III) complexes have been discussed in the literature (Nam, Kang et al., 2016, Pracharova, Vigueras et al., 2018, Teiten, Bezdetnaya et al., 2003, Yuan, Liu et al., 2019, Zhou, Wei et al., 2020).

1.4 – Upconverting Lanthanide Nanoparticles

Despite efforts to red-shift PS to improve PDT tissue penetration, many still have maximal absorption wavelengths within regions which have limited tissue penetration. An alternative to altering the PS, is to couple it with an entity capable of converting NIR light to blue light, so that indirectly a blue light activating PS can be activated by deeper penetrating NIR light. In this thesis the use of upconverting lanthanide nanoparticles to convert NIR to blue light for PDT is investigated.

1.4.1 – Upconverting Lanthanide Nanoparticles (UCNPs)

Upconverting materials emit higher energy photons than those it absorbs leading to an anti-Stokes emission. These upconverting materials can be synthesised into nanoparticles (UCNPs) whereby an absorption of NIR light precedes an emission of blue-shifted visible light (de Araújo, Maciel et al., 2002). This phenomenon occurs primarily through multiple NIR absorptions which progressively occupy higher energy electronic states. The radiative decay of these higher energy states then leads to the emission of blue-shifted light which is the product of multiple electron and energy transfer processes (Zhang, Song et al., 2009). NIR I is the region of light which is most penetrating to tissue meaning that PS photoactivation in this range is highly desired (Zhao, Xu et al., 2021). Lanthanide ions (Ln^{3+}) have been renowned for their luminescent properties and as suitable UCNP materials. This interest began in 1964 when Nd^{3+} was doped into $Y_2Al_5O_{12}$ making an efficient stimulated four-level energy laser (Gnach and Bednarkiewicz, 2012). This led to the development of other Ln^{3+} doped materials for their light producing properties due to Ln^{3+} making suitably fluorescent centres. This originates from the electronic structure $[Xe]4f^n$ (n = 1-14 depending on the exact species) of Ln^{3+} which generate a multitude of levels estimated by 14!/n!(14-n)! (Eliseeva and Bünzli, 2010). For example, Tm^{3+} with the structure $[Xe]4f^{12}$ has ~ 91 excited state energy levels accessible through irradiation. In addition, the 4f electrons lie closer to the Ln^{3+} nucleus and are shielded by further $5s^25p^6$ electrons resulting in sharp f-f transitions. This shielding effect also retains 4f orbital energies upon a change in chemical environment which do not alter Ln^{3+} luminescence (Eliseeva and Bünzli, 2010). Ln^{3+} doped UCNPs present many advantages over fluorescent dyes, quantum dots and gold nanorods for light upconversion including NIR absorption, high resolution on a wide field microscope and multiple narrow blue light emission bands (Gnach and Bednarkiewicz, 2012). Through NIR I absorption, UCNPs make good imaging agents by reducing autofluorescence owing to the lack of excitable biomolecules in this region (Mader, Kele et al., 2010). UCNPs also resist photobleaching giving their luminescent properties high *in vivo* stability (Park, Kim et al., 2009).

1.4.2 – PS Conjugated to UCNPs

UCNPs can upconvert NIR I light within the optimum tissue penetrating window leading to the emission of higher energy visible light which lies in the region of PS photoactivation. Through the pairing of UCNPs with a suitably absorbing PS, NIR I PDT is theoretically possible (Gnanasammandhan, Idris et al., 2016). This is facilitated through energy transfer from UCNPs to the conjugated PS. Additionally, PDT favoured PS advantages can be simultaneously achieved owing from UCNP properties which can impart increases to water solubility, excretion and/or cell uptake (do Reis, Helal-Neto et al., 2021, Konan, Gurny et al., 2002). This multi-faceted NIR PDT process occurs through multiple energy transfers which begin with UCNP NIR absorption leading to the population of higher energy UCNP states. These excited UCNP states can then interact with closely embedded PS, leading to their photoactivation. The normal processes of PDT then occur by which ISC generates $^{3}PS^{*}$ which then causes $^{1}O_{2}$ generation and finally culminates in cell death (Figure 1.1, Figure 1.22).

1.4.3 – PS Suitability for UCNP Coupling

In conjugating PS to UCNPs for NIR PDT, several pre-requisites must be considered during PS development to make the whole system feasible to carry out multi energy transfers.

- The PS has high phototoxicity and low cytotoxicity in the dark.
- The PS can be embedded upon the UCNP surface.
- UCNPs can engage in energy transfer with the PS to cause photoactivation.
- The PS absorption spectra overlaps with UCNP upconversion emission.
- The UCNP must remain non-toxic in the dark with/without PS conjugation.
- UCNP-PS should be uptaken by cells.
- UCNP should upconvert under NIR I irradiation.
- UCNP upconversion should be appreciably high.

- UCNP-PS should be suitably soluble for administration/distribution.
- $^3O_2$ should be able to interact with $^3PS^*$.

1.4.4 – Ln^{3+} Doped $NaYF_4$ UCNPs

Overview

Nanoparticles which have doped amounts of highly luminescent Ln^{3+} into their metal salt framework have been shown to be efficient light upconverters (Wang, Zhu et al., 2015). This is through the selection of a suitable host lattice which holds Ln^{3+} in close proximity whilst also remaining inert. $NaYF_4$ has been determined as a good host candidate owing to the size similarity between Y^{3+} and Ln^{3+} due to the lanthanide contraction. In addition, $NaYF_4$ is chemically inert, transparent to NIR light and has low structural phonon energy which increases photon upconversion (Chen, Fu et al., 2021). Within $NaYF_4$ there exists two cationic sites which hold Na^+ and Y^{3+} in addition to a selected doping ratio of Ln^{3+} which are introduced into Y^{3+} sites (Mader, Kele et al., 2010). The exact species of Ln^{3+} for doping should then be selected to absorb in the NIR I range (700 – 1000 nm) (Zhao, Xu et al., 2021). Generally, these UCNPs use a dual modal approach whereby two or more Ln^{3+} are co-doped into $NaYF_4$ to partake in photon upconversion and are classed as either sensitisers or activators depending on their exact role. Sensitisers are responsible for absorbing NIR I photons before sequential energy transfer leads to the population of higher energy electronic states of the activator (Auzel, 2004). The upconverted light is then emitted through the radiative decay of the activator's higher energy levels. Yb^{3+} possess strong 980 nm absorption which lies at the far end of the NIR I and can increase UCNP NIR absorption by two orders of magnitude through diode irradiation (Chen, Fu et al., 2021, Chien, Chan et al., 2018). Therefore, Yb^{3+} is commonly selected as a sensitiser in NIR upconversion. In terms of the activator, a suitable Ln^{3+} species should be selected which emits within the region of PS photoactivation which tends to be in blue light region. Tm^{3+} are blue/UV light emitters through the radiative decay of their $^1D_2$ and $^1G_4$ electronic levels which overlap with PS absorption (Chien, Chan et al., 2018)(Figure 1.20). In combination $NaYF_4$ doped with Yb^{3+} and Tm^{3+} would be suitable to facilitate NIR PDT through a sequential NIR

absorption by Yb^{3+}, energy transfer to Tm^{3+}, photoactivation of PS process which results in $^1O_2$ induced cell death. These UCNPs have been studied for this particular purpose to some success (Gnanasammandhan, Idris et al., 2016, Krämer, Biner et al., 2004, Mader, Kele et al., 2010).

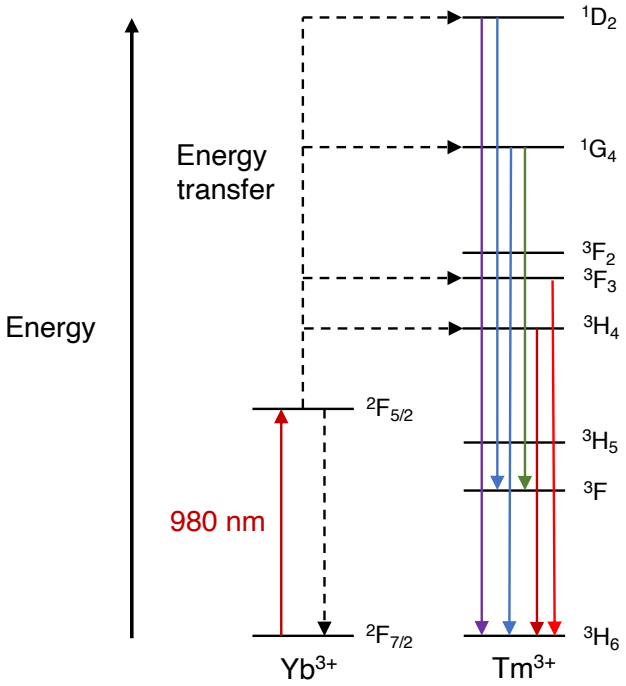

Figure 1.20 An energy level diagram describing the mechanism of $NaYF_4$; Yb^{3+}, Tm^{3+} UCNP light upconversion. Sensitisation occurs through 980 nm absorption by Yb^{3+} before sequential energy transfers populate the upper excited states of Tm^{3+}. Emission from Tm^{3+} leads to PS activation. Adapted from (Schafer and Haase, 2011).

Tuning upconversion

Photon upconversion can be enhanced by achieving high UCNP phase purity and also through the modulation of the Ln^{3+} ratio, both of which can cause profound effects on the type and intensity of emission (Aebischer, Hostettler et al., 2006, Gulzar, Xu et al., 2017). Two major crystalline forms exist for $NaYF_4$, namely cubic α phase (α-$NaYF_4$) and hexagonal β phase (β-$NaYF_4$). β-$NaYF_4$ has the higher efficiency rate of photon upconversion due to lower bulk lattice phonon energy which increases the rate of excited state radiative decay (Ding, Huang et al., 2012, Qian and Zhang, 2008). In contrast, α-$NaYF_4$ is less efficient at light upconversion which lowers the overall rate (Mader, Kele et al., 2010).

The ratio of Yb^{3+} and Tm^{3+} which are co-doped into the UCNPs also effect photon upconversion emission intensity. The Ln^{3+} dopant concentrations must be negotiated in firstly maximising photon upconversion through the addition of appreciable amounts of Yb^{3+} and/or Tm^{3+} (Mader, Kele et al., 2010). However, excess Tm^{3+} and Yb^{3+} can negatively affect photon upconversion through excited state self-quenching caused by high ionic ratios. UCNPs co-doped with Yb^{3+} and Tm^{3+} have had their upconversion emissions measured upon an increase in both the activator and sensitiser (Figure 1.21).

Figure 1.21 A summary of β-$NaYF_4$ light upconversion alongside the responsible Tm^{3+} orbital transitions and the ratio of Yb^{3+}, Tm^{3+} upon 980 nm (250 mW) excitation. (Li, Liu et al., 2016)

Wavelength/nm	Transition	Composition
800	$^3H_4 \rightarrow {}^3H_6$	5% Yb^{3+}, 0.5 % Tm^{3+}
750	$^3H_4 \rightarrow {}^3H_6$	10% Yb^{3+}, 0.5% Tm^{3+}
725	$^3F_2 \rightarrow {}^3H_6$	10% Yb^{3+}, 0.5% Tm^{3+}
700	$^3F_3 \rightarrow {}^3H_6$	10% Yb^{3+}, 0.5% Tm^{3+}
650	$^1G_4 \rightarrow {}^3F_4$	10% and 5% Yb^{3+}, 0.5% Tm^{3+}
550	$^1D_2 \rightarrow {}^3H_5$	10% and 5% Yb^{3+}, 0.5% Tm^{3+}
475	$^1G_4 \rightarrow {}^3H_6$	10% and 5% Yb^{3+}, 0.5% Tm^{3+}
450	$^1D_2 \rightarrow {}^3F_4$	10% and 5% Yb^{3+}, 0.5% Tm^{3+}
350	$^1D_2 \rightarrow {}^3H_6$	10% and 5% Yb^{3+}, 0.5% Tm^{3+}

Alongside upconversion peak position, the variation of Yb^{3+} content causes considerable changes in the intensity of emitted wavelengths. The highest energy peaks, in particular 350 nm and 450 nm, are more intense in lower Yb^{3+} (5 %) concentrations compared to lower energy peaks (650 nm) which are more intense in higher Yb^{3+} (10%) concentrations (Li, Liu et al., 2016). Due to high energy light often being more favourable for PS photoactivation, the reduction of Yb^{3+} should be sufficient to intensify the higher energy emissions. Conversely, the concentration of the activator, Tm^{3+}, was less affective to photon upconversion suggesting that the sensitiser efficiency is the rate limiting factor (Li, Liu et al., 2016). The highest photon

upconversion efficiency has been measured in UCNPs with an ionic ratio of 74.7% Y^{3+}, 25% Yb^{3+} and 0.3% Tm^{3+} which produces 450 nm, 350 nm and 275 nm emission at an appreciable intensity and is therefore compatible for blue-light absorbing PS (Gnanasammandhan, Idris et al., 2016).

1.4.5 – Synthesis Methods

UCNPs can be synthesised through thermal decomposition and co-precipitation routes which have differing phase compositions. Co-precipitation routes are easier to perform and are less aggressive compared to thermal decomposition routes but majorly form spectroscopically undesirable α-$NaYF_4$. Conversely, thermal decomposition routes majorly favour β-$NaYF_4$ but require high temperatures (up to and exceeding 300 °C) and aggressive reagents. Thermal decomposition routes favour β-$NaYF_4$ formation due to thermolysis of pre-formed $NaYF_4$ crystals which are then subjected to slow reformation of the more thermodynamically stable β-$NaYF_4$. This process is mediated by an oleic acid/octa-1-decene micellar solvent system by firstly forming lanthanide-oleate complexes followed by crystal precipitation induced by fluoride addition (Qian and Zhang, 2008). Thermal decomposition methods are favoured in terms of UCNP synthesis which begin with trichloride metal/lanthanide salts (Boyer, Vetrone et al., 2006, Gnanasammandhan, Idris et al., 2016). Following the formation of the oleate complexes and the addition of F^-, the solution is rapidly heated to above 300 °C which reforms β-$NaYF_4$ inside a growth-mediating micelle which results in a narrow size distributed UCNP mixture (Gnanasammandhan, Idris et al., 2016). Other methods which separately synthesis and purify the pre-cursor oleate complexes, to form $L(OA)_3$ do exist which can reduce side reactions (L= Y, Yb, Tm and OA = oleate)(Kang, Ai et al., 2018). However, in all thermal decomposition routes, it is critical that a high temperature is reached to majorly favour β-$NaYF_4$ formation (Boyer, Vetrone et al., 2006, Gnanasammandhan, Idris et al., 2016, Kang, Ai et al., 2018, Qian and Zhang, 2008).

1.4.6 – UCNP Coatings

In addition to photon upconversion, other favourable biological UCNP properties must be imparted which includes water solubility and PS binding into the UCNP structure design. UCNPs which are synthesised through micellar-assisted thermal decomposition routes are water insoluble due to a hydrophobic oleic acid surface coating (Peltomaa, Benito-Peña et al., 2021). Water solubilisation of UCNPs can be achieved through the burying of these hydrophobic caps (encapsulation methods) or through cap exchange with water soluble agents (exchange methods). Encapsulation methods layer the UCNP surface with amphiphilic, amorphous silica which causes water solubilisation through hydrophobically binding to the UCNP surface whilst hydrophilically interacting with the aqueous environment (Hlavacek, Sedlmeier et al., 2014). An amorphous silica layer also increases UCNP stability as 'naked' UCNPs in media can degrade and leak toxic F^- and Y^{3+} alongside Na^+ (Agalakova and Gusev, 2012). Additionally, Ln^{3+} can form precipitates with biologically abundant PO_4^{3-} which can form a deposit onto the naked UCNP surface but is preventable through silica layering (Gao, Jin et al., 2018, Torresan and Wolosiuk, 2021). Secondly, the UCNPs must sufficiently bind PS in order to cause its photoactivation. This can be achieved through a 2nd layer of mesoporous silica performed through a sol-gel method involving the hydrolysis and condensation of silica groups (Li, Barnes et al., 2012). Through the addition of C18-TMS, a high boiling point solvent, the resulting mesoporous silica layer is left with filled pores. C18-TMS is then evaporated and removed by heating in a calcined furnace which leaves vacated Si-O-Si lined pores in the outermost layer (Gnanasammandhan, Idris et al., 2016, Yoo, Lee et al., 2009). Through the controlled addition of suitably hydrophobic PS, its inflow and retention into the vacated UCNP pores should be facilitated by the hydrophobic effect (Grüner, Arai et al., 2018)(Figure 1.22).

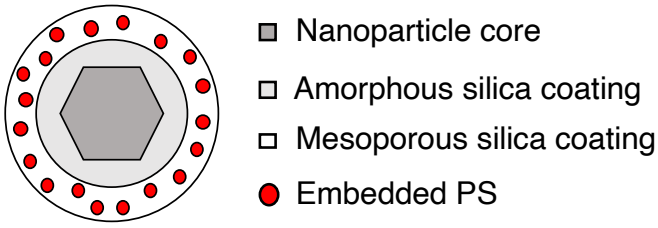

Figure 1.22 A multi-layered UCNP-PS system theoretically facilitates NIR PDT; The UCNP cores upconvert NIR I light into blue light which leads to photoactivation of embedded PS. This then leads to ROS production resulting in cell death.

1.4.7 – Application

UCNPs have been tested in *in vitro* and *in vivo* models to assess their biodistribution and biocompatibility alongside their effect on cell viability. PEG-coated UCNPs ($NaYF_4$:Yb^{3+}, Tm^{3+}) were applied to bone marrow derived stem cells which produced little cytotoxicity up to 2 days following a 25 μg/mL administration (Chatterjee, Rufaihah et al., 2008). Additionally, UCNP's were intravenously administered to live rats with biodistribution subsequently detected in the lungs and to a lesser degree, the heart, kidneys and spleen. Upon 30 minutes post administration, the maximum upconversion response was detected within the lungs which shifted to the spleen at around 24 hours, albeit to a lesser degree. After 7 days, all organs had a negligible upconversion response which suggested their clearance (Chatterjee, Rufaihah et al., 2008). Additionally, any resulting upconversion signal was both deeper and more intense in tissue than the upconversion produced by quantum dots (Chatterjee, Rufaihah et al., 2008). In terms of solution stability prior to administration, coated UCNPs in PBS had only a minor measured decrease in the solution's upconversion response which suggested a high and prolonged stability (Chatterjee, Rufaihah et al., 2008).

The biological properties of PS loaded UCNP's have received less investigation. However, one such study has explored the conjugation of MC540 and ZnPc (two photosensitising dyes) to UCNPs which subsequently measured *in vitro* and *in vivo* effects in mice and B16-F0 cells (melanoma tissue)(Gnanasammandhan, Idris et al., 2016). PS-unloaded, folic acid/PEG-coated UCNPs were intravenously administered to C57BL/6 mice which bore subcutaneous B16-F0 tumours. A greater upconversion

response was measured in tumour vs normal tissue which showed that folic acid and PEG surface coatings can further enhance tumour selectivity. This was accompanied by negligible upconversion being measured in tissue samples taken of healthy major organs (liver, spleen, kidney, bladder, heart and skin). Furthermore, these UCNPs were PS loaded and administered to B16-F0 tumour bearing mice followed by 980 nm of tumour localised irradiation. The resulting tumour sections were found to have a 50% increase in apoptotic cells when compared to the relevant control groups (Gnanasammandhan, Idris et al., 2016).

1.5 – Hypothesis and Aims

This thesis investigates and hypothesises that development to transition metal mediated PDT can be improved through the following:

1.5.1 – Hypotheses

1. PDT can be improved through the modulation of transition metal complexes and the employment of NIR light technologies.
2. NIR PDT can be achieved using a suitable and potent transition metal PS coupled to NIR UCNPs.
3. Structural components of pre-identified transition metal PS can be explored and elucidated as causative factors for their phototoxic effects.

1.5.2 – Aims

To test the listed hypotheses, this thesis will aim to do the following:

1. IrNew will be structurally modified through the exchange of its ancillary ligands to create a new compound, IrTHPyBenz. This compound will be subsequently tested and investigated for improved PDT activity.
2. IrNew will undergo structural modification through the exchange of its NN bearing ligand with/without co-exchange of its ancillary ligands, to create IrPPyMes and IrTHPyMes. These compounds will be subsequently tested and investigated for improved PDT activity.

3. PorphyrinPlus's PDT activity will be investigated through the isolation of a structurally simplified fragment, PtCNNH followed by re-evaluation of PS activity.
4. Any subsequent PS improvements will be further mechanistically investigated using co-localisation assays, cell death pathway identification and uptake/elimination studies as well as translation to more clinically relevant 3D *in vitro* spheroid models.
5. UCNPs will be synthesised and their ability to upconvert 980 nm light will be scrutinised for PS photoactivation for NIR PDT.
6. Potent and suitable PS will be coupled with UCNPs and any phototoxic effects to cells will be ascertained following 980 nm irradiation.

2. Methods and Materials

2.1 – Biological Materials

2.1.1 – List of Chemicals Used for Biological Studies

Material	**Full name**	**Company**
γH2AX (Ser139) monoclonal antibody		Millipore
58K-9 Golgi protein antibody		Abcam
Agarose powder	Agarose (Protein Electrophoresis Grade)	Fisher Scientific
Anti-mouse 488		Invitrogen
Anti-rabbit 488		Invitrogen
BSA	Bovine serum albumin	Sigma-Aldrich
Calnexin monoclonal antibody		ThermoFisherScientific
CellEvent™ Caspase 3/7 Green Detection Reagent		ThermoFisher Scientific
Chloroquine	Chloroquine diphosphate salt	Sigma Aldrich
Clear DMEM	Dulbecco's Modified Eagle's Medium. DMEM 4.5 g/L glucose without L-glutamine and phenol red	Lonza
CyQUANT™ LDH Cytotoxicity Assay Kit		ThermoFisher Scientific
Cytochrome C monoclonal antibody		ThermoFisher Scientific
DMEM	Dulbecco's Modified Eagle's Medium. DMEM 4.5 g/L glucose, glutamine, phenol red	Sigma-Aldrich
DMSO	Dimethyl sulfoxide	Lonza
EDTA	Ethylenediaminetetraacetic acid	Sigma Aldrich
Ethanol		ThermoFisher Scientific
FCS	Foetal calf serum	Biosera
HEPES		Sigma Aldrich
IMMU-mount	Thermo Scientific™ Shandon™ IMMU-mount™	Life Technologies Ltd, Paisley, UK
Methanol		ThermoFisher Scientific
Methylene blue		ThermoFisher Scientific

NaCl	Sodium chloride	SigmaAldrich
NP40	Nonyl phenoxypolyethoxylethanol	ThermoFisher Scientific
PBS	Phosphate buffered saline solution	Oxoid
PFA	Paraformaldehyde solution	ThermoFisher Scientific
PhosphoHistone 3 antibody	anti-HistoneH3 (phosphoS10)	Abcam
PI	Propidium iodide	Sigma-Aldrich
Precept		Johnson and Johnson medical limited
Pro-long gold mountant	Molecular Probes Pro Long Gold Antifade Mountant	Fisher Scientific
Protein Assay Dye Reagent Concentrate		BIO-RAD
Sodium resazurin		ThermoFisher Scientific
Sucrose		SigmaAldrich
Tetraethyl ammonium chloride		Alfa Aesar
Triton X-100		ThermoFisher Scientific
Trypsin		Sigma-Aldrich
Valinomycin	Valinomycin ≥ 98% (TLC), ≥ 90% HPLC	Sigma-Aldrich

2.1.2 – Equipment

Name	Company
Cell culture centrifuge – Heraeus MegaFuge 16	ThermoFisher Scientific
Colony counter	Stuart scientific
Haemocytometer	Hawksley
Incubator	Weis Gallenkamp
Nikon dual-cam widefield live-cell system	Nikon
Waterbath	Grant Instruments
U100/U100 H Ultrasonic cleaning bath	Ultrawave
Plate reader	ThermoScientific Multiskan FC

2.1.3 – Cell Lines

Cell lines	Genotype	Reference
A375	Human epithelial malignant melanoma	(Giard, Aaronson et al., 1973)
C1861	Human cutaneous melanoma	(Welch, Bisi et al., 1991)
EJ	Human epithelial bladder carcinoma	(O'Toole, Povey et al., 1983)
HCT116	Transformed human colon carcinoma cell line	(Brattain, Fine et al., 1981)
HeLa	Human papillomavirus-related endocervical adenocarcinoma	(Gey, 1952)
MCF7	Human epithelial mammary carcinoma	(Soule, Vazquez et al., 1973)
OPSCC72	Human oropharynx small cell carcinoma	(Nair, Thomas et al., 2020)
Shepp1	Human neuroblastoma	(Ross, Spengler et al., 1983)
U2OS	Human osteosarcoma	(Ponten and Saksela, 1967)

2.2 – Methods Used for Biological Studies

2.2.1 – Passaging Cell Lines

Cells were routinely cultured and grown in suitable medium (DMEM, 10 % FCS) unless otherwise stated and incubated at 37 °C, 5% CO_2. Cells were grown in a T-75 flask until reaching a suitable confluency 80 – 100 %, depending on the cell type. Media was removed from confluent cells and washed with PBS (10 mL) before being detached with Trypsin-EDTA (1 mL). Fresh media (9 mL) was added to dilute the cells followed by gentle resuspension. A fraction of the resuspended cell solution was then diluted to a suitable fraction with fresh media and made up to a total volume of 10 mL. This solution was then moved into a T-75 flask and incubated.

2.2.2 – Plating Cell Lines

Throughout all experiments, cells were plated when they had reached a suitable confluency. The media was drained from each flask followed by a PBS wash (10 mL) and detachment with Trypsin-EDTA (1 mL). The cells were then re-suspended in

fresh media and counted on a haemocytometer slide with an average taken of the four quadrants. In some cases, this was repeated, and a further average was calculated to give a cell number x 10^4/mL. The stock solution was then diluted by a calculated amount and plated at a desired number in a suitable dish and incubated.

2.2.3 – Freezing Cells

Cells were incubated in media until they had reached 80% confluency. The media was then drained, cells washed with PBS (10 mL) and detached with Trypsin-EDTA (1 mL). Cells were re-suspended in fresh media and pelleted by centrifugation using a cell culture centrifuge (1200 *g*, 3 mins). The supernatant was then discarded followed by addition of fresh media complemented with 5 % DMSO and then gently re-suspended (2 mL). The solution was then halved and transferred into cryovial tubes (2 x 1 mL) before storage in a – 80°C electric freezer which can store cells for months up to years. For long term storage all cells were stored under liquid nitrogen.

2.2.4 – Thawing Cells

A cryovial containing frozen cell solution (media, 5 % DMSO) was removed from the freezer and placed in a water bath until fully melted. The solution was transferred into a centrifuge tube and diluted up to 10 mL with fresh media and re-suspended. The solution was centrifuged (1200 *g*, 3 mins) to leave behind a cell pellet. The media was drained, and the pellet re-suspended in fresh media (10 mL) before being transferred to a T-25 flask. The cells were allowed to grow to confluency and were passaged three times before subsequent experimental use.

2.2.5 – Cell Imaging

Coverslips were first sterilised by submerging in IMS solution for 5 – 10 minutes, ensuring all air bubbles were removed. The coverslips were then stood up in each well of a desired dish until all the IMS had evaporated before being laid flat. Cells were then counted and diluted in fresh media to give a cell count to be plated in each well. The cells were then allowed to adhere to the coverslips overnight.

The imaging agent was then applied to the wells by first draining the media and applying the imaging agent diluted in fresh media at a specific concentration. The cells were then incubated to allow sufficient cellular uptake of the imaging agent.

After a specific time, the media was drained and each well washed with PBS (3 x 1 mL). PFA (3% in PBS, 1 mL/well) was then added and gently agitated by placing the dish onto a bellydancer for 20 minutes to allow for cell fixation. PFA was then drained and each well washed with PBS (3 x 1 mL) before the coverslips were removed and placed vertically on a tissue to remove any excess PBS. The coverslips were then submerged in distilled water to remove any salt and the excess drained onto tissue paper. The coverslip was then mounted cell-side down onto a microscope slide using IMMU-Mount or ProLong Gold Antifade mountant as the adherent. The slides were allowed to dry overnight and stored in the dark at 4 ^{o}C before being subsequently imaged.

2.2.6 – Dark Toxicity Clonogenic Survival Assays

Cells were allowed to grow to an adequate number in a T-75 flask before having their media drained, washed with PBS (10 mL) and detached with Trypsin-EDTA (1 mL). Cells were then counted and diluted with a determined volume of fresh media to give a stock solution of 1000 cells/mL. Each well of a 6 well dish was then filled with 2 mL of fresh media before the addition of a given volume of stock 1000 cells/mL solution to give a specific cell number at both low and high density (dependent on cell line). The cells were allowed to adhere overnight through incubation.

PS solutions of varying concentrations were made through dilution of the stock drug in fresh media. In the cases where the stock solvent was DMSO, a DMSO concentration balance was made in each well to account for any DMSO toxicity effects. Each well was drained of its media and 1 mL of PS solutions were added to each dish over a range of doses. The dishes were then incubated for a specific time to allow cellular uptake and cytotoxic effects to occur. After the given time, PS-containing media was drained, and each well was carefully replenished with 2 mL of fresh media. The dishes were then incubated for varying amounts of time to allow

colonies to form. For dark toxicity assays, the procedure was performed ensuring any light exposure was kept to a minimum with the fume hood light being switched off during drugging.

After colonies were seen upon visual inspection, the media was drained from each well followed by staining with methylene blue solution (4% in 7:3 ethanol/water). After 30 minutes, the staining solution was removed, and the wells carefully washed to remove excess solution before being dried. After drying, the number of colonies were counted in each well to form a PS dose survival curve.

2.2.7 – Light Toxicity Clonogenic Survival Assays

Cells were allowed to grow to an adequate number in a T-75 flask before having the media drained, washed with PBS (10 mL) and detached with Trypsin-EDTA (1 mL). Cells were then counted and 1 mL of 60,000 – 100,000 cells/well (cell line dependent) were placed into wells in a 12 well dish. The cells were allowed to adhere overnight through incubation.

Solutions of varying PS concentrations were made through dilution of the stock in fresh media. Where DMSO was the stock solvent, a DMSO concentration equity was made in each well to account for DMSO toxicity effects. Each well was drained of its media and 1 mL of various PS concentrations were added to each well to give a range of doses in one 12 well plate. The dish was then incubated for a specific time to allow for cellular uptake and dark toxicology effects to occur.

After the given time, the PS-containing media was drained, and each well was washed with PBS (3 x 1 mL). 150 µL of Trypsin-EDTA was added to each well followed by incubation to detach the drug-uptaken cells. Sufficient detachment was confirmed by microscope inspection to ensure maximum cell detachment. 0.85 mL of clear media (DMEM w/o L-glutamine or phenol red) was added to each well and the cells gently re-suspended. A cell count was then taken of the untreated condition to calculate the volume of cell solution corresponding to 10,000 cells. This volume was taken out of each well and complemented with clear media up to a 1 mL volume and

then moved into a soda glass vial or an Eppendorf per each dosed condition and placed on ice.

The desired irradiation power from the laser was confirmed using a power meter prior to cell solution exposure. The soda glass vials were then irradiated for a given time and power under a specified wavelength of excitation. After irradiation, the cells were plated into 6 well dishes to give one low cell count and one high cell count /condition for both the irradiated (soda glass vials) and non-irradiated (Eppendorf tube) conditions. The plates were then incubated at 37 °C until visible colonies were formed.

Following this, the media from each well was drained and the colonies stained with methylene blue solution (4%, in 7:3 ethanol/water, 30 mins). The methylene blue solution was then removed, and each plate was gently submerged in warm water and left to dry. The colonies were then counted in each well and a dose survival curve was plotted.

2.2.8 – Microscope Imaging

Multiphoton imaging was performed using a confocal Inverted Zeiss LSM 510 NLO microscope. This operates by exciting fluorophores with a multiphoton excitation source followed by image capture. Widefield imaging was taken on a Nikon dual cam widefield live cell microscope system.

Exact excitation wavelengths varied depending on the PS under investigation. For multiphoton imaging, a Chameleon two-photon laser (Ti:Sapphire) was used to produce wavelengths within the range of 800 – 1000 nm. This was then visualised with a 60 X oil based lens: Plan Apochromat VC 60x oil (NA 1.4).

For widefield imaging, excitation was performed using a SpectraX LED source using the FITC (470 nm) or DAPI (395 nm) wavelengths. The emission was captured by monitoring the relevant filter channels to specifically capture light from the target fluorophore. The relevant filters used in this project were DAPI, FITC or TRITC.

Images were collected as a series of z stacks using a 100X Ph oil (NA 1.4) lens.

All images were processed using FIJI imaging software (a version of ImageJ). For widefield z stacked images, deconvolution was performed using the Richardson-Lucy algorithm to reduce out of focus light.

2.2.9 – Colocalisation Studies

General Protocol

Specific organelle staining was conducted using immunofluorescence performed by selecting a specific organelle-associated protein. The relevant primary antibody to these proteins was applied to form an antibody-protein conjugate which was visualised by the application of another relevant fluorophore-bound secondary antibody.

Primary and Secondary Antibodies for organelle staining

- Mitochondria; primary antibody; anti-cytochrome c oxidase (1:200, host: rabbit, in PBS), secondary antibody anti-rabbit 488 (1:500)
- Endoplasmic reticulum; primary antibody anti-calnexin (1:100, host: mouse, in PBS), secondary antibody anti-mouse 488 (1:500)
- Golgi apparatus; primary antibody anti-58K-9 (1:200, host: mouse, in PBS), secondary antibody anti-mouse 488 (1:500)

Staining protocol

Cells were plated onto glass coverslips at a density between 100,000 – 200,000 /well in a 6-well dish and left overnight to adhere. IrTHPyBenz (30 μM, 2 hr) was added to the relevant conditions and incubated at 37 °C. The media was then removed, the coverslips washed (3 x PBS, 1 mL/well) and then fixed (4% PFA in PBS, 10 mins, RT, gentle agitation). Cells were then permeabilised (Triton X-100, 0.2 % in PBS, RT, 10 mins) and then washed (3 x PBS, 1 mL/well). Cells were then blocked (BSA 2 % in PBS, RT, 1 hr) and then washed (3 x PBS, 1 mL). Coverslips were then inverted onto 100 μL of relevant primary antibody and incubated in a

humidified chamber at 4 °C overnight.

The next day, coverslips were washed (3 x PBS, 1 mL/well) and inverted onto 100 μL of relevant secondary antibody (1 hr, RT). The coverslips were finally washed (3 x PBS, 1 mL/well) and then mounted with Prolong Gold Antifade onto glass microscope slides before being dried and stored at 4 °C until ready to image.

Imaging and co-localisation analysis

Microscopy was used to analyse the extent of emission overlap between the drug channel and the fluorescently labelled immuno-stained organelle channel. Drug only and immuno-stained organelle only conditions were firstly imaged to ascertain experimental parameters to validate and assess how effective the two channels are in terms of solely capturing the separate emissions. The emission in both channels were then captured under these parameters in the combination slide as a z stack. The z stacks were then deconvoluted and processed in ImageJ to single images. The Coloc2 analysis programme in ImageJ was then used to assess and quantify the pixel overlap between the drug fluorescence and the organelle-stained fluorescence as a Pearson's Correlation Co-efficient (0 – 1).

2.2.10 – Cell Cycle FACS

Cell drugging and fixing

1 x 10^6 cells were plated onto petri dishes and allowed to adhere overnight. The next day, cells were drugged with mesBIAN compounds at their LD_{50} and left for 24 hours. The next day, the media was collected into a 50 mL falcon tube and each petri dish washed twice (PBS, 10 mL/dish) before detachment with Trypsin-EDTA (1 mL/petri dish). The cell solutions were then re-suspended in PBS (10 mL/petri dish) and transferred to their corresponding falcon tubes. The petri dishes were then washed (PBS, 10 mL/petri dish) which was poured into the falcon tube. The falcon tubes were then centrifuged to form cell pellets (1200 rpm, 3 mins) and the supernatant discarded. Cells were then fixed in 70% ice-cold EtOH/H_2O through dropwise addition to the pellet under gentle agitation. Fixed cell pellets were then

stored at – 20 °C in eppendorfs.

phosphoHistone3 and PI staining

Fixed cell solutions were centrifuged to form pellets (1200 rpm, 2 mins) with the supernatant then discarded and the pellets washed (2 x PBS, 1 mL/tube, 1200 rpm, 3 mins). Cells were simultaneously permeabilised/blocked by addition of 2 mL's of 0.5% BSA, 0.25% Triton X-100 in PBS for 15 minutes on ice. The solutions were then centrifuged (1200 rpm, 3 mins) and incubated with 100 μL of 1:500 anti-HistoneH3 (phosphoS10) in 0.5% BSA, 0.25% Triton X-100 in PBS for 1 hour. After this, the solutions were centrifuged into pellets (1200 rpm, 3 mins), washed twice (Triton X-100 0.25% in PBS, 1 mL/tube) and centrifuged into pellets. Each cell pellet was then stained with secondary antibody, anti-rabbit 488 (1:200, in 1% BSA/PBS) and incubated in the dark for 30 minutes. Cells were again washed with PBS (1 mL) and centrifuged to cell pellets (1200 rpm, 3 mins). The pellets were finally gently re-suspended in 500 μL of PI 18 μg/mL and RNase 8 μg/mL in PBS.

FACS and analysis

Cell solutions were then analysed with a FACS Calibur machine to assess the proportion of cells in M phase (green channel, phosphoH3 intensity) and subG_1, G_1, S, G_2 phase alongside polyploidy (red channel, PI intensity).

2.2.11 – Caspase 3/7 Detection Assay

20,000 cells/well were plated onto sterilised coverslips in two 24 well dishes and incubated overnight. The next day, the media was drained, and the cells drugged (IrTHPyBenz, 10 μM in media) and then incubated for 2 hours. All the wells were then washed (3 x PBS, 1 mL) and the media replaced with PBS (1 mL/ well). Selected wells were then irradiated (405 nm, 3 mins, 20 mW/cm^2/well) followed by incubation at (37 ^{o}C, 30 min) in a re-addition of media (1 mL/well). Following this, CellEvent™ Caspase-3/7 Reagent (7.5 μM, PBS/5% FCS) was added to selected wells (100 μL) and incubated (37 °C, 30 mins). All coverslips were then washed (3 x PBS, 1 mL), fixed (4% PFA in PBS, 10 mins, RT), washed (2 x PBS, 1 mL), stained

with DAPI (1:1000, PBS, 5 mins, RT) and then washed again (3 x PBS, 1mL). Finally, each coverslip was mounted onto glass slides (ProLong Gold Antifade, 1 drop).

Analysis

The detection kit contains a fluorophore which only becomes fluorescent in the presence of activated caspase 3/7 and will emit in the green (FITC) fluorescence channel of a microscope. In each condition, 100 cells were scored as either positive or negative for signal in the green channel.

2.2.12 – γH2AX staining and scoring

Primary and Secondary Antibodies

- Primary; Anti-γH2AX (Ser139) monoclonal antibody (1:500, host: mouse in 1% BSA in TBS
- Secondary; Anti-mouse 488 (1:500, 1% BSA in TBS alongside 1:1000 DAPI)

Staining

Cells were plated onto sterilised coverslips in a 24 well dish (20,000 cells/well) and incubated overnight. The next day, IrTHPyMes and IrPPyMes (0.1 μM) were added followed by incubation at 37 °C for 2 hr. Wells were then drained of media, washed (PBS, 0.5 mL/well, 5 mins, RT) and then fixed (4% PFA in PBS, 10 mins, RT). Cells were again washed (TBS, 0.5 mL/well, 5 mins), permeabilised (0.5 % Triton X-100 in PBS, 10 mins, RT) and then washed (3 x TBS, 0.5 mL/well, 5 mins). Coverslips were blocked (3% BSA in TBS, 0.5 mL/well, 1 hr, RT) and then washed (2 x TBS, 0.5 mL/well, 10 mins). Selected wells were then exposed to primary antibody (100 μL) and placed in a humidified chamber overnight at 4 °C. The next day, each coverslip was washed (4 x TBS, 0.5 mL/well, 10 mins) and then exposed to secondary antibody (100 μL) and incubated in the dark (RT, 1 hr). Coverslips were then washed (3 x TBS, 0.5 mL/well, 5 mins) and mounted onto glass microscope slides (ProLong Gold Antifade, 1 drop).

Analysis

Widefield microscopy was used to score each condition based on the number of γH2AX foci, a marker of DNA damage. For each glass slide, 100 DAPI-stained cell nuclei were imaged in the blue channel and then overlayed onto the channel of the immuno-stained γH2AX. ImageJ was then used to threshold the number of cell nuclei collected in the blue channel and saved as region of interests. Each pixel point maxima in the green channel were then marked and overlayed onto the regions of interest from the blue channel. The number of pixel maxima per each cell nuclei was then counted and plotted over 100 cells per condition.

2.2.13 – Cellular Uptake and Elimination Assays

Uptake inhibition assay

Cells were plated onto sterilised coverslips in 6 well plates (100,000 – 200,000 cells/well) and incubated overnight. The next day, media was discarded and the cells washed (3 x PBS, 1 mL/well) before the addition of the following inhibitors to three separate wells:

- Endocytosis: 50 μM chloroquine for 1 hr.
- Transmembrane potential: 50 μM valinomycin for 30 mins.
- Cationic transporters: 1 mM Et_4NCl for 20 mins.

After this, each well was washed (3 x PBS, 1 mL/well) before being drugged with IrTHPyBenz (20 μM, 30 mins). 4 wells (3 x inhibitor/drugged + 1 x drugged) were incubated at 37 °C for 30 mins whilst the remaining 1 well (1 x drugged) was incubated on ice for 30 mins. Coverslips were then washed (3 x PBS, 1 mL/well), fixed (4 % PFA in PBS, 10 mins, RT), washed (3 x PBS, 1 mL/well) and finally mounted onto glass slides (ProLong Gold Antifade, 1 drop).

Elimination assay

Cells were plated onto sterilised glass coverslips in 6 well plates (50,000 cells/well) and incubated overnight at 37 °C. IrTHPyBenz was then added (30 μM, 2

hrs) to each well and incubated at 37 °C. After two hours the media was removed and each coverslip washed (PBS, 1 mL/well) before being replenished with fresh media. After the timepoints, 0 hr, 24 hr, 48 hr, the coverslips had their media removed, were washed (3 x PBS, 1 mL/well) and then fixed (4 % PFA in PBS, RT, 10 mins). Each coverslip was then washed (3 x PBS, 1 mL/well) and then mounted onto glass microscope slides (ProLong Gold Antifade Mountant, 1 drop) before being allowed to dry and then stored in the fridge until imaged.

Imaging and analysis

Each slide was imaged on a widefield dual-cam Nikon live-cell microscope. The excitation and emission of the PS was imaged over 100 cells/condition. In ImageJ, the background deducted cell integrated fluorescence density was divided by the cell area to give an area accounted for mean intensity. These values were measured in each condition and then plotted against each other to monitor PS uptake/elimination.

$$Area\ accounted\ for\ mean\ intensity = \frac{(cell's\ integrated\ denisty\ of\ PS\ fluorescence - average\ intensity\ of\ background)}{area\ of\ cell}$$

2.2.14 – ICP-MS Uptake Assay

Cell plating, drugging, and protein extract harvesting

Cells were plated into T-75 flasks and grown to 80% confluency. Prior to drugging, certain flasks were drugged with inhibitors against a certain active uptake pathway as described in 2.2.13. Following this, the media of each flask was deposed of and re-placed with dosed PS media. A flask which contained no uptake inhibitor was replenished with cold PS dosed media and placed on ice for 30 minutes to block all active transport pathways. All the remaining flasks were incubated at 37 °C for 30 minutes. After this, every flask was drained of its media and (3 x ice cold PBS, 10 mL /flask). Using a cell scraping spatula, the cells of each flask were scraped into the residual PBS in each flask before being transferred into an Eppendorf. Each cell solution was then centrifuged to form a pellet (10,000 rpm, 5 mins) before the supernatant was discarded. To each cell pellet, 1 x RIPA solution (100

μL/Eppendorf) was added and incubated on ice for 30 minutes. After this, each solution was gently vortexed and aerated through a syringe tip to homogenise the cell extract solution. To test the protein concentration, 20 μL of each condition was drawn off and saved for Bradford analysis. The remaining 80 μL was stored in the freezer and then submitted to ICP-MS for iridium content analysis.

Subcellular fractionation

Cells were plated, drugged and harvested as previously detailed in 2.2.14. Cells were then mixed with buffers of different compositions and then centrifuged. Subcellular extracts were solubilised depending on the buffer which were then collected in the supernatant after centrifugation and hence contained isolated protein extracts from either the cytoplasm, soluble nuclear or chromatin components. The buffers were made as described:

- **Cytoplasmic** – 10 mM HEPES pH 7, 50 mM NaCl, 0.3 M sucrose, 0.5 % triton X-100 in 10 mL ddH_2O
- **Nuclear** – 10 mM HEPES pH 7, 200 mM NaCl, 1 mM EDTA, 0.5 % NP40 in 10 mL ddH_2O.
- **Chromatin** – 10 mM HEPES pH 7, 500 mM NaCl, 1 mM EDTA, 1 % NP40 in 10 mL ddH_2O

Harvested cells were re-suspended in 200 μL of cytoplasmic extract buffer and incubated on ice for 10 mins. The solution was then centrifuged (2000 rpm, 5 mins, 4 ^oC) followed by collection of the cytoplasmic supernatant. The pellet was then re-suspended in 200 μL of nuclear buffer, incubated for 10 mins on ice and centrifuged (12000 rpm, 2 mins, 4 ^oC). The supernatant was then collected as the soluble nuclear extract fraction. The remaining pellet was then re-suspended in 200 μL of chromatin buffer, incubated on ice for 10 mins before being passed through a 25G needle 5 times. The solution was then centrifuged (12000 rpm, 30 s) to afford the chromatin extract. 20 μL of extract was then removed for Bradford and Western Blot analysis and the remaining submitted for ICP-MS analysis for iridium content detection. Western blot analysis was used to confirm subcellular exclusivity by

blotting for ORC2 (present only in chromatin) and GRB2 (not present in chromatin).

Bradford assay

Cell lysate protein content was quantified by first constructing a standard curve. BSA was dissolved and diluted to known concentrations (0, 1, 5, 10, 15, 20 μg/mL) in ddH_2O to a final volume of 800 μL. This was followed by addition of 200 μL of Protein assay dye reagent. At the same time, 1 – 4 μL of cell lysate solutions were added to 800 μL ddH_2O followed by 200 μL of protein assay dye reagent. Every solution was vortexed and left at RT for 10 mins before being transferred to a 96 well plate (200 μL/well). The absorbance at 595 nm was then measured on a plate reader. The standard curve was constructed as a straight-line graph by plotting absorbance at 595 nm against BSA concentration. The line of best fit from this was then used to calculate cell lysate protein concentration.

Analysis

Submitted samples were measured based on iridium concentration (μg/L) which was then extrapolated to the total iridium concentration per extract. From the Bradford assay, the protein concentration was measured. These two values were then combined to give iridium content per amount of protein (μg/g) to account for cell number differences.

2.2.15 – Cell Studies on UCNPs

Dark toxicity assay

UCNP powder (either drugged or undrugged) was first weighed out and mixed with suitable media to make a final concentration of 1 mg/mL. This mixture was vortexed and sonicated for 15 minutes and then sterilised by UV light for 10 minutes. UCNP doses were then diluted from the stock solution to give x μg of UCNP in 1 mL of media. For drugged UCNPs, the calculated IrTHPyBenz μg/mg was used to calculate the μg of UCNP required for a certain dose of IrTHPyBenz. This diluted mixture was again vortexed, sonicated and sterilised. To a 6-well dish of adequately plated cells, 1 mL of UCNP suspension was added to each well to give x mg/mL of

UCNPs. After incubation for a certain amount of time, the mixture was removed, and the wells washed (3 x PBS, 1 mL) to remove traces of nanoparticle aggregates. Cells are then allowed to grow into visible colonies, before being stained with methylene blue solution (3% 70:30 EtOH/H_2O) and counted.

Light toxicity assays

Cells were plated at a suitable density in a 12 well dish and incubated overnight. Wells were drugged with either 1 mL containing z dose of IrTHPyBenz alone, x mass of UCNP alone or x mass of UCNP with a z dose of bound IrTHPyBenz. Cells were exposed for 2 hours, before the drugged solutions were removed and the cells washed (3 x PBS, 1 mL/well). The cells were detached in each well with trypsin (150 μL/well) before being counted. 20,000 cells from each condition were then diluted with phenol red free DMEM to a final volume of 1 mL and transferred to an Eppendorf and a soda glass vial. The Eppendorfs were kept on ice whilst each soda glass vial was irradiated with a 980 nm laser diode at x power for 3 minutes.

After irradiation each solution in the Eppendorf and soda glass vial was replated at a smaller density for a clonogenic survival assay e.g. 300 cells and 600 cells for EJ/condition. Colonies were allowed to grow to a visible size and then stained with methylene blue solution and counted.

2.2.16 – Spheroid Studies

Preparing the agarose coated plates

Agarose solution was prepared through addition of agarose powder to phenol red free DMEM (1.5 %) which was then sterilised by autoclaving. This solution was stored in the fridge until needed. The agarose solution was then microwaved until fully melted before 100 μL was added to each well of a 96 well plate. In doing this, care was taken to ensure no bubbles were introduced to the agar. The agar was allowed to set for 1 hour at room temperature before being inverted and stored in the fridge until needed.

Plating and growing spheroids

Before plating, the agarose coated 96 well dishes were put into an incubator for 1

hour and warmed to 37 °C. C8161 cells were grown to a suitable confluency, before being washed, trypsinised and counted. To each agarose coated well, 3,000 – 9,000 cells were plated in 100 μL of DMEM and incubated for 3 – 5 days. Spheroid growth was monitored by light microscopy until spherical morphologies with consistent diameters were formed. Every 3 days the media was replenished by adding 100 μL of fresh DMEM and then removing 100 μL. Care was taken to not disrupt spheroids upon their manipulation.

Monitoring spheroid growth

Spheroid growth was monitored using light microscopy whereby each well was imaged under 10X magnification. The area of each imaged spheroid was then quantified using ImageJ to assess growth/shrinkage.

Alamar blue staining

Spheroid growth through drug penetration was monitored using alamar blue staining. The alamar blue solution was made by dissolving resazurin powder in TBS to a final concentration of 0.3 mg/mL which was then subjected to sterile filtration and protected from light. Resazurin was diluted in fresh media (1:10) and applied to cells for between 2 – 4 hours. Upon the cellular uptake of resazurin (weakly fluorescent), cellular metabolic activity caused a drug reduction which produced resorufin (highly fluorescent). 100 μL of cell exposed media was transferred to a 96 well plate and the 600 nm emission at 570 nm excitation was measured to give a value of cell metabolic activity.

PS dark and light toxicity in spheroids

Spheroids were plated and grown to ~ 500 μm diameter size with visually established heterogeneity. Two columns of the 96 well plate was sampled for each of the 4 conditions; vehicle control/not irradiated, drugged/not irradiated, vehicle control/irradiated and drugged/irradiated. Prior to drug incubation, each well was imaged for size analysis. PS/vehicle control was added at 2X concentration in 100 μL to each well before 100 μL was removed to give a final 1X dose which was then incubated at 37 °C for 24 hours. Each well was imaged before being washed in PBS through adding/removing 100 μL (x 3) before the relevant wells were irradiated in a 2

x 2 well grid (405 nm; 20 mW/cm^2, 3 mins or 455 nm, 30 mW/cm^2, 3 mins). Cell media was then added to each well by adding/removing media (3 x 100 μL) followed by incubation. For subsequent PDT treatments, the final addition of media was exchanged for 2X PS dose in 100 μL followed by removal of 100 μL.

LDH detection

LDH (lactate dehydrogenase) was detected as a marker of cell death. Upon the loss of cell membrane integrity, this cytosolic enzyme is leaked into the media whereby the conversion of lactate into pyruvate is performed through the reduction of NAD^+ to NADH. Diaphorase couples with NADH to reduce an iodo-nitro-tetrazolium salt which forms a red formazan product which can be detected through 490 nm and 680 nm absorbance. In the presence of LDH, which is released during a cell death event, a direct proportionality can be observed with the absorption intensity at 490 nm and 680 nm.

The day after spheroid irradiation at 455 nm, 50 μL of cell media from each well was transferred to a 96 well plate and mixed with 50 μL of LDH detection kit reaction mixture. After 30 minutes, 50 μL of LDH detection kit stop solution was added and the absorption at 490 nm and 680 nm was measured using a plate reader. The average relative increase in absorption was then plotted against the average absorption in the untreated condition.

2.3 – Materials and Methods Used in Chemistry

2.3.1 – Materials

Material	Full name	Vendor
1-octadecene	1-octadecene tech grade, 90%	Sigma-Aldrich
NH_4F	Ammonium Fluoride	Sigma Aldrich
Cyclohexane		Sigma Aldrich
DCM	Dichloromethane	Sigma Aldrich
DMSO	Dimethyl sulfoxide	Sigma Aldrich
EtOH	Ethanol	Sigma Aldrich
Hexane		Sigma Aldrich
MeOH	Methanol	Fisher Chemical

Oleic acid	Oleic acid, tech grade, 90%	Alfa Aesar
Thulium (III) chloride hexahydrate		Sigma-Aldrich
Ytterbium (III) chloride hexahydrate		Sigma-Aldrich
Yttrium (III) chloride hexahydrate		Sigma-Aldrich
IGEPAL CO-520		Sigma-Aldrich
NaOH	Sodium hydroxide	VWR Chemicals
C18TMS	octadecyltrimethoxysilane	Sigma Aldrich
TEOS	Tetraethyl orthosilicate	Sigma Aldrich
NH_4OH	Ammonium hydroxide solution 33% in water	Sigma Aldrich

2.3.2 – Chemical Storage and Handling

All iridium complexes were synthesised within the Weinstein Group; IrTHPyBenz by myself and Dr. Marta Martinez-Alonso, Benz ligand by Mr. Liam Kirby and Mr. Ryan Bell and MesBIAN compounds/IrNew by Mr. Liam Kirby. All platinum complexes were synthesised outside of the Weinstein Group and posted to the Department of Chemistry for further PDT-related analysis as solids.

Dissolution in water was first attempted to improve biological administration and failing this were dissolved in DMSO. For certain photophysical studies (e.g. singlet oxygen generation), solutions were made in DCM and acetonitrile due to DMSO/water incompatibility with the apparatus. Solutions were made by weighing out the desired amount of solid to make a very dilute solution, usually 10 mM, and if any solid remained more liquid was added to make concentrations of 5 mM. Stocks used for chemical analysis were made when needed and for biology were made in bulk and stored in the freezer in a sealed 2 mL Eppendorf tube.

2.3.3 – Spectroscopy

UV/Vis absorption spectra were all obtained on a Varian Cary 5000 UV-Vis-NIR spectrophotometer with the pure solvent baselined to zero. The analyte in solution was measured in a quartz cuvette with a 1 cm path length.

Emission and excitation spectra were all obtained on a Fluormax4 spectrophotometer (HORIBA Johin Yvon) with all solutions measured in quartz cuvettes with 1 cm path lengths.

Time-decay lifetime measurements were all performed on a mini-t Edinburgh Instrument with a pulsed time modifiable laser diode source. Various filters were selected to measure the desired emission from the excited state.

2.3.4 – Quantum Yield

The quantum yield, Φ_F, of the emissive compound was experimentally determined by making up a series of solutions at variable absorbances under a fixed wavelength using UV/vis spectroscopy. The emission spectrum of the compound, excited at the fixed wavelength, was then recorded by excitation and the integrated fluorescence intensity (i.e. area under the curve) calculated. This was performed in tandem with a standard, $[Ru(bpy)_3]^{2+}$, by again making up solutions at identical absorbance at the same wavelength as the analyte solution. The AUC of the two compounds (x), at various absorbances, were then plotted against their measured integrated fluorescence intensity, y, to form two straight lines.

The gradient of the line of best fit for the standard, m_s, and that of the analyte, m_a, were then calculated and manipulated to determine the quantum yield, Φ_F. By conducting the experiment under the same solvent conditions, the refractive indices, η, cancel out. The quantum yield of $[Ru(bpy)_3]^{2+}$, was found from the literature to be 0.042 (Caspar and Meyer, 1983)

$$\Phi_F = \Phi_s(\frac{m_a}{m_s})(\frac{\eta_a^2}{\eta_s^2})$$

2.3.5 – Singlet Oxygen Generation

The method was replicated using the outline from previous Bryant/Weinstein group member, Dr. Luke McKenzie detailed in his published work (McKenzie, Sazanovich et al., 2017). All potential PS and reference perinapthenone were first dissolved in either DCM or acetonitrile and diluted to give an absorbance value of 0.1 (± 0.01) at 355 nm which is the third harmonic of the Nd:YAG laser source. Singlet oxygen yield was calculated by excitation of a potential air saturated PS solution in a 1 cm quartz cuvette with the detection of the singlet to triplet oxygen relaxation emission (em = 1275 nm). The laser source used was a Q-SW Nd:YAG 3rd harmonic 355 nm, 8 ns pulses (Ls-1231M LOTISII 2006 model) and the emission detected on a InGaAs photodiode Æ3 mm active area (J22D-M204-R03M- 60-1.7, Judson Technologies). The photodiode used for excitation was coupled with a low-noise current amplifier (DLPCA-200, FEMTO Messtechnik GmbH), with the amplified signal recorded by a digital oscilloscope (TDS 3032B Tektronix). This set-up effectively detects the decay signal of $^1O_2$ into $^3O_2$ with a high-contrast bandpass optical filter (1277 nm centre wavelength, 28 nm FWHM, custom-made by Izovac, Belarus) which is fitted onto the front of the detector.

A singlet oxygen generation value is calculated by irradiating a sample of both PS and perinapthenone (the reference) made up in an air-saturated solution at a concentration to produce 0.1 absorbance at 355 nm. Irradiation was carried out at various powers, in µJ of the Nd:YAG laser source and the decay signal of singlet oxygen recorded. This was then performed 4 times, per power, per solution and an average singlet oxygen decay signal generated. The amplitude was then corrected by taking into account the exact optical density values at 355 nm (0.1 ± 0.01) using the following equation:

$$corrected\ initial\ amplitudes = \frac{initial\ amplitude}{1 - 10^{-OD(355\ nm)}}$$

Singlet oxygen generation was then calculated using the corrected initial amplitudes of both reference and PS for each power value before an average is taken over the range of tested powers. The solvent was then taken into account due to potential quenching effects which can reduce the amount of singlet oxygen present by a fixed amount depending on the exact solvent system (Schmidt, Tanielian et al., 1994).

$$\frac{corrected\ PS\ initial\ amplitude}{corrected\ reference\ initial\ amplitude} \times solvent\ value = compound\ singlet\ oxygen\ value\ (\Phi_{\Delta})$$

2.3.6 – Dynamic Light Scattering (DLS)

All dynamic light scattering experiments were conducted using suspensions in water in disposable cuvettes, 1 cm path length. All measurements were at 25 °C and with suspensions sonicated for a couple of minutes beforehand. All measurements were measured on a Malvern Zetasizer NanoZS Model ZEN 3600 operating at 633 nm wavelength from a 4 mW He-Ne solid state laser. Back-scattered light was measured at 173 ° using the amorphous silica standard. The results obtained were calculated over thirty runs of 10 seconds and taken 3 times.

2.3.7 – Transmission Electron Microscopy (TEM)

TEM imaging was used to assess the morphology and size of the UCNP to validate their purpose for light upconversion and to assess coatings. Hexagonal phase crystals with dimensions around 50 nm were cited as the most ideal morphology for $NaYF_4$; Yb^{3+}, Tm^{3+} for photon upconversion (Gnanasammandhan, Idris et al., 2016). For the nanoparticle cores, suspensions in cyclohexane were applied and air dried onto copper coated carbon grids (10 μL). For coatings suspended in aqueous solvent, air drying was extended overnight to sufficiently allow for the complete evaporation of water. Images were taken with a FEI Tecnai

120 kV G2 Biotwin transmission electron microscope which is equipped with an Orius SC100 mounted camera using Gatan Digital Micrograph software. All images were processed for presentation in ImageJ.

2.4 – Synthesis

2.4.1 – Synthesis of IrTHPyBenz

Iridium (III) thiophenylpyridine chloride dimer (80 mg, 0.073 mmol, 1 mol eq.) and 2,2'-bisbenzimidazole (37.2 mg, 0.16 mmol, 2.2 mol eq.) were placed under argon. Degassed methanol/DCM (1:1 v:v, 20 mL) was then added and the solid dissolved to form an orange solution. The solution was then heated to 70 ^{o}C for 24 hours under stirring and argon. The solution was cooled to room temperature and the solvent removed under reduced pressure. The solid was re-dissolved in minimum DCM (~ 5 mL) before addition of hexane (~ 10 – 20 mL) to induce precipitation. The solution was left overnight and the solid collected by vacuum filtration (86.2 mg, 75%). Subsequent characterisation was performed using ^{1}H/^{13}C NMR and mass spectroscopy (Appendix 2, 3, 4).

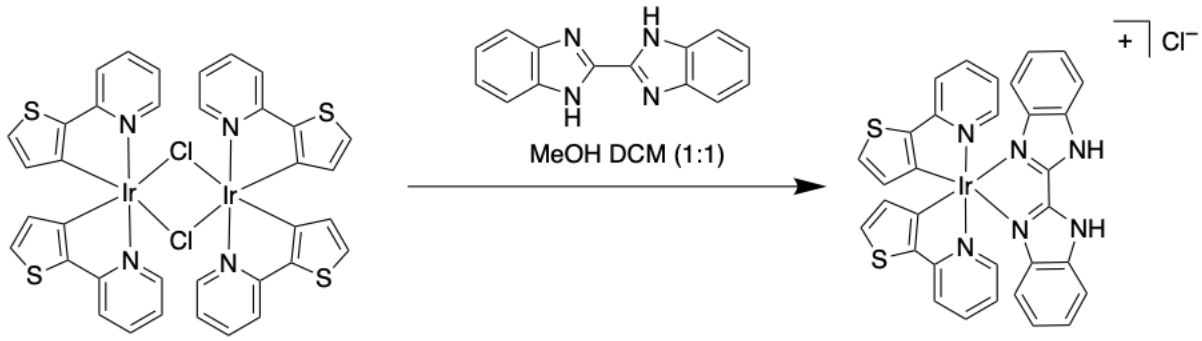

2.4.2 – Synthesis of $NaYF_4$; Yb^{3+}, Tm^{3+} Cores

$YCl_3.6H_2O$ (342 mg) and $YbCl_3.6H_2O$ (146 mg) were weighed out and dissolved in 0.2 mL of deionised water and added to a 50 mL three-necked round bottom flask. To this, 0.1 mL of $TmCl_3.6H_2O$ stock solution (10.7 mg/mL) was added. The flask was then connected to a dual fold Schlenk line and placed under vacuum. Heating was then applied until all the water had evaporated to leave behind white powders. The flask was then filled with inert argon and left overnight.

A magnetic stirrer bar was added into the flask followed by addition of 1-octadecene (25.5 mL) and oleic acid (5.4 mL) and stirred until solid dissolution. The solution was then placed under vacuum for 10 minutes before heating to 150 °C – 160 °C for 1 hour. The solution was then allowed to cool to below 60 °C before a solution of NaOH (14 mg) and NH_4F (200 mg) in MeOH (7 mL) was added dropwise under stirring. The solution was then stirred at 50 °C for 30 minutes, before the temperature was raised to 60 °C – 90 °C to remove methanol for 20 minutes. The flask was then placed under vacuum for an additional 10 minutes to remove any volatiles. A condenser was then fitted to the top of the flask with flowing cold water along with a quick-fit thermometer in the side-arm. The flask was then subdued to three cycles of vacuum/argon flushes to create an inert atmosphere and heated to 310 °C for 75 minutes. The heat was then turned off and the solution allowed to cool to room temperature overnight.

The solution was then poured into a 50 mL falcon tube and topped up to 40 mL with acetone to induce precipitation. This was then centrifuged (7000 *g*, 20 mins) to form a pellet and the supernatant discarded. The pellet was then re-dispersed in cyclohexane (15 mL), sonicated for 10 minutes and centrifuged (7,000 *g*, 10 mins) with the supernatant collected as suspended nanoparticle cores.

2.4.3 – Amorphous Silica Coating of Core UCNPs

To a one-necked 50 mL round bottom flask equipped with a magnetic stirrer bar, nanoparticle core solution (4 mL) was pipetted followed by addition of cyclohexane (21 mL). To this, IGEPAL C0-520 (1.5 mL) was added and the mixture sonicated for 2 minutes. Ammonium hydroxide solution (160 μL, 33% in water) was pipetted followed by stirring at room temperature for 30 minutes. Finally, TEOS (80 μL) was added and the mixture stirred at room temperature for 2 days.

The mixture was then split in half and transferred to two 50 mL falcon tubes. The flask was then rinsed with EtOH (20 mL) before being split and added to each of the two falcon tubes. Acetone (15 mL) was then added to each tube to induce

precipitation, the mixture centrifuged (10, 400 *g*, 20 mins) and the supernatant discarded. The pellet was then re-dispersed in EtOH (10 mL/tube) and sonicated for 10 minutes before being combined into one falcon tube. The suspension was then centrifuged (10,400 *g*, 20 minutes), the supernatant discarded, and the pellet re-suspended in 1:1 EtOH/water (30 mL). The suspension was then vortexed and sonicated for 10 minutes followed by centrifugation (10,400 *g*, 20 minutes). The pellet was finally re-suspended in distilled water (20 mL), vortexed and sonicated for 20 minutes and stored in the fridge.

2.4.4 – Mesoporous Silica Coating of UCNPs

Amorphous silica coated nanoparticles (8 mL) were transferred to a falcon tube and centrifuged (10,400 *g*, 20 minutes) and the supernatant discarded. The pellet was then re-dispersed in EtOH (20 mL) and sonicated for 3 minutes. The solution was then transferred into a one-necked 50 mL round bottom flask equipped with a magnetic stirrer bar followed by addition of ammonium hydroxide solution (1.3 mL, 33 % in water). To a falcon tube, EtOH (6.5 mL), TEOS (130 μL) and C18TMS (52 μL) were vortexed and sonicated for 10 minutes. This solution was then pipetted in 1 mL increments into the nanoparticle solution and left stirring at room temperature for 6 hours.

The mixture was distributed equally into two 50 mL falcon tubes and centrifuged to a pellet (10,400 *g*, 20 mins). The two pellets were then re-suspended in EtOH (10 mL/tube) followed by vortexing and sonicating for 20 minutes and then centrifuging (10,400 *g*, 20 mins). This washing step was then repeated. The pellets were then re-suspended in EtOH (2 mL/tube), vortexed and then sonicated (2 mL) before being transferred to a 5 mL crucible and dried to a powder overnight.

The crucibles were then placed in a muffle oven furnace and heated to 500 °C (10 °C/min) for 6 hours to remove the porogen, C18TMS. The powders were then combined and scraped into an agate pestle and grounded finely with a mortar before being transferred into Eppendorfs for cell studies.

2.4.5 – Binding of IrTHPyBenz to Coated UCNPs

An exact mass of mesoporous coated UCNPs was weighed out into an Eppendorf tube ~ 0.5 – 2 mg. In a separate Eppendorf tube, a mass of IrTHPyBenz was dissolved in ethanol to a final concentration of 5.9 mg/mL. A 20 μL sample of IrTHPyBenz solution was pipetted into a separate Eppendorf and allowed to dry to a powder overnight. Simultaneously, the UCNP powder was re-suspended in IrTHPyBenz/ethanol solution, vortexed at high speed, sonicated (30 mins) to remove air bubbles and left overnight. The next day, the UCNP suspension was centrifuged (microcentrifuge, 2,000 rpm, 5 mins) to afford a powder. 20 μL of supernatant was then pipetted into an Eppendorf tube and air-dried to powder. The rest of the supernatant was then removed and the powder resuspended in ddH_2O (100 μL) before centrifugation (2,000 rpm, 5 mins). The supernatant wash was then removed and air-dried in an Eppendorf alongside the resulting IrTHPyBenz bound powder in another Eppendorf.

Analysis

The dried powders of all supernatant samples (pre UCNP, post UCNP and wash) were re-dissolved in DMSO (3 mL). In three cuvettes filled with 3 mL DMSO, volumetric increments of sample DMSO solutions were added, and the UV/Vis absorption spectra measured. To each cuvette, the absorbances at 455 nm, 425 nm, 400 nm and 350 nm were measured and the subsequent concentration of IrTHPyBenz calculated. From these values, the mass of IrTHPyBenz in solution both pre and post UCNP addition were measured and corrected with IrTHPyBenz in the washings. The mass loss of IrTHPyBenz was then divided by the mass of the weighed UCNP powder to give a mg/mg value of UCNP loaded IrTHPyBenz dose.

3. IrTHPyBenz

3.1 – Chemical Analysis

Previous work at the University of Sheffield identified a compound with impressive PDT activity, IrNew (McKenzie, Sazanovich et al., 2017)(Appendix 5). However, IrNew's clinical translation was limited by its 405 nm light activated PDT activity, which lies within a region of low tissue penetration. Additionally, structural components responsible for its successful PDT activity were unknown, meaning any potential advances or improvements were hindered. To probe the importance of the ancillary ligands, 2-phenyl pyridine (PPy), was substituted with 2-thiophenyl pyridine (THPy) to form IrTHPyBenz, which was followed by a re-analysis of PDT activity (Figure 3.1).

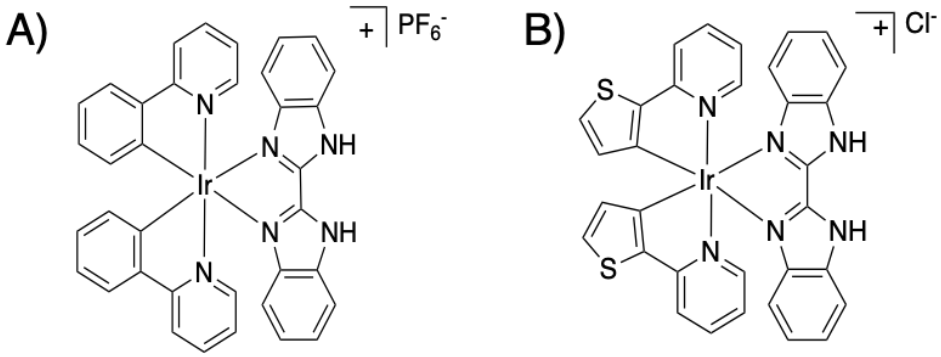

Figure 3.1 A comparison between the structures of two related Ir(III) complexes. A) Iridium (III) (2-phenyl pyridine)$_2$(bisbenzimidazole) PF_6 referred to as 'IrNew' . B) A sister complex to A), Iridium (III) (2-thiophenyl pyridine)$_2$(bisbenzimidazole) chloride, referred to as IrTHPyBenz.

In the exchange of PPy with THPy, a red shift in complex absorption was sought facilitated by the exchange of ligand-based C atoms with S atoms, previously documented to cause an additive red-shift in complex absorption and thereby increasing IrNew's tissue penetration (Mbambisa, Tau et al., 2007, Pandian, Reddy et al., 1990). Furthermore, the Benz ligand (1,1'-bisbenzimidazole) was hypothesised to be responsible for IrNew's PDT active MLCT band due to its uncharged character, which likely forms the HOMO, and so was retained. Through the synthesis of a sister

complex, IrTHPyBenz, PDT effects could be retained and/or improved whilst being photoactive in a more red-shifted and hence more tissue penetrating wavelength range. Following this, several key PS parameters, such as intracellular location, uptake, type of cell death, clearance and translation to 3D *in vitro* models were performed to add further information to complex dynamics responsible for PDT activity.

3.1.1 – IrTHPyBenz Synthesis

IrTHPyBenz was synthesised through a ligand substitution reaction on a pre-prepared iridium (III) THPy chloride dimer (provided by Dr. Marta Martinez Alonso) who synthesised the dimer through the reaction of iridium (III) chloride with THPy ligand. Benz ligand was additionally prepared by Mr. Ryan Bell. Benz together with the iridium dimer was heated under reflux in a MeOH/DCM solution to afford the product (Figure 3.2).

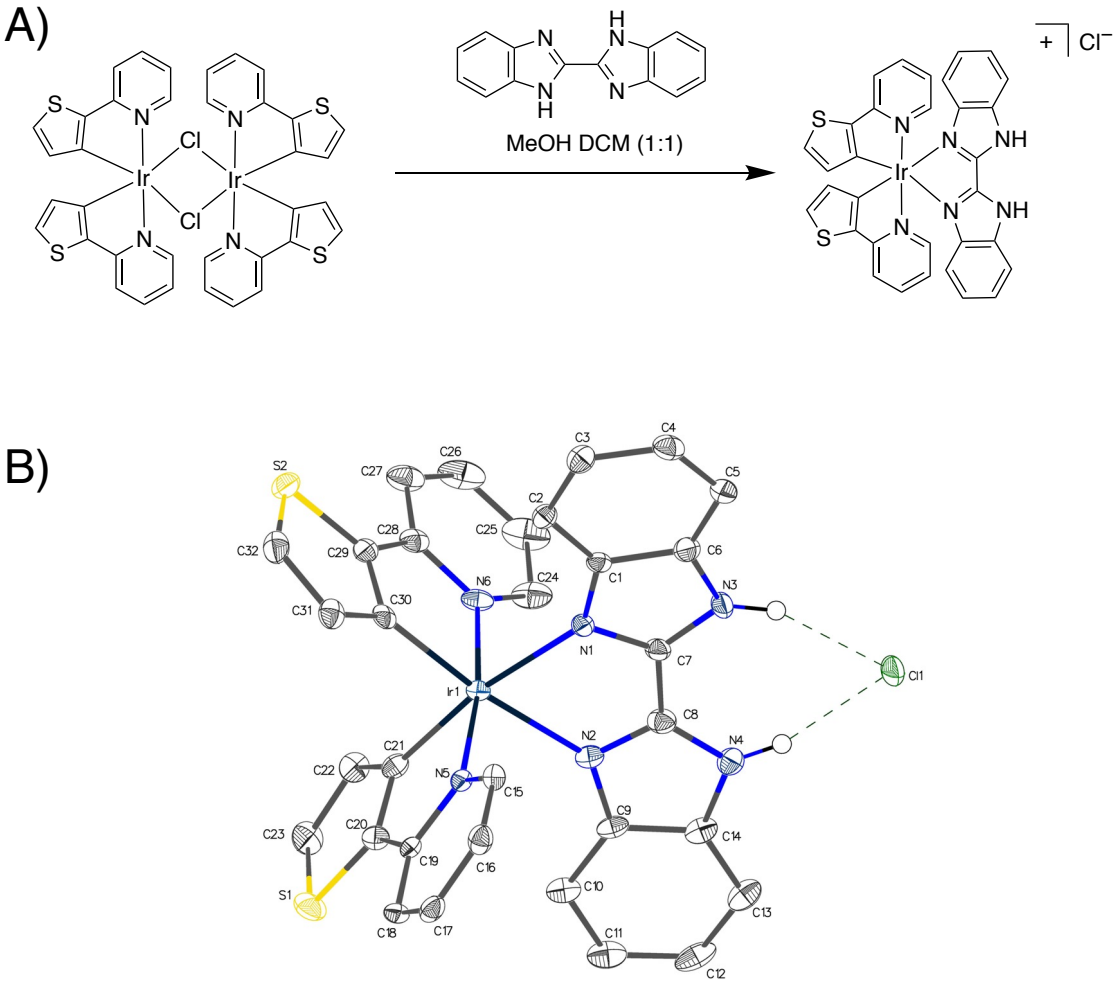

Figure 3.2 A) The synthesis of IrTHPyBenz involved the reaction of 1,1,-bisbenzimidazole (Benz) with the thiophenyl diiridium chloride dimer. B) The crystal structure of IrTHPyBenz determined by x ray diffraction studies. The diiridium dimer was prepared by Dr. Marta Martinez-Alonso, the Benz ligand by Mr. Ryan Bell and the crystal structure determined by Dr. Craig Roberts.

Purification of the crude product was performed by dissolution in DCM followed by precipitation on hexane addition. An orange solid, IrTHPyBenz, was confirmed as highly pure by H^1/C^{13} NMR alongside mass spectrometry (Appendix 2 - 4). The crystal structure was determined through x ray diffraction (by Dr. Craig Roberts) which observed the chloride ion also acting as a hydrogen bond acceptor with the NHs on Benz.

3.2.2 – Photophysical Analysis

Spectroscopic analysis was performed on IrTHPyBenz to measure any suitable photophysical properties in tandem with IrNew, whereby any apparent red-shifted absorptions were directly scrutinised (Figure 3.3).

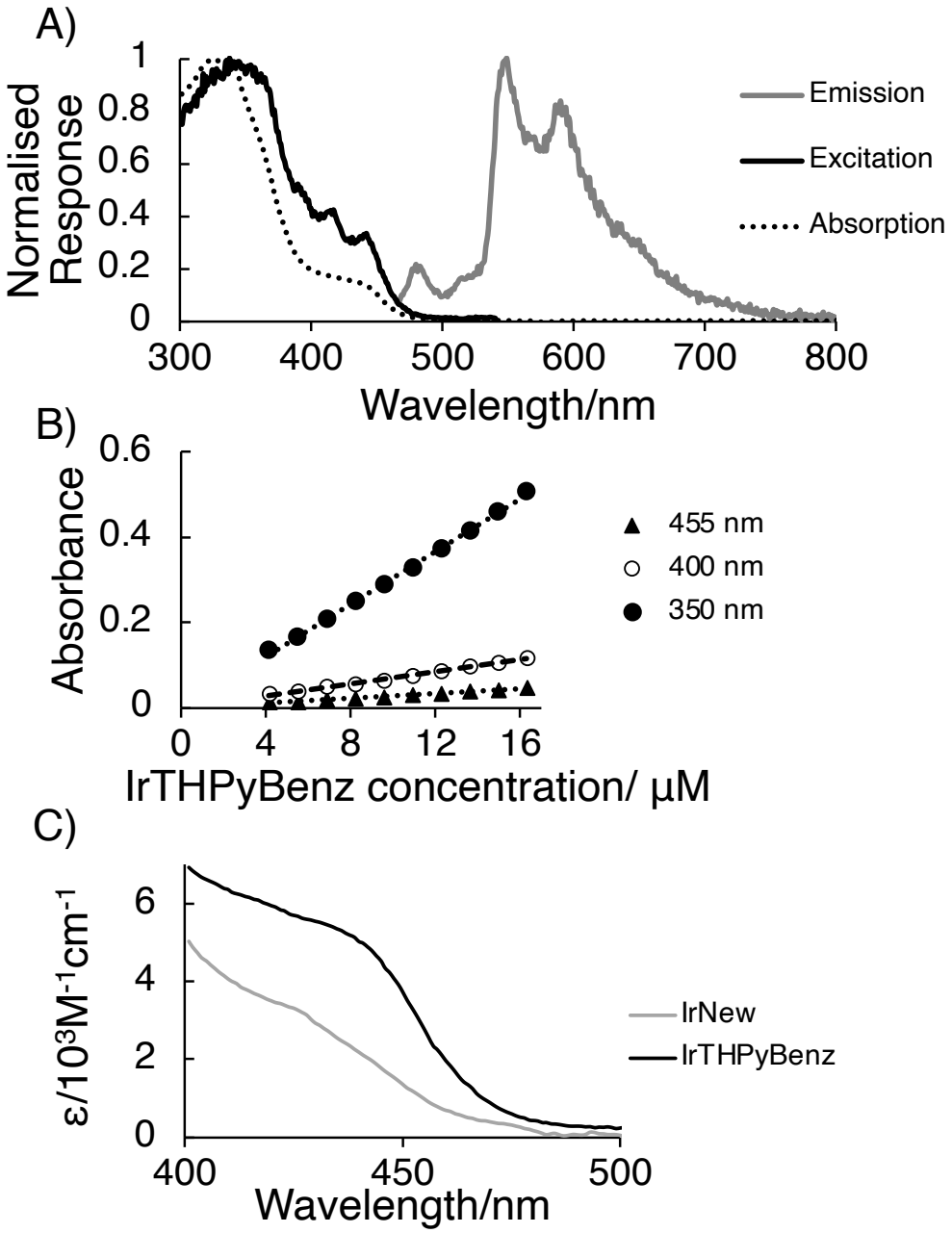

Figure 3.3 (A) The absorption, emission (λ_{exc} 455 nm) and excitation (λ_{em} 550 nm) spectra of IrTHPyBenz in DCM. B) The change in complex absorption at various wavelengths upon the increase of IrTHPyBenz concentration in DCM. C) The of molar absorption coefficients, ε, of IrNew (grey) and IrTHPyBenz (black) in DMSO in the visible region.

Two distinct types of absorptions were present in the UV-Vis absorption spectra which were assigned as UV-based ligand-centred (LC) transitions and a visible light lying MLCT (400 – 475 nm) (Figure 3.3A). Within these regions, the molar absorption coefficients, ε, were measured at 2800 $M^{-1}cm^{-1}$ (455 nm), 7100$M^{-1}cm^{-1}$ (400 nm) and 30,600 $M^{-1}cm^{-1}$ (355 nm) whose magnitudes garnered extra support for the previous assignments. IrTHPyBenz was then excited within its visible light MLCT absorption band (455 nm) which produced an emission extending over the yellow-orange visible region (Figure 3.3B). The Stokes shift (the energy difference between the absorption and the emission maxima) was measured at 0.83 eV (MLCT; λ_{exc} 400 nm – λ_{em} 550 nm) with energy loss suggestive of decay from a lower energy triplet excited state. A higher Stokes shift is observed on triplet-singlet excited state decay in comparison to singlet-singlet decay due to energy losses accrued by non-radiative internal conversion processes (IC). The shape of the emission also contained some vibrational progression, through two distinct peaks, which can characterise the excited state. Radiative decay from ^{3}MLCT* to the ground state would theoretically produce a broad emission due to little vibrational progression given the differences between excited and ground state orbital character. Therefore, due to the presence of sharp peaks, the emission is likely produced from an excited state decay from intra ligand orbitals (IL*) which are similar in character to the ground state and hence contain vibrational progression. The measured Stokes shift, alongside the emission shape, would therefore suggest an emissive triplet state decay from either solely ^{3}IL* or a mixture of ^{3}IL* and ^{3}MLCT*. Furthermore, the observed overlap between the absorption and excitation spectra showed that the same excited states are populated irrespective of the initial absorption being through the MLCT or LC. In terms of any red-shift, a measured decrease of 20 nm in wavelength was observed within IrTHPyBenz's MLCT when directly compared to IrNew (Figure 3.3C). Additionally, an approximate trebling to the molar extinction coefficient at 455 nm (ε(IrNew) 900 M^{-1} cm^{-1} vs ε(IrTHPyBenz) 2800 $M^{-1}cm^{-1}$) provided a further handle to facilitate more red-shifted PDT.

The quenching ability of ground state molecular oxygen on the excited state of IrTHyBenz was investigated through spectroscopic measurements in aerobic and

anoxic conditions. This was to ascertain whether the radiative decay and lifetime of IrTHPyBenz's triplet excited state was sensitive to oxygen (Figure 3.4).

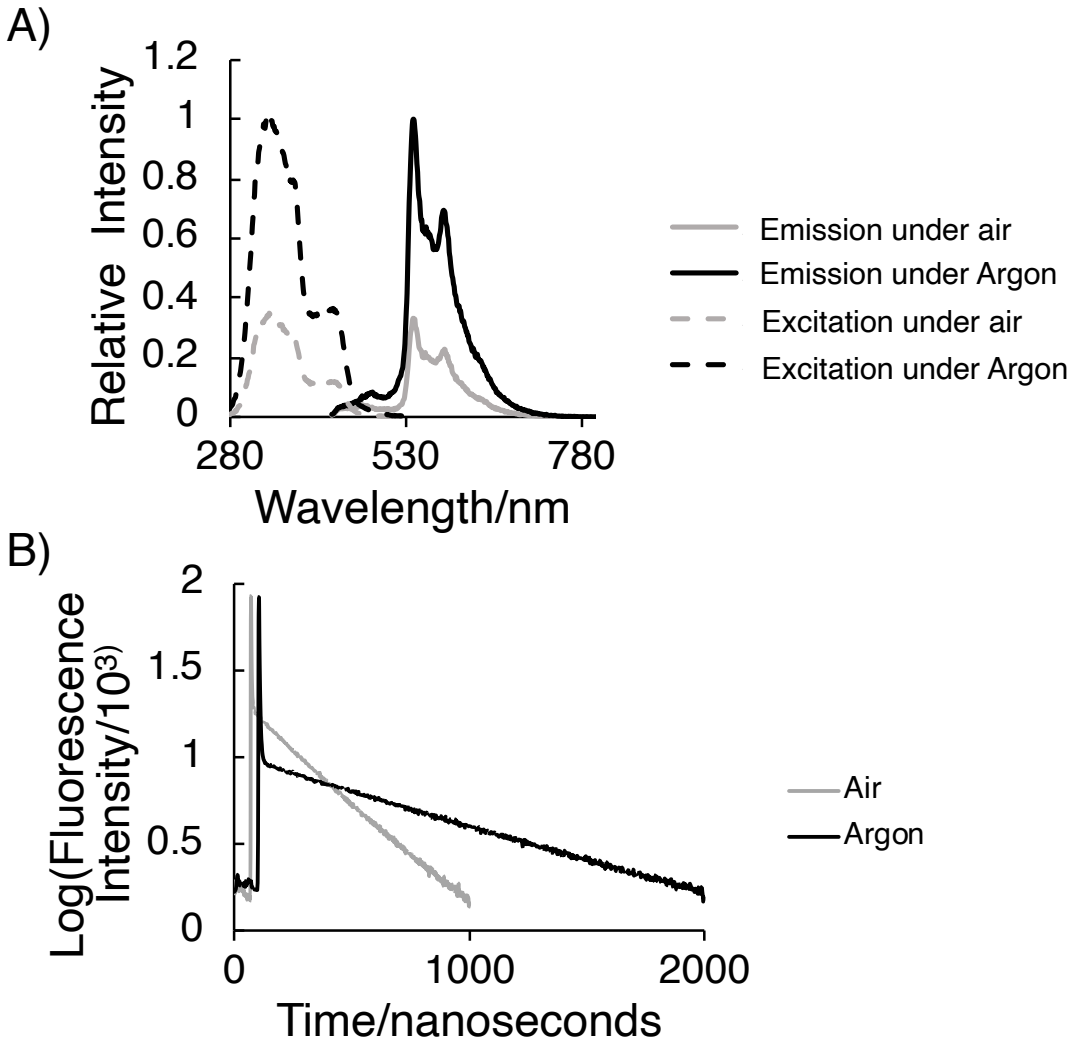

Figure 3.4 A) The emission (λ_{exc} 410 nm) and excitation (λ_{em} 550 nm) spectra of IrTHPyBenz in a solution of DCM under air and argon. B) the time-resolved excited state decay of IrTHPyBenz (DCM, λ_{em} 510 nm, λ_{exc} 410 nm) under air and argon.

The emission of IrTHPyBenz increased by a factor of three in an argon containing solution when compared to the same solution with oxygen present (Figure 3.4A). The increase in phosphorescence is through the loss of a non-radiative energy transfer decay pathway through interaction with molecular oxygen. Therefore, the excited state is forced to decay more through emission upon the removal of oxygen. Consequently, the lifetime of the excited state also increased by a factor of three upon the removal of oxygen from 330 ns to 990 ns (Figure 3.4B). This was

rationalised due to the increase in the radiative phosphorescent decay pathway being a spin forbidden process which stabilised the excited state population and hence the lifetime. The Stern-Volmer equation was used to calculate the rate constant of quenching by oxygen, k_q, under the assumption that O_2 behaves as an ideal gas. The concentration of O_2 was calculated in aerated DCM at room temperature/pressure, at 1.234 mM using an experimentally pre-determined mole fraction, x_g, from the literature (Sato, Hamada et al., 2014, Young, Battino et al., 1979). By incorporating the excited state lifetime differences in aerated vs anoxic solutions, a κ_q (O_2) value for IrTHPyBenz was calculated at 1.64 x 10^9 $M^{-1}s^{-1}$ which directly quantified a quenching effect. Altogether the differences in emission and excited state lifetimes evidenced the quenching of molecular oxygen with the triplet excited state, a critical pre-requisite for efficient energy transfer and hence generation of lethal $^1O_2$ for PDT.

Currently approved 1st and 2nd generation PS are disadvantaged by autophotobleaching which are particularly problematic with porphyrin-based PS (Georgakoudi, Nichols et al., 1997). Photobleaching weakens the efficacy of PDT through the destruction of excited state dynamics which are critical for singlet oxygen generation. Additionally, photobleaching and/or photoreactions could produce off-target cytotoxicity through by-product creation. To test this, a solution of IrTHPyBenz was irradiated at high energy visible light (405 nm) for up to 36 minutes and the MLCT band monitored for degradation by UV-vis spectroscopy (Figure 3.5).

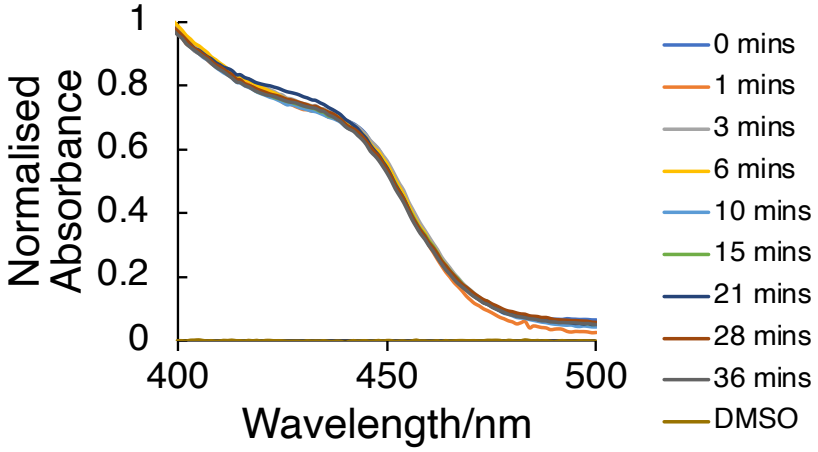

Figure 3.5 The absorbance spectra of IrTHPyBenz (in DMSO) after 405 nm irradiation at constant power (20 mWcm^{-2}). The same solution was irradiated in intervals to give cumulative irradiation times with the absorption spectra being measured in between.

The MLCT band of IrTHPyBenz was highly stable and resisted photobleaching, evidenced by no changes in absorption up to 36 minutes of 405 nm irradiation. The lack of absorption changes indicated high structural integrity of IrTHPyBenz upon a high exposure of high energy light. The irradiation conditions were parametrised through the replication of IrNew's PDT conditions (20 $mWcm^{-2}$, 3 mins) which produced excellent *in vitro* PDT activity (McKenzie, Sazanovich et al., 2017). Therefore, if IrTHPyBenz can retain IrNew's PDT effects, the therapeutic irradiation time range could be highly flexible with the potential to increase with no concurrent loss of complex integrity arising from photobleaching.

The quantum yield, Φ, of IrTHPyBenz was measured by comparing the integrated emission against that of $[Ru(bpy)_3]Cl_2$, a standard emissive compound, with Φ 0.042 (Caspar and Meyer, 1983)(Figure 3.6)

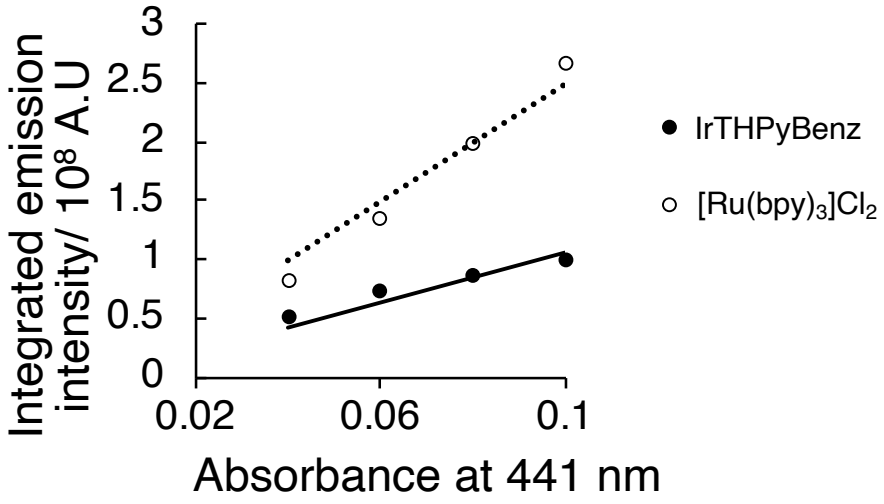

Figure 3.6 A plot of the integrated emission (λ_{exc} 441 nm) at varying optical densities of solutions of IrTHPyBenz and $[Ru(bpy)_3]Cl_2$ in acetonitrile.

Φ (IrTHPyBenz) was calculated at 0.018 in an aerated solution of CH_3CN. Consequently, the radiative rate constant, k_r (IrTHPyBenz) was calculated to be 5.44 x 10^4 s^{-1} and the non-radiative constant in aerated DCM was k_{nr} (IrTHPyBenz) 2.93 x 10^6 s^{-1}. These values quantify the extent to which IrTHPyBenz decays via radiative and non-radiative decay pathways with ~ 98.2% being non-radiative (e.g. vibrational cooling, energy transfer) and ~ 1.8 % through phosphorescence.

Ultimately, the ability to generate singlet oxygen is an important factor in creating PDT activity. The generation of $^1O_2$ can be monitored through the decay of its emission. The emission of such was measured upon the irradiation of IrTHPyBenz solution, and compared relatively against a reference compound, perinapthenone (Figure 3.7).

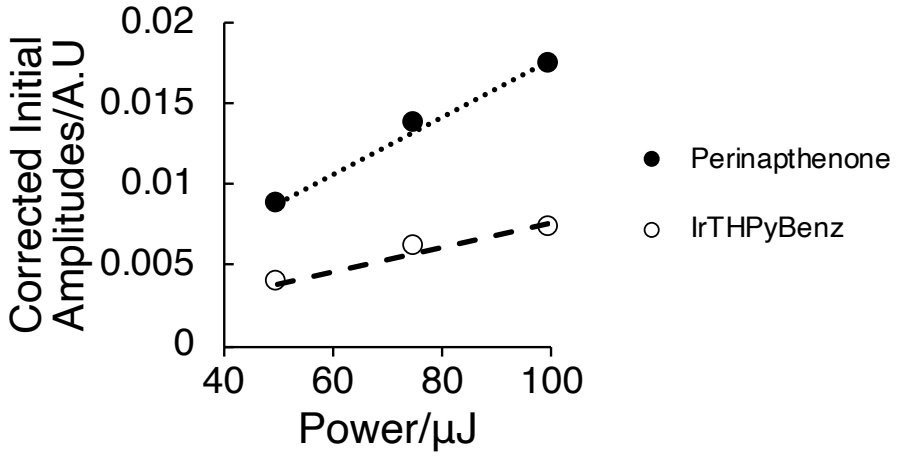

Figure 3.7 The initial amplitudes of the radiative decay of singlet oxygen (λ_{em} 1275 nm) upon the irradiation of solutions of IrTHPyBenz and perinapthenone (acetonitrile) at 355 nm by a Nd:YAG laser.

IrTHPyBenz generated $^1O_2$ at 43 % the levels relative to perinapthenone, for which the yield of $^1O_2$ is assumed to be 100%. The ability to generate singlet oxygen occurs by a catalytic cycle upon which many molecules of $^3O_2$ can be excited by the repeated deactivation of the IrTHPyBenz excited state. Therefore, the ability for IrTHPyBenz to be part of such a cycle is the key requirement for PDT activity.

3.2 – Biological Analysis

3.2.1 – Cellular Uptake Studies

Given favourable spectroscopic properties for PDT, IrTHPyBenz was added to cells followed by fluorescence imaging. This was to assess cellular uptake and to look for any gross cellular toxicity effects being present (Figure 3.8).

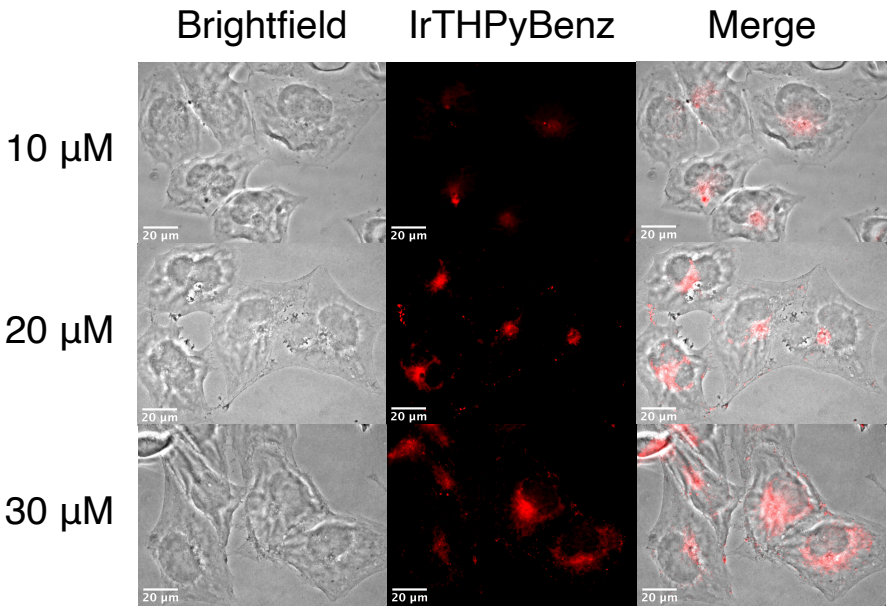

Figure 3.8 Fluorescence imaging of EJ cells following 2h treatment with varying doses of IrTHPyBenz (λ_{exc} 350 – 400 nm, λ_{em} 570 nm). Cells were incubated with drug, fixed and then imaged by widefield microscopy.

EJ cells (bladder carcinoma) present a relevant *in vitro* model, with bladder cancer being PDT treatable through the use of a catheter coupled laser (Bader, Stepp et al., 2013). The phosphorescence of IrTHPyBenz was seen in the cytoplasm of EJ cells following 2 hours of incubation, demonstrating cellular uptake which increased proportionally to drug dose, suggesting that a saturation in uptake had not been met at 30 µM. Furthermore, no phosphorescence was detected in the cell nucleus. This suggests that the drug cannot penetrate through the nuclear membrane and/or has no affinity for nuclear material. This is advantageous for PDT, given that drugs which localise to the nucleus tend to be mutagenic and toxic, even in the dark, and can therefore elicit off-target cytotoxicity (Ashfaq, Najam et al., 2014). Additionally, no obvious changes in cellular morphology were observed which indicates no superficial short-term dark toxicity was occurring, again advantageous for PDT.

Given that uptake occurred, the time parameter was investigated in an effort to ascertain the optimum window for any subsequent PDT effects (Figure 3.9).

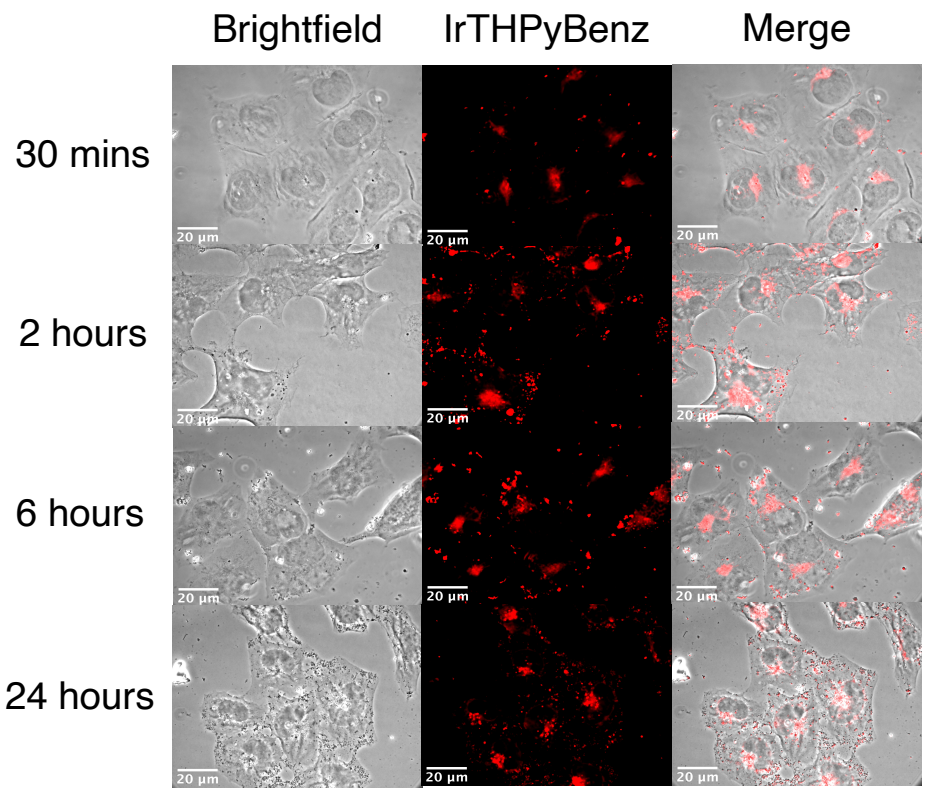

Figure 3.9 Fluorescence imaging of EJ cells following treatment of IrTHPyBenz (30 µM) at different exposure time points (λ_{exc} 350 – 400 nm, λ_{em} 570 nm). Cells were incubated with drug, fixed and then imaged by widefield microscopy.

By eye the intracellular concentration (fluorescence intensity) increased between 30 mins to 2 hours with no further increase in intensity after 6 hours and 24 hours. Instead, cell membrane bound precipitate of IrTHPyBenz could be observed, which was particularly pronounced at 24 hours as validated by the overlap of the phosphorescence image with the brightfield image. Therefore, in translation to PDT experiments, 2 hours of drug incubation was considered optimum due to the balance of maximal cellular concentration with minimal membrane bound precipitate. Too much precipitate could be problematic in causing off target toxicity effects through the disruption of membrane trafficking and/or cell suffocation. Furthermore, cell necrosis could be favoured over regulated cell death due to the oxidative destruction of the cell membrane, which could increase inflammation.

Cellular uptake was also validated in other appropriate cell lines, namely malignant melanoma, A375, and transformed oropharyngeal, OPSCC72, cell lines (Figure 3.10). IrTHPyBenz was uptaken in all three cell lines with no obvious differences in

cell fluorescence and intracellular distribution. In all three cell lines IrTHPyBenz accumulated in the cytoplasm. Cell line uptake and localisation independence is advantageous when translating potential PDT activity to multiple cancer cell lines.

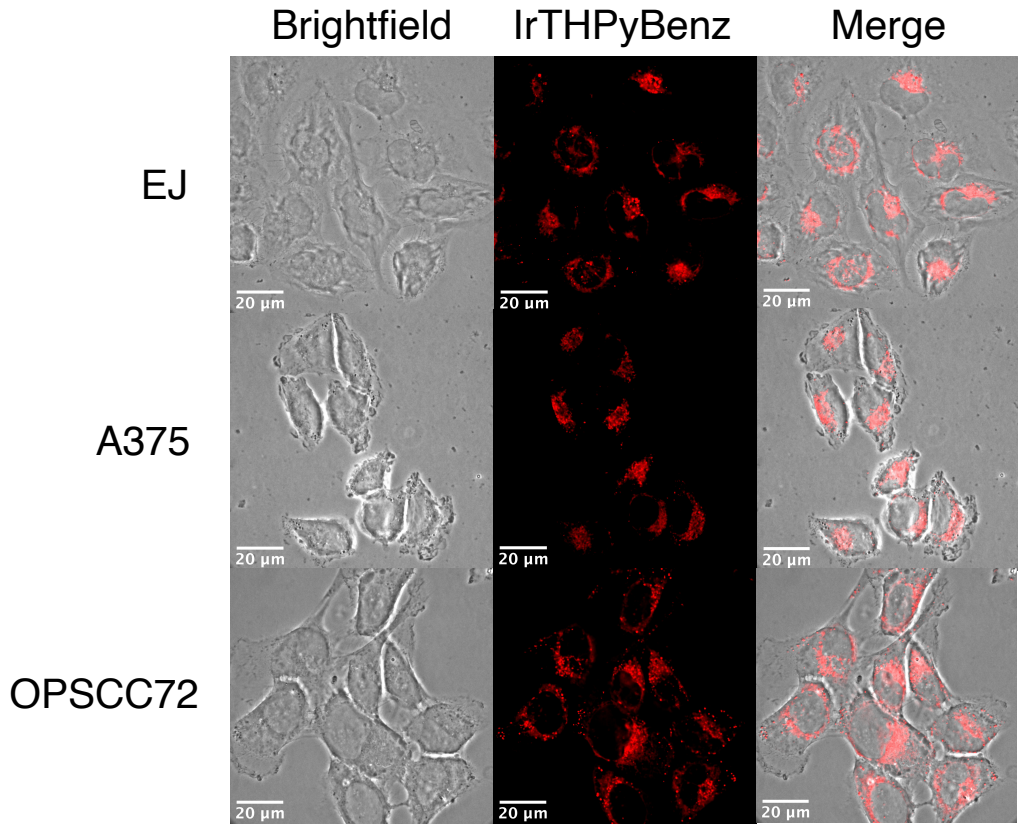

Figure 3.10 Fluorescence imaging of IrTHPyBenz (2hr, 20 µM) in three PDT relevant cancer cell lines; EJ (bladder carcinoma), A375 (malignant melanoma) and OPSCC72 (oropharyngeal carcinoma) (λ_{exc} 350 – 400 nm, λ_{em} 570 nm). Cells were incubated with drug, fixed and then imaged on a widefield microscope.

Next the mechanism of uptake was explored, focusing on both passive and active pathways (Figure 3.11). To probe the extent of active uptake, cells were incubated on ice to arrest ATP production, theoretically disabling all active pathways but permitting passive membrane diffusion. Additionally, specific active mechanisms were inhibited through pre-incubation with inhibiters, namely Et_4NCl (cationic transporters), valinomycin (transmembrane potential) and chloroquine (endocytosis) before IrTHPyBenz exposure. Uptake was again assessed by cellular phosphorescence.

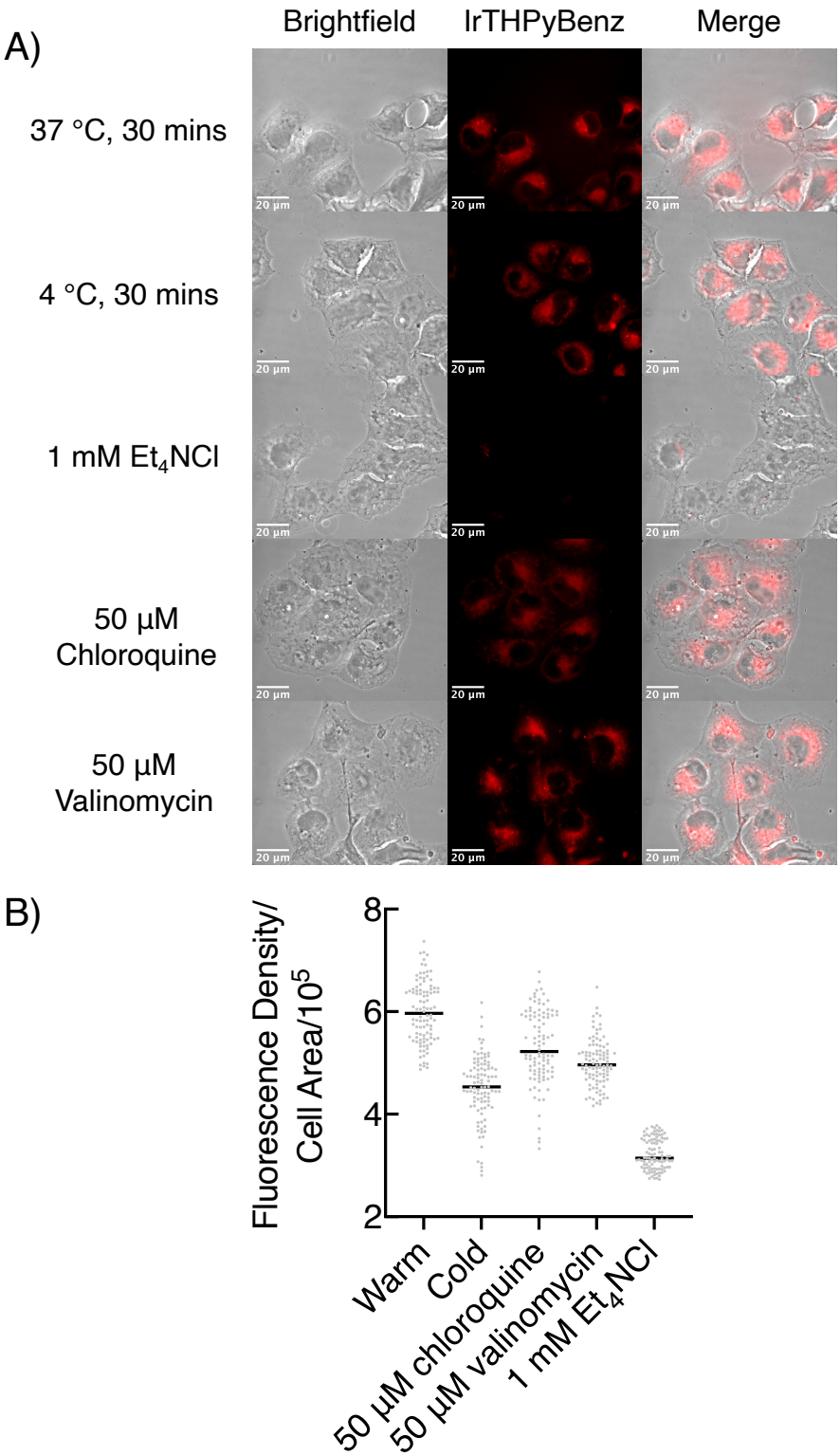

*Figure 3.11 EJ cells were incubated with IrTHPyBenz (20 µM, 30 mins) at either 37 °C (warm) or on ice (cold) (λ_{exc} 350 – 400 nm, λ_{em} 570 nm). The remaining 3 conditions had active transport mechanisms inhibited pre-drug exposure. Namely endocytosis (chloroquine, 50 µM, 1 hr), transmembrane potential (valinomycin, 50 µM, 30 mins) or cationic transporters (Et_4NCl, 1 mM, 20 mins) A) Representative images B) The fluorescence quantification of 100 cells on 1 independent occasion. One way ANOVA **** $p < 0.0001$*

A marked decrease in measured phosphorescence occurred in samples with inhibited cationic transport pathways (Et_4NCl), consistent with Ir(III) complexes (Yu, Zhao et al., 2008). Measured phosphorescence was also reduced after pre-incubation on ice, suggesting a component of passive cellular uptake. Additionally, a slight decrease in phosphorescence was observed upon the inhibition of both endocytosis and transmembrane potential mechanisms when compared to the untreated condition. Therefore, IrTHPyBenz was uptaken through a mixture of passive diffusion, endocytosis, cationic and transmembrane potential transporters, albeit to different degrees.

For PDT, rapid and effective PS elimination is an important parameter given the onset of unfavourable side effects and latent photosensitivity, specifically attributed to slow and unfavourable bioelimination (Bellnier, Ho et al., 1989). Therefore, the elimination/stability of IrTHPyBenz was scrutinised by fluorescence microscopy at different time points following the removal of drugged media (Figure 3.12).

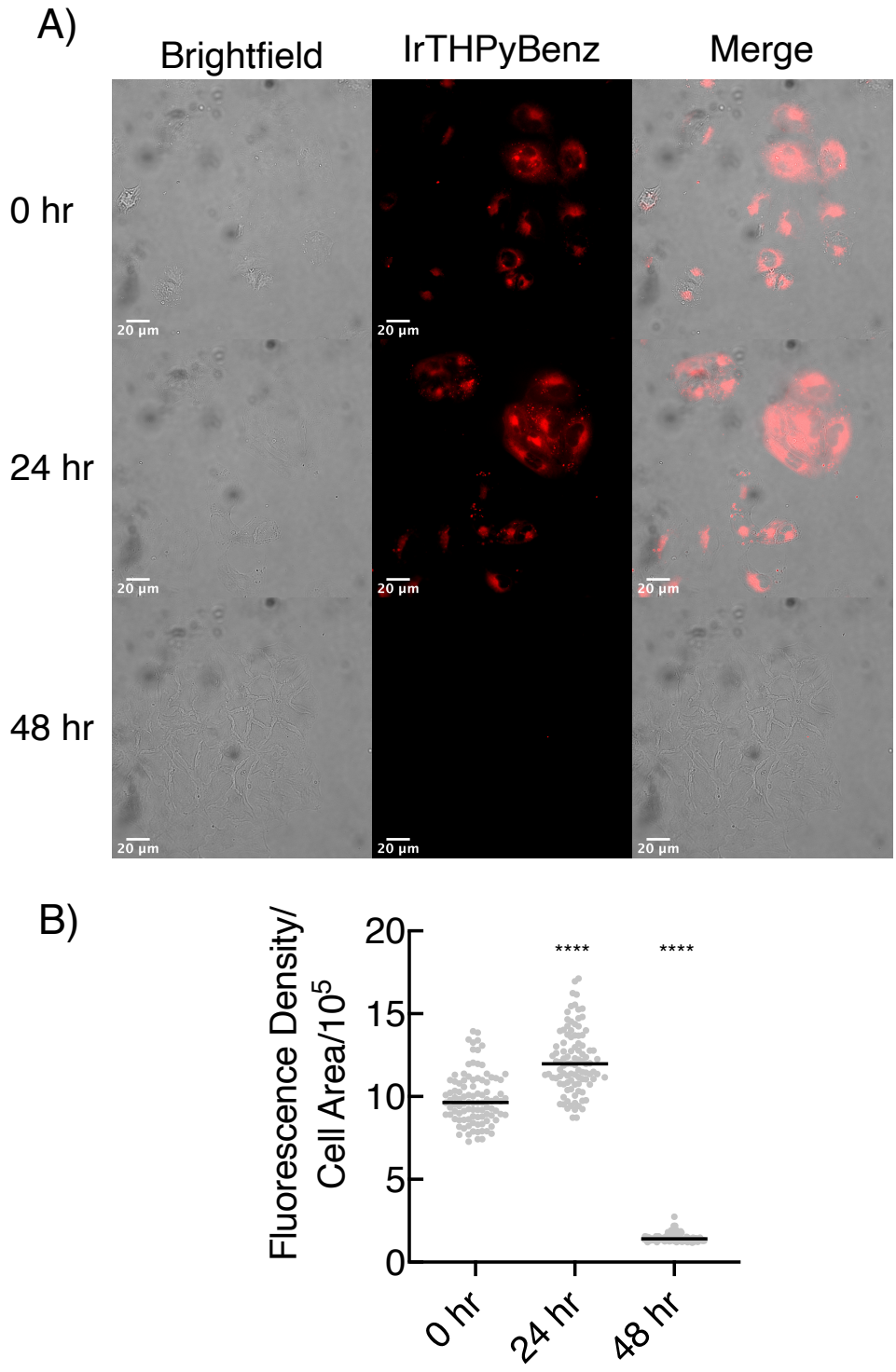

*Figure 3.12 IrTHPyBenz was added to EJ cells for 2 hr prior to the addition of fresh undrugged media. Cells were then fixed and imaged (λ_{exc} 350 – 400 nm, λ_{em} 570 nm) at various timepoints post removal of IrTHPyBenz. A) Representative images B) The fluorescence quantification of 100 cells on 1 independent occasion. Student T test (2 way, paired): p = 2.43 x 10^{-17} **** (0 hr vs. 24 hr), p = 1.19 x 10^{-21} **** (0 hr vs 48 hr). One way ANOVA **** p < 0.0001.*

IrTHPyBenz phosphorescence was monitored in the intracellular environment up to 48 hours post drug removal and quantified by ImageJ. After drug removal IrTHPyBenz was retained for 24 h and then lost from cells between 24 - 48 hours, suggesting favourable parameters for both retention (to elicit PDT effects) and elimination (for quick and efficient removal). Exposed EJ cells were also crudely observed to be healthy and proliferating suggesting that IrTHPyBenz is relatively non-toxic. However, a suitable *in vivo* model is required to scrutinise any possible elimination routes in a body e.g. hepatic, renal. Despite this, IrTHPyBenz has cell membrane dynamism, with both effective uptake and retention in addition to favourable elimination which produced no obvious toxic effects.

3.2.2 – Cell Toxicity

Upon the confirmation of a suitable uptake timepoint and dose, A375 (melanoma), EJ (bladder epithelial carcinoma) and OPSCC72 (oropharyngeal small cell carcinoma) were incubated with IrTHPyBenz and their survival assessed. Firstly, the dark toxicity was determined to assess any possible upper limits to the phototoxic dose and following this, PDT was attempted through light exposure (Figure 3.13).

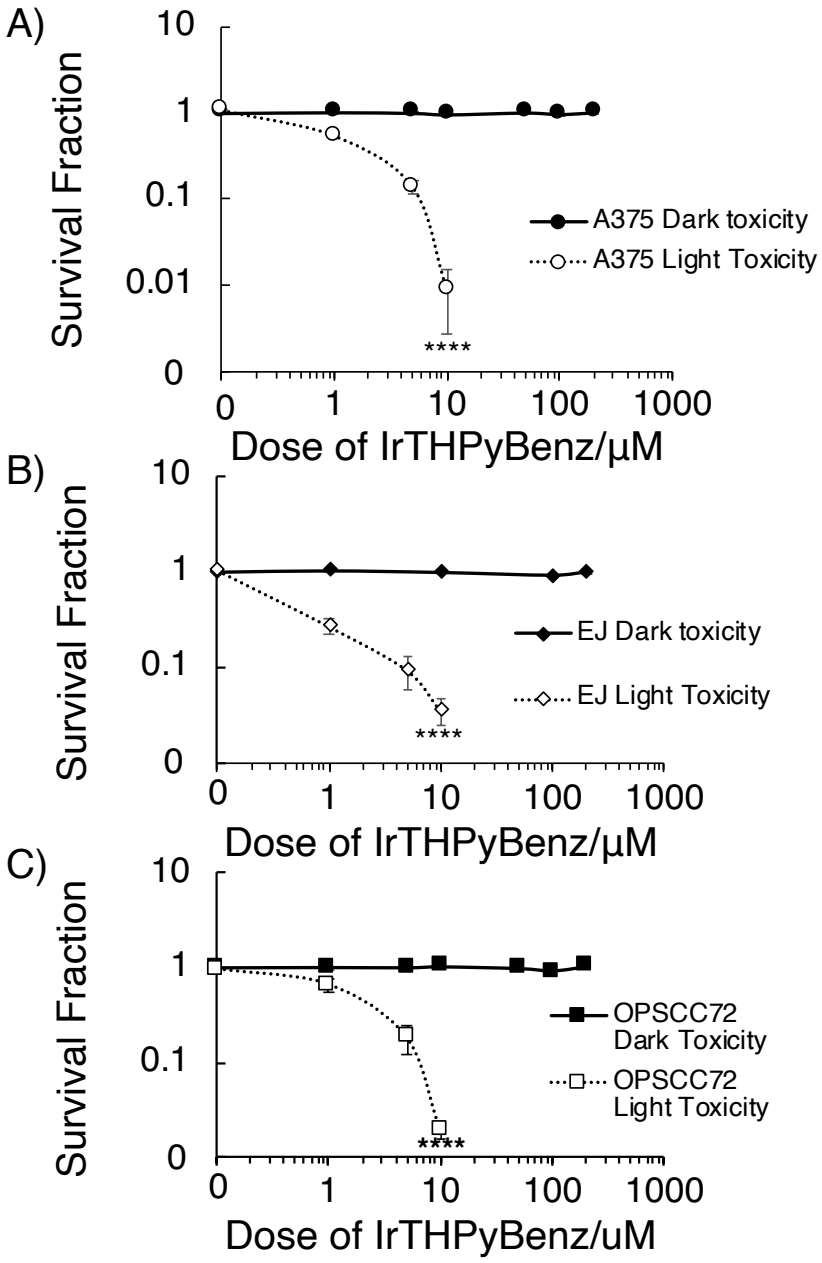

Figure 3.13 Clonogenic survival assays. Cells were treated with increasing doses of IrTHPyBenz for 2 hours followed by addition of undrugged media. Cells were then left for 7-14 days to form colonies (dark toxicity) or exposed to 405 nm light (20 mWcm^{-2}, 3 mins) and then left for 7-14 days to form colonies. A) A375 malignant melanoma B) EJ Bladder carcinoma C) Oropharyngeal small cell carcinoma. In each case the mean and SDs of 3 independent repeats are shown.

Students's T Test at the highest dose was conducted (two way, paired)

*$p = 1.34 \times 10^{7}$ (OPSCC72, ****), $p = 7.26 \times 10^{6}$ (EJ, ****) and $p = 5.63 \times 10^{6}$ (A375, ****).*

IrTHPyBenz induced no dark toxicity in any of the three cell lines up to 200 μM. At 200 μM, DMSO is at a concentration of 4 % which limits further increases. In contrast, IrTHPyBenz exhibited high levels of light toxicity which resulted in high lethality in all cell lines. These effects were measured upon mild irradiation at 405 nm (20 $mWcm^{-2}$, 3 mins).

Phototoxicity is usually measured through the phototoxic index, PI = LD_{50}(Dark)/ LD_{50}(Light). IrTHPyBenz has a dark toxicity value of LD_{50}(dark) at $>$ 200 μM in all three cell lines, while its LD_{50}(light) varied between 2 and 0.53 μM. Thus, large PI values of between 100 and 378 were calculated (Figure 3.14). A large difference in dark and light toxicity allows for large flexibility in dosage which can accommodate modifications.

Figure 3.14 A summary of the phototoxic index and LD50/10 (light) of IrTHPyBenz in the three tested cell lines.

Cell line	LD_{10}(light)/μM	LD_{50}(light)/μM	PI
EJ	0.16	0.53	> 378
A375	0.23	1.20	> 166
OPSCC72	0.14	2	> 100

3.3.3 – Mechanism of Cell Death

Given high measured phototoxic effects, the type of cell death elicited was investigated. Cells were irradiated (405 nm, 20 $mWcm^{-2}$, 3 mins) following IrTHPyBenz incubation (10 μM, 2 hrs) and then fixed at different time points. Apoptosis was then crudely assessed based on visible markers such as membrane blebbing which were visible at 1 hour post irradiation. To further examine the role of apoptosis, a probe which detects cells in the apoptotic executioner phase via caspase 3/7 was incubated with cells and its fluorescence response collected (Figure 3.15).

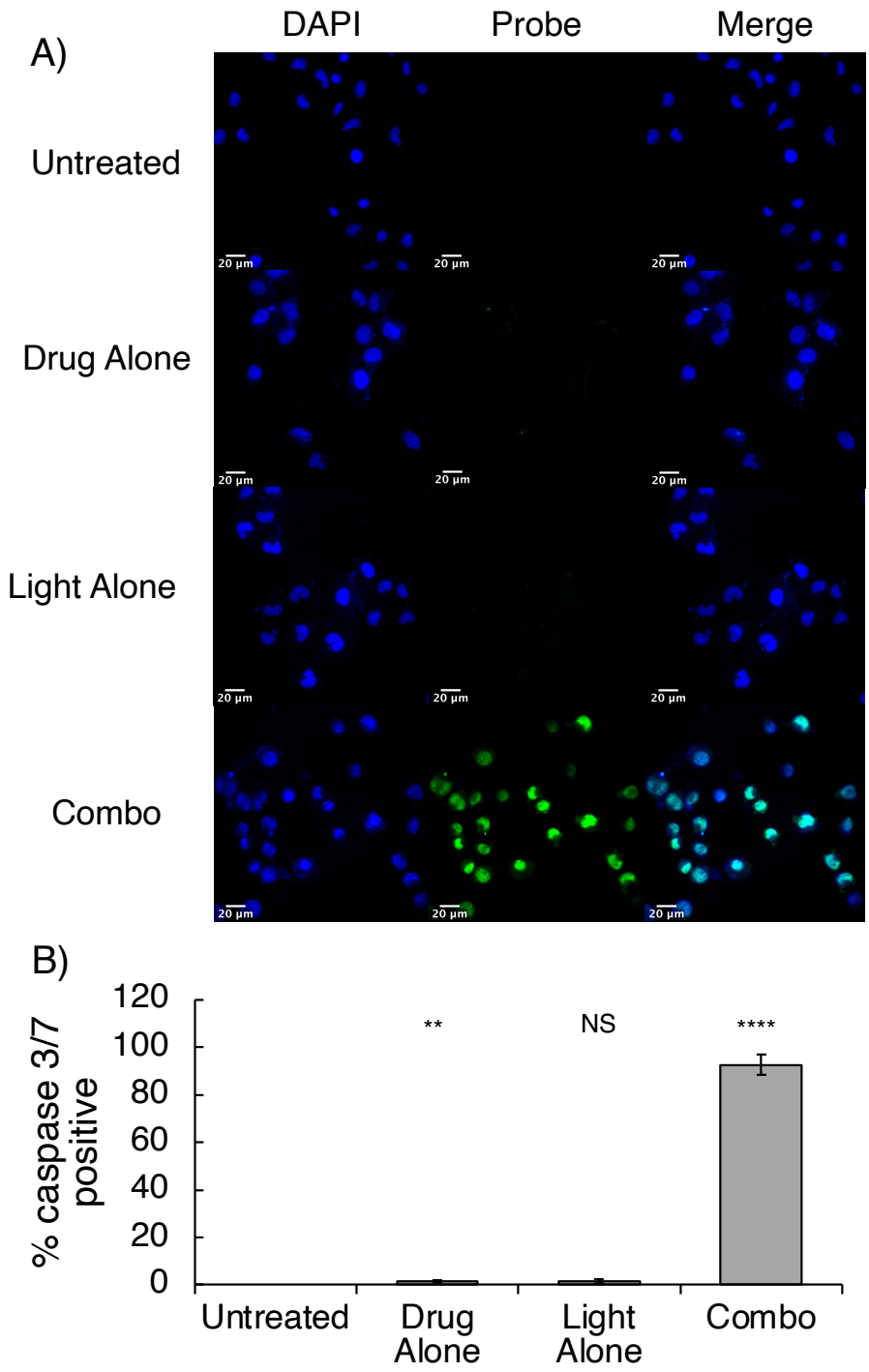

*Figure 3.15 EJ cells were drugged (10 µM IrTHPyBenz, 2hrs) and then irradiated (405 nm, 20 mW/cm^2, 3 mins). At 1 hour post irradiation, cells were exposed to a probe which fluoresces at 488 nm when caspase 3/7 (a marker of apoptosis) (λ_{exc} 488 nm, λ_{em} 520 nm) is active and DAPI (λ_{exc} 350 nm, λ_{em} 450 nm) which are then detected by fluourescence microscopy A) Representative images B) 100 cell nuclei are scored as + or – for fluorescence response and hence caspase 3/7 activation. The mean and SDs of 3 independent repeats are shown. Student T test p values; Drug alone (p = 0.0067, **), light alone (0.13, NS) combination (p = 2.9 x 10^3, ****) all vs untreated.*

Caspase 3/7 was detected using a probe constituted of a four amino-acid peptide (DEVD) conjugated to a dye. Upon the activation of caspase 3/7, which is known for its cleaving 'executioner' activity, the DEVD/dye bond is broken which allows for an association between the dye and DNA which produces fluorescence. When caspase 3/7 is inactive, the dye cannot associate to DNA, due to DEVD sequestration and hence is non-fluorescent. Therefore, the detection of dye-DNA fluorescence is a quantitative marker for caspase 3/7 activity. In cells which were subjected to an incubation with IrTHPyBenz followed by 405 nm irradiation, an overwhelming fluorescence response was detected in the nuclei when compared to the untreated condition. Furthermore, IrTHPyBenz incubation and irradiation separately resulted in very little nuclear fluorescence, indicative of inactive caspase 3/7 which suggested minimum off-targeted cell toxicity. In addition to detecting active caspase 3/7, the DNA association of the probe gives an observation as to the extent of apoptotic breakdown. For example, early in the apoptotic response, chromatin remains uncleaved, unpackaged and intact and will appear as whole nuclei. Further on in the process, chromatin is cleaved into smaller fragments, packaged and secreted on the cell membrane. Caspase 3/7 are known as the executioners and are activated downstream of caspase 9 initiation meaning apoptosis is irreversible. Therefore, at 1 hour post irradiation, the initiation of apoptosis has been signalled, likely through oxidative damage, and has proceeded into the executioner phase. However, nuclei still appeared to be largely intact, as well as the cell membrane, which suggested that the cells were early into the phase. This shows that IrTHPyBenz can elicit PDT effects to therapeutically and rapidly trigger a regulated cell death pathway in cancerous cells.

3.2.4 – Cellular Localisation

The sub-cellular localisation of IrTHPyBenz was analysed in an effort to understand its phototoxic effects. PS which are highly associated with specific organelles cause oxidative damage which leads to disfunction and cell death. Common organelle targets for highly phototoxic iridium (III) PS include the mitochondria, the endoplasmic reticulum and the Golgi apparatus. Given this, each of the three common organelle targets were immunostained with a fluorescently

tagged antibody and the fluorescence overlap quantified with IrTHPyBenz's phosphorescence to give a measure of co-localisation (Figure 3.16).

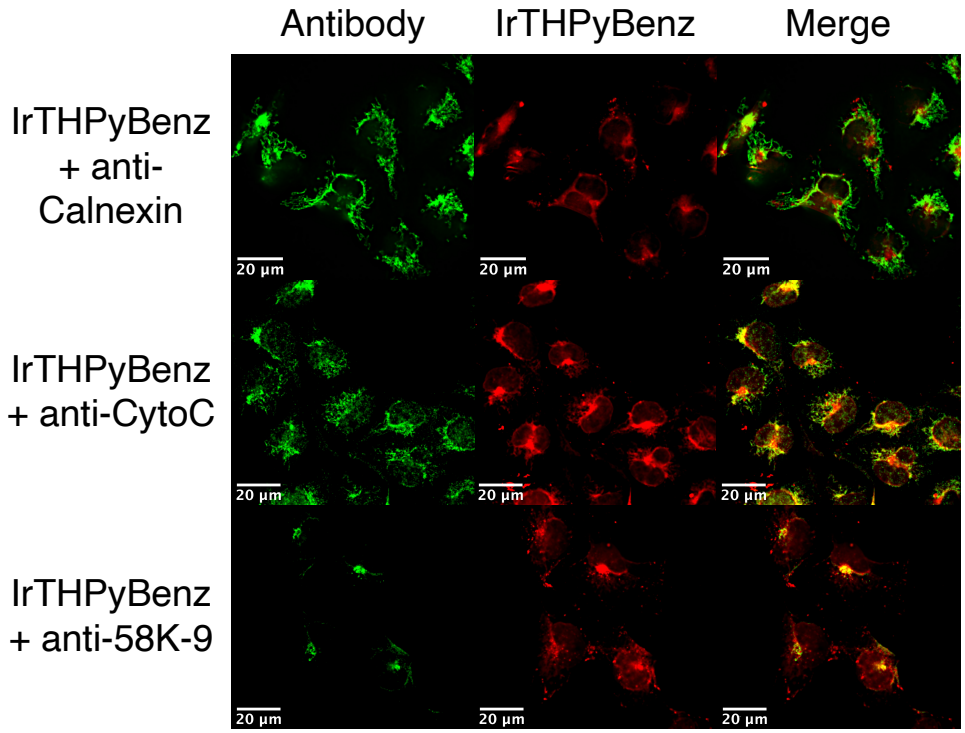

Figure 3.16 EJ cells were incubated with IrTHPyBenz (30 µM, 2 hr) (λ_{exc} 350 – 400 nm, λ_{em} 570 nm) and then fixed. Fixed cells were then immunostained with antibodies specific to an organelle protein (ER – calnexin, mitochondria – cytochrome c oxidase, Golgi apparatus – 58K-9) before being treated with a fluorescently tagged secondary antibody (λ_{exc} 488 nm, λ_{em} 520 nm) . The fluorescence overlap (orange) of the secondary antibodies (green) was then analysed against the phosphorescence of IrTHPyBenz (red) to determine co-localisation.

IrTHPyBenz localised to the mitochondria, ER and the Golgi apparatus following incubation, albeit to different extents. A Pearson's Correlation Coefficient (PCC) algorithm was calculated for luminescence in the red (IrTHPyBenz) and green (organelle) channels, this quantifies the degree of pixel overlap by producing a value scaled between 0 (no overlap) and 1 (complete overlap). PCC values were IrTHPyBenz:ER 0.64, IrTHPyBenz:mitochondria 0.71 and IrTHPyBenz:Golgi 0.85, i.e the highest measured PCC of IrTHPyBenz was at the Golgi apparatus, followed closely by the mitochondria and to a lesser degree the ER. Given the relationship between the integrity of the mitochondria membrane and the initiation of intrinsic apoptosis, a likely lethal pathway could be through localised photodamage causing

cytochrome c oxidase leakage into the cytosol. Furthermore, the Golgi apparatus regulates membrane trafficking by exporting and packaging intracellular material into endosomes which are then exocytosed or transported to the lysosomes for degradation and therefore presents a passive target for drugs (Xing, Zheng et al., 2021). Similarly, PDT-mediated cell death has been linked to Golgi photodamage which could therefore rationalise IrTHPyBenz phototoxicity (Soldani, Bottone et al., 2004).

Given the high degree of localisation to the Golgi apparatus, PCC values were also measured in the other cell lines tested for PDT activity (Figure 3.17).

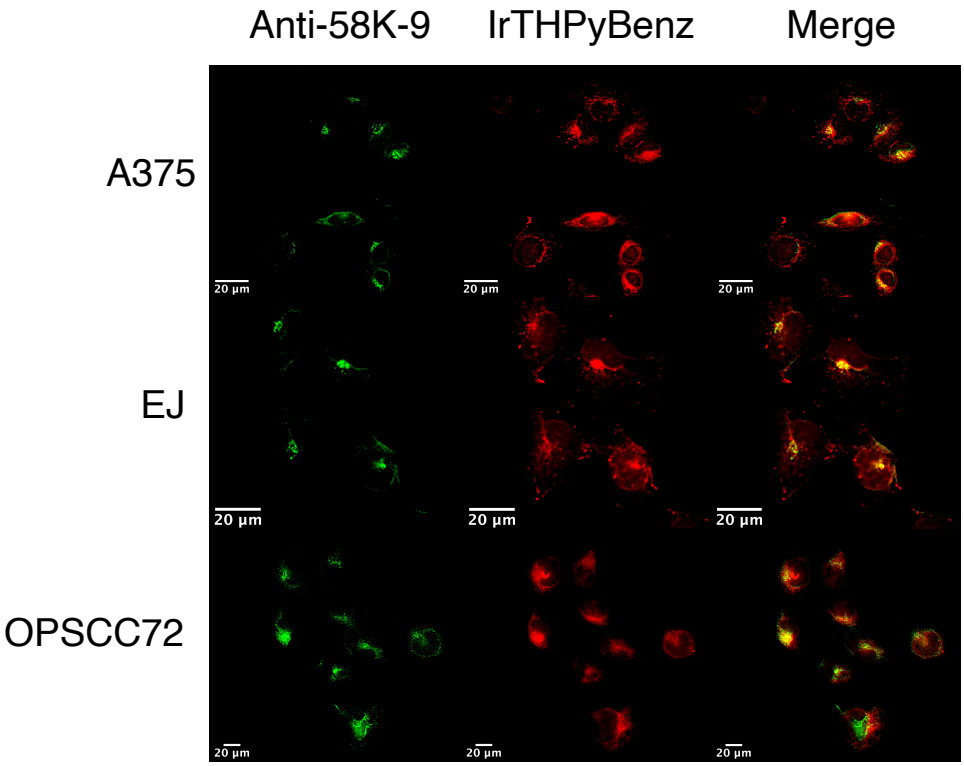

Figure 3.17 IrTHPyBenz (30 µM, 2hrs) (λ_{exc} 350 – 400 nm, λ_{em} 570 nm) was exposed to EJ cells, A375 and OPSCC72 before being fixed and immunostained (Golgi, anti-58K-9) and imaged (λ_{exc} 488 nm, λ_{em} 520 nm).

IrTHPyBenz co-localised to the Golgi apparatus in A375, OPSCC72 and EJ cells. PCCs were calculated as 0.85 (EJ), 0.76 (A375) and 0.86 (OPSCC72), suggesting significant co-localisation. Given that the PDT approved Photofrin® strongly localises to the Golgi apparatus and produces excellent PDT effects, subsequent analysis of

the Golgi-centred photodamage response was conducted (Hsieh, Wu et al., 2003)(Figure 3.18).

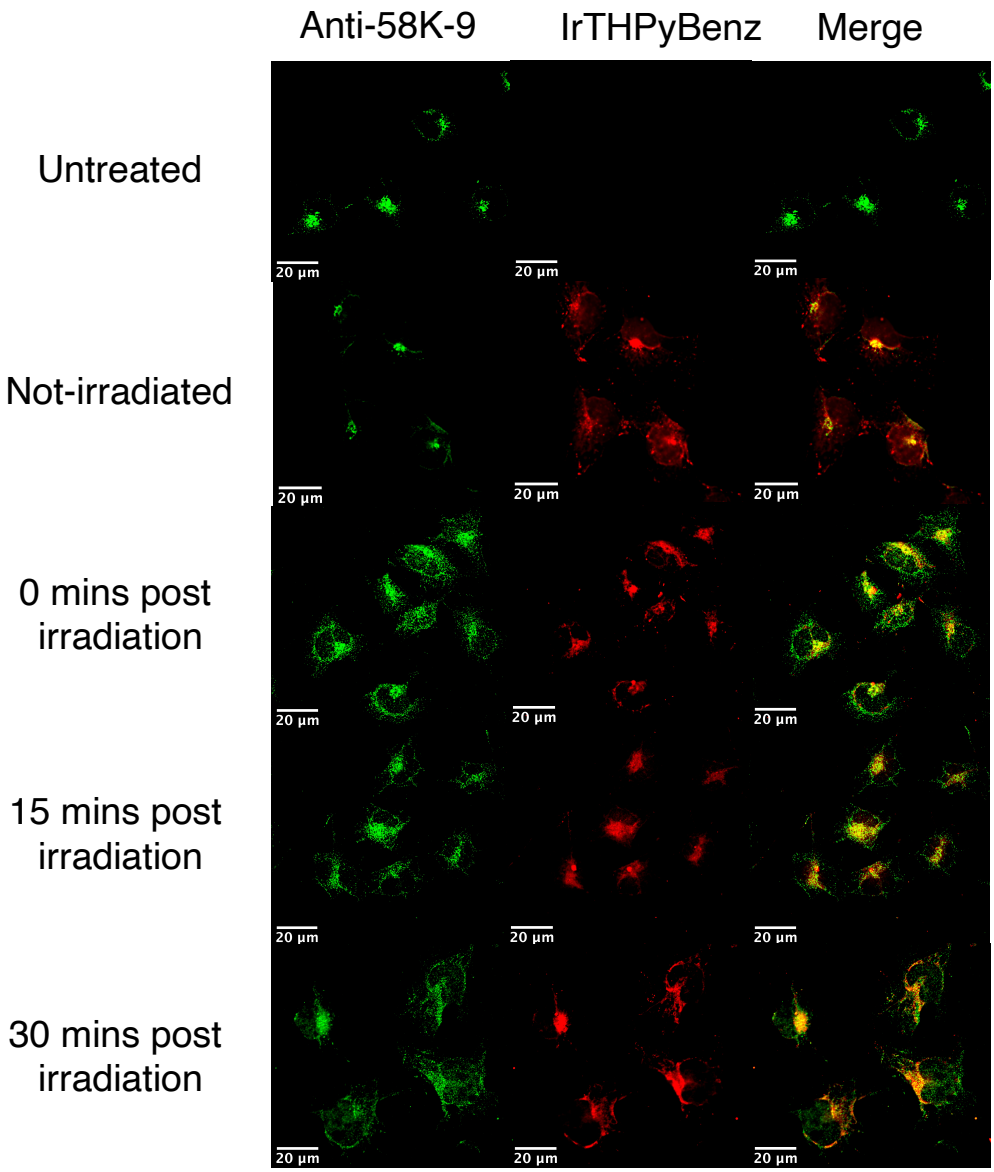

Figure 3.18 EJ cells were treated with IrTHPyBenz (10 µM, 2hr) (λ_{exc} 350 – 400 nm, λ_{em} 570 nm) and then irradiated (405 nm, 20 mWcm^{-2}, 3 mins). Cells were then fixed at different time points and immunostained with anti-58K-9 followed by a fluorescently tagged secondary antibody (λ_{exc} 488 nm, λ_{em} 520 nm). Imaging was then taken to analyse the response of the Golgi apparatus (green) to photodamage.

The Golgi apparatus is known to change its configuration throughout the cell cycle and hence normally reversibly fragments during cytokinesis. In addition, fragmentation can occur irreversibly in response to damage which has been linked to

the activation of apoptosis and/or autophagy (Sütterlin, Hsu et al., 2002). IrTHPyBenz incubated samples (10 μM, 2 hrs) were fixed at increasing time intervals post irradiation (405 nm, 20 $mWcm^{-2}$, 3 mins) and then subsequently immunostained with 58K-9, a Golgi protein marker. Post irradiation, the Golgi apparatus immediately dispersed throughout the cytoplasm indicating the rapid onset of Golgi fragmentation. This was in direct contrast to both the untreated and non-irradiated conditions which showed a high degree of Golgi integrity. The dispersion visually increased with time post-irradiation suggesting irreversible fragmentation. This is not likely ascribed to mitotic effects as no increase in M phase cells were observed in any of the imaging experiments conducted but should be confirmed by cell cycle analysis using FACS PI/pH3 staining. Additionally, co-localisation between the fragmented Golgi material and IrTHPyBenz persisted further suggesting a high adherence to Golgi material. Further postulation of high cross talk between Golgi fragmentation and caspase 3/7 activation can be made due to the two measured events existing in the same timeframe.

3.2.5 – 3D Cell Spheroid Models

3D cell spheroid models represent an improvement in mimicking the *in vivo* cancer cell environment whilst remaining as an easier-to-perform *in vitro* method. Conventional 2D cell culturing falls short of replicating tumour characteristics such as heterogeneity, complex architecture and communal growth which can all directly impact treatment efficacy (Lee, Kenny et al., 2007). Conversely, 3D cell spheroid models capture *in vivo* tumour properties such as hypoxia, reduced drug/light penetration, cell-cell interactions and in some cases even extracellular matrix components (Zanoni, Piccinini et al., 2016)(Figure 3.19).

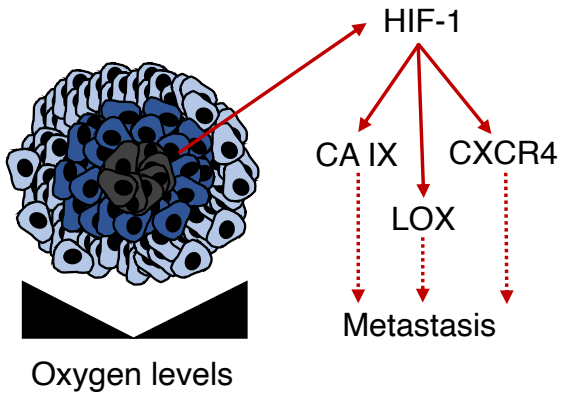

Figure 3.19 The establishment of hypoxia in solid state tumors. Due to poor vascularisation of the tumor microenvironment (TME) and the tissue diffusion limit of oxygen, a gradient of increasing hypoxia exists upon core penetration.

The spheroid-forming ability of a cell line is dependent on a variety of factors which leads to differing methods of culturing based on their anchorage dependency. The exact method is decided upon by the ability of a cell to avoid anchorage dependent cell death (anoikis)(Sant and Johnston, 2017). For anchorage independent cell lines, which are generally highly malignant and transformed, the soft agar method suitably induces spheroid formation by preventing cell adherence through coating a flask with agar (Horman, To et al., 2013). Upon spheroid establishment, a 3D layered system is observed whereby centralised 'core' cells are necrotic compared to the outermost cells which are proliferative, thereby invoking heterogeneity. These layers are categorised into three regions namely the core (necrotic, acidic and hypoxic), the middle (quiescent, non-normoxic) and outermost (proliferative and normoxic)(Sutherland, 1988). These varying layers have properties which effect PDT such as differing drug/light penetration and hence these models provide an opportunity to test these parameters e.g. is there a PDT limitation to superficial levels using a given PS?(Achilli, McCalla et al., 2014). However, these models are not a complete representation of *in vivo* tumours due to the lack of a TME, blood vessels and light absorbing tissue components such as blood (haemoglobin). Additionally, spheroid models cannot be used to measure pharmacokinetics and/or pharmacodynamics but do offer an ethical advantage in the early stages of drug development.

C8161 melanoma cells are an established cell line with the ability to spontaneously form spheroids and are highly anchorage independent. This arises through strong autonomy which leads to a highly metastatic cell phenotype permitted by the avoidance of anoikis (Kim, Koo et al., 2012). Therefore, C8161 cells present ideal 3D cultured PDT applicable models allowing the effect of variable oxygen levels and drug and light penetration on PDT to be assessed without the cost and ethics of *in vivo* studies. Firstly, the optimisation of 3D spheroid models needed to be done. Increasing numbers of C8161 cells were therefore monitored after plating into agarose-lined dishes and imaged at various time points (Figure 3.20).

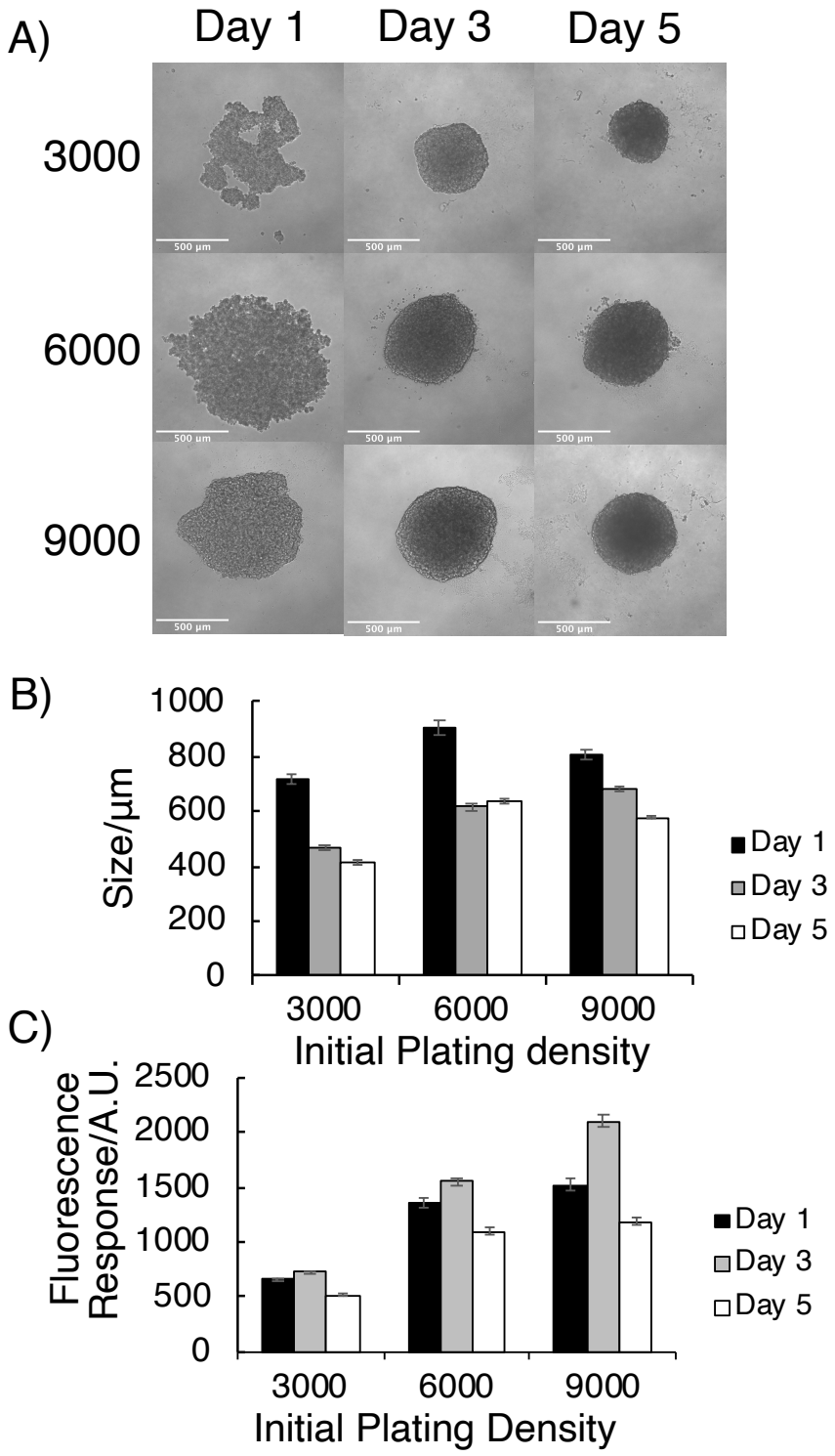

Figure 3.20 C8161 cells were plated into agar-coated 96 well dishes and cultured for 5 days. After days 1, 3 and 5, the size and metabolic activity of each spheroid was measured in order to optimise and establish 3D cell models. A) Representative images of spheroid growth B) Spheroid diameter represented as the mean and SD (n = 1, N = 12) C) The alamar blue fluorescence response of the spheroids stained (n = 1, N = 12).

The pre-requisites of consistent size, uniform shape and exhibition of 3D heterogeneity were analysed. Spheroid compaction and formation was observed between days 1 – 5 through the organisation of a dysregulated cell mass which gradually became more spherical in a day-by-day manner. The chaotically linked cell masses became more established and formed spheres between day 1 – 3; ultimately stabilising by day 5 with sizes proportional to their initial plating densities. Additionally, at day 5, necrotic cell centres could be observed by light microscopy which were particularly more pronounced in the 6000 and 9000 initial plate densities (Figure 3.20). The necrotic cell centres were observed as densely compacted and poorly transparent to light and hence appeared as dark opaque regions in light microscopy. In addition to this alamar blue metabolic assays were used to analyse cell proliferation and ultimately necrotic core formation. Alamar blue (resazurin), a non-fluorescent compound, is uptaken by cells which is followed by cell-active metabolic reduction into its fluorescent form (resorufin). Therefore, the fluorescence response of resorufin can be measured and directly related to cell metabolic activity. As cells proliferated and spheroids formed, fluorescence increased (days 1-3), then between days 3-5 well-formed and necrotic centred spheroids had a measured decrease in resorufin fluorescence reflecting either reduced metabolic activity in the core or reduced alamar blue penetration. Given that light microscopy did not show a reduction in spheroid sizes or death, the decrease in resorufin fluorescence was likely due to alamar blue failing to be uptaken in the spheroid core in 2 hours. This is documented within the literature which cites a 24-hour alamar blue incubation period rather than the conventional 2-4 hours for 2D cell cultures which have a higher degree of uptake due to media access (Eilenberger, Kratz et al., 2018). Therefore, drug penetration heterogeneity was evidenced in the spheroid models. Through the analysis of both spheroid growth and heterogeneity, an initial plating density of 9,000 cells was selected for PDT experiments with PS exposure between day 3 - 5. The following protocol was then developed for subsequent dark/light PDT toxicity assays in 3D spheroid models (Figure 3.21).

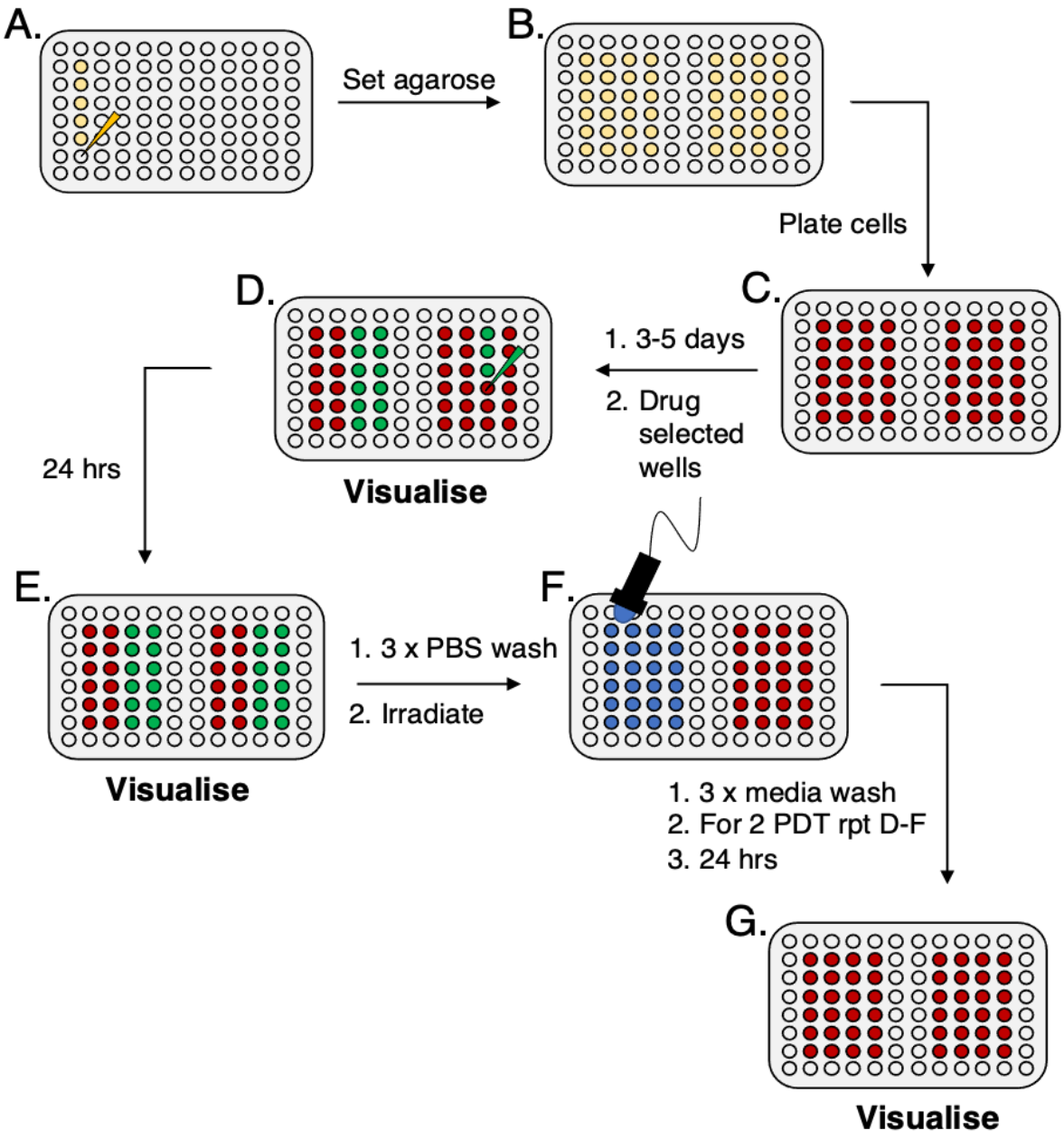

Figure 3.21 A schematic of the experiment used to investigate IrTHPyBenz PDT on 3D C8161 spheroid models cultured using the soft agar method. Irradiation conditions: 405 nm, 20 mW/cm^2, 3 mins or 455 nm, 30 mW/cm^2, 3 mins.

3.2.6 – 3D Spheroid Phototoxicity

C8161 spheroids were cultured in 96 well dishes coated with agarose which prevented adherence. Each condition (untreated, drugged, light and combination) was tested on a 2 x 6 spheroid sample size within each dish. To account for DMSO toxicity effects, spheroids were either drugged with IrTHPyBenz (10 μM, 24 hrs) or with the corresponding volume of DMSO. Irradiation was performed by sequentially holding a 405 nm or a 455 nm diode above 2 x 2 wells (3 mins) after the exchange of growth media with PBS. Initially, PDT effects were attempted after 2 hrs of drug incubation, a timepoint which produced strong phototoxicity in 2D cultures (data not shown), but no such lethality was observed. This was hypothesised as due to a reduction in drug penetration. Therefore, the incubation time was increased to 24 hours, which restored phototoxicity (Figure 3.22).

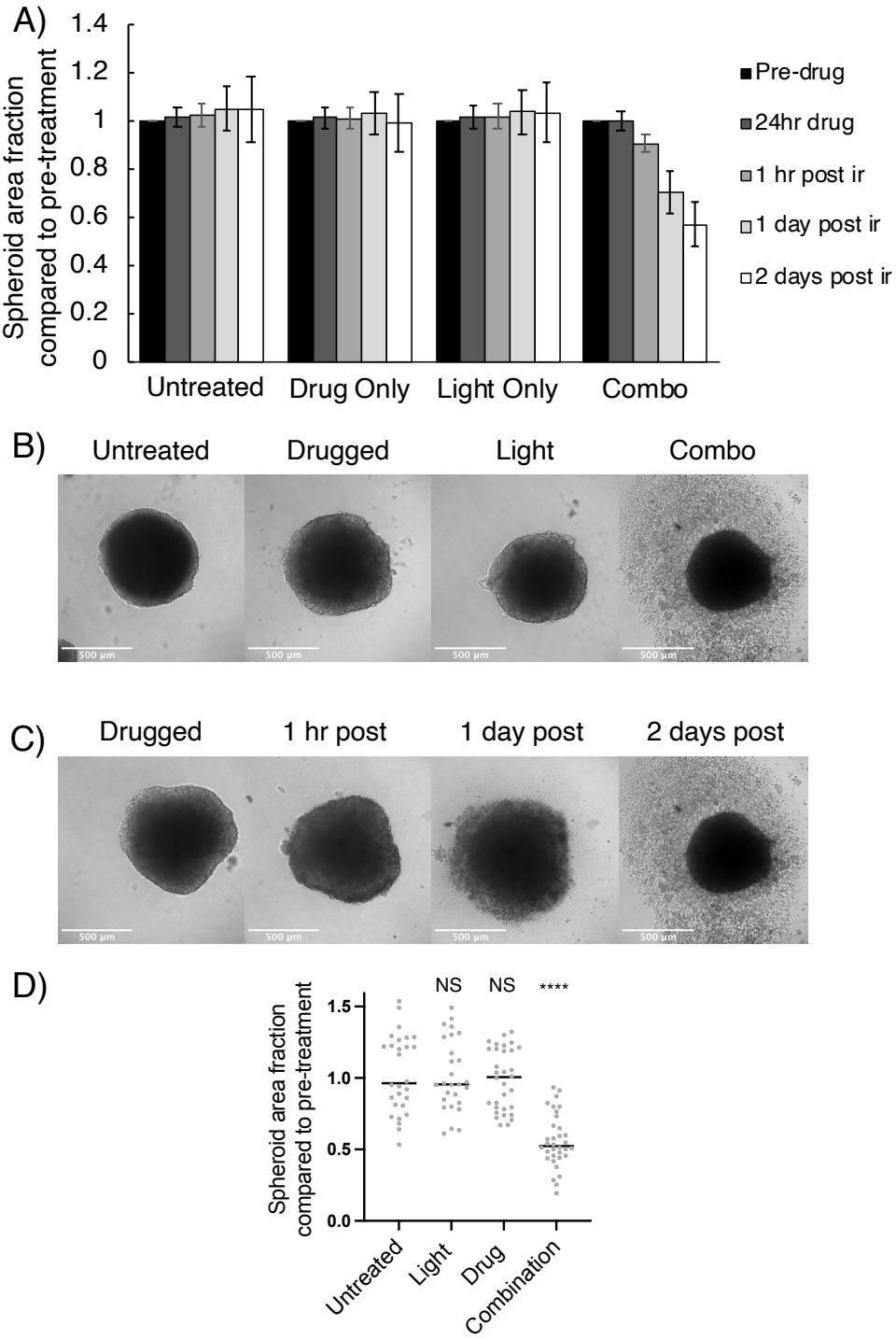

*Figure 3.22 C8161 spheroids were cultured to an appropriate size. As per Figure 3.21, spheroids were drugged with IrTHPyBenz (10 µM, 24 hrs) or vehicular control and then irradiated (405 nm, 20 mWcm^{-2}, 3 mins) or not. Spheroid areas were then quantified by microscopy at various timepoints. A) Spheroid areas represented by the mean and SDs (n = 3, N = 8 - 10) B) Representative images of spheroid size analysis at 2 days post treatment C) Spheroid shrinkage was observed in the combination treatment D) The quantification of each individual spheroid area at 2 days post irradiation (n = 3, N = 8 - 10). One way ANOVA **** $p < 0.0001$. Student T test (2 ways, paired vs. Untreated) $p = 1$ NS (Light), $p = 0.51$, NS (Drug), $p = 4.7 \times 10^{-11}$ **** (Combo).*

Spheroids which received a combination of light and drug underwent statistically significant cell death as measured by their area compared to spheroids which were singly treated or untreated. Spheroid morphological changes, and hence the onset of phototoxicity, could be observed at 1 hour post irradiation. The outer spheroid border became more ill-defined and lined with blebs due to dead and dying surface cells detaching from the spheroid bulk. To simultaneously investigate 2D vs 3D PDT responses, 2D cultured C8161 cells were subjected to 405 nm PDT and their metabolic activity assessed by alamar blue after one week of growth. Cell metabolic activity decreased by 98.4 % $\pm$ 0.7 (n = 2) compared to the untreated condition. This was substantially more than the average 3D spheroid shrinkage, measured at 46 % 24 hr post combination treatment. Substantial PDT responses were measured depending on the cell model type which directly observed how tumour heterogeneity negatively impacts PDT.

In an effort to enhance spheroid shrinkage i.e cell death, fractionated PDT was performed. This should be through the theoretical breaking apart and hence sequential increase in drug and light access to more deeper lying cells on a round-by-round basis. Additionally, given the measured red-shift in the absorption spectrum of IrTHPyBenz, 455 nm irradiation was employed to maximise spheroid light penetration due to the increase of blue light (455 nm) compared to near UV light (405 nm) (Figure 3.23).

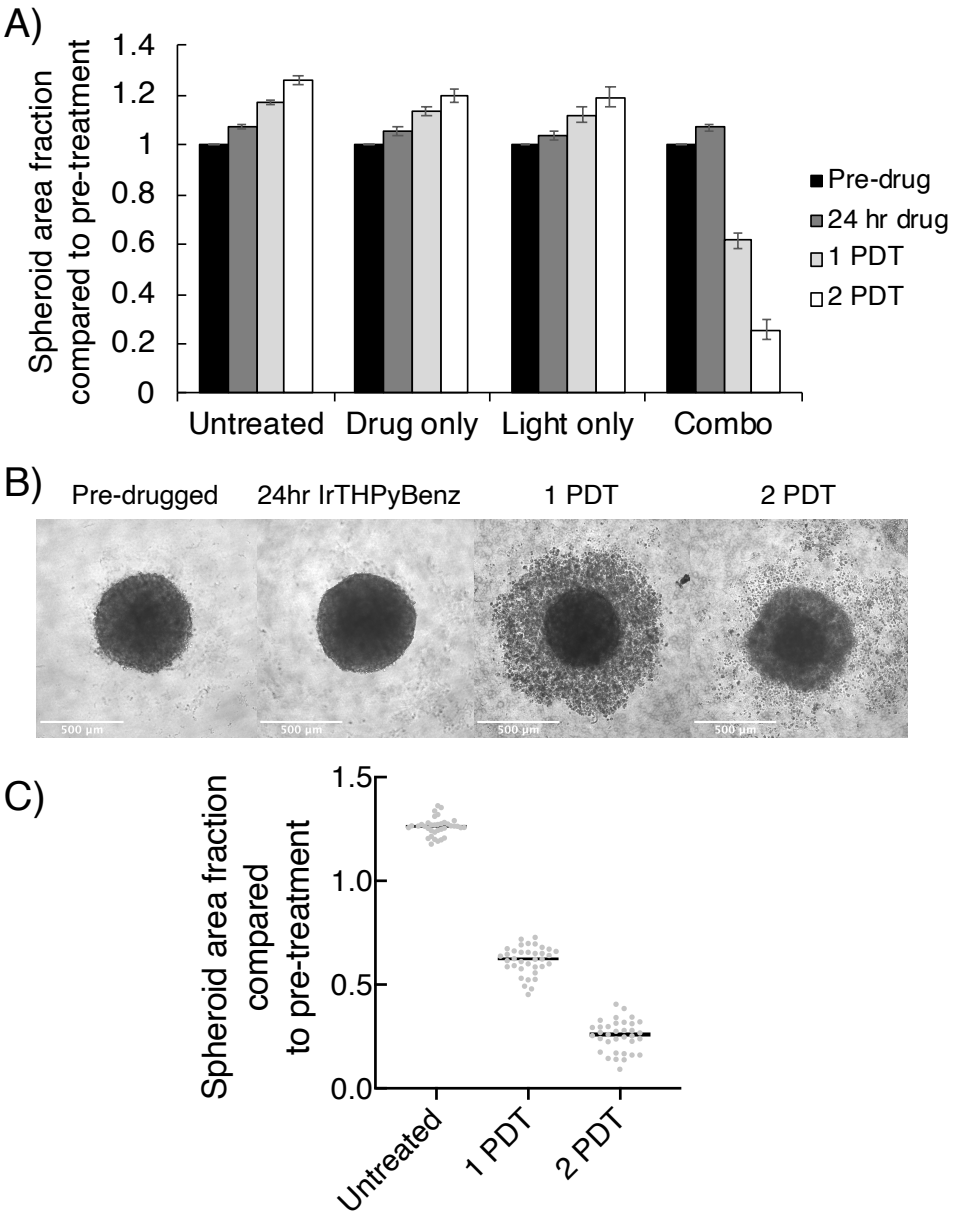

*Figure 3.23 C8161 spheroids were cultured to an appropriate size. As per Figure 3.21, drugging with IrTHPyBenz (10 µM, 24 hr) occurred followed by irradiation (455 nm, 30 mWcm^{-2}, 3 mins) and re-addition of drugged media (10 µM, 24 hr). The following day, spheroids areas were quantified by microscopy (1 PDT) before a second irradiation (455 nm, 30 mWcm^{-2}, 3 mins) and addition of media. After 24 hrs, spheroid areas were again quantified (2 PDT). A) Spheroid areas represented by the mean and SDs (n = 3, N = 12). B) Representative images of the spheroid shrinkage observed in the combination treatment upon 1 and 2 rounds of PDT. C) Individual spheroid areas of the combination treatment (n = 3, N = 12). One-way ANOVA p < 0.0001 ****. Student T Test (two ways, paired vs Untreated) p = 9.5 x 10^{-56} , **** (1 PDT), p = 6.0 x 10^{-66}, **** (2 PDT).*

Despite 455 nm being more penetrating to light, identical spheroid shrinkage effects to 405 nm irradiation were observed (46 % reduction in size 405 nm vs. 39 % reduction at 455 nm). However, by subsequently performing an additional PDT treatment, spheroid shrinkage can be increased from 39 % (1 PDT) to 75 % (2 PDT). This is roughly additive whereupon each PDT treatment reduced spheroid size by ~ 40 %. Spheroid models further mimic *in vivo* tumour samples and so the measurement of such PDT effects increased the feasibility for its translation to the clinic. Additionally, the issue of tumour heterogeneity can be alleviated through applying multiple rounds of PDT to consistently increase both drug and light penetration. However, essential inhibitory components to PDT in *in vivo* tumours are still absent which includes vasculature parameters and the lack of porphyrin containing tissue which absorbs purple – blue light and hence limits tissue penetration.

In order to quantify the cell death in PDT treated spheroids, an LDH release experiment was devised. Lactate dehydrogenase (LDH) is leaked into the growth media upon a cell death event which leads to loss of cell membrane integrity and cytosolic spillage. This enzyme produces NADH which cross reacts with an NADH sensitive probe which becomes reduced into a fluorescent formazan dye whose emission is detectable by a plate reader (Figure 3.24).

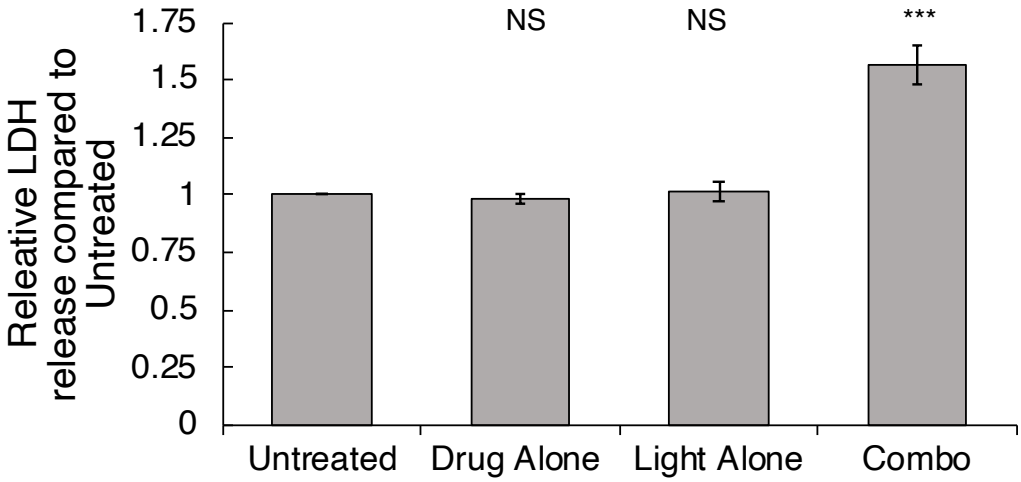

*Figure 3.24 C8161 spheroids were cultured to an appropriate size. As per Figure 3.21, spheroids were drugged with IrTHPyBenz (10 µM, 24 hr) or vehicular control and then irradiated (455 nm, 30 mWcm^{-2}, 3 mins) or not. The following day, a sample of media was removed and tested for the presence of LDH with a commercially available probe and quantified using a plate reader. The mean and SDs of the relative emission of the formazan dye compared to the untreated are shown in each condition (n = 3). Student T test (two-way, paired vs Untreated), p = 0.52 NS (Drug Alone), p = 0.67 NS (Light Alone), p = 0.003 *** (Combo).*

LDH activity was 1.5 fold greater in the combination treatment than untreated samples. This supports the cell death seen after 1 round of 455 nm PDT as measured by spheroid shrinkage. Furthermore, LDH levels were not statistically increased in the singly treated conditions compared to untreated control, suggesting low levels of off-target toxicity are likely.

3.2.7 – Further Spheroid Experiments

In order to validate drug uptake after 24 h, fluorescence microscopy was performed to measure uptaken IrTHPyBenz phosphorescence (Figure 3.25).

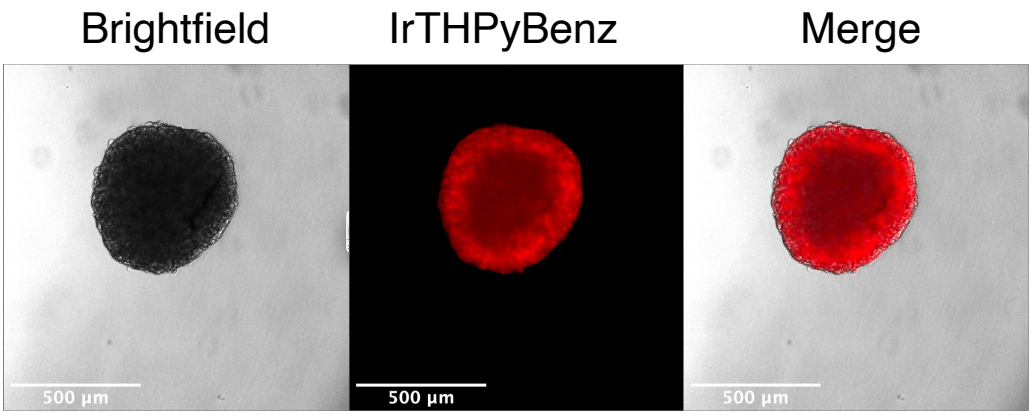

Figure 3.25 C8161 spheroids were cultured to an appropriate size and then drugged with IrTHPyBenz (10 µM, 24 hr) (λ_{exc} 350 – 400 nm, λ_{em} 570 nm). Spheroids were then fixed and observed by fluorescence microscopy to monitor IrTHPyBenz phosphorescence.

Spheroid uptake of IrTHPyBenz was confirmed after a 24-hour incubation period. Although IrTHPyBenz phosphorescence was imaged in spheroids, no additional information with regards to drug penetration depth could be measured without the use of more sophisticated microscopic techniques. Preliminary protocols were developed which further investigated drug penetration parameters in spheroids. This would be through the fixation of treated spheroids which could then be stained against cell markers. This was crudely attempted by creating a pellet of suspended and fixed spheroids in an agarose matrix which was then wax embedded in paraffin. Following this, a cryostat was used to carefully cut thin slices of the spheroids which were then stained with haematoxylin and mounted onto coverslips (data not shown). Theoretically the mounted spheroid slices can then be IHC stained and probed for markers throughout the entire heterogenous spheroid structure. Potential IHC targets include caspase 3/7 activation (as seen in 2D models) and/or HIF-1 (hypoxia) (Bressenot, Marchal et al., 2009, Raleigh, Miller et al., 1987). In addition, lightsheet microscopy can be employed to detect the drug phosphorescence depth and hence penetration effects. Again, an attempt was made at this which produced promising results, but the method was in need of further optimisation and improvement (data not shown). These two additional experiment plans were effectively stalled due to the loss of time owing to the ongoing COVID-19 pandemic. However, despite this,

successful PDT activity was translated to 3D spheroid models through several readjustments, which showed a high degree of promise and power in IrTHPyBenz as a successful PS.

3.3 – Discussion

3.3.1 – IrTHPyBenz as a PDT Agent

IrTHPyBenz was primarily investigated for any marked improvements on the PDT activity of IrNew through the substitution of PPy with THPy. In terms of photophysics, IrTHPyBenz absorbed visible light ranging from 400 – 475 nm which consequently produced a red-shift of ~ 20 nm compared to IrNew which theoretically could facilitate more tissue penetrating PDT. In addition, the emission of IrTHPyBenz was slightly more red-shifted, occurring from 550 nm – 700 nm due to a larger Stokes shift which validated that the modification of the complex structure could alter the excited state orbitals. In the absence of oxygen, non-radiative energy transfer with oxygen was removed, which henceforth increased both the excited state lifetime and the emission intensity by a factor of 3 evidencing that oxygen has a quenching effect on IrTHPyBenz's excited state. Upon irradiation at 355 nm, the phosphorescence of $^1O_2$ decay was detected which directly evidenced IrTHPyBenz's ability to generate the critically important lethal molecule for PDT with a relative yield of 43%. Furthermore, IrTHPyBenz induced large PDT effects at 405 nm with PI values ranging from > 378 – 100 in three PDT appropriate cell lines. These cancers (bladder, melanoma and head and neck) have all received coverage for their PDT applicability within the literature whereby diseased tissue is accessed by a laser coupled to catheters and fibre optics (Hopper, Niziol et al., 2004, NSEYO, DeHAVEN et al., 1998, Shi, Liu et al., 2019). These large PDT effects covered a large dose range, permitting specific treatment flexibility and optimisation as well as non-existent dark toxicity up to 200 μM, whereby the stock solvent is the limiting factor. In rationalising IrTHPyBenz's potent PDT activity, immunofluorescence assays determined that IrTHPyBenz localised to the mitochondria, ER and Golgi apparatus. Damage to these organelles is well documented to trigger regulated cell death and/or activate the immune system for efficient debris clearance (Buytaert,

Callewaert et al., 2006, Kessel and Luo, 1998, Sütterlin, Hsu et al., 2002). Cells which received a treatment of both IrTHPyBenz followed by irradiation underwent apoptosis which was detected through activated caspase 3/7 at 1 hr post irradiation. This is advantageous for PDT due to the rapid activation of a regulated cell death pathway which promotes immunoclearance alongside short treatment times. Simultaneously, Golgi associated photodamage was observed through its instantaneous fragmentation following irradiation, suggesting high levels of disruption to cell functioning which could lead to cell death (He, Liu et al., 2020). However, given that IrTHPyBenz also accumulated at the mitochondria, and the mitochondria's association with apoptosis induction, it could be theorised that photodamage at this locus could cause apoptotic cell death. Which damaged site is the predominate cause can be debated. The integrity of the mitochondrial membrane plays a paramount role in determining apoptosis initiation, whereby cytosolic cytochrome c oxidase leakage is upstream of caspase 9 (the initiator caspase) activation and is a rapid effect initiator of apoptosis. The executioner phase of apoptosis was detected through caspase 3/7 activation at 60 minutes post irradiation, consistent with mitochondria based photodamage. Conversely, Golgi and ER triggered apoptosis have additional upstream cellular responses which culminate in cytochrome c leakage such as caspase 2 (Golgi) and Ca^{2+} release (ER) (Buytaert, Callewaert et al., 2006, Hsieh, Wu et al., 2003). Therefore, despite the Golgi being severely fragmented this may not be as important in eliciting immediate PDT effects. In terms of PDT safety, IrTHPyBenz was rapidly eliminated with reduced phosphorescence detected between 24 - 48 hours of administration. Additionally, cells subjected to either irradiation or a drug incubation alone suffered no inhibition to cell growth and no onset of apoptosis thereby increasing the likelihood that IrTHPyBenz will have low levels of off-target effects. However, all of these discussed properties were measured in *in vitro* models and therefore require replication in appropriate *in vivo* models to ascertain more accurate and clinically relevant drug dynamics. In terms of other Ir(III) PS in the literature, IrTHPyBenz proves superior to the vast majority in terms of phototoxicity. For example, 10 out of 12 of the test compounds listed in Appendix 1, have measured PI values which are lower than IrTHPyBenz. This is largely due to two factors: namely large phototoxicity in IrTHPyBenz and negligible

dark toxicity up to 200 μM. Furthermore, the biological behaviour is explored in more depth that what is generally found within the literature which largely describe the light/dark toxicity behaviour. IrTHPyBenz also has a large and flexible dose-response window which permits dose optimisation to combat clinically limiting factors such as poor tissue penetration, hypoxia and tumour heterogeneity.

3.3.2 – IrTHPyBenz as a Mechanistic Comparison to IrNew

IrTHPyBenz was originally synthesised under the hypothesis of further probing the structural components of IrNew to try and improve its PDT ability (McKenzie, Sazanovich et al., 2017)(Appendix 5). This was firstly attempted through the measurement of any direct PDT increases, such as an increase in $^1O_2$, higher phototoxicity or increases in apoptosis etc followed by any improvements to clinically beneficial effects (e.g. red-shifted irradiation, water solubility). A small red-shift in the UV/Vis spectra was measured at 20 nm when compared to IrNew, which effectively permitted blue light PDT. Upon the detection of $^1O_2$, the quantum yields generated were similar with 43 % IrTHPyBenz vs 42 % IrNew which suggested no overt differences. Therefore, the ancillary ligands were unlikely to affect the complex's $^1O_2$ generating ability which therefore rationalised the role of Benz. THPy and PPy ligands both contain negative charges which likely increase the orbital energy of their associated LUMOs compared with the neutral ligand Benz. Therefore, the LUMO of Benz is likely to be directly involved in MLCT excitation, which then generates $^1O_2$ via energy transfer. The reason as to why THPy ligand caused a slight red-shift in absorption could be ascribed to a change in the metal-based d-orbitals energy caused by changes to the crystal field splitting energy which ultimately shifts the energy of the HOMO. In terms of their biological properties, IrNew and IrTHPyBenz co-localised differently to the cellular environment. IrNew has a time-dependent localisation with the mitochondria (4 hrs) and lysosomes (24 hrs) with the latter possibly being due to an elimination pathway. IrTHPyBenz similarly co-localised to the mitochondria with a PCC of 0.71 (IrNew 0.547) alongside its simultaneous localisation to the Golgi (0.85) and ER (0.61). In terms of solubility, IrTHPyBenz retained water insolubility which can be disadvantageous to drug administration. Similarly, both compounds were strongly phototoxic under 405 nm irradiation with PI

values of IrTHPyBenz > 100 – 378, IrNew 238 > 555. Owing to a lack of dark toxicity in the entire dose range tested, both compounds have a big therapeutic window with high dosage flexibility. Subsequently, owing to a small red-shift, IrTHPyBenz could elicit 455 nm PDT effects under a 2 hr incubation with a measured PI of > 132 in EJ cells (30 $mWcm^{-2}$, 3 mins, n = 3)(data not shown). In contrast, IrNew PDT was attempted under the same irradiation conditions but produced no phototoxicity which is likely due to low complex absorption at 455 nm absorption (being reduced by ~ 3 compared to IrTHPyBenz). Therefore, upon the exchange of PPy with THPy, blue-light PDT became possible which improved the tissue penetration for subsequent PDT treatment compared to IrNew. Furthermore, activity at 405 nm was not substantially altered which showed that the addition of blue light PDT did not sacrifice previous measured PDT activity. Therefore, compound ancillary ligands are important and effective targets for further red-shifting absorption and hence improving the PDT activity through the consolidation of the HOMO-LUMO energy gap.

3.3.3 – PDT in *in vitro* 3D Spheroid Models

After favourable PDT activity in 2D cell models, 3D models were used in order to test additional parameters which plague PDT development. C8161 melanoma cell spheroids, a PDT applicable cell line, were successfully cultured and formed. Additionally, a reduction in drug penetration was observed alongside the visualisation of a densely packed necrotic core thereby establishing structural heterogeneity, in a first step towards actual tumours. Subsequently, favourable PDT effects were measured as seen through spheroid shrinkage and increased LDH release in conditions which received a combination of IrTHPyBenz and light treatments. PDT effects did not substantially increase after 455 nm light compared to 405 nm light with an average measured spheroid shrinkage at 46 ± 1.1 % (405 nm, n = 3, N = 12) vs. 39 ± 3.2 % (455 nm, n = 3, N = 8 – 10)(Student T Test, two-ways, paired, p = 0.093, NS). Despite the increase in tissue penetration, the equation of the shrinkage under both wavelengths was likely due to differences in IrTHPyBenz photon absorption whereby 455 nm photons are absorbed at ~ ½ the absorption at

405 nm. However, fractionated PDT resulted in further spheroid shrinkage, suggesting the limits of light and possibly drug penetration at low wavelengths could be overcome by repeated treatment. Therefore, PDT using IrTHPyBenz was successful when translated to more clinically relevant 3D spheroid models, paving the way for further clinical trialling. IrTHPyBenz's PDT ability could consequently be attempted in *in vivo* models which possess additional parameters such as ECM, tissue and vasculature, all of which can further hinder PDT. Additionally, further experiments in 3D spheroid models could be employed to scrutinise other important parameters, such as the quantification of drug penetration, cell death mechanisms and hypoxia.

3.3.4 – IrTHPyBenz as a Candidate for UCNP Mediated NIR PDT

Despite favourable PDT activity, one major disadvantage for IrTHPyBenz is its photoactivation in the 400 – 475 nm region which is poorly tissue penetrating. This hinders clinic translation by creating difficulties in treating tumours at depths ≤ 3 mm (Li, Chen et al., 2020). This weakening of incidence light in the region of 400 – 475 nm arises due to absorption by the Soret bands of naturally occurring porphyrins and/or porphyrin-related components which are present in tissue and ECM (Gold and Goldman, 2004). A second disadvantage was compound hydrophobicity which resulted in poor water solubility, leading to potential PS administration difficulties. Upconverting lanthanide nanoparticles (UCNPs) have the ability to overcome both these problems. UCNPs absorb NIR I light and subsequently emit higher energy visible light through photon upconversion. The specific upconverted and emitted wavelengths can be tailored through the consolidation of the UCNP ionic/dopant compositions to majorly coincide within the photoactivation range of IrTHPyBenz. Suitably, $NaYF_4$; Yb^{3+}, Tm^{3+} UCNPs emit at the blue end of the visible spectrum and hence favour blue light activated PS, such as IrTHPyBenz. Secondly, the hydrophobicity of IrTHPyBenz could specifically aid UCNP binding and its retention by eliciting the hydrophobic effect when translated to an aqueous environment. UCNPs with an additional surface coating of mesoporous silica contain a sufficiently hydrophobic porous network which can be solvent accessed and favourable for

hydrophobic drug binding. Therefore, IrTHPyBenz could potentially display a high binding affinity and retention with hydrophobic silica pores when mixed with sufficiently coated UCNPs in an aqueous environment. IrTHPyBenz could then produce $^1O_2$ by excited-state interaction with molecular oxygen, which has been validated as possible and capable of invoking lethality upon photoexcitation. This will be discussed in Chapter 4.

3.4 – Conclusion

IrTHPyBenz was designed, synthesised and scrutinised for any marked improvements to the PDT activity of IrNew through an exchange of ancillary ligands (PPy with THPy). A 20 nm red-shift in absorption was achieved, ascribed to the introduction of S atoms over C atoms which in turn affect crystal field splitting, and increases the energy of the Ir-based HOMO. In addition to this, the exchange retained IrNew's favourable PDT effects at 405 nm whilst also facilitating potentially more tissue penetrating 455 nm PDT. Additionally, cellular localisation differences existed, whereby IrNew had a time-dependent mitochondria-lysosomal localisation whilst IrTHPyBenz had measurable affinity for the mitochondria, ER and Golgi. Due to this, IrTHPyBenz elicited strong apoptotic cell death after a short time post irradiation, likely due to specific photodamage at these organelle sites. Furthermore, these effects were translated to 3D spheroid models whereby successful protocol consolidation produced spheroid shrinkage whilst circumventing heterogeneity, a property which inhibits PDT of clinical tumours. In conclusion, the exchange of THPy with PPy had a positive effect in terms of IrNew's PDT activity. This was rationalised due to a red-shift in absorption with a simultaneous retention of phototoxicity. In terms of further development, modifications to the ancillary ligands can be performed to increase tissue penetration. Therefore, further designs could be made in extending this effect towards a more clinically accessible region of light by the further introduction appropriate moieties.

4. Upconverting Lanthanide Nanoparticles

4.1 – Synthesis

IrTHPyBenz was measured to have impressive PDT activity in a range of epithelial cancer cell lines (Chapter 3). This was accompanied by a 20 nm red-shift in the complex's absorption spectra compared to IrNew which in turn facilitated 455 nm PDT. Despite this, blue light PDT still hinders IrTHPyBenz's clinical application due to limited tissue penetration within this region of visible light. One way to circumvent this issue is by using upconverting lanthanide nanoparticles, UCNPs, which are composed of a $NaYF_4$ crystal doped with Yb^{3+} and Tm^{3+}. Consequently, IrTHPyBenz can be bound to the layered UCNP vessel to potentially aid in both drug delivery and NIR photoactivation (Figure 4.1).

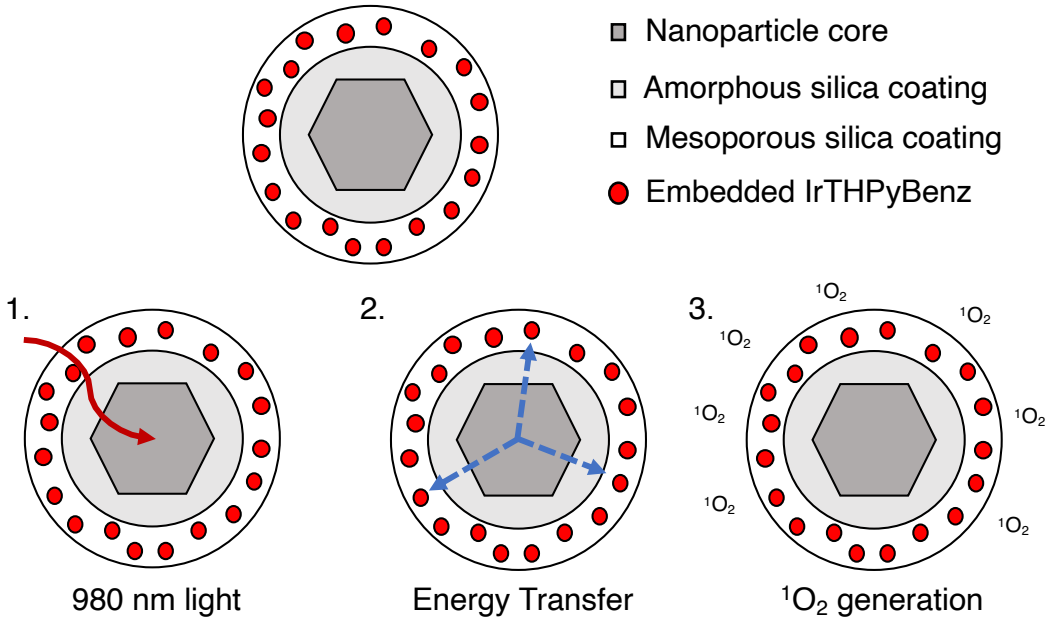

Figure 4.1 The schematic of silica coated UCNPs in order to facilitate NIR photoactivation of embedded IrTHPyBenz. 980 nm irradiation is followed by energy transfer from the excited UCNP cores onto IrTHPyBenz. A second excited state energy transfer from IrTHPyBenz onto $^3O_2$ generates $^1O_2$ leading to cell death.

Here the hypothesis that successful NIR photoactivation can be achieved through the synthesis and coupling of NIR absorbing UCNPs to IrTHPyBenz was tested. This was to complement the long-term aim to improve the depth at which IrTHPyBenz-

mediated PDT can be achieved. UCNP cores were firstly formed before subsequent silica coatings were added to impart water solubility, stability, and reduced toxicity. Following this, mesoporous silica was layered onto the surface to trap and hold solubilised IrTHPyBenz in a hydrophobic porous network. The UCNP-IrTHPyBenz complex was then exposed to cells before NIR irradiation. The UCNPs should permit energy transfer, hence PS activation and finally $^1O_2$ generation to allow NIR PDT.

4.1.1 – UCNP Synthesis

UCNP cores, $NaYF_4$, were synthesised using a thermal decomposition method to produce a composition of 74.7 % Y^{3+} with dopant concentrations of 25 % Yb^{3+} and 0.3 % Tm^{3+} which were taken from the literature (Gnanasammandhan, Idris et al., 2016). The thermal decomposition pathway was selected to favour phase-pure hexagonal UCNPs due to their optimal upconverting ability (Chen, Fu et al., 2021). UCNPs were successfully synthesised and imaged using transmission electron microscopy (Figure 4.2).

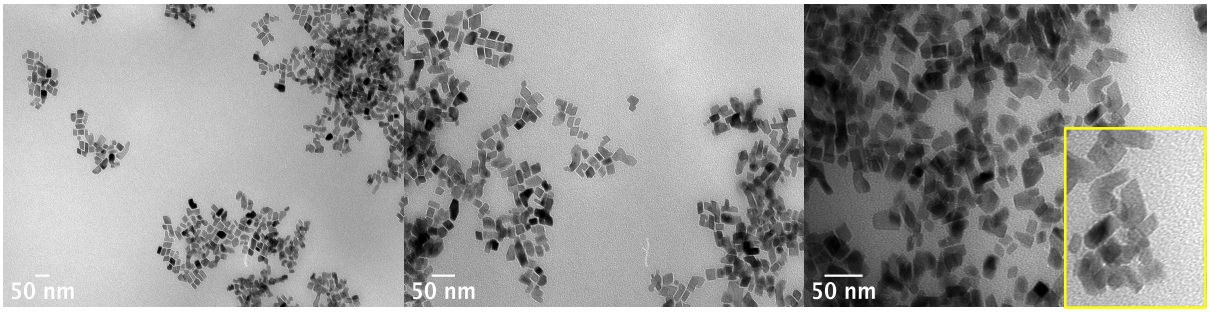

Figure 4.2 TEM imaging of UCNP cores on different magnifications.

All batches of UCNP cores, suspended in cyclohexane, were subjected to 980 nm diode irradiation to observe upconversion by eye, with suitable batches being carried forwards for subsequent coatings and coupling (Figure 4.6C). A micellar solvent system of oleic acid and 1-octadecene was employed to control and limit the size distribution of resulting particles and hence create dimensions within a size range suitable for cellular uptake. This is facilitated through the formation of ion-oleate complexes before the addition of NH_4F to initiate UCNP nucleation with the oleate

groups forming capped nucleation vesicles. Subsequent heating to 300 °C under an inert atmosphere led to UCNP breakdown and reformation.

Upon UCNP core formation, the micellar system leaves behind a surface cap of long-tailed hydrophobic oleate groups which prevents water solubilisation. To reverse this, an amorphous silica layer was coated onto the surface of the cores over a period of 2 days. In addition to water solubilisation, an inert shell also prevents ion leakage and reduces surface quenching effects through blocking non-radiative excited state decay with water molecules (Würth, Fischer et al., 2018). After two days, centrifugation in a gradually increasing aqueous environment (acetone – water) led to the isolation of suitably coated and water soluble UCNP cores (Figure 4.3).

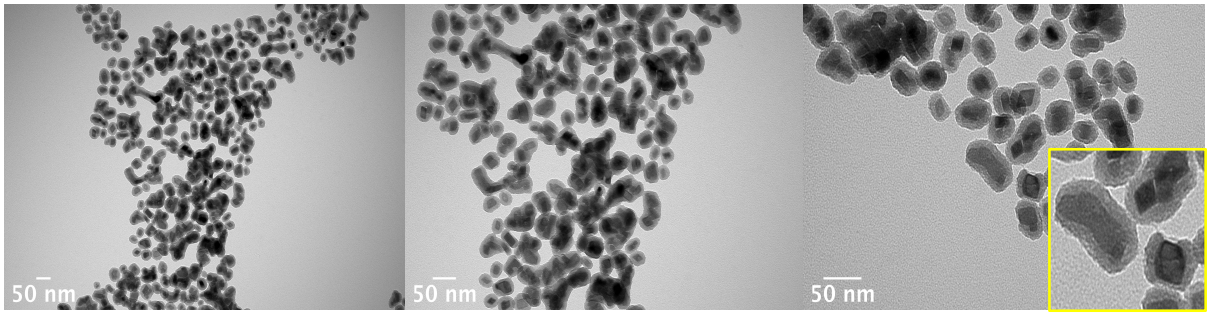

Figure 4.3 TEM imaging of UCNP cores coated with amorphous silica on different magnifications.

Although water solubilisation was improved, an amorphous silica coating is inadequate to bind and hold IrTHPyBenz and therefore a second silica layer is required. Mesoporous silica is suitable for this and was deposited through addition of NH_4OH and TEOS alongside a porogen, C18TMS. After stirring at RT for 6 hrs, the resulting UCNPs were isolated by centrifugation. This afforded a wet white powder which was then air dried. At this point, the porous network was occupied by C18TMS and thus required heating to 500 °C in a calcined furnace to evaporate the porogen. Resulting UCNPs were imaged via TEM and their appearance visually scrutinised for porosity (Figure 4.4).

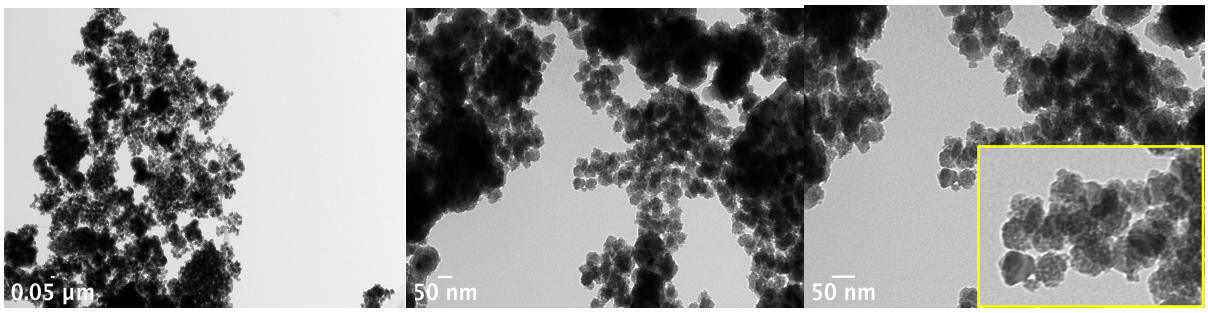

Figure 4.4 TEM imaging of amorphous silica coated UCNP cores further coated with mesoporous silica on different magnifications

Upon the coating of a mesoporous silica layer, the outer area of the UCNPs obtained a grainy feature typical of a porous network which should then facilitate IrTHPyBenz binding. Due to mesoporous silica being hydrophobic, an ideal characteristic to encourage IrTHPyBenz adherence, water solubility was reduced compared to amorphous silica. Therefore, before any subsequent experiments, silica coated UCNP suspensions were sonicated to break apart sticky aggregates. Under the assumption that the solvent can freely flow in and out of the porous network, IrTHPyBenz should be attracted to and retained by these hydrophobic pores through the hydrophobic effect. Therefore, suitably porous UCNP batches were selected and carried forward for IrTHPyBenz binding.

4.1.2 – Size Analysis

DLS size analysis was carried out after each sequential layering to quickly and easily validate whether the coatings were successful. Incidence light was shone into the colloidal solution before the angle of the scattered light was recorded to subsequently calculate particle size. Following this, TEM was used to visualise the UCNPs and measure particle dimensions which were manually measured in ImageJ (Figure 4.5).

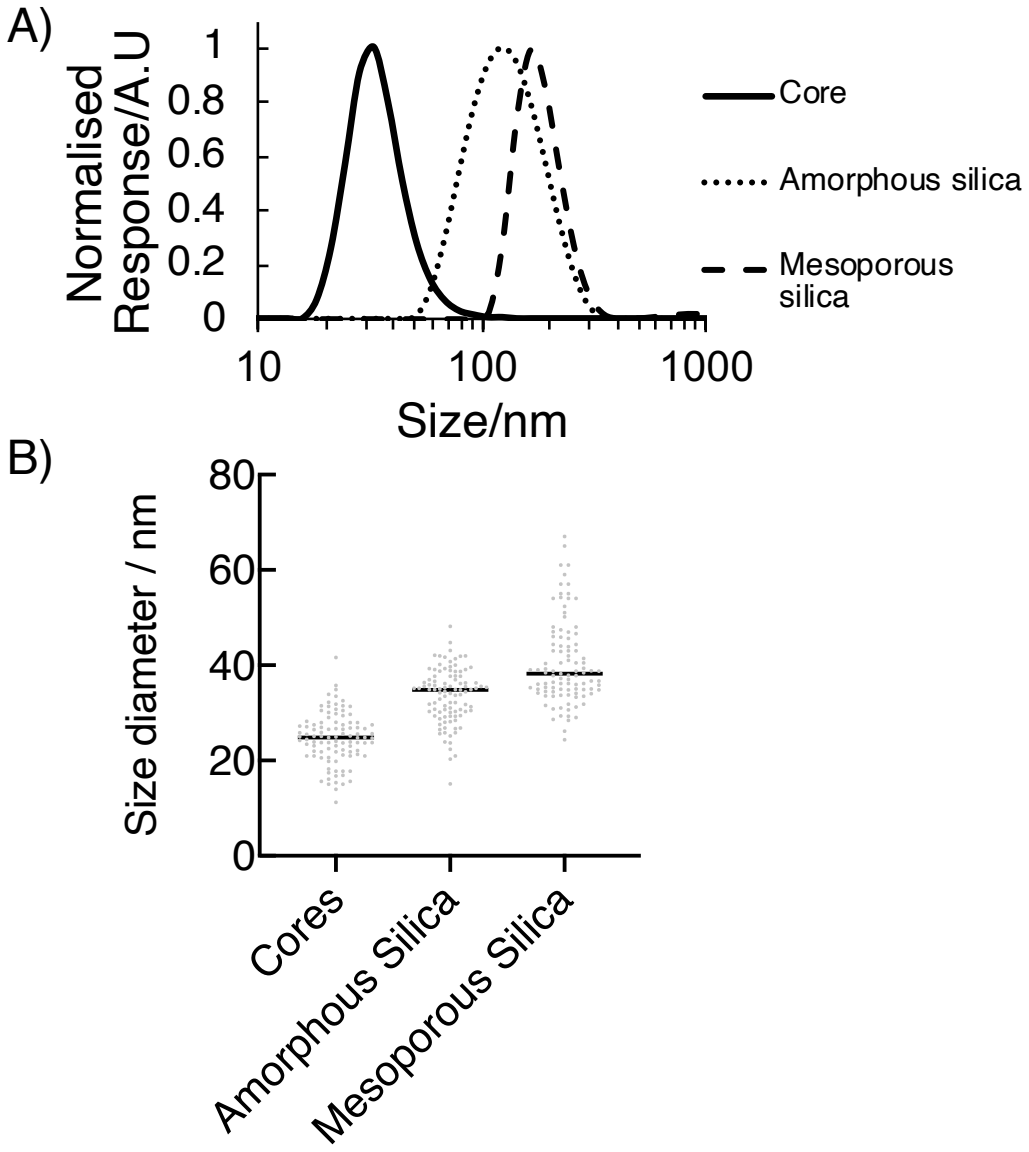

Figure 4.5 A) The DLS size distribution of solutions of UCNP cores (cyclohexane), amorphous silica coated UCNPs (water) and mesoporous silica coated UCNPs (water) B) The same size distribution as measured by TEM analysis n = 1, sample size 100 particles per condition.

DLS size analysis measured successive UCNP enlargement upon the addition of silica layers with maxima size responses at 33 nm (core), 122 nm (amorphous silica) and 164 nm (mesoporous silica). When compared to TEM imaging, the mean particle size (n = 100) had slight discrepancies with the measured values of 27 nm (cores), 35 nm (amorphous silica) and 38 nm (mesoporous silica). These instrument size differences are larger for silica coated UCNPs in an aqueous environment

compared against UCNP cores which evidences a hydrodynamic sphere. Solvent water molecules orient themselves around the surface of silica coated UCNPs to form a molecular organised sphere. These water molecules diffuse at the same speed as the coated UCNPs and additionally scatter incidence light allowing for their size to be measured by DLS (Tomaszewska, Soliwoda et al., 2013). Conversely, TEM images UCNPs as dried powders on copper coated carbon grids and as such are absent of a hydrodynamic sphere. This allowed for the size calculation of the hydrodynamic sphere at 87 nm (amorphous silica coated) and 126 nm (mesoporous silica coated) which were relatively larger than the actual UCNP dimensions. Furthermore, TEM measured only a narrow layer of surface deposited silica after each consecutive layer with 8 nm (amorphous silica) followed by an additional 3 nm (mesoporous silica). Due to the oleic acid/1-octadecene micellar solution, all suspensions were measured to be monodisperse with size dimensions compatible with cellular uptake, which are measured to be optimum at ~ 50 nm for mesoporous silica nanoparticles (Lu, Wu et al., 2009). In terms of water stability, DLS found that a small percentage of mesoporous coated UCNPs (~ 1.1 %, 1 – 4 μm) formed microaggregates in solution which could be minimised by sonication.

4.1.3 – Upconversion

The ability for UCNPs to perform photon upconversion from the NIR I range into higher energy visible light was confirmed by eye upon the isolation of UCNP cores. This was performed by shining a 980 nm laser into a sonicated and dilute suspension of UCNPs cores in cyclohexane which were visually blue and became more intense at higher powers (Figure 4.6C). To quantify which excited states were being occupied and hence emissive, an emission spectrum was recorded by coupling a 980 nm laser to a fluorimeter (Figure 4.6A). The emission was most intense at 347 nm and 362 nm, which corresponds to decay from the higher energy Tm^{3+} excited states ($^1D_2 \rightarrow {}^3H_6$) as tailored by the selected UCNP ion ratio (Figure 4.6B)(Li, Liu et al., 2016). Furthermore, the UCNP emission spectra produced good overlap with the absorption of IrTHPyBenz particularly at 347/362 nm and to a lesser degree at 453 nm paving the way for energy transfer and NIR PDT (Figure 4.6A).

A)

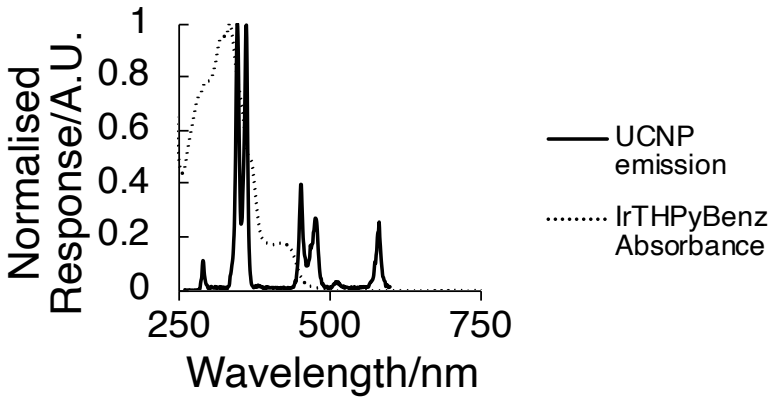

B)

Wavelength/nm	Relative Intensity	Colour
291	0.104	UV
347	1	UV
362	0.973	UV
453	0.396	Blue
478	0.241	Blue
581	0.256	Yellow

C)

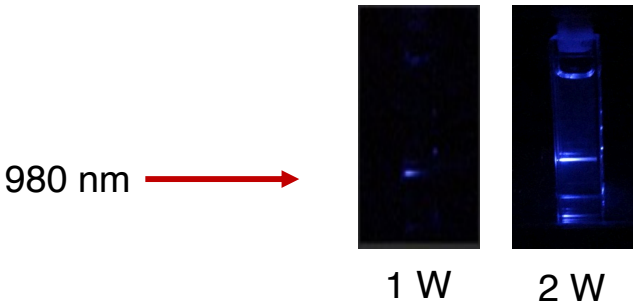

Figure 4.6 A) The emission spectrum of a solution of UCNP cores in cyclohexane overlapped onto the absorption spectrum of IrTHPyBenz B) A table of the emission peaks observed in the upconversion spectra C) Observed upconversion following 980 nm irradiation of UCNP cores suspended in cyclohexane.

4.1.4 – IrTHPyBenz Binding

As described above, UCNPs were created which could perform photon upconversion, were suitably water soluble, had ideal particle sizes and were sufficiently porous to allow for IrTHPyBenz coupling. Next, to promote hydrophobic binding with the vacated mesoporous silica layer, a solvent system which would suitably solubilise IrTHPyBenz but would also relinquish it to the pores was desired.

A trial of various solvent systems concluded that ethanol could fit this criterion, with a calculated solubility of 5.9 mg/mL. To promote IrTHPyBenz deposition, a volume of ethanol was added to a weighed mass of IrTHPyBenz to form a solution at the solubility limit. To quantify the mass of bound IrTHPyBenz per mass of UCNP powder, UV/vis spectroscopy was used to assess IrTHPyBenz supernatant contents both pre and post UCNP introduction (Figure 4.7B). UV/vis spectroscopy was used given its highly sensitive and accurate probing ability under the presumption that micro masses of IrTHPyBenz will be removed from solution upon UCNP addition. To do this, a small volume of ethanol solution was removed, and air dried to form a powder of IrTHPyBenz from the supernatant both prior to and after UCNP addition. To encourage the solvent to flow into and out of the porous outer layer, along with displacing any trapped air, multiple rounds of sonication and vortexing were performed. The UCNP solution was left overnight under the assumption that binding was maximised, rationalised by the colour change of the UCNP powder (white to orange) and a further constant supernatant volume was removed from the bulk and air dried. The coloured powder was then washed in water and vortexed to remove any precipitate of IrTHPyBenz and to strengthen hydrophobic binding through the hydrophobic effect. The resulting solid was isolated by centrifugation and dried to a powder which, after quantification, was applied to cells (Figure 4.7A).

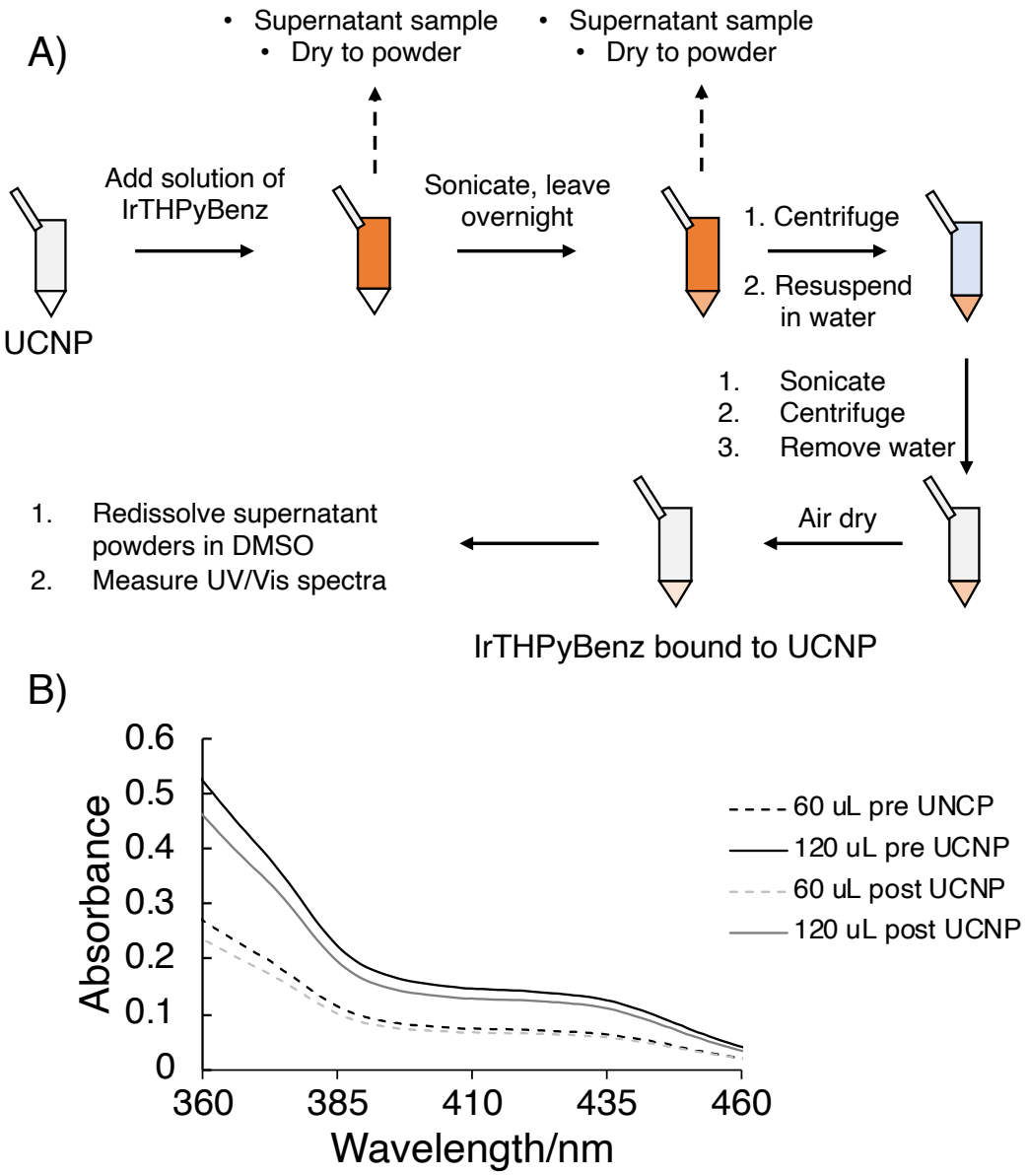

Figure 4.7 A) A schematic for binding IrTHPyBenz to a mass of UCNPs B) The UV/Vis absorption spectra of a sample of IrTHPyBenz dissolved in ethanol both pre and post UCNP addition. The sample was air-dried to a powder overnight and re-dissolved in DMSO.

UV/vis analysis of dissolved IrTHPyBenz supernatant samples detected a mass change of 79 μg upon the addition of 1.3 mg of UCNPs to give a calculated binding concentration of 61 μg/mg (mass of IrTHPyBenz/mg of UCNP). This process was repeated before the use of every specific batch of UCNP-IrTHPyBenz to ascertain the exact dosage. Furthermore, a pre-calculated mass of UCNP-IrTHPyBenz was weighed to give a 10 μM dose of IrTHPyBenz (7.82 μg in 1 mL). These masses were

then re-suspended in media and UV sterilised before cellular exposure.

4.2 – Cellular Behaviour

4.2.1 – Cellular Uptake

Firstly, the uptake of IrTHPyBenz was scrutinised upon exposure to cells using equimolar doses with and without UCNP coupling (Figure 4.8).

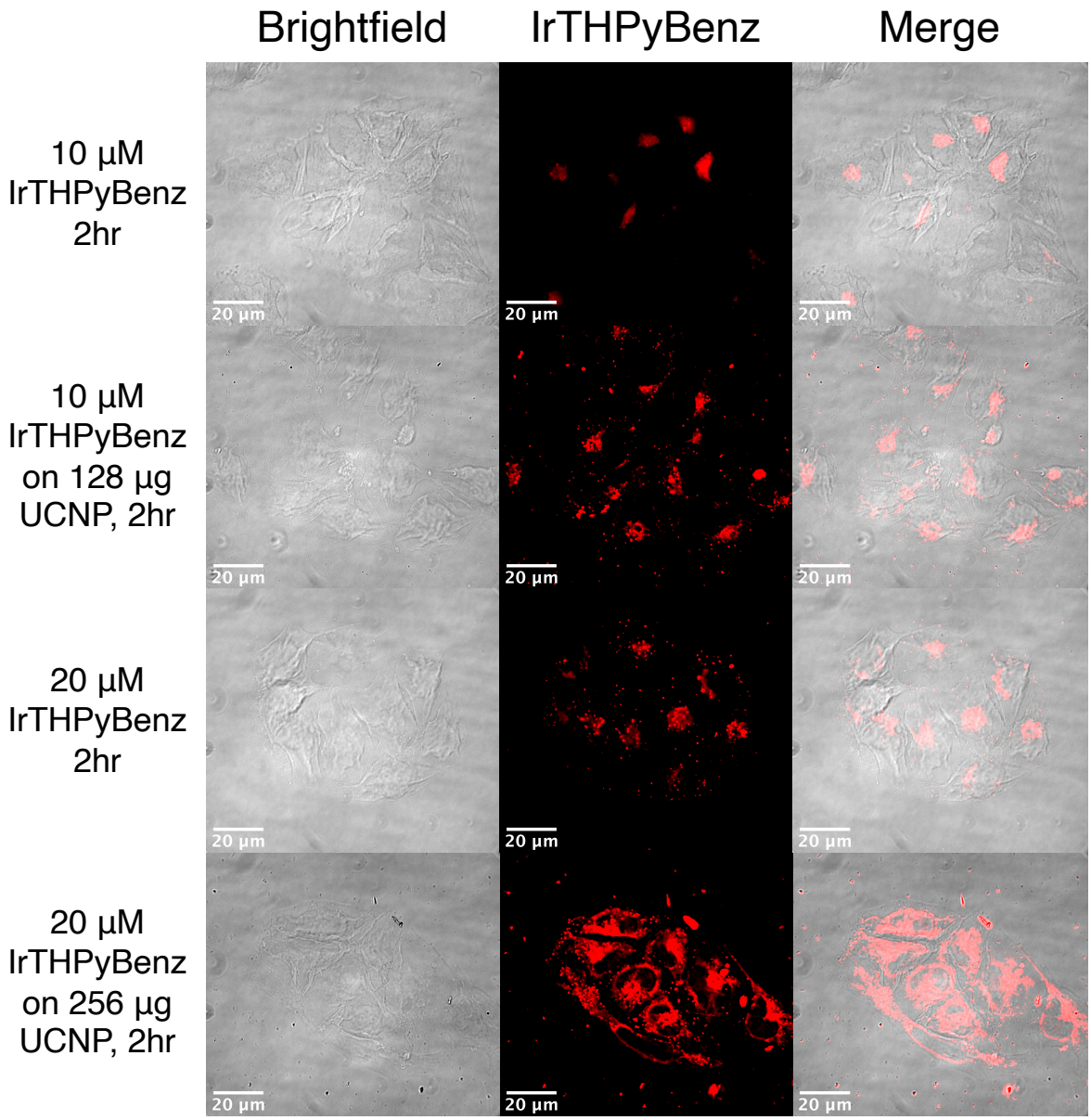

Figure 4.8 EJ cells were exposed to 10 µM and 20 µM IrTHPyBenz (λ_{exc} 350 – 400 nm, λ_{em} 570 nm) either alone or as bound to a corresponding mass of UCNP (128 µg and 256 µg) and incubated at 37 °C for 2 hours.

Upon cellular exposure of IrTHPyBenz-UCNPs, the presence of precipitate and insoluble debris was noticeable. This was proportional to the mass of UCNPs used. This was likely microaggregates of IrTHPyBenz-UCNPs, evidenced by the luminescence signal overlapping with the microaggregates imaged in the brightfield channel. This is somewhat unsurprising given the measurement of a small proportion of microaggregates in the UCNP DLS analysis which found that the intensity increased with time and conversely decreased upon sonication. Upon the binding of IrTHPyBenz to UCNPs, water solubilisation of IrTHPyBenz was achieved which was otherwise not possible. This increased the clinical applicability of IrTHPyBenz through potentially facilitating administration as an aqueous suspension rather than as a solution in organic solvents e.g. DMSO which can incur toxicity effects. Additionally, IrTHPyBenz dose increases to test dark toxicity were limited due to off target DMSO toxicity which would otherwise be removed upon aqueous solubilisation. Superficially, the intensity of IrTHPyBenz luminescence was observed to be more intense upon UCNP binding which is especially noticeable at 20 μM. This was suggestive of IrTHPyBenz-UCNPs being uptaken by cells through a different pathway than IrTHPyBez alone and is hence subjected to different rate limiting effects at higher and lower dosages. In terms of cellular localisation, an agreement of cytoplasmic accumulation in bound vs unbound IrTHPyBenz was measured which was found to collect around the cell nucleus (Chapter 3). However, upon UCNP binding, a small increase in cell membrane bound UCNP-IrTHPyBenz was observed which is likely due to UCNP precipitates. This increased at higher UCNP-IrTHPyBenz doses and was therefore likely to be UCNP microaggregates, which are too large to be cellularly uptaken. Most importantly, the cellular uptake of IrTHPyBenz was not inhibited upon UCNP binding.

To test the dose/time uptake response of IrTHPyBenz-UCNPs, suspensions of such in media were exposed to EJ cells at different times and IrTHPyBenz doses to ascertain the parameters for subsequent NIR PDT testing (Figure 4.9).

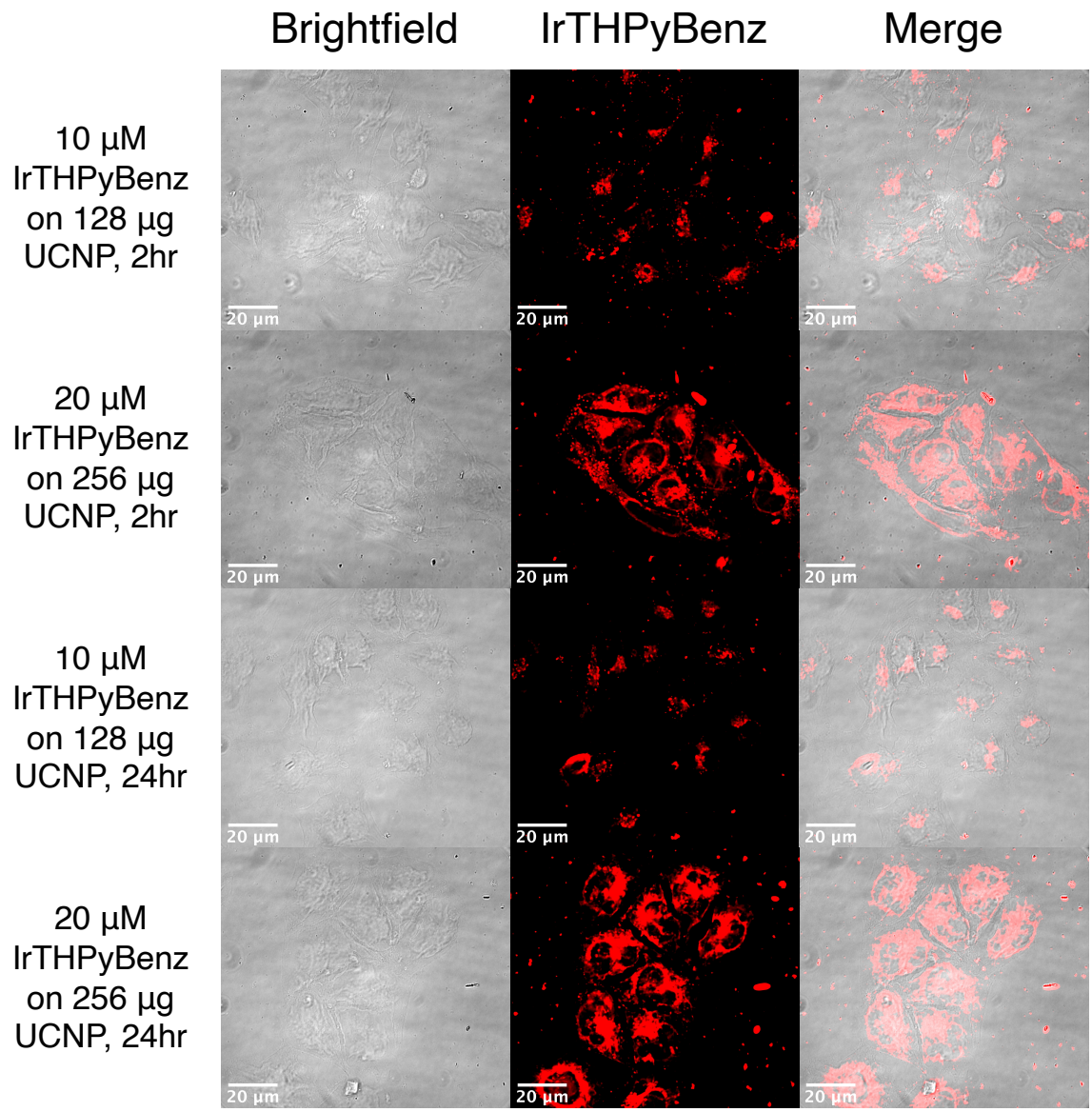

Figure 4.9 EJ cells were exposed to 10 µM and 20 µM IrTHPyBenz (λ_{exc} 350 – 400 nm, λ_{em} 570 nm) bound to a corresponding mass of UCNP (128 µg and 256 µg) and incubated at 37 °C for 2 hours and 24 hours.

After two hours, the luminescence of IrTHPyBenz was detected in the intracellular region of EJ cells and hence uptaken at the incubation time used for IrTHPyBenz alone PDT. Upon a crude visual inspection, the luminescence intensity did not appear to increase upon a further incubation to 24 hours (at an equidose) which suggested rapid and consistent uptake. Therefore, a 2 hr exposure of 10 µM of IrTHPyBenz on UCNPs was to be trialled for any NIR PDT effects.

4.2.2 – Cell Toxicity

Having demonstrated cellular uptake, cell survival assays were conducted to determine whether UCNPs (both alone and with loaded IrTHPyBenz) were inherently cytotoxic (Figure 4.10).

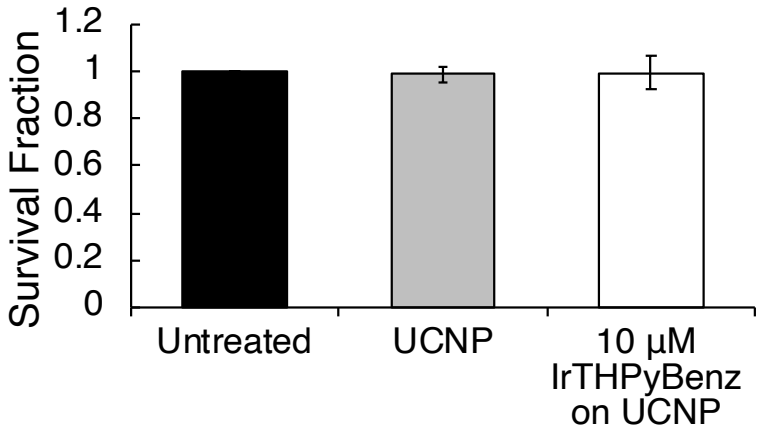

Figure 4.10 EJ cells were exposed to a mass of UCNPs alone or with the same mass of UCNPs coupled to a 10 µM dose of IrTHPyBenz for 2 hours. The media was then removed and each well washed with PBS. The survival was then assessed through colony formation over 7-10 days. The means and SEM are shown over three repeats.

UCNPs exposed to EJ cells were not cytotoxic in themselves and with conjugated IrTHPyBenz after 2 hours. Given that 405 nm PDT of IrTHPyBenz alone at this timepoint was effective, replication of these parameters was selected for subsequent UCNP NIR PDT testing. Cellular uptake of IrTHPyBenz conjugated to UCNPs was confirmed as sufficient through fluorescence microscopy as shown in Figure 4.9 and therefore any potential phototoxic effects would likely damage the intracellular environment.

Given the lack of UCNP/UCNP-IrTHPyBenz dark toxicity, the translation to measure any phototoxic effects would be performed after parametrising the limit of 980 nm irradiation power. The documented threshold for 808 – 980 nm tissue irradiation has been noted as 0.33 – 1 W. Despite this, 2 W irradiation was used for the *in vitro* studies with the purpose of measuring maximum NIR PDT. (Figure 4.11)(Zhao, Xu et al., 2021).

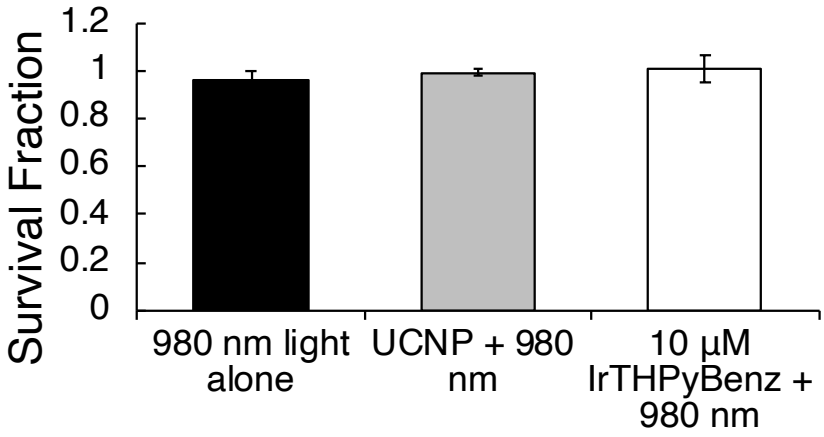

Figure 4.11 EJ cells were either untreated, exposed to a mass of UCNPs alone (the same as in Figure 4.10) or with 10 μM IrTHPyBenz for 2 hours. Cells were then detached and irradiated at 980 nm (2 W, 3 mins) and re-plated. The survival was then assessed through colony formation over 7-10 days. The means and SEM are shown over three repeats.

Irradiation at 980 nm (2 W, 3 mins) elicited negligible toxicity effects in *in vitro* cell models. Additionally, 980 nm phototoxic effects were not present upon incubations with UCNPs and 10 μM of IrTHPyBenz alone. Even though 2 W is unsuitable for clinical use, given off targeting heating effects in this region, any such NIR PDT activity could be re-assessed to fit within the acceptable limits. Any measured phototoxicity occurring at 2 W 980 nm was to be repeated whilst decreasing the laser power and/or exposure time until diminishment of such effects was observed. Subsequently, NIR PDT was attempted in EJ cells incubated with UCNPs coupled to a 10 μM dose of IrTHPyBenz (Figure 4.12).

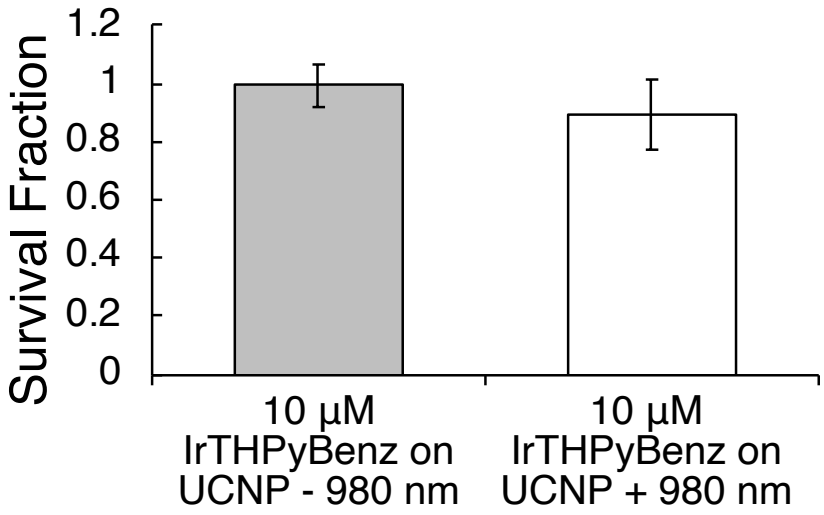

Figure 4.12 EJ cells were exposed to a mass of UCNPs with a 10 µM bound dose of IrTHPyBenz for 2 hours. Following this, cells were either irradiated (980 nm, 2 W, 3 mins) or not followed by re-plating. Survival was then assessed by colony formation after 7-10 days. Means and SEM are shown over three repeats (n=3). Student t-test (two ways, paired) p = 0.51 NS.

980 nm irradiation after cellular exposure of IrTHPyBenz-UCNP resulted in no phototoxicity. Given the small observed decrease in the light treated condition's mean, statistical analysis was conducted which consequently recorded no biological significance. Given that the uptake of IrTHPyBenz-UCNPs was validated by fluorescence microscopy after 2 hours, the absence of NIR PDT is likely due to an insufficient energy transfer process from the UCNPs to IrTHPyBenz. This was rationalised by IrTHPyBenz been previously measured to invoke PDT effects once photoactivated at 405 nm and 455 nm, which lie within the UCNP emission peaks. The reason as to why the energy transfer process is absent remains to be discussed.

4.3 – Discussion

4.3.1 – NIR PDT

UCNPs were synthesised with the aim of creating an NIR – blue light energy relay vessel which would permit NIR PDT upon the binding of a suitable and effective PS. UCNPs were successfully synthesised with measured desirable properties such as a

uniform nanosized distribution, suitable water solubility and the ability to perform NIR – blue light photon upconversion. IrTHPyBenz binding was validated alongside cellular uptake and low dark toxicity suggesting these could be a valuable future therapeutic tool. However, a lack of NIR PDT was measured which will be discussed. An emission of blue light under 980 nm irradiation was seen both by eye and quantified by an emission spectrum recorded from a sample of UCNP cores diluted in cyclohexane. However, upon the addition of silica layers, the emission was visually a lot weaker, at least by eye (Figure 4.13).

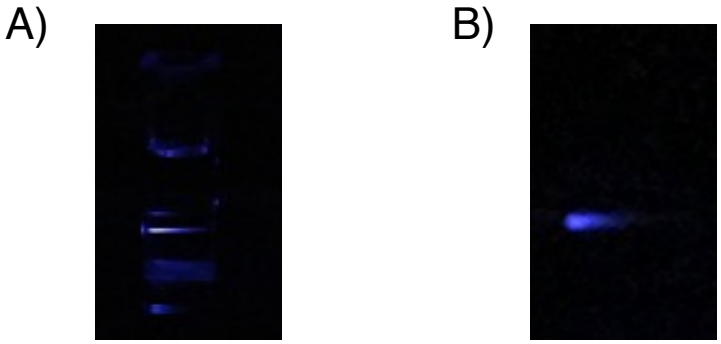

Figure 4.13 A) Observed upconversion of UCNP cores in cyclohexane B) Observed upconversion of UCNPs coated with amorphous silica in water. Both taken under the same dilution at 2 W of 980 nm irradiation.

The weakening of the emission could be due to both the addition of a silica layer interfering with incident light and the aqueous environment. Water has a small absorption at 980 nm thereby a reduction to incidence light will be observed through solvent absorption. The absorption of 980 nm light by water is validated through solution heating which was apparent in irradiated solutions (Chen, Ågren et al., 2015). A secondary weakening effect could also be due to the aggregation of UCNPs which increased in water, particularly when coated with mesoporous silica and in IrTHPyBenz-UCNPs, in comparison to solvation in cyclohexane. The increase to solvation in cyclohexane is due to UCNP cores being capped with hydrophobic oleic acid tails which interact with the solvent and aid dispersal. Upon burial of these caps with silica, the layering becomes stickier which leads to aggregation and an increase in surface-surface interactions which can be measured by DLS and observed in Figure 4.8 and Figure 4.9.

Additionally, the effect of surface interactions and aggregation on upconversion can be observed in more concentrated UCNP solutions which could explain why the energetic transfer between UCNP and IrTHPyBenz is not sufficient for PDT (Figure 4.14).

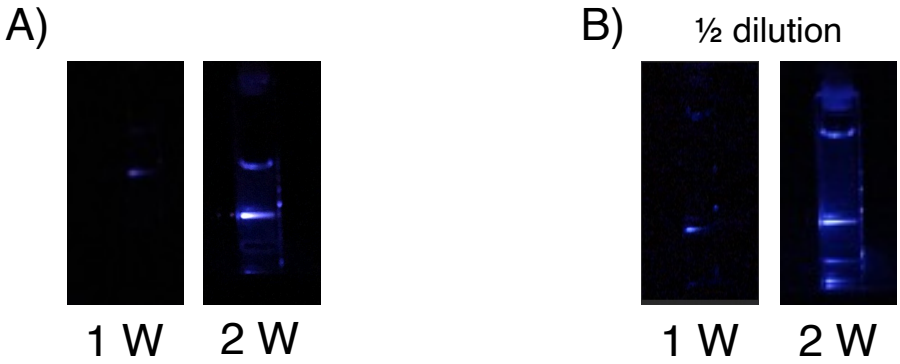

Figure 4.14 A) The observed emission of UCNP cores under 1 W and 2 W of 980 nm irradiation B) The observed emission of UCNP cores under 1 W and 2 W of 980 nm irradiation at half the dilution as A).

Given the presence of microaggregates in the UCNP-IrTHPyBenz suspensions applied to cells, upconversion could be reduced in the same way that is observed in more concentrated and hence more aggregated solutions. Therefore, the photon upconversion efficiency and process is likely too weak to be able to sufficiently photoactivate the PS and generate lethal levels of $^1O_2$. In order to boost photon upconversion efficiency, improvements can be made in the design and structure of UCNPs. Firstly, surface modifications can be added to not only improve photon upconversion but to also improve qualities such as water solubility or specific cell type targeting. For example, surface attached charged molecules would aid dispersal through electrostatic repulsion and have been shown to increase photon upconversion efficiency in $NaYF_4$; Yb^{3+}, Tm^{3+} by a factor of 29 (Yi and Chow, 2007).

Secondly, the embedding of a dye which further light sensitises UCNPs can increase absorption. For example, it has been shown that synthesising $NaYF_4$; Yb^{3+}, Tm^{3+} UCNPs which are conjugated to a hydrophilic NIR II absorbing dye, IR-1061, enhanced photon upconversion by a factor of 283. Enhancement was due to the strong light harvesting dye undergoing non-radiative energy transfer to Yb^{3+} (Hazra, Ullah et al., 2018).

A limit for laser irradiation power on tissue at 808 – 980 nm was reported at 0.33 – 1 W. This must be adhered to when applied to a patient as the surpassing of this range causes localised heating leading to tissue damage and the onset of pain (Zhao, Xu et al., 2021). Here we tested beyond this limit (2 W) in an *in vitro* model and observed no phototoxic effects, thus increasing laser power is not a strategy open to us. Two strategies present themselves to alleviate heating issues, namely a change in the absorption maxima of UCNPs or an increase in photon upconversion efficiency, which is previously discussed. $NaYF_4$; Yb^{3+}, Tm^{3+} perform photon upconversion firstly through 980 nm NIR absorption centred on the sensitiser ion, Yb^{3+}, which then non-radiatively transfers energy to Tm^{3+} higher energy states. However, through the inclusion of another lanthanide ion, such as Nd^{3+}, the sensitiser wavelength can be tailored to ~ 800 nm which lies outside of the water absorbing region which greatly reduces heating effects and hence also subsequently improves tissue penetration depth (Alkahtani, Alsofyani et al., 2021). 980 nm is bypassed through the replacement of the sensitiser ion from Yb^{3+} to Nd^{3+}. This is then followed by 808 nm irradiation which is absorbed by Nd^{3+}, transferred to Yb^{3+} before Tm^{3+} state occupation leads to energy transfer and PS photoactivation (Zhang, Yu et al., 2017).

4.3.2 – UCNPs as Drug Delivery Vehicles

UCNPs are suitable for more general use as PS delivery vehicles. We have demonstrated that they bind IrTHPyBenz but they have also been documented to bind other porphyrin-based PS (Gnanasammandhan, Idris et al., 2016). In doing so they can overcome inherent PS chemical properties which can limit the PS's use. For example, as we have seen by layering silica onto the surface of UCNPs, water solubilisation can be achieved. Water solubilisation is important because it aids PS administration, especially through intravenous methods which can otherwise cause phlebitis with hydrophobic drugs. The biodistribution ratio of UCNPs are also dependent upon their administration route, specifically with oral and dermal routes (Zhou, Ge et al., 2019). Therefore, the administration route can be utilised as an additional targeting method whereby the chosen route would maximise the biodistribution to a specific cancerous site. Silica coated UCNPs have an increased

proficiency for cellular uptake and can bio-distribute rapidly and extensively throughout the body and additionally have an increased uptake and retention in tumorous tissue compared to normal tissue when administered intravenously (Gnanasammandhan, Idris et al., 2016). However, whether this behaviour translates to IrTHPyBenz bound UCNPs remains to be tested and would require a suitable *in vivo* experiment. Support for the idea of increased uptake comes from visual comparison of *in vitro* luminescence which suggested increased IrTHPyBenz uptake occurred when bound to UCNPs, particularly at 20 μM (Figure 4.8). This could be due to a change in uptake ratio and mechanisms, with IrTHPyBenz being dominated by cationic transporters whilst surface modified UCNP uptake is largely governed through cell surface mediated endocytosis, although this again remains to be tested (Goh, Song et al., 2018).

An important parameter which also remains undetermined is whether UCNPs and IrTHPyBenz remain bound together within cells or whether the drug diffuses out of the mesoporous shell into the cellular environment. This behaviour could affect energy transfer between UCNPs and IrTHPyBenz due to differences in distances. In bound form, non-radiative energy transfer could occur whilst in an unbound form an increase in PS UCNP distance would be observed which would shift successive energy transfers to solely radiative means. The ability to monitor this was hindered largely due to the difficulty with imaging UCNP upconversion at 980 nm which required a suitable multi-photon microscope. An experimental design whereby the phosphorescence of IrTHPyBenz and the upconversion emission of UCNPs could be used to quantify the pixel overlap. This would subsequently give a direct measure of the spatial similarity of UCNPs and IrTHPyBenz, with strong overlap indicating the bound form. The leaching of IrTHPyBenz has been crudely tested, whereby drug bound UCNPs have been washed in water followed by supernatant analysis. The IrTHPyBenz content was measured by UV/vis spectroscopy which showed a negligible amount of IrTHPyBenz (data not shown). This would suggest that in aqueous environments, IrTHPyBenz remains bound to UCNPs.

4.4 – Conclusion

UCNPs, specifically $NaYF_4$; Yb^{3+}, Tm^{3+}, were synthesised and found to upconvert 980 nm NIR light into an emission of blue light/low energy UV with subsequent overlap within IrTHPyBenz's photoactivation range. These UCNPs were subsequently coated in layers of silica to make them suitable for biological use before being coupled with IrTHPyBenz for NIR PDT. Encouragingly, low dark toxicity was observed for the UCNPs alone and when bound to IrTHPyBenz. However, despite the energetic overlap between UCNP upconversion and IrTHPyBenz's photoactivation, NIR PDT was not observed in cells. This could be largely due to low UCNP upconversion efficiency which was measurably weaker upon successive coatings. Schemes to improve upconversion can be imparted which include an increase in hexagonal phase production by using specialist heating equipment (e.g. furnaces and autoclaves), dye sensitising surface modifications and overcoming laser power limits through a reduction to tissue heating effects via incorporation of Nd^{3+}.

5. MesBIAN Complexes

5.1 – Chemical Analysis

Previous studies on IrNew identified impressive PDT activity under both one-photon (405 nm) and two photon (760 nm) excitation which became the first documented case of 2-photon PDT using an Ir(III) complex (McKenzie, Sazanovich et al., 2017)(Appendix 5). IrNew bears two cyclometallating ligands, 2-phenyl pyridine (PPy), and one diimine ligand, bis-benzimidazole (Benz) resulting in a monocationic metal complex, for which PF_6^- or Cl^- can be used as counterions (Figure 5.1). In this thesis, we explore how additional structural alterations to both the PPy and Benz ligands would influence the PDT activity of this complex. The identification of such allows for structural consideration and/or improvement to potentially design better PS in the future.

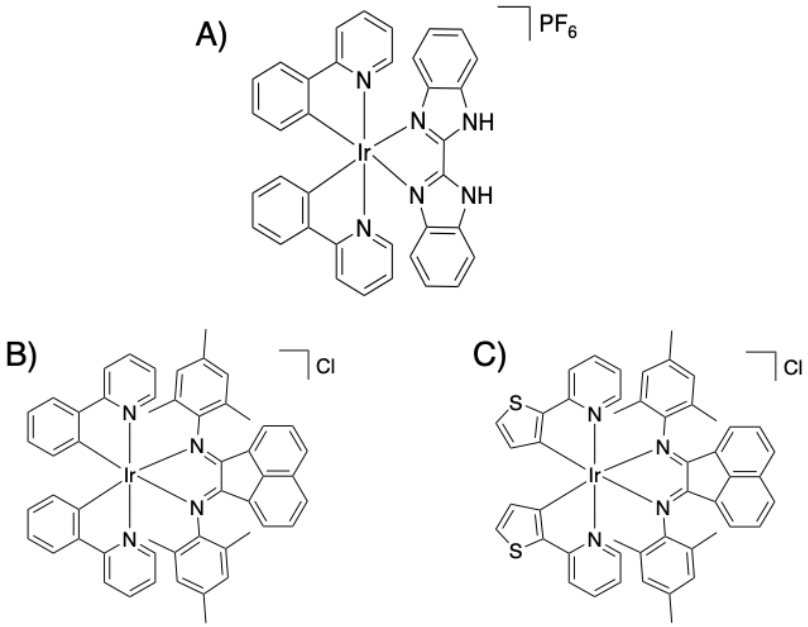

Figure 5.1 Structures of several Ir(III) cyclometallated complexes: A) The previously studied "IrNew" which demonstrated photoinduced killing of diverse cell lines under visible light as well as under 2 - photon NIR excitation. B) Iridium (III) (2-phenyl pyridine)$_2$(bis(mesitylimino)acenapthene) chloride, IrPPyMes C) Iridium (III) (2-thiophenyl pyridine)$_2$(bis(mesitylimino)acenapthene) chloride, IrTHPyMes.

In considering the two ligands, exchange to both the two ancillary anionic CN co-ordinating ligands, 2-phenyl pyridine (PPy) and one neutral NN co-ordinating ligand,

bis-benzimidazole (Benz) can be performed. Through the replacement of carbon atoms with electron donating sulphur atoms, a red-shift to the overall complex absorption spectra has been previously reported (Chapter 3)(Mbambisa, Tau et al., 2007, Pandian, Reddy et al., 1990). Therefore, the PPy ligands were exchanged with 2-thiophenyl pyridine (THPy) to shift the absorption spectrum of IrNew to the red which would consequently improve the tissue penetration of photoactivation. Additionally, the lowest energy UV/vis absorptions in the spectrum of $Ir(CN)_2(NN)$ complexes arises from a mixture of intraligand CN-based π - π^* transitions and an MLCT transition from Ir(III) to Benz. Therefore, by exchanging Benz with a more electron-accepting ligand, a potential red-shift to the MLCT absorption band could be observed. Such a ligand, namely (bis-(mesitylimino)acenapthene)(Mes) would be a suitable candidate which simultaneously presents characteristics such as high rigidity, aromaticity and planarity, all of which can favour DNA intercalation and hence potentially also increases phototoxicity through chromatin photodamage (Glinton, Latifi et al., 2019, Ihmels, Karbasiyoun et al., 2019, Pyle, Rehmann et al., 1989). Through the exchange of Benz for Mes with/without concurrent exchange of PPy for THPy, two new compounds were synthesised, IrPPyMes and IrTHPyMes which were then investigated for any increases to IrNew's PDT activity. This was rationalised under the hypothesis that structural modifications can increase complex PDT activity and also clinical applicability of Ir(III)-based therapeutics. Both compounds as such were synthesised in the Weinstein/Bryant group by Mr. Liam Kirby.

5.1.1 – Photophysical Properties

The absorption spectra of IrTHPyMes and IrPPyMes were compared to IrNew's to establish whether the exchange of any ligands caused a red-shift in the lowest visible light absorption band (Figure 5.2).

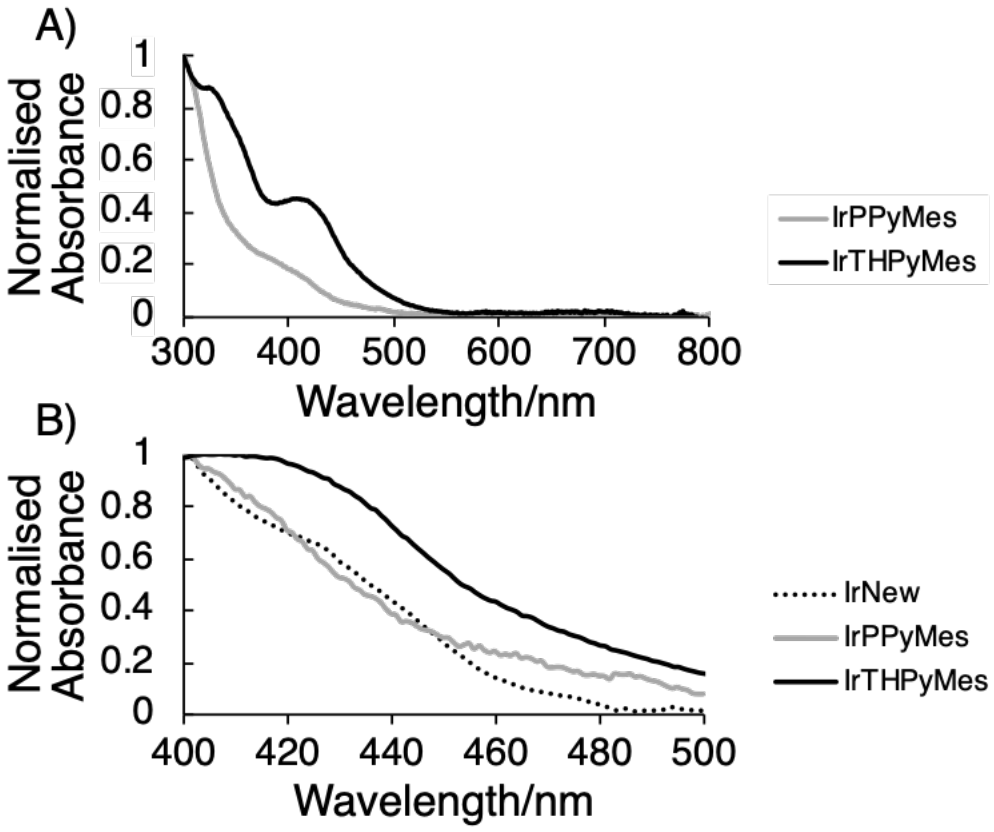

Figure 5.2 A) The absorption spectra of IrPPyMes and IrTHPyMes in DMSO B) The lowest energy absorption region of IrPPyMes and IrTHPyMes compared to IrNew in DMSO

Both IrPPyMes and IrTHPyMes absorb in the blue/green region of the spectrum, 400 – 500 nm (Figure 5.2). An observed red shift of approximately 30 nm to the lowest absorption band was measured for IrTHPyMes compared to IrNew, whereas IrPPyMes was found to absorb light very similarly to IrNew. The molar extinction coefficients in the visible region were 9900 $M^{-1}cm^{-1}$ (400 nm), 5600 $M^{-1}cm^{-1}$ (450 nm) for IrTHPyMes and 1000 $M^{-1}cm^{-1}$ (400 nm) and 300 $M^{-1}cm^{-1}$ (450 nm) for IrPPyMes indicating that the THPy ligand increased visible light absorption by ~ 10 – 16-fold. Following this, no detectable emission was observed up to 850 nm (from a 400 nm excitation) in both Mes compounds. This observation could be explained by the excited state lifetime being too short to be detected, or that the emissive state lies within the NIR region of the spectrum which lies outside of the equipment's detection limit. In order to test whether the Mes compounds can act as PS for singlet oxygen production, a singlet oxygen detection experiment was performed. The Mes compounds were irradiated at 355 nm in acetonitrile solution whilst the emission at

the wavelength of singlet oxygen phosphorescence, 1270 nm, was monitored. Both Mes compounds did not show any production of singlet oxygen (data not shown). Therefore, the loss of the NN bearing Benz ligand caused a complete diminishment to the complex's overall ability to generate singlet oxygen. Despite this, both Mes compounds were scrutinised for any possible phototoxicity effects applicable for PACT (photoactivated chemotherapy) treatment. PACT effects induce phototoxicity through processes such as electron transfer and/or ligand substitution reactions following irradiation and do not rely on a compound's singlet oxygen generation (Farrer, Salassa et al., 2009, Imberti, Zhang et al., 2020).

5.2 – Cellular Behaviour

5.2.1 – Cellular Uptake and Localisation through ICP-MS

Mes compounds were added to cells to test for cellular uptake. Uptake could be through either passive membrane diffusion, an active transport mechanism(s) or a mixture of these two. As the Mes compounds are charged and sterically bulky, passive membrane diffusion would likely be minimal due to the hydrophobic effect preventing movement across the cell membrane. Additionally, the cationic charge of the compounds could favour uptake through active cationic transporter pores, such as those meant for potassium ions, or by copper based CTR1 receptors. Transition metal compounds are usually luminescent which allows for their uptake monitoring through fluorescence microscopy. However, due to the lack of luminescence, a different route of analysis had to be used. Inductively coupled plasma mass spectrometry (ICP-MS) was chosen as the optimum technique through the detection of biologically absent iridium. This involved incubation of EJ cells with Mes compounds followed by cell lysis to create cell extracts. ICP-MS was then carried out on these extracts to measure the iridium volumetric concentration which was then subsequently divided by the total protein concentration to give a final value of iridium which incorporated cell number. This is made relatively straight forward due to iridium being naturally absent from cells which leads to the assignment of all detected iridium being from the Mes compounds (Figure 5.3).

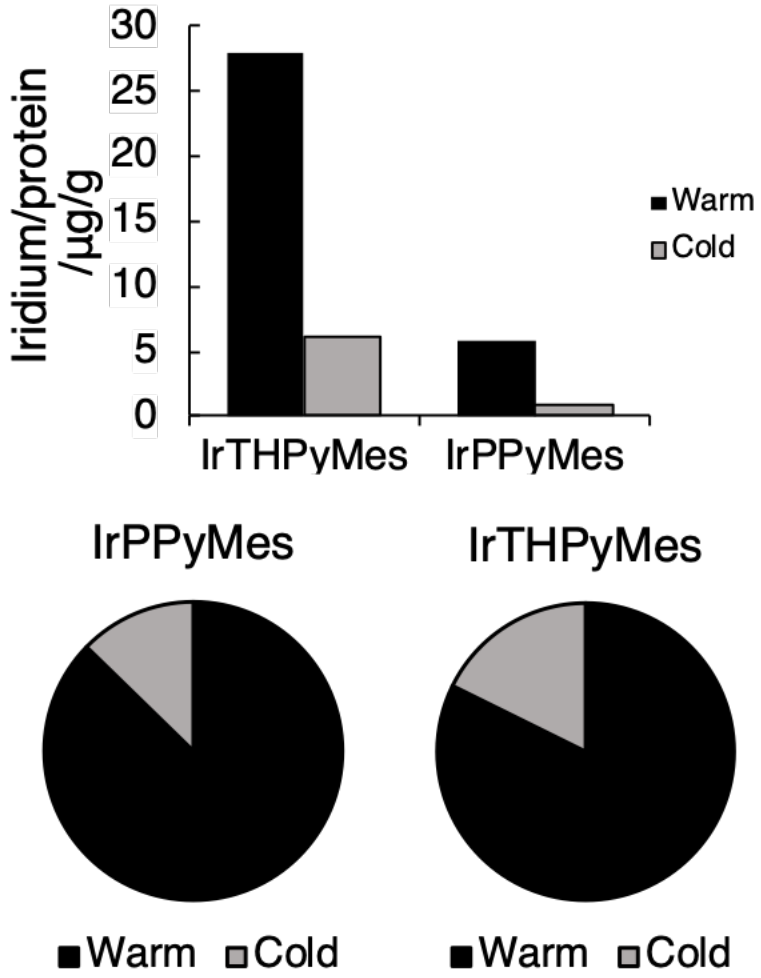

Figure 5.3 Measured iridium content in EJ cell lysates which have been incubated for 30 mins with drug at 4 °C (cold) or 37 °C (warm); n = 1

After incubation at 37 °C for 30 mins, IrTHPyMes was measured at an intracellular concentration 3.73 ± 1.07 times greater (n = 2) than IrPPyMes. EJ cells incubated with compounds at 4 °C were restricted to uptake by passive membrane diffusion only due to arrested ATP production, which is required for active uptake. Therefore, only iridium which has passively diffused across the cell membrane is present in the cell extracts at 4 °C. At 37 °C, ATP production allows for active transport and therefore iridium uptake by both active and passive mechanisms can occur in cell extracts. Both drugs were taken up by passive membrane diffusion and active transport mechanisms, albeit to differing extents (Figure 5.3). Uptake through active transport mechanisms accounted for 82% of IrTHPyMes (18% passive) and 87 % of IrPPyMes (13% passive) total uptake. Due to a near identical ratio of active and

passive uptake for Mes componds, it is likely that both species undertake the same pathways.

As the Mes ligand possesses suitable properties for DNA intercalation, cell lysates were then subjected to subcellular fractionation through the separation of cytoplasmic material with chromatin. Following incubation, iridium was detected in both the cytoplasm and chromatin fractions with drug-dependent differences found in the distribution ratio (Figure 5.4).

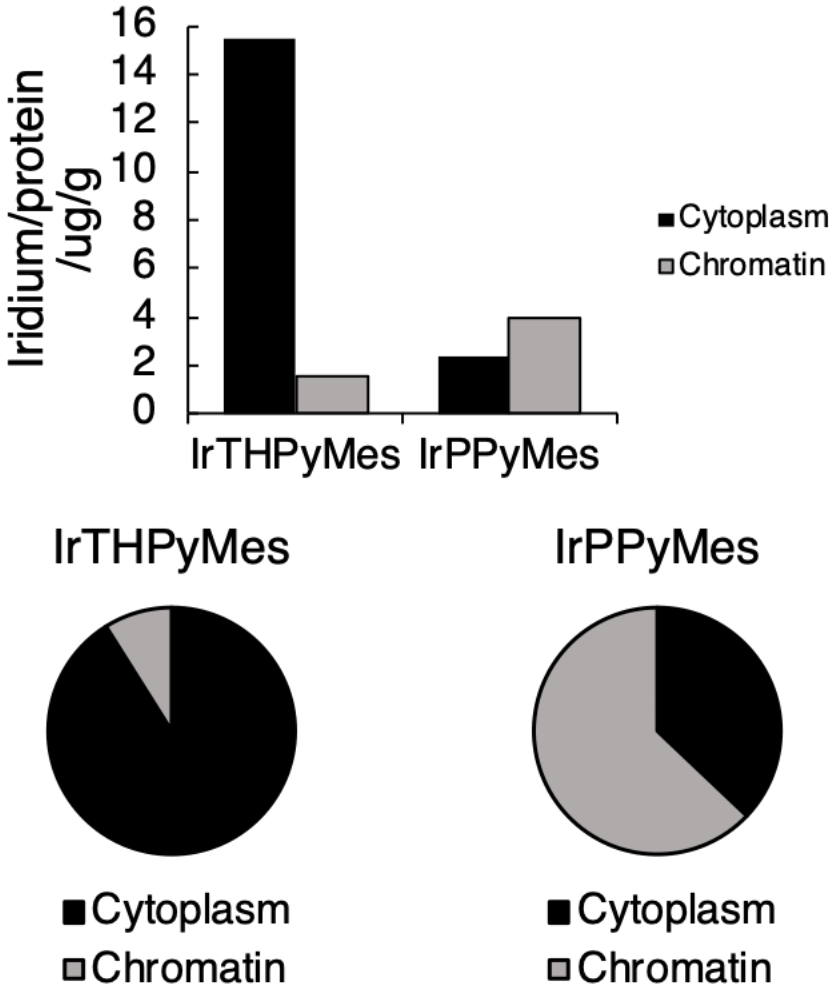

Figure 5.4 iridium content of EJ cell extracts after 2 hr of drug incubation at 37 °C. Lysates were subjected to fractionation into cytoplasmic and chromatin extracts through centrifugation solvated in selective buffers. n = 1

The cytoplasm was found to contain 91% of IrTHPyMes compared with 37 % of IrPPyMes. Iridium content in the chromatin fraction was 63% for IrPPyMes compared with only 11 % of IrTHPyMes. In terms of total uptake, IrTHPyMes's chromatin

concentration was 2.6 x smaller but 6.7 x higher in the cytoplasm compared to IrPPyMes.

5.2.2 – Dark Toxicity and Phototoxicity

Following validation of cellular uptake, the dark toxicity was determined using clonogenic survival assays (Figure 5.5).

A)

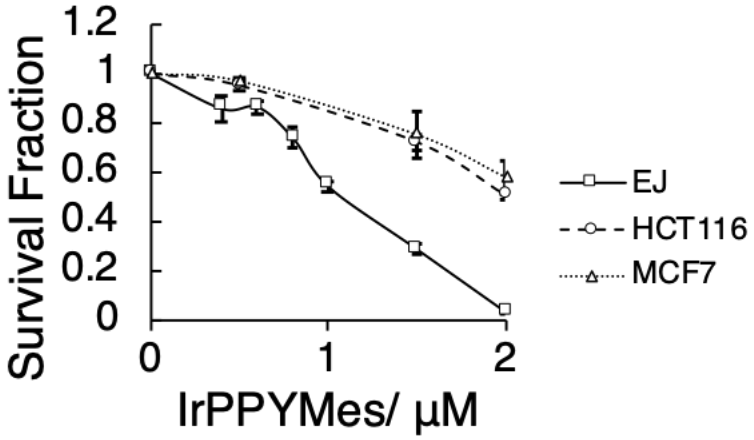

B)

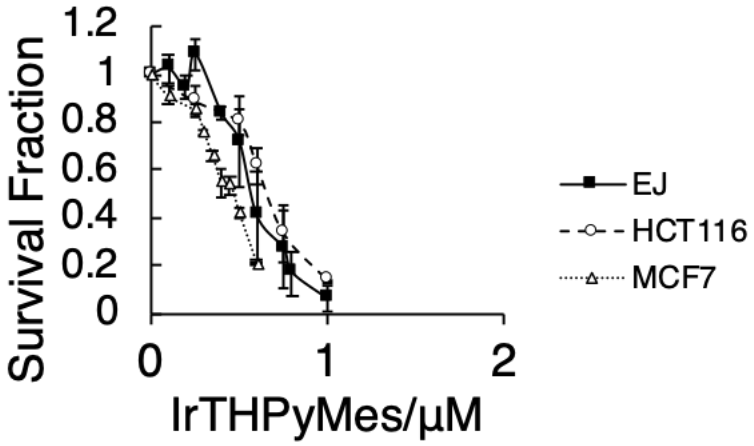

C)

Cell line	IrPPyMes LD_{25}, LD_{50}/ µM	IrTHPyMes LD_{25}, LD_{50}/ µM
EJ	0.8, 1.06	0.48, 0.58
HCT116	1.47, 2.0	0.36, 0.64
MCF7	1.5, 2.2 (projected)	0.30, 0.47

Figure 5.5 A) the survival fraction of different cell lines upon exposure to IrPPyMes, n≥2 ; B) the survival fraction of different cell lines upon exposure to IrTHPyMes n≥2; C) a table of the LD_{25} and LD_{50} of IrPPyMes and IrTHPyMes on three different cell lines

EJ cells were originally selected as a suitable *in vitro* model due to bladder cancer being a PDT applicable cancer type with MCF7's and HCT116's also investigated as examples of other epithelial cancers. IrNew has a low dark toxicity (LD_{50}(dark) >100 μM) whilst both IrTHPyMes, and IrPPyMes had vastly increased dark toxicity in comparison (McKenzie, Sazanovich et al., 2017). Furthermore, in all cell lines, IrTHPyMes was found to be between 2 - 5 x more toxic than IrPPyMes (Figure 5.5). A small difference in cell-line sensitivity was measured for IrTHPyMes compared to an increase in sensitivity of IrPPyMes towards EJ cells. However, this could have been due to compound stock degradation over time which likely caused slight alterations to applied dosage on HCT116s and MCF7s.

During the chemical characterisation of IrTHPyMes and IrPPyMes, the singlet oxygen yield was shown to be null which suggested that PDT activity may be negated, however PACT activity was possible. Therefore, EJ cells were subjected to 405 nm irradiation post drug incubation to invoke any possible phototoxic effects (Figure 5.6).

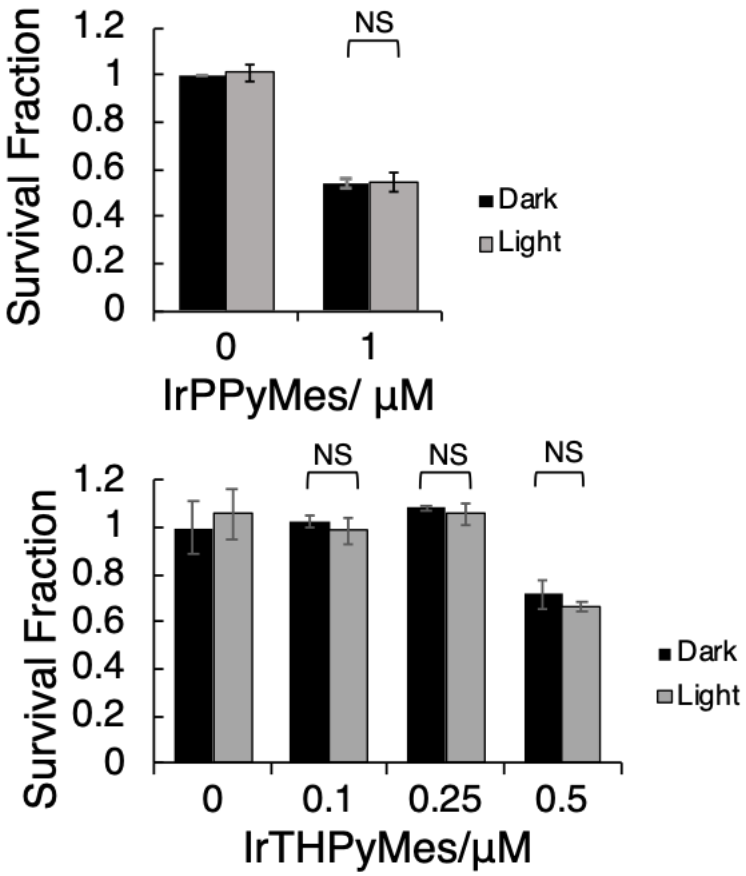

Figure 5.6 a comparison between toxicity of EJ cells upon exposure to IrPPyMes (top) and IrTHPyMes (bottom). Following 2 hours of incubation, cells were either irradiated with 20 mWcm^{-2} 405 nm of light (light; grey) for 3 mins or not (dark; black) n ≥ 2 for each value, p > 0.05

There were no appreciable differences between dark and light toxicity for both drugs upon statistical analysis (Figure 5.6). Light irradiation was carried out up to the LD_{50}(dark) doses of both compounds due to effects being theoretically at their most profound. However, no such differences existed, and the PI values of both compounds was calculated to be ~1. Taken together the light and dark toxicities of IrTHPyMes, and IrPPyMes suggest they are unlikely to be suitable for clinical translation as PDT agents. However as toxic agents in the dark they were still of interest and further analysis of cellular effects was carried out.

5.2.3 – Cell Cycle Effects and DNA Damage

Both Mes compounds were found to localise to chromatin, albeit to differing degrees. Therefore, cell cycle progression was studied for any disruptions which could lead to cell death (Figure 5.7). For example, cisplatin induces apoptosis due to crosslinked DNA and is accompanied by G_2/M phase arrest (Bergamo, Gagliardi et al., 1999, Sorenson, Barry et al., 1990).

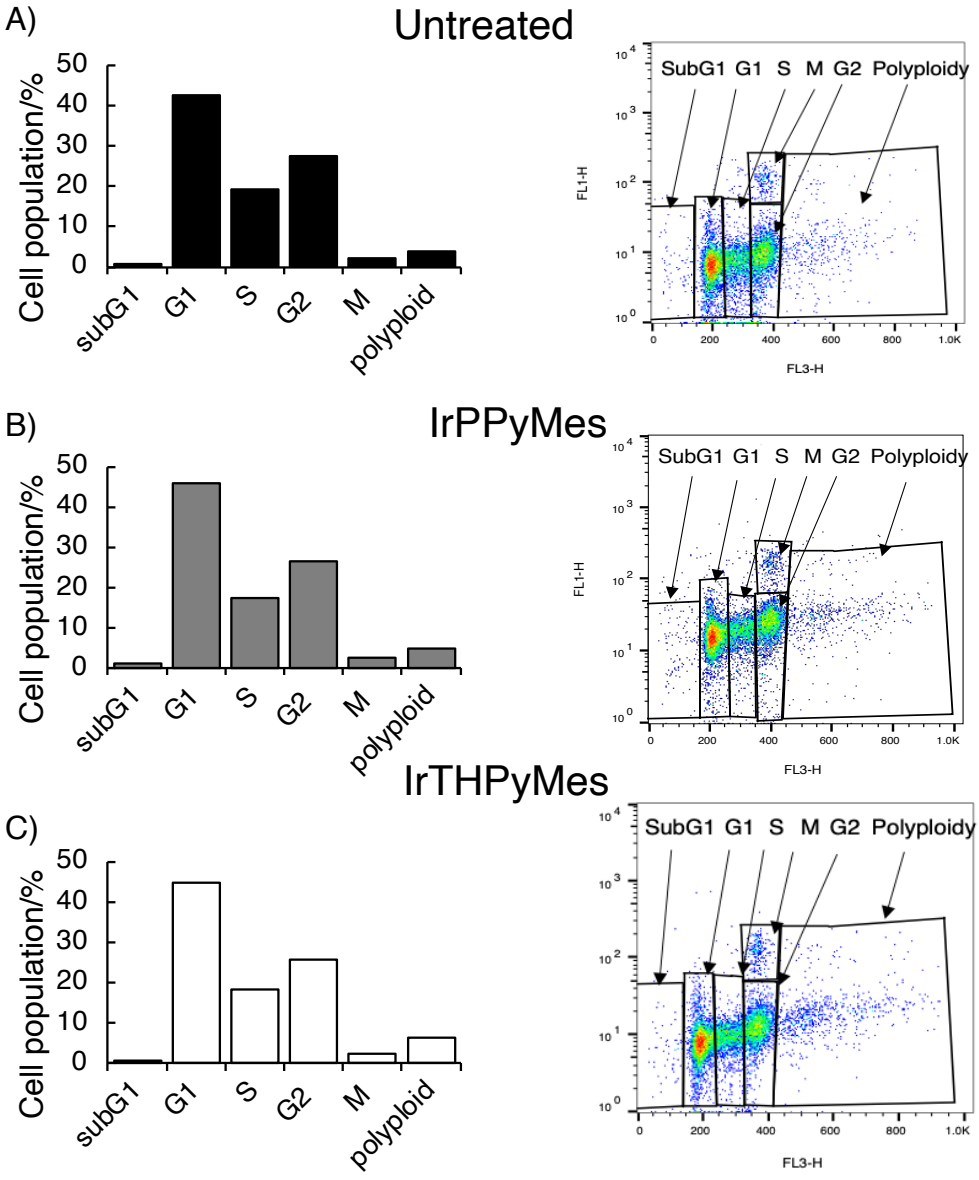

Figure 5.7 A cell cycle composition of either untreated, IrPPyMes (1 μM, 24 hrs) or IrTHPyMes (0.5 μM, 24 hours) EJ cells. Cells were drugged, fixed and stained with either PI (λ_{exc} 520 nm, λ_{em} 620 nm) or a fluorescent secondary antibody to phosphoHistone3 (λ_{exc} 488 nm, λ_{em} 520 nm) with the fluorescence collected by FACS n = 1.

EJ cells were drugged at their LD_{50} doses and incubated for 24 hours to allow full cell cycle progression and any potential drug-induced disruptions to occur. FACS analysis identified no obvious differences between the cell cycle of treated and untreated cells (Figure 5.7). This showed that toxicity effects were not due to any interference with the cell cycle. However, additional repeats would need to be carried out in in order to fortify the reliability of these findings.

Following on from this, both compounds were analysed for their ability to induce DNA damage through the counting of γH2AX foci. Histone 2AX (H2AX) becomes phosphorylated by ATM to form γH2AX in response to DNA damage and can be seen as discreet foci in cells (Burma, Chen et al., 2001, Mah, El-Osta et al., 2010). The number of foci seen per cell increases upon damage caused by γ radiation, oxidative chemicals and ultraviolet radiation amongst others (Mah, El-Osta et al., 2010). If DNA damage is not sufficiently repaired, then apoptosis can be initiated by p53 leading to cell death (Jackson, 2002). Immunofluorescent staining of γH2AX with a fluorescent secondary antibody can be visualised by fluorescence microscopy with the number of fluorescent foci counted per 100 cells post drug exposure (Figure 5.8).

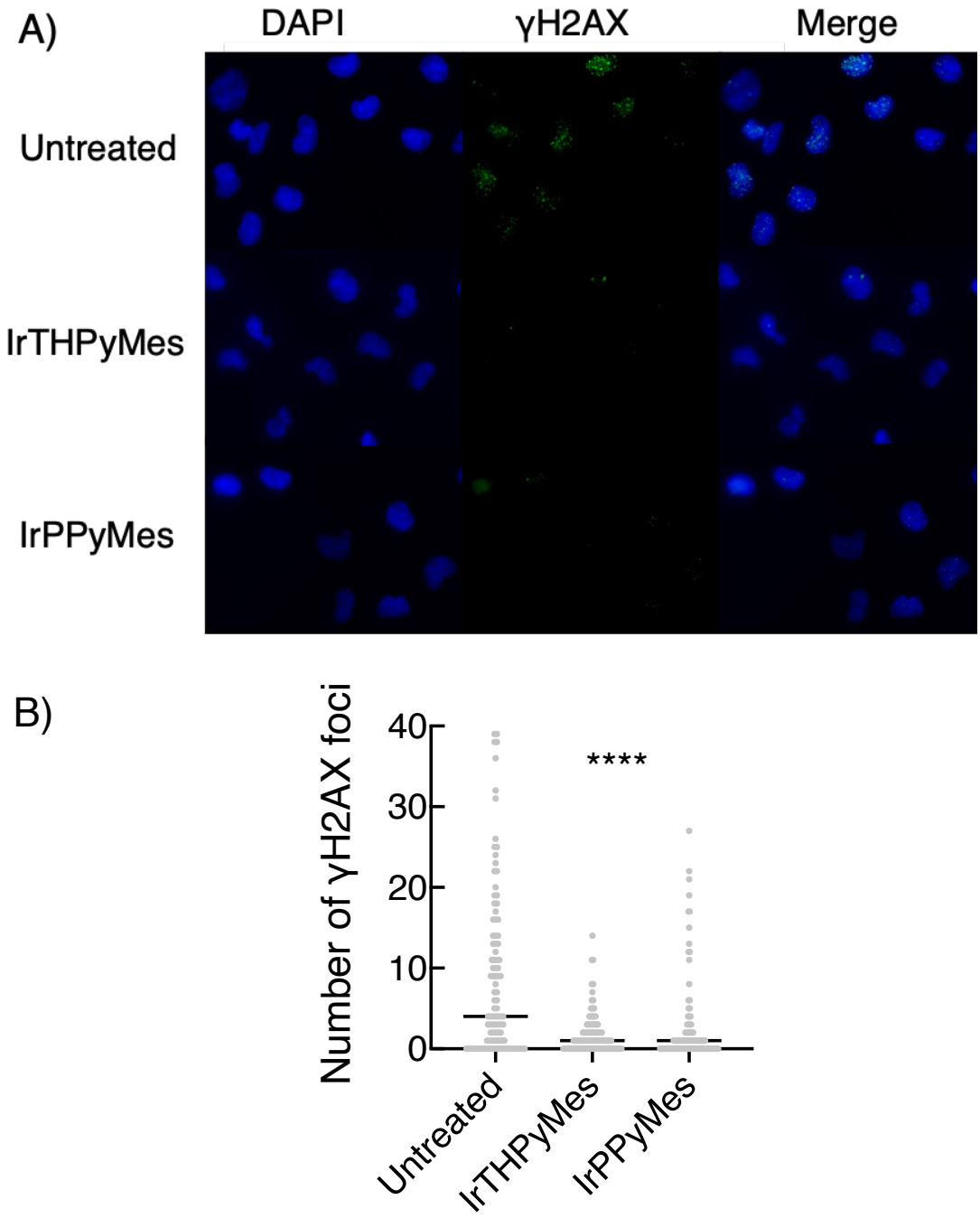

Figure 5.8 A) EJ cells were either left untreated or incubated with IrTHPyMes (0.1 μM) or IrPPyMes (0.1 μM) for 2 hours followed by immunostaining with anti-γH2AX (λ_{exc} 488 nm, λ_{em} 520 nm) alongside DAPI (λ_{exc} 350 nm, λ_{em} 450 nm). B) The number of γH2AX foci, a site of DNA damage, counted over 100 EJ cells in either untreated condition or after treatment of IrPPyMes and IrTHPyMes (0.1 μM, 2 hrs). n = 1, $p < 0.0001$ ANOVA

In comparison to the untreated condition, γH2AX foci were found to be significantly reduced in drug treated cells, suggesting that DNA damage is reduced or that sub

lethal doses of IrPPyMes and IrTHPyMes can block H2AX phosphorylation. Why this would be the case is unclear and would require further experimentation beyond the scope of this project.

5.3 – Discussion

5.3.1 –MesBIAN Complexes as Improvements to IrNew

The modifications on IrNew to make IrPPyMes and IrTHPyMes produced inferior PDT effects, IrNew has a measured PI of > 238 (in EJ cells) which is much higher than IrPPyMes and IrTHPyMes which we calculated here as PI ~ 1. The lack of phototoxicity could be due to a lack of singlet oxygen generation which was notably lost upon replacement of Benz diimine ligand with MesBIAN (IrNew $\Phi(^1O_2)$ 42%) (McKenzie, Sazanovich et al., 2017). In IrNew, the ^{3}MLCT (which likely co-exists with the ^{3}LC state of PPy) was responsible for both the phosphorescence, and singlet oxygen generation. Therefore, the presence of Benz is necessary for the desirable PDT activity. It appears that the MesBIAN ligand is too electron-withdrawing which potentially shifts the energy of the triplet state too low to effectively generate singlet oxygen, and/or causing the excited state lifetime to be too short for it to engage in a bimolecular reaction with oxygen.

Although IrPPyMes and IrTHPyMes did not have PDT activity, both complexes did show significant dark toxicity. IrNew had an LD_{50}(dark) > 100 μM compared with LD_{50}(dark) 0.8 μM (IrPPyMes) and LD_{50}(dark) 0.48 μM (IrTHPyMes). Cytotoxicity increased by 125 x (IrPPyMes) and 208 x (IrTHPyMes) which can be attributed to the replacement of Benz ligand with Mes.

The difference in the toxicity of PPy vs. THPy containing complexes, as well as IrPPyMes and IrTHPyMes vs. IrNew (IrPPyBenz) can also be discussed. By comparing the absorption spectra of Mes compounds with IrNew, it was observed that IrTHPyMes red-shifted absorption by ~ 30 nm, whereas IrPPyMes was spectroscopically nearly identical. Given the findings in Chapter 3, the ancillary ligands (PPy vs THPy) dictate compound absorption which is why IrNew (IrPPyBenz) and IrPPyMes are spectroscopically similar whilst IrTHPyMes is more red-shifted. Additionally, IrTHPyMes was found to be 2 – 5 x more toxic than IrPPyMes in three

cancer cell lines. Cytotoxicity was cell line independent for IrTHPyMes but for IrPPyMes, EJ cells were twice as sensitive than other cells. This increase in EJ sensitivity is likely due to stock stability issues with tiny amounts of IrPPyMes precipitate being visible at the time of HCT116 and MCF7 testing. This did not occur with IrTHPyMes which suggested an enhancement in solvation stabilisation. IrTHPyMes was uptaken 3.73 ± 1.07 x more than IrPPyMes and majorly localised to the cytoplasm (91%) as opposed to IrPPyMes which slightly favoured chromatin (63%). In combination, iridium in the cytoplasm was 6.9 x higher in IrTHPyMes than IrPPyMes but only 2.6 x smaller in chromatin. Therefore, the increase in cytotoxicity for IrTHPyMes could be due to an increase in the Mes toxicity in the cytoplasm. Despite the high levels of cell killing by both agents, the cell cycle and DNA damage response via γH2AX formation were small when compared to untreated cells. If DNA damage or nuclear cytotoxicity were to occur, then this is likely would not have been the case.

5.3.2 – IrPPyMes and IrTHPyMes as General Antitumour Agents and Methods of Further Investigation

Although IrPPyMes and IrTHPyMes are unsuitable for PDT, they could be used as general chemotherapeutics or for the treatment of multidrug resistant tumours. However, the mode of action, the mechanism of cell death and any cellular interactors are currently unknown.

TEM could be used as an alternative to fluorescence-based cell studies to further investigate cytotoxicity. Iridium has been visualised in cells by TEM through measured increases to subcellular membrane contrast caused by the scattering of incidence x rays from accumulated iridium (Tian, Zhu et al., 2017). TEM has additionally visualised changes to both chromatin and mitochondria to describe the cytotoxic effects of other iridium (III) drugs (Cao, Tan et al., 2017, Hearn, Romero-Canelón et al., 2013). However, TEM using iridium as the contrast agent would require a sufficiently high yet non-toxic dose (e.g. 50 μM) which IrPPyMes and IrTHPyMes do not possess (Shewring, Cankut et al., 2017). Chromatography could also be used to fractionate the iridium-containing protein extracts by preliminary

excluding based on size followed by more specific exclusions. This method would rely on metallo-protein stability, with the iridium content of each fraction validated through ICP-MS due to the lack of iridium luminescence. Targets involved in iridium (III) conjugation have been identified as mitochondrial proteins (VDAC1), histidine rich proteins and albumin (Lu, He et al., 2014, Wang, Chen et al., 2017, Zhou, Ding et al., 2020). However, these were covalently attached through ligand substitution of a protein residue with the iridium pro drug. IrTHPyMes and IrPPyMes are unlikely to possess a sufficiently labile ligand for this to be possible and would likely bind non-covalently.

5.4 – Conclusion

The PDT activity of IrNew was found to be drastically altered upon ligand substitutions. Upon the exchange of the diimine ligand, Benz, with the more electron-accepting and bulkier ligand, Mes, cytotoxicity effects increased whilst singlet oxygen generation, emission, and phototoxicity disappeared. Thus, this specific structural change led to severely reduced PDT activity. Less detrimental differences were observed upon the interchange of PPy and THPy ligands. These included changes in cellular uptake and localisation which were attributed to toxicity differences between IrTHPyMes with IrPPyMes. The Mes ligand was originally hypothesised to increase PDT activity through DNA localisation and damage upon irradiation. However, findings suggested that the increase in dark toxicity was caused by an interaction with Mes in the cytosol rather than on chromatin. The mode of action in toxicity effects of IrTHPyMes and IrPPyMes could be useful to identify suitability to treat multi drug resistance cancers. This could be facilitated through TEM analysis and/or drug-protein isolation and purification to further probe toxicity mechanisms. Specific results and methods detailed in this chapter could also be made further reliable by repetition. However, given that the drugs lack selectivity, lose PDT activity and do not have any obvious advantages over current chemotherapies, it would not qualify as been overall important.

6. PDT Activity of a Cyclometallated Pt(II) Species, PtCNNH

6.1 – Chemical Analysis of PtCNNH

Previous investigation into the use of a conjugated metalloporphyrin-organoplatinum compound, 'Porphyrin Plus', afforded very promising results for its use as a powerful PDT agent with a PI of > 500 (Bryant/Weinstein Group,*unpublished work*)(Figure 6.1)(Appendix 6) .

A)

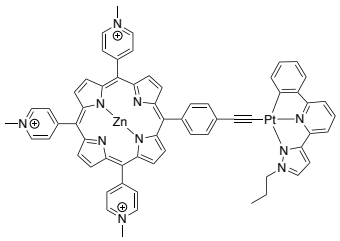

B)

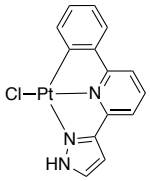

Figure 6.1: A) The chemical structure of 'Porphyrin Plus', a metalloporphyrin-organoplatinum conjugate which previously displayed very promising PDT activity (unpublished work). B) The chemical structure of PtCNNH; a fragment of 'Porphyrin Plus' comprising of solely the unpropylated organoplatinum component.

Well-known inherent problems exist when using porphyrins as drugs which includes PorphyrinPlus. This is largely due to the asymmetric porphyrin ring component, which is synthesised by a long, difficult, and wasteful route. Therefore, the compound was simplified to its platinum fragment. This was then followed by a re-analysis of PDT to test whether such structural simplification could simultaneously retain favourable PS activity. To this hypothesis, the organoplatinum group was cleaved via the acetylide bridge and instead replaced with a chloride ligand. By removing the unsaturated acetylide bridge, the compound's ability to undergo electron transfer from its porphyrin component to its platinum component was lost. This would provide a better mechanistic understanding of PorphyrinPlus's ability to cause photosensitisation to see if only the metal-based electronic excited states

were essential. An initial problem with this modification was that the compound was very hydrophobic which gave rise to drug administration issues. To circumvent this, an amine group was de-propylated to afford a more hydrophilic NH moiety, producing 'PtCNNH'. The synthesis of PtCNNH was performed within the Weinstein Group with subsequent PDT analysis to be presented in this chapter.

6.1.1 – Photophysical Properties

To validate whether PtCNNH would be suitable as a PS, a UV-Vis absorption spectrum was measured (Figure 6.2). This was to ascertain the complex's lowest energy absorption alongside the absorptivity of such as quantified by the molar extinction coefficient. PtCNNH had a visible light absorbing transition in the region of 400 – 475 nm, essentially covering the entire blue light region. In order to investigate what type of transition this was, the molar absorptivity co-efficient, ε, was calculated and compared against those of the higher energy UV peaks. The measured ε value in the region of 400 – 475 nm was 7,000 $M^{-1}cm^{-1}$, indicative of metal-to-ligand charge transfers (MLCT)(Ko, Kwok et al., 2006). In comparison, the peaks in the region of 300 – 350 nm were found to have ε values of 104,000 $M^{-1}cm^{-1}$ (356 nm) and 139,400 $M^{-1}cm^{-1}$ (325 nm), indicative of ligand-based π - π^* transitions (Ko, Kwok et al., 2006). The UV associated peaks were discarded for PDT, although more highly absorbing, as they lie within the mutagenic UVA-UVB part of the spectrum. The MLCT state was then investigated further by measuring the emission and excitation spectra. The compound was emissive under blue light excitation (425 nm), occurring in the green light region (500 nm – 700 nm) with a Stokes shift of 0.46 eV (425 nm_{exc} – 505 nm_{em}). From the excitation spectra shown in Figure 6.2, the measured emission was only produced upon excitation in the MLCT region (400 – 475 nm). The excitation spectra showed good overlap with the absorption spectra of the MLCT region (albeit slightly more red-shifted as is normal in excitation spectra). The presence of a moderate Stokes shift is indicative of the emissive state being a triplet excited state, which is necessary for PDT. As is typical in transition metal complexes, the initially populated singlet excited state undergoes an energy conserving ultrafast intersystem crossing into a triplet excited state (McKenzie, Bryant et al., 2019). The

S - T transition in transition metal complexes is strongly facilitated by spin orbit coupling due to the presence of a heavy, multielectron metal atom such as platinum. The triplet excited state then decays to the ground state through a combination of non-radiative and radiative decay (phosphorescence) by emission of a lower energy photon. Upon observation of the emission spectra, some vibrational progression could be seen which suggested radiative decay from a ligand-based triplet excited state ^{3}IL* or a combination with ^{3}MLCT* decay. Sole emission from ^{3}MLCT* was unlikely due to the absence of a broad emissive peak which arises due to the Franck-Condon Principle.

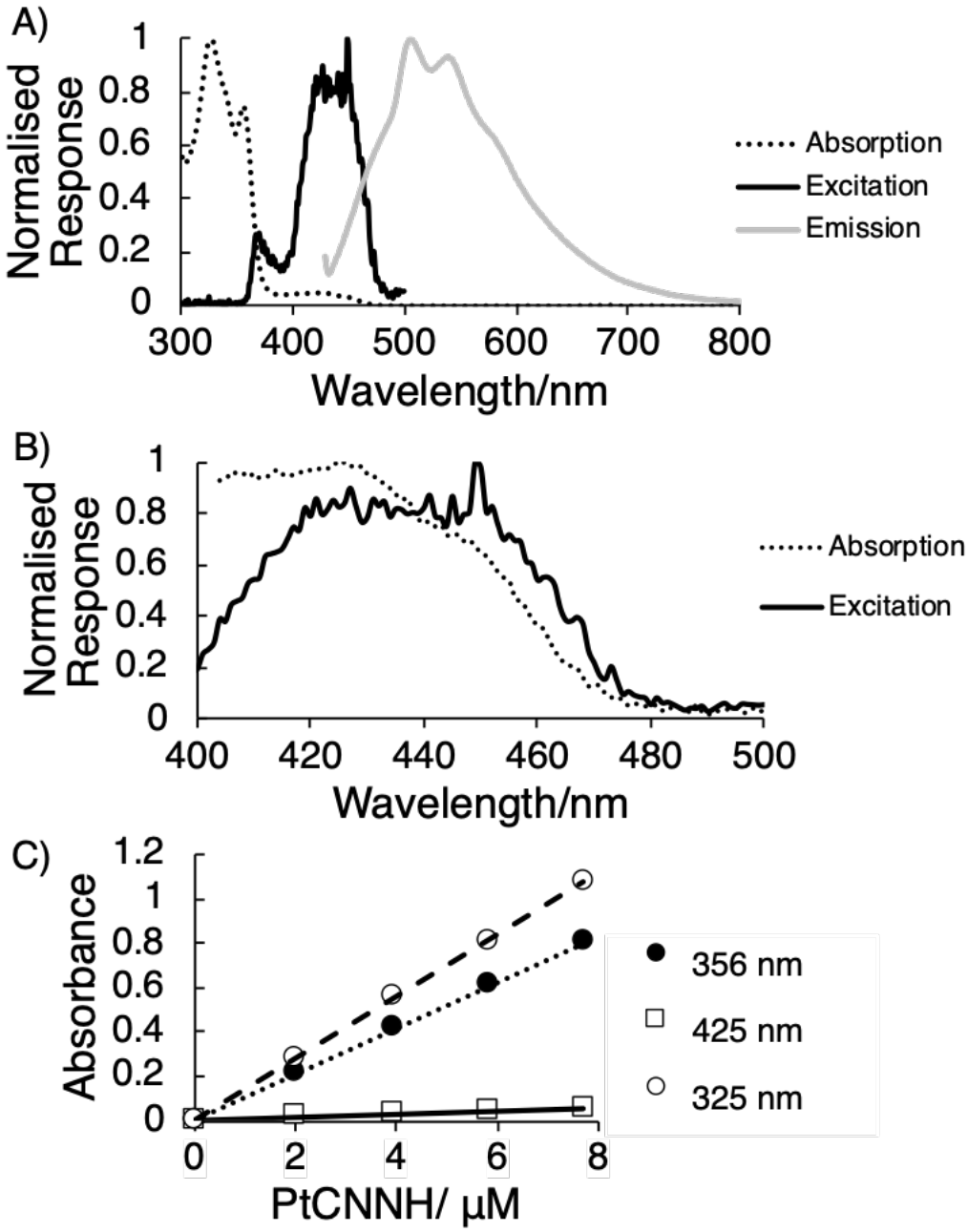

Figure 6.2 A) The emission (λ_{exc} 425 nm, grey), excitation (λ_{em} 505 nm, black) and absorption spectra (dashed) of PtCNNH in DMSO. B) The expanded MLCT region of A) showing the overlap between the absorption and excitation spectra. C) A plot to show how the absorbance of PtCNNH (in DMSO) changes with concentration at various wavelengths.

To further characterise the emissive state, the emission decay lifetime was measured (Figure 6.3).

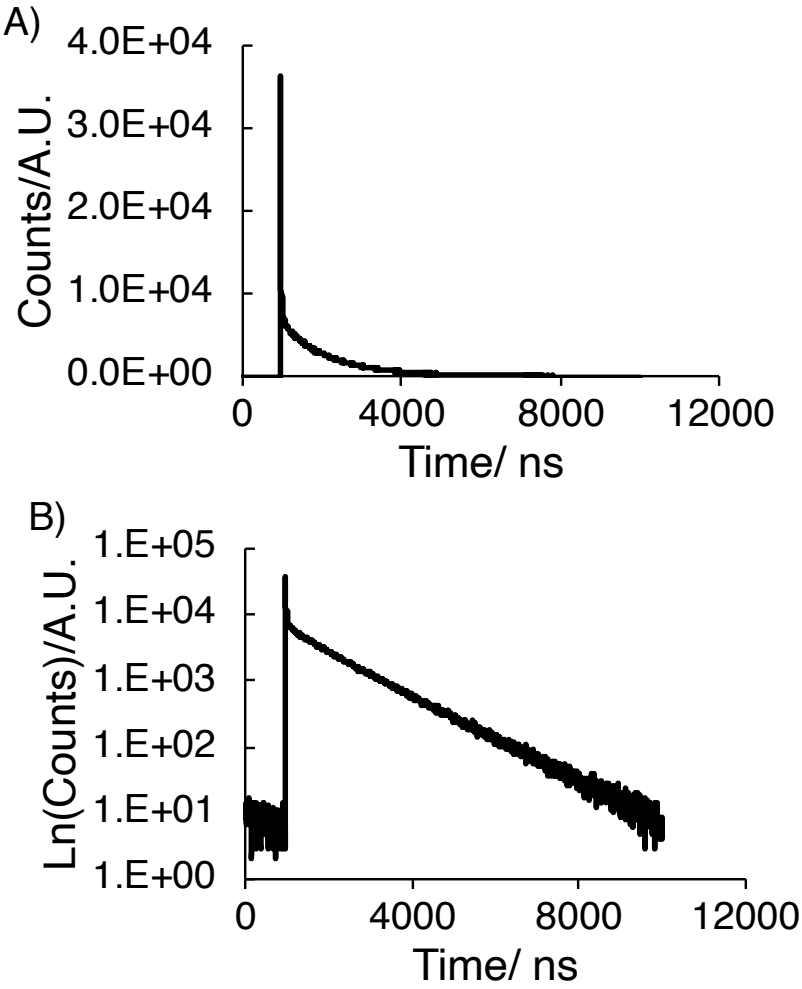

Figure 6.3 A) A linear plot of the phosphorescent, excited state decay of PtCNNH (DMSO, λ_{em} 505 nm, λ_{ex} 405 nm). B) A) expressed as a logarithmic plot.

Firstly, the 505 nm excited state was populated by excitation at 405 nm and the decay then monitored by the detection of emitted photons against time. By observation, the time-decay curve displayed two separate decaying components. This comprised firstly of a very short lived, high intensity emission at 13.43 ns followed by a longer-lived decay with a duration of 1.6 μs. The very short-lived component was likely produced due to scattering of incidence light and can therefore be taken away from the decay as a whole. The second, longer decay component was indicative of a triplet excited state, existing in the realm of microseconds and hence phosphorescent as opposed to fluorescent, similar to other Pt(II) compounds (Baggaley, Weinstein et al., 2012, Whittle, Weinstein et al., 2001, Wu, Zhao et al., 2013). The phosphorescence arose due to a transition from an electronic triplet

excited state to an electronic singlet ground state. Selection rules dictate that triplet-to-singlet transitions are forbidden, which causes stabilisation of the excited state, allowing for longer decay lifetimes compared to singlet-to-singlet emissions, which are spin allowed and occur on the nanosecond timescale. The large difference in energy between absorption and emission maxima, and the microsecond lifetime of the excited state confirm the triplet nature of the emissive excited state in PtCNNH.

Excited state dynamics are some of the most important factors for explaining PDT activity through the capacity to generate singlet oxygen. This would be facilitated through energy transfer from the MLCT triplet excited state to ground state oxygen. The detection of a time-resolved, near infra-red, radiative decay of $^1O_2$ upon the irradiation of a solution of PtCNNH in acetonitrile evidenced PtCNNH's ability to generate such (Figure 6.4). The singlet oxygen yield was obtained by measuring and comparing the initial amplitude of the $^1O_2$ decay against that generated by perinapthenone, a well-known singlet oxygen generator, under identical conditions. PtCNNH's $^1O_2$ yield was measured to be 70% compared to that of perinapthenone. This provided a high degree of promise for PDT activity due to fulfilling the criteria of producing high levels of singlet oxygen.

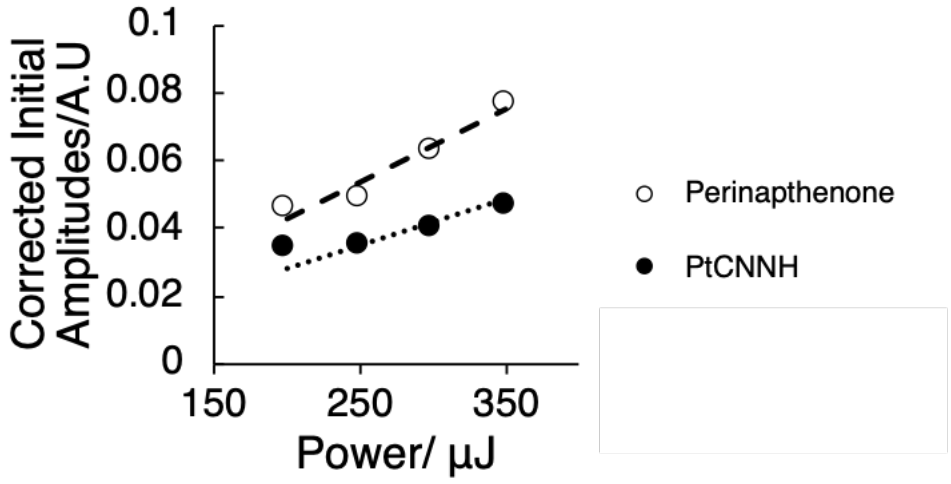

Figure 6.4 Measured initial amplitudes of the singlet oxygen decay signal (λ_{em} 1275 nm) of PtCNNH and the reference, perinapthenone, upon excitation at 355 nm at varying powers (QSW, Nd:YAG, 3rd harmonic).

6.2 – Biological Studies on PtCNNH

6.2.1 – Cellular Uptake of PtCNNH

Before determining the potential PDT activity of PtCNNH it was important to check that it was uptaken by cells in addition to any overt intracellular location(s). Preliminary experiments with low and high PtCNNH doses were performed whereby low doses failed to be sufficiently luminescent and high doses completely killed cells (data not shown). Following this a variety of different cancer cell lines, were incubated with 10 μM PtCNNH. Cells of epithelial (EJ and HeLa), mesenchymal (U2OS) and neural (Shep1) origins were chosen to observe whether any cell line dependent differences in uptake and/or preliminary location existed. All cell lines took up the complex, with cytoplasmic staining being seen (Figure 6.5). By visual inspection, there appeared to be agreement in the intracellular localisation and the intensity of the luminescence pattern in all 4 cell lines chosen. In addition, PtCNNH localised to the cell cytoplasm which is unusual for Pt(II) compounds which typically bind to chromatin in the cell nucleus (Baggaley, Weinstein et al., 2012, Bednarski, Grünert et al., 2006, Hall, Alderden et al., 2006, Hall, Dillon et al., 2003).

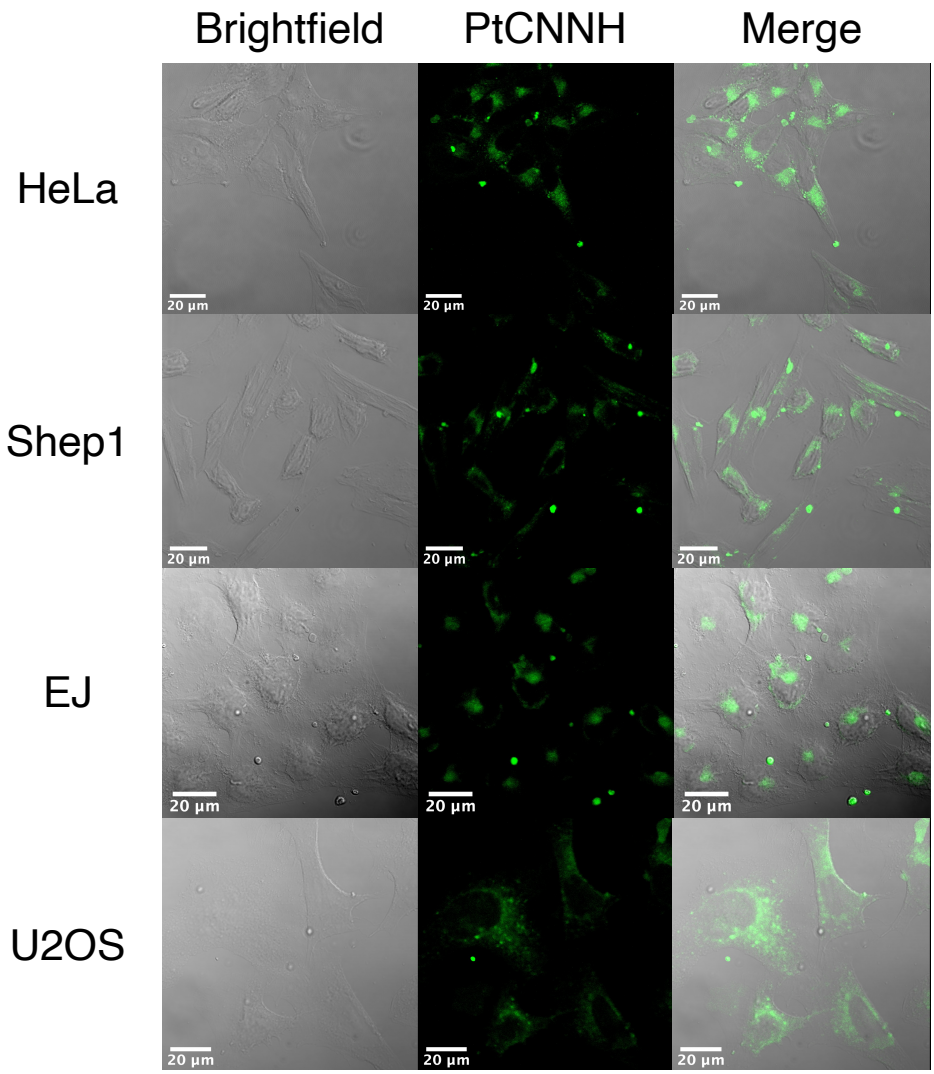

Figure 6.5 Multiphoton images (λ_{ex} 350 nm, λ_{em} 700 nm) of PtCNNH (10 µM, 2 hours) in various cell lines.

6.2.2 – Dark and Light Toxicity of PtCNNH

Having observed that PtCNNH entered cells with a similar agreement in uptake intensity and localisation in all cell lines, a more careful analysis of cell killing was undertaken (Figure 6.6).

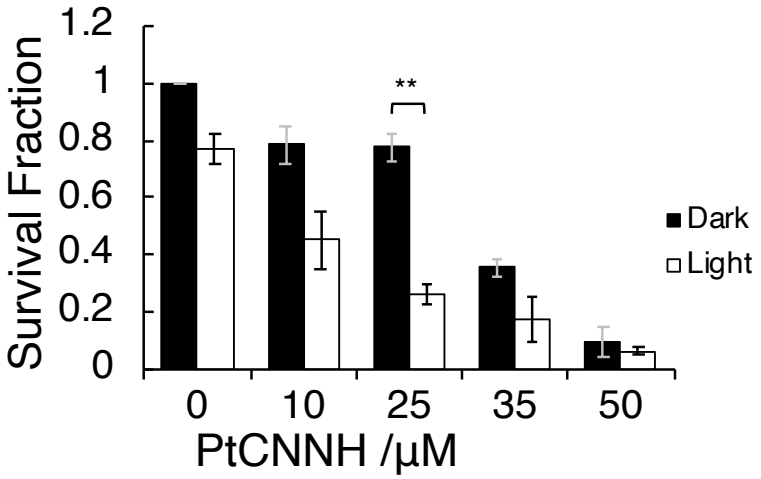

*Figure 6.6 The survival fraction of EJ cells after 2 hours of incubation in the dark (bold, top; black, bottom) and after 3 minutes of irradiation (405 nm, 20 mWcm^{-2}) (dash, top; white, bottom). Dark toxicity = 3, light n = 3. Mean and SEM are shown. ** = $p < 0.01$*

EJ cells (bladder epithelial carcinoma) were either exposed to vehicle control (DMSO) or increasing doses of PtCNNH and incubated for 2 hours prior to exposure to 405 nm light followed by re-plating for clonogenic survival assays (light toxicity). Alternatively, cells were left unirradiated and allowed to form colonies after PtCNNH exposure (dark toxicity). A drug incubation time of 2 hrs allowed for sufficient uptake and any potential intracellular localisations to occur before subsequent irradiation to produce any singlet oxygen. In both light and dark conditions, cell survival was reduced in a dose dependent fashion between 10 μM and 50 μM PtCNNH. The calculated LD_{50} (Dark) was 31.8 μM while the LD_{50}(Light) was 7.7 μM. By combining the dark and light LD_{50}'s, a relatively low PI value of 4.1 was determined with an observed therapeutic window at 25 μM. At this dose there was low dark toxicity with relatively high phototoxicity. As the PtCNNH dose increased above 25 μM, greater dark toxicity occurred resulting in a convergence with phototoxicity at 50 μM. PDT effects at 25 μM were calculated as being statistically significant in comparison to light and dark conditions but were insignificant at other tested doses. This shows that

PtCNNH's capacity to serve as a sufficient PDT agent would be limited to a narrow dose window.

6.3 – Discussion

6.3.1 – PtCNNH as a PS

PtCNNH possessed suitable photophysical properties for a PDT agent i.e. a blue light absorbing MLCT band, an accessible triplet excited state and a high yield of singlet oxygen generation. However, upon cellular exposure, PtCNNH displayed toxicity without light irradiation. A small increase in phototoxicity at 405 nm was observed which produced an LD_{50}(light) of 7.7 μM with a PI value of 4.1 which is relatively small in comparison to current literature researched Pt(II) PDT agents (Ramu, Gautam et al., 2018, Ramu, Gautam et al., 2019, Zhong, Zhang et al., 2019). As well as a low PI, there was a small therapeutic window such that a statistical difference in light and dark toxicity only occurred at 25 μM. Below 25 μM, light toxicity was low, whereas after 25 μM the dark toxicity increased drastically. This small window could be problematic when translated to the clinic because there would be little flexibility in the effective dose – meaning that the risks of unwanted toxicity would be high.

The reason why PtCNNH had comparatively low PDT activity whilst generating a large singlet oxygen yield (70%) is unknown but could be attributed to pharmacodynamics. Even though PtCNNH was uptaken by cells, it could be that the intracellular dose remained low. An applied dosage of 25 μM could be at the uptake saturation limit at 2 hours and hence the intracellular concentration would be fixed upon increasing the applied dosage. However, this seemed unlikely as dark toxicity increased when applied dosage was increased rather than plateauing. PtCNNH's pharmacokinetic properties and mechanisms could also explain low PDT effects. The singlet oxygen generation was measured to be high under dissolution in acetonitrile at 355 nm excitation. This is not an accurate representation of the cellular environment that PtCNNH would be subjected to. A biological environment is an aqueous system with a high concentration of drug-interacting biomolecules. This could lead to excited state quenching through interactions with biomolecules such as

proteins, reducing any singlet oxygen production. Self-quenching between two or more PtCNNH molecules could also have occurred through molecular clustering in an aqueous environment. This can be particularly problematic for hydrophobic metal complexes, like PtCNNH, which contain intermolecular interactive moieties such as NH (Li, Tong et al., 2016, Mauro, Aliprandi et al., 2014). Furthermore, any cellular chemical reactions could change PtCNNH's structure which can alter excited state dynamics leading to the loss of singlet oxygen generation. However, the retention of PtCNNH luminescence was measured after cellular uptake which suggested that excited state dynamics are maintained.

6.3.2 – PtCNNH as a Potential Imaging Agent

Although PtCNNH's dark toxicity was a disadvantage for PDT, the window for application for cell imaging is much less narrow. As seen in Figure 6.5, PtCNNH was measurably phosphorescent at 10 μM with little dark toxicity seen at this dose. Through microscopy, PtCNNH was found to localise to a non-nuclear region in a variety of cell lines. This is somewhat unusual for platinum (II) complexes which are known to adhere to DNA and chromatin and hence localise to the nucleus (Baggaley, Weinstein et al., 2012, Bednarski, Grünert et al., 2006, Hall, Alderden et al., 2006, Hall, Dillon et al., 2003). Given that this isn't the case for PtCNNH, the complex must either have a strong affinity for cytoplasmic components or be impermeable to the nuclear membrane. PtCNNH contains an NH moiety which has the capability to hydrogen bond to biomolecules, which could prevent passive nuclear membrane transport via the hydrophobic effect. In terms of localisation, PorphyrinPlus, as well as a similar compound, PtCNNC (see Appendix 6), co-localised with a fluorescent mitochondrial probe (Bryant/Weinstein Group, *unpublished work*). The phosphorescence pattern of PtCNNH was visually cytoplasmic and dispersed similar to PorphyrinPlus and hence may also be mitochondrial. However, this hypothesis would need to be validated through a co-localisation experiment before any conclusions could be made. Therefore, PtCNNH possessed the desired properties for cellular imaging; being phosphorescently active to a large region of the cell's cytoplasm at a dose that was minimally toxic. There

are, however, a large selection of Pt (II) imaging complexes within the literature reducing the necessity for such a probe (Baggaley, Weinstein et al., 2012, Banerjee, Capper et al., 2019, Gao, Liu et al., 2009, Wu, Wong et al., 2009).

6.3.3 – PtCNNH as a Comparison to PorphyrinPlus

PtCNNH was investigated with the aim of creating a related, but simpler to synthesise complex to the previously investigated PorphyrinPlus. However, PtCNNH was measured to have a low PI of 4.1, which is majorly diminished in comparison to PorphyrinPlus (PI was > 500). Therefore, the impressive PDT activity of PorphyrinPlus was reduced 100-fold upon the loss of the organometalloporphyrin component. Both compounds possessed similar singlet oxygen yields, 70 % for PtCNNH and 83 % for PorphyrinPlus, so why was there such a marked difference in PI? The largest difference between the two complexes was in their dark toxicities. Upon the removal of the organometalloporphyrin component, a greater than 15-fold increase in dark toxicity was observed (PtCNNH LD_{50}(Dark) 31.8 μM vs PorphyrinPlus's LD_{50}(Dark) > 500 μM). The light toxicities were also different with PtCNNH having an LD_{50}(Light) of 7.7 μM and PorphyrinPlus an LD_{50}(Light) of 1 μM but the magnitude was not as great. The reasons as to why there are drastic toxicity differences between PtCNNH and PorphyrinPlus are discussed below. Firstly, the acetylide bridge between the porphyrin and platinum components was removed and substituted with a Cl^- ligand. The introduction of a chloride group is known to promote covalent bonding to biomolecules through Cl^- loss and nucleophilic substitution, a famous example being cis-platin amongst others (Vezzu, Lu et al., 2014, Wong and Giandomenico, 1999, Zwelling and Kohn, 1979). PtCNNH could have sufficient lability to covalently alter cellular entities such as proteins, organelles and membranes which contain nucleophilic residues, inducing high levels of dark toxicity and potentially quenching ROS production (as discussed above). Secondly, an NH group introduces a hydrogen bonding site, being both an acceptor and a donor. Strong non-covalent interactions could therefore form between organelles and/or biomolecules with PtCNNH, introducing toxicity and/or quenching. PtCNNH

can also be compared to a structurally similar Pt(II) compound, PtCNNC (*Bryant/Weinstein Group, unpublished work)*(Figure 6.7).

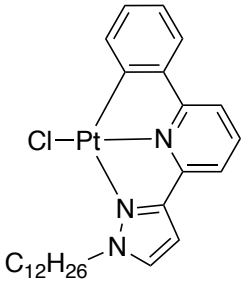

Figure 6.7 PtCNNC, a previously experimented compound and a partial fragment of PorphyrinPlus (Bryant/Weinstein, unpublished work)

PtCNNC (also a partial fragment of PorphyrinPlus) was found to have an LD_{50}(Dark) of 70 μM and LD_{50}(Light) of ~ 10 μM. This produced a PI value of ~ 7, which is closer to the PI of PtCNNH (4.1) than PorphyrinPlus (> 500). PtCNNC also possessed a chloride ligand and as such the dark toxicity increased dramatically when compared to PorphyrinPlus, similar to PtCNNH.

In addition to high dark toxicity, PtCNNH is inferior to PorphyrinPlus for clinical applications due to photophysical and solubility differences. PorphyrinPlus's most strongly absorbing visible light maxima was in the region of 400 – 475 nm, with smaller bands at 560 nm and 600 nm. These excitations are centred on the porphyrin π system, with the former assigned as a Soret or B band ($S_0 \rightarrow S_2$) whilst the latter two are Q bands ($S_0 \rightarrow S_1$)(Karolczak, Kowalska et al., 2004). The PDT activity measured for PorphyrinPlus involved photoactivation at 455 nm, within the Soret band region. PtCNNH displayed PDT effects, through 405 nm photoactivation of its MLCT. Soret bands, which involve p-orbitals, are more highly absorbing than MLCTs, and have molar absorptivity coefficients on the order of 5×10^5 $M^{-1}cm^{-1}$ (Karolczak, Kowalska et al., 2004, Rahman and Harmon, 2006). Therefore, for PorphyrinPlus, lower irradiation powers could be used as opposed to PtCNNH which relies on the lesser absorbing MLCT photoactivation. PorphyrinPlus also has Q bands at ~ 560 nm and ~ 600 nm, in a region of higher tissue penetration. Although PDT of PorphyrinPlus through its Q bands has not been measured, there are similar

porphyrin compounds in the literature that have (Babu, Soy et al., 2020, Deda, Uchoa et al., 2009, Pavani, Uchoa et al., 2009). This could present an opportunity for more highly penetrating PDT compared to PtCNNH which does not have one-photon absorptions above ~ 475 nm. PorphyrinPlus is also cationic and can be administered as an aqueous solution. PtCNNH on the other hand is neutral, poorly water soluble and exists as a solution in DMSO. This would impose a limit on the maximum dose of PtCNNH due to DMSO toxicity effects. However, the problems previously discussed around porphyrin-based PDT should not be forgotten. This generally includes poor tissue penetration, poor clearance times, a propensity to photobleaching and poor water solubility (da Silveira, Vieceli et al., 2020, Finlay, Conover et al., 2001, O'Connor, Gallagher et al., 2009).

6.4 – Conclusions

PtCNNH was comparatively investigated against a parent compound, PorphyrinPlus. PorphyrinPlus was previously found to have high PDT activity but was disadvantaged by a complicated synthesis route, typical of asymmetric porphyrins. PtCNNH was a synthetically simpler alternative PS based on PorphyrinPlus if PDT activity was preserved. In terms of photophysics, PtCNNH's lowest energy visible light absorption was in the region of 400 – 450 nm, the same as PorphyrinPlus's Soret band. However, PorphyrinPlus has lesser absorbing Q bands at 560 nm and 600 nm, potentially allowing for an increase in tissue penetration if excited at these wavelengths. PtCNNH was found to generate singlet oxygen (70 %), similar to PorphyrinPlus (83 %), providing some promise for a retention of the two compound's properties. However, the PDT activities between the two were drastically different with PtCNNH having a much smaller PI (4.1) compared to PorphyrinPlus (> 500). The organometalloporphyrin fragment is therefore an essential and integral part of PorphyrinPlus's PDT activity and is subsequently likely centred on the structure of the porphyrin fragment rather than the Pt. In conclusion, synthetic simplification of PorphyrinPlus for PDT via PtCNNH was not possible.

What is left unanswered is the role of the platinum component in PorphyrinPlus. PorphyrinPlus contains an acetylide bridge allowing for electron movement from one

fragment to the other upon photoactivation which could combine the absorbing properties of the porphyrin with the triplet excited state dynamics of the platinum upon charge transfer. Therefore, it is possible that each component alone is only a weak PS, but combined they become powerful. To test this, the organometallo-porphyrin fragment would have to be re-analysed alone providing a further mechanistic understanding and some synthetic simplicity.

7. Summary

7.2 – Have The Aims Been Met?

This investigation has developed Ir(III) and Pt(II) complexes for their use as PS to facilitate PDT cancer treatment. This was largely through building on previous published work within the group, which identified two transition metal PS, namely IrNew and PorphyrinPlus (Appendix 5)(Appendix 6). Through a structural re-analysis of these compounds, changes were implemented to alter key components, such as ligand exchange and/or structural fragmentation to improve PDT effects. This was analysed through the scrutiny of direct PDT properties e.g., improving the phototoxicity, $^1O_2$ generation or through the measurement of improved indirect properties i.e., PS red-shift, water solubility and cellular uptake. Additionally, UCNPs were synthesised and investigated for their ability to perform photon upconversion which could hence theoretically permit NIR PDT via compound conjugation.

7.2.1 – Development of IrNew

IrNew was structurally altered through a series of separate ligand exchanges to identify each ligand's specific role in generating IrNew's PDT activity. Subsequently, the identification to which of these sites could be altered without drastically effecting or diminishing the overall PDT ability was made. The two ligands contained in the structure of IrNew, the ancillary CN bearing ligand, 2 - phenyl pyridine (PPy) and the NN bearing ligand, bis-benzimidazole (Benz) were exchanged either solely or in tandem. Chapter 3 described the effects of exchanging the ancillary ligands PPy for 2 - thiophenyl pyridine, THPy, whilst retaining Benz. This was hypothesised to alter the HOMO-LUMO energy gap responsible for the complex's PDT activity through modulation of the crystal field splitting energy and hence Ir(III) d orbital energy. Upon its synthesis, IrTHPyBenz was re-investigated for any PDT enhancements which concluded a retention to PDT potency, PI values > 100 – 378 (IrTHPyBenz) vs. > 238 – 555 (IrNew)(McKenzie, Sazanovich et al., 2017). In addition, PDT effects were successfully translated into more clinically relevant 3D *in vitro* spheroid models, previously untested for IrNew. Most importantly, the inclusion of a S atom in the ancillary ligand caused a complex absorption red shift of 20 nm compared to IrNew,

as intended by the complex's design (Mbambisa, Tau et al., 2007, Pandian, Reddy et al., 1990). This permitted blue light PDT (455 nm) which elicited phototoxicity in 2D and 3D cultured C8161 melanoma cells whereupon IrNew could not. Chapter 5 then investigated the role of Benz. This was tested through its exchange both with and without concurrent ancillary ligand substitution (PPy with THPy) to generate two compounds, IrPPyMes and IrTHPyMes. This was hypothesised to directly alter the HOMO-LUMO energy gap by altering the energy of the HOMO which is likely centred on Benz given its uncharged nature (Dedeian, Shi et al., 2005, Gu, Fei et al., 2008). In Benz's place, a more electron-accepting, bulky and planar ligand, Mes, was inserted which was simultaneously hypothesised to intercalate with DNA and hence increase phototoxicity. Upon complex re-evaluation, key PDT effects were altered which included the loss of $^1O_2$ generation, diminishment of the PI, a loss of emission and substantial cytotoxic effects in both Mes compounds. Therefore, the loss of Benz was concluded to be critical in rationalising IrNew's PDT activity and was subsequently highlighted that no drastic future alterations should be made at this locus (Chapter 5). In terms of other Ir(III) compounds in the literature, IrTHPyBenz presents superior as a PS in 10 out of the 12 PS presented in Appendix 1. This is largely due to the combination of both powerful phototoxic effects alongside the lack of dark toxicity up to 200 μM. Therefore, IrTHPyBenz was superior to both IrNew and to a range of Ir(III) PS in the literature ascribed to both potent PDT activity upon a more red-shifted absorption.

7.2.2 – Future Designs for Further IrNew Improvements

Within Chapters 3 and 5, two important findings were described; firstly, IrNew's PDT activity was determined by Benz and secondly, the ancillary ligand presents a target site for any such future improvements without sacrificing overall PDT potency. Therefore, in future structural designs, modifications made to the ancillary ligands present ideal candidates for improvements. Further inclusion of red-light absorbing moieties, conjugation of organelle targeting molecules and/or charged residues to improve solubility are options which could be implemented in compound design. Specific conjugations have been detailed which include inclusion of the triphenyl

phosphonium ligand, peptides (mitochondrial targeting sequence) and cationic rhodamine dyes (Lu, Bruno et al., 2016, Murphy, 1997, Sun, Du et al., 2020). Due to diminished PDT effects upon Mes substitution, small modifications to the Benz ligand should be made with careful and concurrent testing for the retention of $^1O_2$ generation. Given that the HOMO-LUMO gap which produces the PDT active MLCT is likely based on d orbitals of Ir(III) and p orbitals of Benz, any such electronic alterations to these sites could powerfully dictate a potential complex red-shift in absorption and hence improve overall PS tissue penetration.

7.2.3 – Improvements to PorphyrinPlus

PorphyrinPlus presented itself as a powerful PS agent which incorporated both a zinc (II) porphyrin fragment linked to a Pt(II) fragment. Despite powerful PDT activity, the compound suffered from complexity in its synthetic design which would hinder its clinical translation. Therefore, the Pt(II) fragment was isolated and treated as a separate PS entity, PtCNNH. This complex was then re-analysed for retainment or improvement to PDT activity in comparison to its parent complex. Despite a retention in cellular uptake, $^1O_2$ generation and some phototoxicity, the compound proved largely inferior when compared to PorphyrinPlus, PI 4.1 vs > 500 (Porphyrin Plus). This was concluded by favourable PDT properties potentially arising due to the porphyrin fragment rather than the Pt fragment.

7.2.4 – Future Development for PorphyrinPlus

PorphyrinPlus's PDT activity was concluded to be largely due to the zinc (II) porphyrin fragment (or a combination of the two) rather than the Pt(II) fragment alone. Therefore, alternative structural simplifications could be implemented through the isolation of the porphyrin fragment. Upon the removal of the unsaturated alkyne bridge, the porphyrin would become symmetrical which is synthetically simpler and less wasteful as the number of isomeric side products would be reduced throughout its synthesis. Through the investigation of the porphyrin fragment, the role of the alkyne bridge can also be ascertained. Given the unsaturated nature of the bridge, electron transfer could be occurring between the Pt(II) and the porphyrin fragment

which would henceforth be removed if the bridge was lost. Such an interaction, whereby electron transfer from the transition metal to a conjugated 'antenna' BODIPY dye light harvester, attached via acetylide bridges, have been validated and hypothesised to elicit PDT activity (Zhao, Hou et al., 2021).

7.2.5 – UCNP as NIR PDT Vehicles

The lack of NIR absorbing PS plagues both PDT development as well as specifically with IrNew. Therefore, the ability to circumvent this through photoactivation in the optimum tissue penetrating light window (800 – 1000 nm) could open treatment for tumours which lie below 3 mm of the skin. Photon upconverting nanomaterials were presented as a solution to this. The synthesis of upconverting lanthanide nanoparticles was performed with suitably photon upconverting batches being subsequently modified for their biological application and PS coupling. These vessels (coupled to IrTHPyBenz) were then scrutinised for their ability to accomplish NIR PDT through 980 nm photon absorption – photon upconversion – PS energy transfer – $^1O_2$ generation – cell death. Suitably, UCNPs were successfully synthesised which emitted within an overlap with IrTHPyBenz's absorption after 980 nm irradiation, as per the design aim. These UCNPs were subsequently coated and dispersed in aqueous media, size validated by DLS and visualised by TEM. UCNPs were then applied to cells which measured minimal dark toxic effects and then coupled with IrTHPyBenz. However, when applied to cells and irradiated at 980 nm, little phototoxicity was exhibited. UCNPs therefore provide a powerful tool in achieving NIR PDT due to being non-toxic by themselves, can suitably bind PS and emit within a region of PS photoactivation overlap.

7.2.6 – The Future for UCNP Mediated NIR PDT

UCNPs coupled with a suitable PS presents a plausible opportunity to achieve NIR PDT, a problem which greatly effects general PDT treatment with all PS (Gnanasammandhan, Idris et al., 2016). Within this thesis, UCNPs were synthesised and scrutinised for their PS activating photon upconversion ability and then coupled to a potent transition metal PS, IrTHPyBenz. Despite the lack of NIR PDT, possible

improvements routes were discussed which centred on boosting photon upconversion efficiency (Hazra, Ullah et al., 2018, Yi and Chow, 2007). This was rationalised by the upconversion efficiency likely being too low to sufficiently photoactivate IrTHPyBenz and hence create lethality. However, given the recent advances in improving upconversion efficiency through the inclusion of dye sensitisers and additional dopants, the power for these vehicles to deliver PS coupled NIR PDT cannot be ignored (Gnanasammandhan, Idris et al., 2016, Kandoth, Barman et al., 2021, Sabri, Pawelek et al., 2018). Therefore, the path for future development for these materials, as well as coupling to transition metal complexes has been paved.

8. References

Achilli, T.-M., et al. (2014). Multilayer spheroids to quantify drug uptake and diffusion in 3D. *Molecular pharmaceutics* 11(7) 2071-2081.

Aebischer, A., et al. (2006). Structural and Spectroscopic Characterization of Active Sites in a Family of Light-Emitting Sodium Lanthanide Tetrafluorides. *Angewandte Chemie International Edition* 45(17) 2802-2806.

Agalakova, N. I. and G. P. Gusev (2012). Molecular mechanisms of cytotoxicity and apoptosis induced by inorganic fluoride. *International Scholarly Research Notices* 2012.

Alexiades-Armenakas, M. (2006). Laser-mediated photodynamic therapy. *Clinics in dermatology* 24(1) 16-25.

Alkahtani, M., et al. (2021). Engineering Red-Enhanced and Biocompatible Upconversion Nanoparticles. *Nanomaterials* 11(2) 284.

Allison, R. R., et al. (2004). Photosensitizers in clinical PDT. *Photodiagnosis and photodynamic therapy* 1(1) 27-42.

Appelqvist, H., et al. (2013). The lysosome: from waste bag to potential therapeutic target. *Journal of Molecular Cell Biology* 5(4) 214-226.

Ashfaq, M., et al. (2014). DNA binding mode of transition metal complexes, a relationship to tumor cell toxicity. *Current medicinal chemistry* 21(26) 3081-3094.

Asin-Cayuela, J., et al. (2004). Fine-tuning the hydrophobicity of a mitochondria-targeted antioxidant. *FEBS letters* 571(1-3) 9-16.

Auzel, F. (2004). Upconversion and anti-stokes processes with f and d ions in solids. *Chemical reviews* 104(1) 139-174.

Babilas, P., et al. (2010). Photodynamic therapy in dermatology: state-of-the-art. *Photodermatology, photoimmunology & photomedicine* 26(3) 118-132.

Babu, B., et al. (2021). Thien-2-yl substituted chlorins as photosensitizers for photodynamic therapy and photodynamic antimicrobial chemotherapy. *Dyes and Pigments* 185 108886.

Babu, B., et al. (2020). Non-aggregated lipophilic water-soluble tin porphyrins as photosensitizers for photodynamic therapy and photodynamic antimicrobial chemotherapy. *New Journal of Chemistry* 44(26) 11006-11012.

Bader, M., et al. (2013). Photodynamic therapy of bladder cancer–a phase I study using hexaminolevulinate (HAL). Urologic Oncology: Seminars and Original Investigations, Elsevier.

Baggaley, E., J. A. Weinstein and J. G. Williams (2012). Lighting the way to see inside the live cell with luminescent transition metal complexes. *Coordination Chemistry Reviews* 256(15-16) 1762-1785.

Banerjee, S., et al. (2019). Dual-action platinum (II) Schiff base complexes: Photocytotoxicity and cellular imaging. *Polyhedron* 172 157-166.

Baran, T. M. (2018). Photofrin® photodynamic therapy with intratumor photosensitizer injection provides similar tumor response while reducing systemic skin photosensitivity: Pilot murine study. *Lasers in surgery and medicine* 50(5) 476-482.

Baryshnikov, G., B. Minaev and H. Ågren (2017). Theory and calculation of the phosphorescence phenomenon. *Chemical reviews* 117(9) 6500-6537.

Baskaran, R., J. Lee and S.-G. Yang (2018). Clinical development of photodynamic agents and therapeutic applications. *Biomaterials research* 22(1) 1-8.
Bayr, H. (2005). Reactive oxygen species. *Critical care medicine* 33(12) S498-S501.
Bednarski, P. J., et al. (2006). Light-activated destruction of cancer cell nuclei by platinum diazide complexes. *Chemistry & biology* 13(1) 61-67.
Bedoya, M., et al. (2006). Humidity sensing with a luminescent Ru (II) complex and phase-sensitive detection. *Sensors and Actuators B: Chemical* 113(2) 573-581.
Beljonne, D., et al. (2001). Spin– orbit coupling and intersystem crossing in conjugated polymers: a configuration interaction description. *The Journal of Physical Chemistry A* 105(15) 3899-3907.
Bellnier, D. A. and T. J. Dougherty (1996). A preliminary pharmacokinetic study of intravenous Photofrin® in patients. *Journal of clinical laser medicine & surgery* 14(5) 311-314.
Bellnier, D. A., et al. (1989). Distribution and elimination of Photofrin II in mice. *Photochemistry and photobiology* 50(2) 221-228.
Bennewith, K. L. and S. Dedhar (2011). Targeting hypoxic tumour cells to overcome metastasis. *BMC cancer* 11(1) 1-6.
Bergamo, A., et al. (1999). In vitro cell cycle arrest, in vivo action on solid metastasizing tumors, and host toxicity of the antimetastatic drug NAMI-A and cisplatin. *Journal of Pharmacology and Experimental Therapeutics* 289(1) 559-564.
Bi, X.-D., et al. (2020). Cyclometalated Iridium (III) Complexes as High-Sensitivity Two-Photon Excited Mitochondria Dyes and Near-Infrared Photodynamic Therapy Agents. *Inorganic Chemistry* 59(20) 14920-14931.
Bonnet, S. (2018). Why develop photoactivated chemotherapy? *Dalton Transactions* 47(31) 10330-10343.
Bown, S., et al. (1986). Photodynamic therapy with porphyrin and phthalocyanine sensitisation: quantitative studies in normal rat liver. *British journal of cancer* 54(1) 43-52.
Boyer, J.-C., et al. (2006). Synthesis of colloidal upconverting NaYF4 nanocrystals doped with Er3+, Yb3+ and Tm3+, Yb3+ via thermal decomposition of lanthanide trifluoroacetate precursors. *Journal of the American Chemical Society* 128(23) 7444-7445.
Brahimi-Horn, M. C., J. Chiche and J. Pouysségur (2007). Hypoxia and cancer. *Journal of molecular medicine* 85(12) 1301-1307.
Brattain, M. G., et al. (1981). Heterogeneity of malignant cells from a human colonic carcinoma. *Cancer research* 41(5) 1751-1756.
Bredesen, D. E., R. V. Rao and P. Mehlen (2006). Cell death in the nervous system. *Nature* 443(7113) 796-802.
Bressenot, A., et al. (2009). Assessment of apoptosis by immunohistochemistry to active caspase-3, active caspase-7, or cleaved PARP in monolayer cells and spheroid and subcutaneous xenografts of human carcinoma. *Journal of Histochemistry & Cytochemistry* 57(4) 289-300.
Burma, S., et al. (2001). ATM phosphorylates histone H2AX in response to DNA double-strand breaks. *Journal of Biological Chemistry* 276(45) 42462-42467.
Buytaert, E., et al. (2006). Role of endoplasmic reticulum depletion and multidomain proapoptotic BAX and BAK proteins in shaping cell death after hypericin-mediated photodynamic therapy. *The FASEB journal* 20(6) 756-758.

Byrne, C., L. Marshallsay and A. Ward (1990). The composition of Photofrin II. *Journal of Photochemistry and Photobiology B: Biology* 6(1-2) 13-27.
Cai, J., J. Yang and D. Jones (1998). Mitochondrial control of apoptosis: the role of cytochrome c. *Biochimica et Biophysica Acta (BBA)-Bioenergetics* 1366(1-2) 139-149.
Calloway, D. (1997). Beer-lambert law. *Journal of Chemical Education* 74(7) 744.
Candide, C., et al. (1986). In vitro interaction of the photoactive anticancer porphyrin derivative photofrin II with low density lipoprotein, and its delivery to cultured human fibroblasts. *FEBS letters* 207(1) 133-138.
Cao, J.-J., et al. (2017). Targeting cancer cell metabolism with mitochondria-immobilized phosphorescent cyclometalated iridium (III) complexes. *Chemical science* 8(1) 631-640.
Cao, J. Y. and S. J. Dixon (2016). Mechanisms of ferroptosis. *Cellular and Molecular Life Sciences* 73(11) 2195-2209.
Casas, A., et al. (1997). Enhancement of aminolevulinic acid based photodynamic therapy by adriamycin. *Cancer letters* 121(1) 105-113.
Caspar, J. V. and T. J. Meyer (1983). Photochemistry of tris (2, 2'-bipyridine) ruthenium (2+) ion (Ru (bpy) 32+). Solvent effects. *Journal of the American Chemical Society* 105(17) 5583-5590.
Castano, A. P., T. N. Demidova and M. R. Hamblin (2004). Mechanisms in photodynamic therapy: part one—photosensitizers, photochemistry and cellular localization. *Photodiagnosis and photodynamic therapy* 1(4) 279-293.
Chamberlain, S., et al. (2020). TLD1433-Mediated photodynamic therapy with an optical surface applicator in the treatment of lung cancer cells in vitro. *Pharmaceuticals* 13(7) 137.
Chapman, J., et al. (1991). Oxygen dependency of tumor cell killing in vitro by light-activated Photofrin II. *Radiation research* 126(1) 73-79.
Chaput, N., et al. (2007). Molecular determinants of immunogenic cell death: surface exposure of calreticulin makes the difference. *Journal of molecular medicine* 85(10) 1069-1076.
Chatterjee, D. K., A. J. Rufaihah and Y. Zhang (2008). Upconversion fluorescence imaging of cells and small animals using lanthanide doped nanocrystals. *Biomaterials* 29(7) 937-943.
Chen, B., et al. (2003). Blood flow dynamics after photodynamic therapy with verteporfin in the RIF-1 tumor. *Radiation research* 160(4) 452-459.
Chen, B., et al. (2006). Tumor vascular permeabilization by vascular-targeting photosensitization: effects, mechanism, and therapeutic implications. *Clinical Cancer Research* 12(3) 917-923.
Chen, B., T. Roskams and P. A. de Witte (2002). Antivascular Tumor Eradication by Hypericin-mediated Photodynamic Therapy¶. *Photochemistry and photobiology* 76(5) 509-513.
Chen, G., et al. (2015). Light upconverting core–shell nanostructures: nanophotonic control for emerging applications. *Chemical Society Reviews* 44(6) 1680-1713.
Chen, H. M., et al. (2005). Successful treatment of oral verrucous hyperplasia and oral leukoplakia with topical 5-aminolevulinic acid-mediated photodynamic therapy. *Lasers in Surgery and Medicine: The Official Journal of the American Society for Laser Medicine and Surgery* 37(2) 114-122.

Chen, J., et al. (2020). A lysosome-targeted ruthenium (II) polypyridyl complex as photodynamic anticancer agent. *Journal of inorganic biochemistry* 210 111132.
Chen, Z., et al. (2021). Can NaYF 4: Yb, Tm nanocrystals with multi-morphologies and various phases be synthesized by solvothermal process. *Journal of Materials Science: Materials in Electronics* 1-14.
Cheng, Y., et al. (2015). Perfluorocarbon nanoparticles enhance reactive oxygen levels and tumour growth inhibition in photodynamic therapy. *Nature communications* 6(1) 1-8.
Cheng, Y., et al. (2008). Dendrimers as drug carriers: applications in different routes of drug administration. *Journal of pharmaceutical sciences* 97(1) 123-143.
Chien, Y. H., et al. (2018). NIR-responsive nanomaterials and their applications; upconversion nanoparticles and carbon dots: a perspective. *Journal of Chemical Technology & Biotechnology* 93(6) 1519-1528.
Chou, P.-T., et al. (2011). Harvesting luminescence via harnessing the photophysical properties of transition metal complexes. *Coordination Chemistry Reviews* 255(21-22) 2653-2665.
Clarke, M. J., F. Zhu and D. R. Frasca (1999). Non-platinum chemotherapeutic metallopharmaceuticals. *Chemical reviews* 99(9) 2511-2534.
Coleman, M. L., et al. (2001). Membrane blebbing during apoptosis results from caspase-mediated activation of ROCK I. *Nature cell biology* 3(4) 339-345.
Coulie, P. G., et al. (1995). A mutated intron sequence codes for an antigenic peptide recognized by cytolytic T lymphocytes on a human melanoma. *Proceedings of the National Academy of Sciences* 92(17) 7976-7980.
Crescenzi, E., et al. (2006). Low doses of cisplatin or gemcitabine plus Photofrin/photodynamic therapy: disjointed cell cycle phase-related activity accounts for synergistic outcome in metastatic non–small cell lung cancer cells (H1299). *Molecular cancer therapeutics* 5(3) 776-785.
da Silveira, C. H., et al. (2020). Investigation of isomeric tetra-cationic porphyrin activity with peripheral [Pd (bpy) Cl]+ units by antimicrobial photodynamic therapy. *Photodiagnosis and Photodynamic Therapy* 31 101920.
Dang, J., et al. (2017). Manipulating tumor hypoxia toward enhanced photodynamic therapy (PDT). *Biomaterials science* 5(8) 1500-1511.
Dave, D., U. Desai and N. Despande (2012). Photodynamic therapy: A view through light. *Journal of Orofacial Research* 82-86.
de Araújo, C. B., et al. (2002). Frequency upconversion in rare-earth doped fluoroindate glasses. *Comptes Rendus Chimie* 5(12) 885-898.
Deda, D. K., et al. (2009). A new micro/nanoencapsulated porphyrin formulation for PDT treatment. *International journal of pharmaceutics* 376(1-2) 76-83.
Dedeian, K., et al. (2005). Photophysical and electrochemical properties of heteroleptic tris-cyclometalated iridium (III) complexes. *Inorganic Chemistry* 44(13) 4445-4447.
Deng, S., et al. (2020). Golgi Apparatus: A Potential Therapeutic Target for Autophagy-Associated Neurological Diseases. *Frontiers in Cell and Developmental Biology* 8 901.
Di, Y.-Q., et al. (2020). Autophagy triggers CTSD (cathepsin D) maturation and localization inside cells to promote apoptosis. *Autophagy* 1-23.

Ding, H., et al. (2011). Photoactivation switch from type II to type I reactions by electron-rich micelles for improved photodynamic therapy of cancer cells under hypoxia. *Journal of controlled release* 156(3) 276-280.
Ding, M., et al. (2012). Flux growth of honeycomb-like β-NaYF4: Yb3+, Er3+/Tm3+ crystals with multicolor upconversion luminescence. *Materials Letters* 86 58-61.
do Reis, S. R. R., et al. (2021). Dual Encapsulated Dacarbazine and Zinc Phthalocyanine Polymeric Nanoparticle for Photodynamic Therapy of Melanoma. *Pharmaceutical Research* 1-12.
Doherty, J. and E. H. Baehrecke (2018). Life, death and autophagy. *Nature cell biology* 20(10) 1110-1117.
Doherty, R. E., et al. (2016). Photodynamic killing of cancer cells by a Platinum(II) complex with cyclometallating ligand.
Dolma, S., et al. (2003). Identification of genotype-selective antitumor agents using synthetic lethal chemical screening in engineered human tumor cells. *Cancer cell* 3(3) 285-296.
Dolmans, D. E., D. Fukumura and R. K. Jain (2003). Photodynamic therapy for cancer. *Nature reviews cancer* 3(5) 380-387.
Dougherty, T., W. Potter and K. Weishaupt (1984). The structure of the active component of hematoporphyrin derivative. *Porphyrins in tumor phototherapy*. Springer. 23-35.
Dougherty, T. J. (1987). Studies on the structure of porphyrins contained in Photofrin® II. *Photochemistry and photobiology* 46(5) 569-573.
Dougherty, T. J., et al. (1978). Photoradiation therapy for the treatment of malignant tumors. *Cancer research* 38(8) 2628-2635.
Drugs, C. o. (1997). Alternative routes of drug administration—advantages and disadvantages (subject review). *Pediatrics* 100(1) 143-152.
Du, J., et al. (2021). Enhanced photodynamic therapy for overcoming tumor hypoxia: From microenvironment regulation to photosensitizer innovation. *Coordination Chemistry Reviews* 427 213604.
Eilenberger, C., et al. (2018). Optimized alamarBlue assay protocol for drug dose-response determination of 3D tumor spheroids. *MethodsX* 5 781-787.
Eliseeva, S. V. and J.-C. G. Bünzli (2010). Lanthanide luminescence for functional materials and bio-sciences. *Chemical Society Reviews* 39(1) 189-227.
Ell, C., et al. (1998). Photodynamic ablation of early cancers of the stomach by means of mTHPC and laser irradiation: preliminary clinical experience. *Gut* 43(3) 345-349.
Fan, K. F., et al. (1997). Photodynamic therapy using mTHPC for malignant disease in the oral cavity. *International journal of cancer* 73(1) 25-32.
Farrer, N. J., L. Salassa and P. J. Sadler (2009). Photoactivated chemotherapy (PACT): the potential of excited-state d-block metals in medicine. *Dalton Transactions*(48) 10690-10701.
Felder, P. S., S. Keller and G. Gasser (2020). Polymetallic Complexes for Applications as Photosensitisers in Anticancer Photodynamic Therapy. *Advanced Therapeutics* 3(1) 1900139.
Figge, F. H., G. S. Weiland and L. O. Manganiello (1948). Cancer detection and therapy. Affinity of neoplastic, embryonic, and traumatized tissues for porphyrins and

metalloporphyrins. *Proceedings of the Society for Experimental Biology and Medicine* 68(3) 640-641.
Finlay, J. C., et al. (2001). Porphyrin Bleaching and PDT-induced Spectral Changes are Irradiance Dependent in ALA-sensitized Normal Rat Skin In Vivo¶. *Photochemistry and photobiology* 73(1) 54-63.
Fitzpatrick, T. B. and M. Pathak (1959). Part IV: Basic Considerations of the Psoralens: Historical Aspects of Methoxsalen and Other Furocoumarins11From the Division of Dermatology, University of Oregon Medical School, Portland, Oregon. *Journal of Investigative Dermatology* 32(2) 229-231.
Foley, N. A., et al. (2009). Ru (II) catalysts supported by hydridotris (pyrazolyl) borate for the hydroarylation of olefins: reaction scope, mechanistic studies, and guides for the development of improved catalysts. *Accounts of chemical research* 42(5) 585-597.
Folkman, J. (1995). Angiogenesis in cancer, vascular, rheumatoid and other disease. *Nature medicine* 1(1) 27-30.
Foroulis, C. N. and J. A. Thorpe (2006). Photodynamic therapy (PDT) in Barrett's esophagus with dysplasia or early cancer. *European journal of cardio-thoracic surgery* 29(1) 30-34.
Freeman, M., et al. (2003). A comparison of photodynamic therapy using topical methyl aminolevulinate (Metvix®) with single cycle cryotherapy in patients with actinic keratosis: a prospective, randomized study. *Journal of dermatological treatment* 14(2) 99-106.
Fuchs, S. M., et al. (2004). Photodynamic therapy (PDT) and waterfiltered infrared A (wIRA) in patients with recalcitrant common hand and foot warts. *German medical science: GMS e-journal* 2.
Galluzzi, L., et al. (2018). Molecular mechanisms of cell death: recommendations of the Nomenclature Committee on Cell Death 2018. *Cell Death & Differentiation* 25(3) 486-541.
Gao, C., et al. (2018). Y2O3 nanoparticles caused bone tissue damage by breaking the intracellular phosphate balance in bone marrow stromal cells. *ACS nano* 13(1) 313-323.
Gao, J., Y.-G. Liu and R. A. Zingaro (2009). Cytotoxic activities, cellular uptake, gene regulation, and optical imaging of novel platinum (II) complexes. *Chemical research in toxicology* 22(10) 1705-1712.
Gao, Y., et al. (2015). Efficacy and safety of topical ALA-PDT in the treatment of EMPD. *Photodiagnosis and photodynamic therapy* 12(1) 92-97.
Garg, A. D., et al. (2012). Hypericin-based photodynamic therapy induces surface exposure of damage-associated molecular patterns like HSP70 and calreticulin. *Cancer Immunology, Immunotherapy* 61(2) 215-221.
Georgakoudi, I., M. G. Nichols and T. H. Foster (1997). The mechanism of Photofrin photobleaching and its consequences for photodynamic dosimetry. *Photochemistry and photobiology* 65(1) 135-144.
Gey, G. (1952). Tissue culture studies of the proliferative capacity of cervical carcinoma and normal epithelium. *Cancer Res.* 12 264-265.
Giard, D. J., et al. (1973). In vitro cultivation of human tumors: establishment of cell lines derived from a series of solid tumors. *Journal of the National Cancer Institute* 51(5) 1417-1423.

Glinton, K., et al. (2019). Synthesis, characterization, and photoluminescent studies of three-coordinate Cu (i)–NHC complexes bearing unsymmetrically-substituted dipyridylamine ligands. *RSC advances* 9(39) 22417-22427.
Gnach, A. and A. Bednarkiewicz (2012). Lanthanide-doped up-converting nanoparticles: Merits and challenges. *Nano Today* 7(6) 532-563.
Gnanasammandhan, M. K., et al. (2016). Near-IR photoactivation using mesoporous silica-coated NaYF4: Yb, Er/Tm upconversion nanoparticles. *Nature protocols* 11(4) 688-713.
Goh, Y., et al. (2018). Cellular uptake efficiency of nanoparticles investigated by three-dimensional imaging. *Physical Chemistry Chemical Physics* 20(16) 11359-11368.
Gold, M. H. and M. P. Goldman (2004). 5-aminolevulinic acid photodynamic therapy: Where we have been and where we are going. *Dermatologic surgery* 30(8) 1077-1084.
Gollnick, S., et al. (2003). Role of cytokines in photodynamic therapy-induced local and systemic inflammation. *British journal of cancer* 88(11) 1772-1779.
Gomer, C. J., et al. (2006). Photodynamic therapy: combined modality approaches targeting the tumor microenvironment. *Lasers in Surgery and Medicine: The Official Journal of the American Society for Laser Medicine and Surgery* 38(5) 516-521.
Gomes-da-Silva, L. C., et al. (2019). Recruitment of LC3 to damaged Golgi apparatus. *Cell Death & Differentiation* 26(8) 1467-1484.
Gomes-da-Silva, L. C., et al. (2018). Photodynamic therapy with redaporfin targets the endoplasmic reticulum and Golgi apparatus. *The EMBO journal* 37(13) e98354.
Griffith, J. S. (1964). *The theory of transition-metal ions*: Cambridge University Press.
Grüner, M. C., et al. (2018). Functionalizing the mesoporous silica shell of upconversion nanoparticles to enhance bacterial targeting and killing via photosensitizer-induced antimicrobial photodynamic therapy. *ACS Applied Bio Materials* 1(4) 1028-1036.
Gu, X., et al. (2008). Theoretical studies of blue-emitting iridium complexes with different ancillary ligands. *The Journal of Physical Chemistry A* 112(36) 8387-8393.
Gualdesi, M., et al. (2021). New poly (acrylamide) nanoparticles in the development of third generation photosensitizers. *Dyes and Pigments* 184 108856.
Gulzar, A., et al. (2017). Upconversion processes: versatile biological applications and biosafety. *Nanoscale* 9(34) 12248-12282.
Guo, S., et al. (2019). Mitochondria-localized iridium (III) complexes with anthraquinone groups as effective photosensitizers for photodynamic therapy under hypoxia. *Science China Chemistry* 62(12) 1639-1648.
Guo, T., et al. (2018). Black phosphorus quantum dots with renal clearance property for efficient photodynamic therapy. *Small* 14(4) 1702815.
Hahn, S. M., et al. (2006). Photofrin uptake in the tumor and normal tissues of patients receiving intraperitoneal photodynamic therapy. *Clinical cancer research* 12(18) 5464-5470.
Hall, M. D., et al. (2006). The fate of platinum (II) and platinum (IV) anti-cancer agents in cancer cells and tumours. *Journal of structural biology* 155(1) 38-44.
Hall, M. D., et al. (2003). The cellular distribution and oxidation state of platinum (II) and platinum (IV) antitumour complexes in cancer cells. *JBIC Journal of Biological Inorganic Chemistry* 8(7) 726-732.

Hall, R. D. and C. F. Chignell (1987). Steady-state near-infrared detection of singlet molecular oxygen: a Stern-Volmer quenching experiment with sodium azide. *Photochemistry and photobiology* 45(4) 459-464.
Hamblin, M. R. and T. Hasan (2004). Photodynamic therapy: a new antimicrobial approach to infectious disease? *Photochemical & Photobiological Sciences* 3(5) 436-450.
Hatse, S., E. De Clercq and J. Balzarini (1999). Role of antimetabolites of purine and pyrimidine nucleotide metabolism in tumor cell differentiation. *Biochemical pharmacology* 58(4) 539-555.
Hayata, Y., et al. (1982). Hematoporphyrin derivative and laser photoradiation in the treatment of lung cancer. *Chest* 81(3) 269-277.
Hayata, Y., et al. (1985). Photodynamic therapy with hematoporphyrin derivative in cancer of the upper gastrointestinal tract. Seminars in surgical oncology, Wiley Online Library.
Hazra, C., et al. (2018). Enhanced NIR-I emission from water-dispersible NIR-II dye-sensitized core/active shell upconverting nanoparticles. *Journal of Materials Chemistry C* 6(17) 4777-4785.
He, L., et al. (2015). Cyclometalated iridium (III) complexes as lysosome-targeted photodynamic anticancer and real-time tracking agents. *Chemical science* 6(10) 5409-5418.
He, Q., et al. (2020). The Golgi Apparatus May Be a Potential Therapeutic Target for Apoptosis-Related Neurological Diseases. *Frontiers in Cell and Developmental Biology* 8 830.
Hearn, J. M., et al. (2013). Organometallic iridium (III) anticancer complexes with new mechanisms of action: NCI-60 screening, mitochondrial targeting, and apoptosis. *ACS chemical biology* 8(6) 1335-1343.
Henderson, B. W. and V. H. Fingar (1987). Relationship of tumor hypoxia and response to photodynamic treatment in an experimental mouse tumor. *Cancer research* 47(12) 3110-3114.
Hersey, P. and X. D. Zhang (2003). Overcoming resistance of cancer cells to apoptosis. *Journal of cellular physiology* 196(1) 9-18.
Higgins, S. L. and K. J. Brewer (2012). Designing Red-Light-Activated Multifunctional Agents for the Photodynamic Therapy. *Angewandte Chemie International Edition* 51(46) 11420-11422.
Hlavacek, A., et al. (2014). Electrophoretic characterization and purification of silica-coated photon-upconverting nanoparticles and their bioconjugates. *ACS applied materials & interfaces* 6(9) 6930-6935.
Ho, C.-L., et al. (2012). A strong two-photon induced phosphorescent Golgi-specific in vitro marker based on a heteroleptic iridium complex. *Chemical Communications* 48(19) 2525-2527.
Homma, T., S. Kobayashi and J. Fujii (2019). Induction of ferroptosis by singlet oxygen generated from naphthalene endoperoxide. *Biochemical and biophysical research communications* 518(3) 519-525.
Hopper, C., C. Niziol and M. Sidhu (2004). The cost-effectiveness of Foscan mediated photodynamic therapy (Foscan-PDT) compared with extensive palliative surgery and palliative chemotherapy for patients with advanced head and neck cancer in the UK. *Oral oncology* 40(4) 372-382.

Horman, S. R., J. To and A. P. Orth (2013). An HTS-compatible 3D colony formation assay to identify tumor-specific chemotherapeutics. *Journal of biomolecular screening* 18(10) 1298-1308.
Hsieh, Y. J., et al. (2003). Subcellular localization of Photofrin® determines the death phenotype of human epidermoid carcinoma A431 cells triggered by photodynamic therapy: when plasma membranes are the main targets. *Journal of cellular physiology* 194(3) 363-375.
Hu, T., et al. (2021a). Recent advances in innovative strategies for enhanced cancer photodynamic therapy. *Theranostics* 11(7) 3278.
Hu, X., et al. (2021b). Synthesis of Sn nanocluster@ carbon dots for photodynamic therapy application. *Chinese Chemical Letters*.
Huang, H., S. Banerjee and P. J. Sadler (2018). Recent advances in the design of targeted iridium (III) photosensitizers for photodynamic therapy. *ChemBioChem* 19(15) 1574-1589.
Huang, H., et al. (2015). Highly Charged Ruthenium(II) Polypyridyl Complexes as Lysosome-Localized Photosensitizers for Two-Photon Photodynamic Therapy. *Angewandte Chemie International Edition* 54(47) 14049-14052.
Huang, L., et al. (2012). Type I and Type II mechanisms of antimicrobial photodynamic therapy: an in vitro study on gram-negative and gram-positive bacteria. *Lasers in surgery and medicine* 44(6) 490-499.
Ichikawa, K., et al. (2004). Antiangiogenic photodynamic therapy (PDT) using Visudyne causes effective suppression of tumor growth. *Cancer letters* 205(1) 39-48.
Ihmels, H., et al. (2019). Structural flexibility versus rigidity of the aromatic unit of DNA ligands: binding of aza-and azoniastilbene derivatives to duplex and quadruplex DNA. *Organic & Biomolecular Chemistry* 17(26) 6404-6413.
Imberti, C., et al. (2020). New designs for phototherapeutic transition metal complexes. *Angewandte Chemie* 132(1) 61-73.
Irving, H. and R. Williams (1953). 637. The stability of transition-metal complexes. *Journal of the Chemical Society (Resumed)* 3192-3210.
Iyer, A. K., et al. (2006). Exploiting the enhanced permeability and retention effect for tumor targeting. *Drug discovery today* 11(17-18) 812-818.
Jackson, S. P. (2002). Sensing and repairing DNA double-strand breaks. *Carcinogenesis* 23(5) 687-696.
James, N. S., et al. (2018). Measurement of cyanine dye photobleaching in photosensitizer cyanine dye conjugates could help in optimizing light dosimetry for improved photodynamic therapy of cancer. *Molecules* 23(8) 1842.
Jeffes, E. (2002). Levulan®: the first approved topical photosensitizer for the treatment of actinic keratosis. *Journal of dermatological treatment* 13(sup1) s19-s23.
Jiang, S., et al. (2021). Formation of protein cross-links by singlet oxygen-mediated disulfide oxidation. *Redox Biology* 101874.
Jiang, X. and X. Wang (2004). Cytochrome C-mediated apoptosis. *Annual review of biochemistry* 73.
Jin, C. S., et al. (2013). Ablation of hypoxic tumors with dose-equivalent photothermal, but not photodynamic, therapy using a nanostructured porphyrin assembly. *ACS nano* 7(3) 2541-2550.
Jori, G., et al. (2006). Photodynamic therapy in the treatment of microbial infections: basic principles and perspective applications. *Lasers in Surgery and Medicine: The*

Official Journal of the American Society for Laser Medicine and Surgery 38(5) 468-481.
Juzeniene, A., Q. Peng and J. Moan (2007). Milestones in the development of photodynamic therapy and fluorescence diagnosis. *Photochemical & Photobiological Sciences* 6(12) 1234-1245.
Jänicke, R. U., et al. (1998). Caspase-3 is required for DNA fragmentation and morphological changes associated with apoptosis. *Journal of Biological Chemistry* 273(16) 9357-9360.
Kagan, V. E., et al. (2017). Oxidized arachidonic and adrenic PEs navigate cells to ferroptosis. *Nature chemical biology* 13(1) 81-90.
Kanaoujiya, R., et al. (2020). Ruthenium based anticancer compounds and their importance. *J. Sci. Res* 64 264-268.
Kandoth, N., et al. (2021). Photoactive Lanthanide-Based Upconverting Nanoclusters for Antimicrobial Applications. *Advanced Functional Materials* 2104480.
Kang, N., et al. (2018). Facile synthesis of upconversion nanoparticles with high purity using lanthanide oleate compounds. *Nanotechnology* 29(7) 075601.
Karolczak, J., et al. (2004). Photophysical studies of porphyrins and metalloporphyrins: accurate measurements of fluorescence spectra and fluorescence quantum yields for Soret band excitation of zinc tetraphenylporphyrin. *The Journal of Physical Chemistry A* 108(21) 4570-4575.
Kelly, J., M. Snell and M. Berenbaum (1975). Photodynamic destruction of human bladder carcinoma. *British journal of cancer* 31(2) 237-244.
Kennedy, J., R. Pottier and D. Pross (1990). Photodynamic therapy with endogenous protoporphyrin: IX: basic principles and present clinical experience. *Journal of Photochemistry and Photobiology B: Biology* 6(1-2) 143-148.
Kessel, D. (2019). Pathways to paraptosis after ER photodamage in OVCAR-5 Cells. *Photochemistry and photobiology* 95(5) 1239-1242.
Kessel, D., et al. (2020). Effects of HPV status on responsiveness to ionizing radiation vs photodynamic therapy in head and neck cancer cell lines. *Photochemistry and photobiology* 96(3) 652-657.
Kessel, D. and Y. Luo (1998). Mitochondrial photodamage and PDT-induced apoptosis. *Journal of Photochemistry and Photobiology B: Biology* 42(2) 89-95.
Kessel, D., et al. (1997). The role of subcellular localization in initiation of apoptosis by photodynamic therapy. *Photochemistry and photobiology* 65(3) 422-426.
Kessel, D. and N. L. Oleinick (2018). Cell death pathways associated with photodynamic therapy: an update. *Photochemistry and photobiology* 94(2) 213-218.
Kessel, D. and J. J. Reiners Jr (2017). Effects of combined lysosomal and mitochondrial photodamage in a non-small-cell lung cancer cell line: the role of paraptosis. *Photochemistry and photobiology* 93(6) 1502-1508.
Khan, A. U. (1976). Singlet molecular oxygen. A new kind of oxygen. *The Journal of Physical Chemistry* 80(20) 2219-2228.
Kim, Y.-N., et al. (2012). Anoikis resistance: an essential prerequisite for tumor metastasis. *International journal of cell biology* 2012.
Ko, A., et al. (2014). Autophagy inhibition radiosensitizes in vitro, yet reduces radioresponses in vivo due to deficient immunogenic signalling. *Cell Death & Differentiation* 21(1) 92-99.

Ko, C. C., et al. (2006). Triplet MLCT Photosensitization of the Ring-Closing Reaction of Diarylethenes by Design and Synthesis of a Photochromic Rhenium (I) Complex of a Diarylethene-Containing 1, 10-Phenanthroline Ligand. *Chemistry–A European Journal* 12(22) 5840-5848.
Kobayashi, W., et al. (2006). Photodynamic therapy with mono-L-aspartyl chlorin e6 can cause necrosis of squamous cell carcinoma of tongue: experimental study on an animal model of nude mouse. *Oral oncology* 42(1) 45-49.
Konan, Y. N., R. Gurny and E. Allémann (2002). State of the art in the delivery of photosensitizers for photodynamic therapy. *Journal of Photochemistry and Photobiology B: Biology* 66(2) 89-106.
Korbelik, M. (1992). Low density lipoprotein receptor pathway in the delivery of Photofrin: how much is it relevant for selective accumulation of the photosensitizer in tumors? *Journal of Photochemistry and Photobiology B: Biology* 12(1) 107-109.
Kostron, H., T. Fiegele and E. Akatuna (2006). Combination of FOSCAN® mediated fluorescence guided resection and photodynamic treatment as new therapeutic concept for malignant brain tumors. *Medical Laser Application* 21(4) 285-290.
Koziar, J. C. and D. O. Cowan (1978). Photochemical heavy-atom effects. *Accounts of chemical research* 11(9) 334-341.
Krysko, D. V., et al. (2012). Immunogenic cell death and DAMPs in cancer therapy. *Nature Reviews Cancer* 12(12) 860-875.
Krämer, K. W., et al. (2004). Hexagonal sodium yttrium fluoride based green and blue emitting upconversion phosphors. *Chemistry of Materials* 16(7) 1244-1251.
Kurakina, D., et al. (2019). Comparative analysis of single-and dual-wavelength photodynamic therapy regimes with chlorin-based photosensitizers: animal study. *Journal of biomedical optics* 25(6) 063804.
Kübler, A. C., et al. (1999). Photodynamic therapy of primary nonmelanomatous skin tumours of the head and neck. *Lasers in Surgery and Medicine: The Official Journal of the American Society for Laser Medicine and Surgery* 25(1) 60-68.
Lamch, Ł., et al. (2014). Polymeric micelles for enhanced Photofrin II® delivery, cytotoxicity and pro-apoptotic activity in human breast and ovarian cancer cells. *Photodiagnosis and photodynamic therapy* 11(4) 570-585.
Lamola, A. A. and G. S. Hammond (1965). Mechanisms of photochemical reactions in solution. XXXIII. Intersystem crossing efficiencies. *The Journal of Chemical Physics* 43(6) 2129-2135.
Lan, M., et al. (2019). Photosensitizers for photodynamic therapy. *Advanced healthcare materials* 8(13) 1900132.
Lawen, A. (2003). Apoptosis—an introduction. *Bioessays* 25(9) 888-896.
Lee, C., et al. (2021). Analysing the mechanism of mitochondrial oxidation-induced cell death using a multifunctional iridium (III) photosensitiser. *Nature Communications* 12(1) 1-11.
Lee, G. Y., et al. (2007). Three-dimensional culture models of normal and malignant breast epithelial cells. *Nature methods* 4(4) 359-365.
Lever, A. (1974). Charge transfer spectra of transition metal complexes. *Journal of Chemical Education* 51(9) 612.
Li, B., et al. (2016). Photosensitized singlet oxygen generation and detection: Recent advances and future perspectives in cancer photodynamic therapy. *Journal of biophotonics* 9(11-12) 1314-1325.

Li, C., et al. (2020). Advanced fluorescence imaging technology in the near-infrared-ii window for biomedical applications. *Journal of the American Chemical Society* 142(35) 14789-14804.
Li, J., H. Ou and D. Ding (2021). Recent Progress in Boosted PDT Induced Immunogenic Cell Death for Tumor Immunotherapy. *Chemical Research in Chinese Universities* 1-7.
Li, K., et al. (2016). Highly phosphorescent platinum (II) emitters: photophysics, materials and biological applications. *Chemical science* 7(3) 1653-1673.
Li, L.-B. and R.-C. Luo (2009). Effect of drug–light interval on the mode of action of Photofrin photodynamic therapy in a mouse tumor model. *Lasers in medical science* 24(4) 597-603.
Li, M., et al. (2016). β-NaYF 4: Yb, Tm: upconversion properties by controlling the transition probabilities at the same energy level. *Inorganic Chemistry Frontiers* 3(8) 1082-1090.
Li, S. P. Y., et al. (2010). Modification of luminescent iridium (III) polypyridine complexes with discrete poly (ethylene glycol)(PEG) pendants: synthesis, emissive behavior, intracellular uptake, and PEGylation properties. *Chemistry–A European Journal* 16(28) 8329-8339.
Li, W., et al. (2019). Targeting photodynamic and photothermal therapy to the endoplasmic reticulum enhances immunogenic cancer cell death. *Nature communications* 10(1) 1-16.
Li, X., et al. (2018). Innovative strategies for hypoxic-tumor photodynamic therapy. *Angewandte Chemie International Edition* 57(36) 11522-11531.
Li, X., et al. (2020). Mitochondrial-DNA-Targeted IrIII-Containing Metallohelices with Tunable Photodynamic Therapy Efficacy in Cancer Cells. *Angewandte Chemie* 132(16) 6482-6489.
Li, Z., et al. (2012). Mesoporous silica nanoparticles in biomedical applications. *Chemical Society Reviews* 41(7) 2590-2605.
Lilge, L., et al. (2020). Evaluation of a Ruthenium coordination complex as photosensitizer for PDT of bladder cancer: Cellular response, tissue selectivity and in vivo response. *Translational Biophotonics* 2(1-2) e201900032.
Liou, G.-Y. and P. Storz (2010). Reactive oxygen species in cancer. *Free radical research* 44(5) 479-496.
LIPSON, R. L. and E. J. BALDES (1960). The photodynamic properties of a particular hematoporphyrin derivative. *Archives of dermatology* 82(4) 508-516.
Liu, B., et al. (2019). New class of homoleptic and heteroleptic bis (terpyridine) iridium (III) complexes with strong photodynamic therapy effects. *ACS applied bio materials* 2(7) 2964-2977.
Liu, D., et al. The application of physical pretreatment in photodynamic therapy for skin diseases. *Lasers in Medical Science* 1-9.
Liu, J., et al. (2018). Harnessing ruthenium (II) as photodynamic agents: Encouraging advances in cancer therapy. *Coordination Chemistry Reviews* 363 17-28.
Lu, C., et al. (2020). In Vitro Photodynamic Therapy of Mononuclear and Dinuclear Iridium (III) Bis (terpyridine) Complexes. *ACS Applied Bio Materials* 3(10) 6865-6875.
Lu, F., et al. (2009). Size effect on cell uptake in well-suspended, uniform mesoporous silica nanoparticles. *Small* 5(12) 1408-1413.

Lu, L., et al. (2014). Luminescent detection of human serum albumin in aqueous solution using a cyclometallated iridium (III) complex. *Sensors and Actuators B: Chemical* 201 177-184.
Lu, P., et al. (2016). Delivery of drugs and macromolecules to the mitochondria for cancer therapy. *Journal of Controlled Release* 240 38-51.
Lu, Y.-g., et al. (2014). Efficacy of topical ALA-PDT combined with excision in the treatment of skin malignant tumor. *Photodiagnosis and photodynamic therapy* 11(2) 122-126.
Lupu, M., et al. (2009). 23Na MRI longitudinal follow-up of PDT in a xenograft model of human retinoblastoma. *Photodiagnosis and photodynamic therapy* 6(3-4) 214-220.
Luzio, J. P., P. R. Pryor and N. A. Bright (2007). Lysosomes: fusion and function. *Nature reviews Molecular cell biology* 8(8) 622-632.
Ma, L., et al. (1992). Cytotoxicity and cytokinetic effects of mitomycin C and/or photochemotherapy in a human colon adenocarcinoma cell line. *The International journal of biochemistry* 24(11) 1807-1813.
Ma, Y., et al. (1998). Electroluminescence from triplet metal—ligand charge-transfer excited state of transition metal complexes. *Synthetic Metals* 94(3) 245-248.
Mader, H. S., et al. (2010). Upconverting luminescent nanoparticles for use in bioconjugation and bioimaging. *Current opinion in chemical biology* 14(5) 582-596.
Mae, Y., et al. (2020). Verteporfin-photodynamic therapy is effective on gastric cancer cells. *Molecular and Clinical Oncology* 13(3) 1-1.
Maeda, H. (2001). The enhanced permeability and retention (EPR) effect in tumor vasculature: the key role of tumor-selective macromolecular drug targeting. *Advances in enzyme regulation* 41 189-207.
Mah, L., A. El-Osta and T. Karagiannis (2010). γH2AX: a sensitive molecular marker of DNA damage and repair. *Leukemia* 24(4) 679-686.
Maier, A., et al. (2000). Hyperbaric oxygen and photodynamic therapy in the treatment of advanced carcinoma of the cardia and the esophagus. *Lasers in Surgery and Medicine: The Official Journal of the American Society for Laser Medicine and Surgery* 26(3) 308-315.
Majno, G., M. La Gattuta and T. Thompson (1960). Cellular death and necrosis: chemical, physical and morphologic changes in rat liver. *Virchows Archiv für pathologische Anatomie und Physiologie und für klinische Medizin* 333(5) 421-465.
Malik, Z. (2020). Fundamentals of 5-aminolevulinic acid photodynamic therapy and diagnosis: An overview. *Translational Biophotonics* 2(1-2) e201900022.
Mancini, M., et al. (2000). Caspase-2 is localized at the Golgi complex and cleaves golgin-160 during apoptosis. *The Journal of cell biology* 149(3) 603-612.
Marian, C. M. (2012). Spin–orbit coupling and intersystem crossing in molecules. *Wiley Interdisciplinary Reviews: Computational Molecular Science* 2(2) 187-203.
Martoccia, C., et al. (2014). Optical spectroscopy of the bladder washout fluid to optimize fluorescence cystoscopy with Hexvix®. *Journal of biomedical optics* 19(9) 097002.
Mauro, M., et al. (2014). When self-assembly meets biology: luminescent platinum complexes for imaging applications. *Chemical Society Reviews* 43(12) 4144-4166.

Mbambisa, G., et al. (2007). Synthesis and electrochemical properties of purple manganese (III) and red titanium (IV) phthalocyanine complexes octa-substituted at non-peripheral positions with pentylthio groups. *Polyhedron* 26(18) 5355-5364.
McFarland, S. A., et al. (2020). Metal-based photosensitizers for photodynamic therapy: the future of multimodal oncology? *Current opinion in chemical biology* 56 23-27.
McKearney, D., et al. (2019). Facile tuning of strong near-IR absorption wavelengths in manganese (iii) phthalocyanines via axial ligand exchange. *Chemical Communications* 55(47) 6696-6699.
McKenzie, L. K., H. E. Bryant and J. A. Weinstein (2019). Transition metal complexes as photosensitisers in one-and two-photon photodynamic therapy. *Coordination Chemistry Reviews* 379 2-29.
McKenzie, L. K., et al. (2017). Metal Complexes for Two-Photon Photodynamic Therapy: A Cyclometallated Iridium Complex Induces Two-Photon Photosensitization of Cancer Cells under Near-IR Light. *Chemistry – A European Journal* 23(2) 234-238.
Mehraban, N. and H. S. Freeman (2015). Developments in PDT sensitizers for increased selectivity and singlet oxygen production. *Materials* 8(7) 4421-4456.
Meier, P., A. Finch and G. Evan (2000). Apoptosis in development. *Nature* 407(6805) 796-801.
Meisel, P. and T. Kocher (2005). Photodynamic therapy for periodontal diseases: state of the art. *Journal of Photochemistry and Photobiology B: Biology* 79(2) 159-170.
Menezes, P., et al. (2007). Photodynamic therapy for Photogem® and Photofrin® using different light wavelengths in 375 human melanoma cells. *Laser Physics Letters* 4(7) 546-551.
Michaeli, A. and J. Feitelson (1994). Reactivity of singlet oxygen toward amino acids and peptides. *Photochemistry and photobiology* 59(3) 284-289.
Michalak, M., et al. (2009). Calreticulin, a multi-process calcium-buffering chaperone of the endoplasmic reticulum. *Biochemical Journal* 417(3) 651-666.
Mignani, S., et al. (2013). Expand classical drug administration ways by emerging routes using dendrimer drug delivery systems: a concise overview. *Advanced drug delivery reviews* 65(10) 1316-1330.
Mitra, S. and T. H. Foster (2005). Photophysical Parameters, Photosensitizer Retention and Tissue Optical Properties Completely Account for the Higher Photodynamic Efficacy of meso-Tetra-Hydroxyphenyl-Chlorin vs Photofrin¶. *Photochemistry and photobiology* 81(4) 849-859.
Mizushima, N., T. Yoshimori and Y. Ohsumi (2011). The role of Atg proteins in autophagosome formation. *Annual review of cell and developmental biology* 27 107-132.
Monro, S., et al. (2018). Transition metal complexes and photodynamic therapy from a tumor-centered approach: challenges, opportunities, and highlights from the development of TLD1433. *Chemical reviews* 119(2) 797-828.
Moriyama, Y., M. Maeda and M. Futai (1992). Involvement of a non-proton pump factor (possibly Donnan-type equilibrium) in maintenance of an acidic pH in lysosomes. *FEBS letters* 302(1) 18-20.

Morseth, Z. A., et al. (2015). Ultrafast dynamics in multifunctional Ru (II)-loaded polymers for solar energy conversion. *Accounts of chemical research* 48(3) 818-827.
Mroz, P., et al. (2010). Photodynamic therapy of tumors can lead to development of systemic antigen-specific immune response. *PloS one* 5(12) e15194.
Murphy, M. P. (1997). Selective targeting of bioactive compounds to mitochondria. *Trends in biotechnology* 15(8) 326-330.
Møller, K. I., et al. (2005). How Finsen's light cured lupus vulgaris. *Photodermatology, photoimmunology & photomedicine* 21(3) 118-124.
Nagata, S. (2018). Apoptosis and clearance of apoptotic cells. *Annual review of immunology* 36 489-517.
Naik, A., et al. (2014). Visible-light-induced annihilation of tumor cells with platinum–porphyrin conjugates. *Angewandte Chemie* 126(27) 7058-7061.
Nair, T. S., et al. (2020). Characteristics of head and neck squamous cell carcinoma cell Lines reflect human tumor biology independent of primary etiologies and HPV status. *Translational oncology* 13(10) 100808.
Nam, J. S., et al. (2016). Endoplasmic reticulum-localized iridium (III) complexes as efficient photodynamic therapy agents via protein modifications. *Journal of the American Chemical Society* 138(34) 10968-10977.
Ngoune, R., et al. (2016). Accumulating nanoparticles by EPR: A route of no return. *Journal of Controlled Release* 238 58-70.
Nolet, M.-C., et al. (2004). Allowed and forbidden dd bands in octahedral coordination compounds: Intensity borrowing and interference dips in absorption spectra. *Optical Spectra and Chemical Bonding in Transition Metal Complexes* 145-158.
NSEYO, U. O., et al. (1998). Photodynamic therapy (PDT) in the treatment of patients with resistant superficial bladder cancer: a long term experience. *Journal of clinical laser medicine & surgery* 16(1) 61-68.
O'Toole, C. M., et al. (1983). Identity of some human bladder cancer cell lines. *Nature* 301(5899) 429-430.
Ogilby, P. R. (2010). Singlet oxygen: there is indeed something new under the sun. *Chemical Society Reviews* 39(8) 3181-3209.
Oleinick, N. L., R. L. Morris and I. Belichenko (2002). The role of apoptosis in response to photodynamic therapy: what, where, why, and how. *Photochemical & Photobiological Sciences* 1(1) 1-21.
Ouyang, M., et al. (2017). Cyclometalated IrIII Complexes as Mitochondria-Targeted Photodynamic Anticancer Agents. *European Journal of Inorganic Chemistry* 2017(12) 1764-1771.
O'Connor, A. E., W. M. Gallagher and A. T. Byrne (2009). Porphyrin and nonporphyrin photosensitizers in oncology: preclinical and clinical advances in photodynamic therapy. *Photochemistry and photobiology* 85(5) 1053-1074.
Pahernik, S., et al. (1998). Distribution and pharmacokinetics of Photofrin® in human bile duct cancer. *Journal of Photochemistry and Photobiology B: Biology* 47(1) 58-62.
Pandey, R. K., T. J. Dougherty and D. Kessel (2016). *Handbook of photodynamic therapy: updates on recent applications of porphyrin-based compounds*: World Scientific.

Pandian, R., et al. (1990). Spectroscopic studies on monomers and dimers of thiaporphyrins. Proceedings of the Indian Academy of Sciences-Chemical Sciences, Springer.
Park, W., et al. (2018). Advanced smart-photosensitizers for more effective cancer treatment. *Biomaterials science* 6(1) 79-90.
Park, Y. I., et al. (2009). Nonblinking and nonbleaching upconverting nanoparticles as an optical imaging nanoprobe and T1 magnetic resonance imaging contrast agent. *Advanced Materials* 21(44) 4467-4471.
Pathak, M. and T. Fitzpatrick (1959). Relationship of molecular configuration to the activity of furocoumarins which increase the cutaneous responses following long wave ultraviolet radiation. *The Journal of investigative dermatology* 32(2, Part 2) 255.
Pavani, C., et al. (2009). Effect of zinc insertion and hydrophobicity on the membrane interactions and PDT activity of porphyrin photosensitizers. *Photochemical & photobiological sciences* 8(2) 233-240.
Pei, P., et al. (2019). ROS-sensitive thioketal-linked polyphosphoester-doxorubicin conjugate for precise phototriggered locoregional chemotherapy. *Biomaterials* 188 74-82.
Peltomaa, R., et al. (2021). Biosensing based on upconversion nanoparticles for food quality and safety applications. *Analyst*.
Phua, S. Z. F., et al. (2019). Catalase-integrated hyaluronic acid as nanocarriers for enhanced photodynamic therapy in solid tumor. *ACS nano* 13(4) 4742-4751.
Pierri, A. E., et al. (2012). A luminescent and biocompatible photoCORM. *Journal of the American Chemical Society* 134(44) 18197-18200.
Pomarico, E., et al. (2018). Photophysical heavy-atom effect in iodinated metallocorroles: Spin–orbit coupling and density of states. *The Journal of Physical Chemistry A* 122(37) 7256-7266.
Ponten, J. and E. Saksela (1967). Two established in vitro cell lines from human mesenchymal tumours. *International journal of cancer* 2(5) 434-447.
Poynton, F. E., et al. (2017). The development of ruthenium (II) polypyridyl complexes and conjugates for in vitro cellular and in vivo applications. *Chemical Society Reviews* 46(24) 7706-7756.
Pracharova, J., et al. (2018). Exploring the effect of polypyridyl ligands on the anticancer activity of phosphorescent iridium (III) complexes: from proteosynthesis inhibitors to photodynamic therapy agents. *Chemistry–A European Journal* 24(18) 4607-4619.
Proskuryakov, S. Y. and V. L. Gabai (2010). Mechanisms of tumor cell necrosis. *Current pharmaceutical design* 16(1) 56-68.
Pyle, A., et al. (1989). Mixed-ligand complexes of ruthenium (II): factors governing binding to DNA. *Journal of the American Chemical Society* 111(8) 3051-3058.
Qian, H.-S. and Y. Zhang (2008). Synthesis of hexagonal-phase core– shell NaYF4 nanocrystals with tunable upconversion fluorescence. *Langmuir* 24(21) 12123-12125.
Qiao, L., et al. (2021). Rational design of a lysosome-targeting and near-infrared absorbing Ru (II)-BODIPY conjugate for photodynamic therapy. *Chemical Communications*.
Raab, O. (1900). Uber die Wirkung fluorescirender Stoffe auf Infusorien. *Z. biol.* 39 524-546.

Rahman, M. and H. J. Harmon (2006). Absorbance change and static quenching of fluorescence of meso-tetra (4-sulfonatophenyl) porphyrin (TPPS) by trinitrotoluene (TNT). *Spectrochimica Acta Part A: Molecular and Biomolecular Spectroscopy* 65(3-4) 901-906.
Raleigh, J., et al. (1987). Fluorescence immunohistochemical detection of hypoxic cells in spheroids and tumours. *British journal of cancer* 56(4) 395-400.
Ramu, V., et al. (2018). Glucose-appended platinum (II)-BODIPY conjugates for targeted photodynamic therapy in red light. *Inorganic chemistry* 57(4) 1717-1726.
Ramu, V., et al. (2019). Diplatinum (II) catecholate of photoactive boron-dipyrromethene for lysosome-targeted photodynamic therapy in red light. *Inorganic chemistry* 58(14) 9067-9075.
Reed, J. C. (2000). Mechanisms of apoptosis. *The American journal of pathology* 157(5) 1415-1430.
Rizzuto, R., et al. (2008). Ca2+ signaling, mitochondria and cell death. *Current molecular medicine* 8(2) 119-130.
Rock, K. L. and H. Kono (2008). The inflammatory response to cell death. *Annu. Rev. Pathol. Mech. Dis.* 3 99-126.
Rohn, W. M., et al. (2000). Bi-directional trafficking between the trans-Golgi network and the endosomal/lysosomal system. *Journal of Cell Science* 113(12) 2093-2101.
Ross, R. A., B. A. Spengler and J. L. Biedler (1983). Coordinate morphological and biochemical interconversion of human neuroblastoma cells. *Journal of the National Cancer Institute* 71(4) 741-747.
Rui, X., et al. (2020). Imperative and effective reversion of synovial hyperplasia and cartilage destruction in rheumatoid arthritis through multiple synergistic effects of O2 and Ca2+. *Materials Science and Engineering: C* 114 111058.
Sabri, T., P. D. Pawelek and J. A. Capobianco (2018). Dual activity of rose bengal functionalized to albumin-coated lanthanide-doped upconverting nanoparticles: targeting and photodynamic therapy. *ACS applied materials & interfaces* 10(32) 26947-26953.
Salvio, A. G., et al. (2020). Photodynamic therapy in combination with surgery for the treatment of an extensive squamous cell carcinoma in situ-A case report. *Photodiagnosis and photodynamic therapy* 30 101700.
Sant, S. and P. A. Johnston (2017). The production of 3D tumor spheroids for cancer drug discovery. *Drug Discovery Today: Technologies* 23 27-36.
Sarcan, E. T., M. Silindir-Gunay and A. Y. Ozer (2018). Theranostic polymeric nanoparticles for NIR imaging and photodynamic therapy. *International journal of pharmaceutics* 551(1-2) 329-338.
Sassa, S. and A. Kappas (1981). Genetic, metabolic, and biochemical aspects of the porphyrias. *Advances in Human Genetics 11* 121-231.
Sato, T., et al. (2014). Solubility of oxygen in organic solvents and calculation of the Hansen solubility parameters of oxygen. *Industrial & Engineering Chemistry Research* 53(49) 19331-19337.
Savary, J.-F., et al. (1998). Photodynamic therapy of early squamous cell carcinomas of the esophagus: a review of 31 cases. *Endoscopy* 30(03) 258-265.
Schaberle, F. A. (2018). Assessment of the actual light dose in photodynamic therapy. *Photodiagnosis and photodynamic therapy* 23 75-77.

Schmidt, R., et al. (1994). Phenalenone, a universal reference compound for the determination of quantum yields of singlet oxygen O2 (1Δg) sensitization. *Journal of Photochemistry and Photobiology A: Chemistry* 79(1-2) 11-17.
Schwarz, D. S. and M. D. Blower (2016). The endoplasmic reticulum: structure, function and response to cellular signaling. *Cellular and Molecular Life Sciences* 73(1) 79-94.
Scurlock, R. D., B. Wang and P. R. Ogilby (1996). Chemical reactivity of singlet sigma oxygen (b1Σg+) in solution. *Journal of the American Chemical Society* 118(2) 388-392.
Sengupta, S., T. R. Peterson and D. M. Sabatini (2010). Regulation of the mTOR complex 1 pathway by nutrients, growth factors, and stress. *Molecular cell* 40(2) 310-322.
Shafirstein, G., et al. (2018). Irradiance controls photodynamic efficacy and tissue heating in experimental tumours: implication for interstitial PDT of locally advanced cancer. *British journal of cancer* 119(10) 1191-1199.
Sharma, S. K. and M. R. Hamblin (2021). Photodynamic Therapy and Antitumor Immune Response. *Cancer Immunology*. Springer. 383-402.
Sheleg, S. V., et al. (2004). Photodynamic therapy with chlorin e6 for skin metastases of melanoma. *Photodermatology, photoimmunology & photomedicine* 20(1) 21-26.
Sheng, T., et al. (2020). Reactive oxygen species explicit dosimetry to predict tumor growth for benzoporphyrin derivative-mediated vascular photodynamic therapy. *Journal of biomedical optics* 25(6) 063805.
Shewring, J. R., et al. (2017). Multimodal probes: Superresolution and transmission electron microscopy imaging of mitochondria, and oxygen mapping of cells, using small-molecule Ir (iii) luminescent complexes. *Inorganic chemistry* 56(24) 15259-15270.
Shi, H., C. Imberti and P. J. Sadler (2019). Diazido platinum (IV) complexes for photoactivated anticancer chemotherapy. *Inorganic Chemistry Frontiers* 6(7) 1623-1638.
Shi, H. and P. J. Sadler (2020). How promising is phototherapy for cancer? *British Journal of Cancer* 123(6) 871-873.
Shi, L., et al. (2019). The effectiveness and safety of X-PDT for cutaneous squamous cell carcinoma and melanoma. *Nanomedicine* 14(15) 2027-2043.
Siemann, D. W. (2011). The unique characteristics of tumor vasculature and preclinical evidence for its selective disruption by tumor-vascular disrupting agents. *Cancer treatment reviews* 37(1) 63-74.
Sitnik, T., J. Hampton and B. Henderson (1998). Reduction of tumour oxygenation during and after photodynamic therapy in vivo: effects of fluence rate. *British journal of cancer* 77(9) 1386-1394.
Skovsen, E., et al. (2005). Lifetime and diffusion of singlet oxygen in a cell. *The Journal of Physical Chemistry B* 109(18) 8570-8573.
Soldani, C., et al. (2004). The Golgi apparatus is a primary site of intracellular damage after photosensitization with Rose Bengal acetate. *European Journal of Histochemistry* 48(4) 443-448.

Song, C., et al. (2020). Photodynamic therapy induces autophagy-mediated cell death in human colorectal cancer cells via activation of the ROS/JNK signaling pathway. *Cell Death & Disease* 11(10) 1-14.
Sorenson, C. M., M. A. Barry and A. Eastman (1990). Analysis of events associated with cell cycle arrest at G2 phase and cell death induced by cisplatin. *JNCI: Journal of the National Cancer Institute* 82(9) 749-755.
Sorrin, A. J., et al. (2020). Photodynamic therapy and the biophysics of the tumor microenvironment. *Photochemistry and photobiology* 96(2) 232-259.
Soule, H., et al. (1973). A human cell line from a pleural effusion derived from a breast carcinoma. *Journal of the national cancer institute* 51(5) 1409-1416.
Sperandio, S., I. de Belle and D. E. Bredesen (2000). An alternative, nonapoptotic form of programmed cell death. *Proceedings of the National Academy of Sciences* 97(26) 14376-14381.
Stoka, V., et al. (2001). Lysosomal protease pathways to apoptosis: cleavage of Bid, not pro-caspases, is the most likely route. *Journal of Biological Chemistry* 276(5) 3149-3157.
Stone, A. (1976). Spin-orbit coupling and the intersection of potential energy surfaces in polyatomic molecules. *Proceedings of the Royal Society of London. A. Mathematical and Physical Sciences* 351(1664) 141-150.
Stoner, K. L., et al. (2015). Intravenous versus subcutaneous drug administration. Which do patients prefer? A systematic review. *The Patient-Patient-Centered Outcomes Research* 8(2) 145-153.
Stylianopoulos, T., et al. (2012). Causes, consequences, and remedies for growth-induced solid stress in murine and human tumors. *Proceedings of the National Academy of Sciences* 109(38) 15101-15108.
Sun, J., et al. (2020). GSH and H2O2 Co-Activatable Mitochondria-Targeted Photodynamic Therapy under Normoxia and Hypoxia. *Angewandte Chemie International Edition* 59(29) 12122-12128.
Sutherland, R. M. (1988). Cell and environment interactions in tumor microregions: the multicell spheroid model. *Science* 240(4849) 177-184.
Swinehart, D. F. (1962). The beer-lambert law. *Journal of chemical education* 39(7) 333.
Sütterlin, C., et al. (2002). Fragmentation and dispersal of the pericentriolar Golgi complex is required for entry into mitosis in mammalian cells. *Cell* 109(3) 359-369.
Tang, D. and G. Kroemer (2020). Ferroptosis. *Current Biology* 30(21) R1292-R1297
Tanida, I. (2011). Autophagosome formation and molecular mechanism of autophagy. *Antioxidants & redox signaling* 14(11) 2201-2214.
Teiten, M., et al. (2003). Endoplasmic reticulum and Golgi apparatus are the preferential sites of Foscan® localisation in cultured tumour cells. *British journal of cancer* 88(1) 146-152.
Thompson, S. A., et al. (2018). Compromising the plasma membrane as a secondary target in photodynamic therapy-induced necrosis. *Bioorganic & medicinal chemistry* 26(18) 5224-5228.
Tian, X., et al. (2017). Localization matters: a nuclear targeting two-photon absorption iridium complex in photodynamic therapy. *Chemical Communications* 53(23) 3303-3306.

Tomaszewska, E., et al. (2013). Detection limits of DLS and UV-Vis spectroscopy in characterization of polydisperse nanoparticles colloids. *Journal of Nanomaterials* 2013.
Torresan, M. F. and A. Wolosiuk (2021). Critical Aspects on the Chemical Stability of NaYF4-Based Upconverting Nanoparticles for Biomedical Applications. *ACS Applied Bio Materials*.
Turubanova, V. D., et al. (2019). Immunogenic cell death induced by a new photodynamic therapy based on photosens and photodithazine. *Journal for immunotherapy of cancer* 7(1) 1-13.
van der Bruggen, P. and B. J. Van den Eynde (2006). Processing and presentation of tumor antigens and vaccination strategies. *Current opinion in immunology* 18(1) 98-104.
van Duijnhoven, F. H., et al. (2005). Photodynamic therapy with 5, 10, 15, 20-tetrakis (m-hydroxyphenyl) bacteriochlorin for colorectal liver metastases is safe and feasible: results from a phase I study. *Annals of surgical oncology* 12(10) 808-816.
van Straten, D., et al. (2017). Oncologic photodynamic therapy: Basic principles, current clinical status and future directions. *Cancers* 9(2) <xocs:firstpage xmlns:xocs=""/>.
Vaupel, P., O. Thews and M. Hoeckel (2001). Treatment resistance of solid tumors. *Medical oncology* 18(4) 243-259.
Vezzu, D. A., et al. (2014). Cytotoxicity of cyclometalated platinum complexes based on tridentate NCN and CNN-coordinating ligands: Remarkable coordination dependence. *Journal of inorganic biochemistry* 134 49-56.
Vogler, A. and H. Kunkely (2001). Luminescent metal complexes: diversity of excited states. *Transition Metal and Rare Earth Compounds* 143-182.
Von Tappeiner, H. and A. Jodlbauer (1907). Die Sensibilisierende wirkung fluorieszierender substanzer. *Gesammte Untersuchungen Uber Die Photodynamische Erscheinung. FCW Vogel, Leipzig*.
Wang, F.-X., et al. (2017). Dual functions of cyclometalated iridium (III) complexes: anti-metastasis and lysosome-damaged photodynamic therapy. *ACS applied materials & interfaces* 9(49) 42471-42481.
Wang, M., Y. Zhu and C. Mao (2015). Synthesis of NIR-responsive NaYF4: Yb, Er upconversion fluorescent nanoparticles using an optimized solvothermal method and their applications in enhanced development of latent fingerprints on various smooth substrates. *Langmuir* 31(25) 7084-7090.
Ward, C., et al. (2013). New strategies for targeting the hypoxic tumour microenvironment in breast cancer. *Cancer treatment reviews* 39(2) 171-179.
Weber, R. A., et al. (2020). Maintaining iron homeostasis is the key role of lysosomal acidity for cell proliferation. *Molecular cell* 77(3) 645-655. e647.
Weissleder, R. (2001). A clearer vision for in vivo imaging. *Nature biotechnology* 19(4) 316-317.
Welch, D. R., et al. (1991). Characterization of a highly invasive and spontaneously metastatic human malignant melanoma cell line. *International journal of cancer* 47(2) 227-237.
Whittle, C. E., et al. (2001). Photophysics of diimine platinum (II) bis-acetylide complexes. *Inorganic Chemistry* 40(16) 4053-4062.

Wilson, B. C., M. S. Patterson and L. Lilge (1997). Implicit and explicit dosimetry in photodynamic therapy: a new paradigm. *Lasers in medical science* 12(3) 182-199.
Wilson, W. R. and M. P. Hay (2011). Targeting hypoxia in cancer therapy. *Nature Reviews Cancer* 11(6) 393-410.
Wong, E. and C. M. Giandomenico (1999). Current status of platinum-based antitumor drugs. *Chemical reviews* 99(9) 2451-2466.
Wormald, R., et al. (2007). Photodynamic therapy for neovascular age-related macular degeneration. *Cochrane Database of Systematic Reviews*(3).
Wu, P., et al. (2009). Cyclometalated Platinum (II) Complexes as Highly Sensitive Luminescent Switch-On Probes for Practical Application in Protein Staining and Cell Imaging. *Chemistry–A European Journal* 15(15) 3652-3656.
Wu, W., et al. (2013). Red-light excitable fluorescent platinum (II) bis (aryleneethynylene) bis (trialkylphosphine) complexes showing long-lived triplet excited states as triplet photosensitizers for triplet–triplet annihilation upconversion. *Journal of Materials Chemistry C* 1(4) 705-716.
Würth, C., et al. (2018). Quantum yields, surface quenching, and passivation efficiency for ultrasmall core/shell upconverting nanoparticles. *Journal of the American Chemical Society* 140(14) 4922-4928.
Wyld, L., M. Reed and N. Brown (2001). Differential cell death response to photodynamic therapy is dependent on dose and cell type. *British journal of cancer* 84(10) 1384-1386.
Wyss, P. (2000). *Photomedicine in Gynecology and Reproduction*: Karger Medical and Scientific Publishers.
Xie, Y., et al. (2016). Ferroptosis: process and function. *Cell Death & Differentiation* 23(3) 369-379.
Xie, Z. and D. J. Klionsky (2007). Autophagosome formation: core machinery and adaptations. *Nature cell biology* 9(10) 1102-1109.
Xing, L., et al. (2021). Complying with the physiological functions of Golgi apparatus for secretory exocytosis facilitated oral absorption of protein drugs. *Journal of Materials Chemistry B* 9(6) 1707-1718.
Xu, T., et al. (2019). Molecular mechanisms of ferroptosis and its role in cancer therapy. *Journal of cellular and molecular medicine* 23(8) 4900-4912.
Yi, G.-S. and G.-M. Chow (2007). Water-soluble NaYF4: Yb, Er (Tm)/NaYF4/polymer core/shell/shell nanoparticles with significant enhancement of upconversion fluorescence. *Chemistry of Materials* 19(3) 341-343.
Yim, W. W.-Y. and N. Mizushima (2020). Lysosome biology in autophagy. *Cell discovery* 6(1) 1-12.
Yoo, J.-H., et al. (2009). Synthesis and characterization of mesoporous core-shell silica with incorporation of dye. *Molecular Crystals and Liquid Crystals* 504(1) 223-230.
Young, C., R. Battino and H. L. Clever (1979). the Solubility of Gases in Liquids. *IUPAC Solubility Data Series* 1 xv.
Yu, L., Y. Chen and S. A. Tooze (2018). Autophagy pathway: cellular and molecular mechanisms. *Autophagy* 14(2) 207-215.
Yu, M., et al. (2008). Cationic iridium (III) complexes for phosphorescence staining in the cytoplasm of living cells. *Chemical communications*(18) 2115-2117.

Yu, W. and L. Zhao (2021). Chemiluminescence Detection of Reactive Oxygen Species Generation and Potential Environmental Applications. *TrAC Trends in Analytical Chemistry* 116197.
Yuan, B., et al. (2019). Endoplasmic reticulum targeted cyclometalated iridium (iii) complexes as efficient photodynamic therapy photosensitizers. *Dalton Transactions* 48(19) 6408-6415.
Zanoni, M., et al. (2016). 3D tumor spheroid models for in vitro therapeutic screening: a systematic approach to enhance the biological relevance of data obtained. *Scientific reports* 6(1) 1-11.
Zhang, J., et al. (2016). ROS and ROS-mediated cellular signaling. *Oxidative medicine and cellular longevity* 2016.
Zhang, Q., et al. (2009). Hexanedioic acid mediated surface–ligand-exchange process for transferring NaYF 4: Yb/Er (or Yb/Tm) up-converting nanoparticles from hydrophobic to hydrophilic. *Journal of colloid and interface science* 336(1) 171-175.
Zhang, Q., et al. (2020). Copper (II) complexes modified with water-soluble porphyrin and various small molecules ligand for DNA binding and potential selectivity antitumor agents. *Dyes and Pigments* 173 107923.
Zhang, X., et al. (2020). Recent development of the transition metal complexes showing strong absorption of visible light and long-lived triplet excited state: From molecular structure design to photophysical properties and applications. *Coordination Chemistry Reviews* 417 213371.
Zhang, Y., et al. (2017). Ultrasmall-superbright neodymium-upconversion nanoparticles via energy migration manipulation and lattice modification: 808 nm-activated drug release. *ACS nano* 11(3) 2846-2857.
Zhao, F., W. Wang and W. Wu (2021). A novel ruthenium polypyridyl complex for selective imaging and photodynamic targeting of Golgi apparatus. *Dalton Transactions*.
Zhao, H., et al. (2021). A versatile strategy for improving phototherapeutic efficacy on deep-sited tumor by tissue optical clearing technique. *Nano Today* 36 101058.
Zhao, J., et al. (2020). An Iridium (III) Complex Bearing a Donor–Acceptor–Donor Type Ligand for NIR-Triggered Dual Phototherapy. *Advanced Functional Materials* 2008325.
Zhao, J., D. Zhong and S. Zhou (2018). NIR-I-to-NIR-II fluorescent nanomaterials for biomedical imaging and cancer therapy. *Journal of Materials Chemistry B* 6(3) 349-365.
Zhao, X., et al. (2021). Triplet Photosensitizers Showing Strong Absorption of Visible Light and Long-Lived Triplet Excited States and Application in Photocatalysis: A Mini Review. *Energy & Fuels*.
Zhong, Y.-F., et al. (2019). Nucleus-localized platinum (II)–triphenylamine complexes as potent photodynamic anticancer agents. *Inorganic Chemistry Frontiers* 6(10) 2817-2823.
Zhou, L., et al. (2020). Enhancing the ROS generation ability of a rhodamine-decorated iridium (iii) complex by ligand regulation for endoplasmic reticulum-targeted photodynamic therapy. *Chemical Science* 11(44) 12212-12220.
Zhou, M., et al. (2019). The bioavailability, biodistribution, and toxic effects of silica-coated upconversion nanoparticles in vivo. *Frontiers in chemistry* 7 218.

Zhou, Y., et al. (2020). Synthesis and Structural Optimization of Iridium (III) Solvent Complex for Electrochemiluminescence Labeling of Histidine-Rich Protein and Immunoassay Applications for CRP Detection. *ACS omega* 5(7) 3638-3645.
Zhu, T. C. and J. C. Finlay (2008). The role of photodynamic therapy (PDT) physics. *Medical physics* 35(7Part1) 3127-3136.
Zhuang, Z., et al. (2020). Type I photosensitizers based on phosphindole oxide for photodynamic therapy: apoptosis and autophagy induced by endoplasmic reticulum stress. *Chemical Science* 11(13) 3405-3417.
Zwelling, L. A. and K. W. Kohn (1979). Mechanism of Action of c/s-Dichlorodiammineplatinum (ll) Leonard A. Zwelling* and Kurt W. Kohn1. *Cancer treatment reports* 63(9-12) 1439-1444.

Appendix 1. Ir(III) PS

Compound	Photoactivation/nm	Localisation	Cell death	LD_{50} (dark)/ μM	LD_{50} (light)/μM	Ref
1	400-550	Mitochondria	Apoptosis	40	1.3	(Lee, Nam et al., 2021)
2	400-550	ER	Apoptosis	4.89	0.83	(Nam, Kang et al., 2016)
3	400-450	Lysosome	Apoptosis	>100	0.12	(He, Li et al., 2015)
4	400 - 600	ER	Apoptosis	>10	1	(Zhou, Wei et al., 2020)
5	400 - 550	Mitochondria/Lysosome	Apoptosis	13.9	2.9	(Lu, Xu et al., 2020)
6	450 - 1000	-	Necrosis	>100	20	(Zhao, Yan et al., 2020)
7	400 - 450	Mitochondria	Apoptosis	22.5	0.15	(Ouyang, Zeng et al., 2017)
8	400 - 500	Lysosome	Apoptosis	>100	0.21	(Wang, Chen et al., 2017)
9	400-500	-	-	>300	0.18	(Liu, Monro et al., 2019)
10	400 - 450	ER	Apoptosis	56.6	0.2	(Yuan, Liu et al., 2019)
11	400 – 500	Mitochondria	Apoptosis	>200	26.4	(Guo, Han et al., 2019)
12	400 - 450	Mitochondria/Lysosome	Apoptosis	>100	0.42	(Doherty, Sazanovich et al., 2016)

Appendix 2. IrTHPyBenz ^{1}H NMR

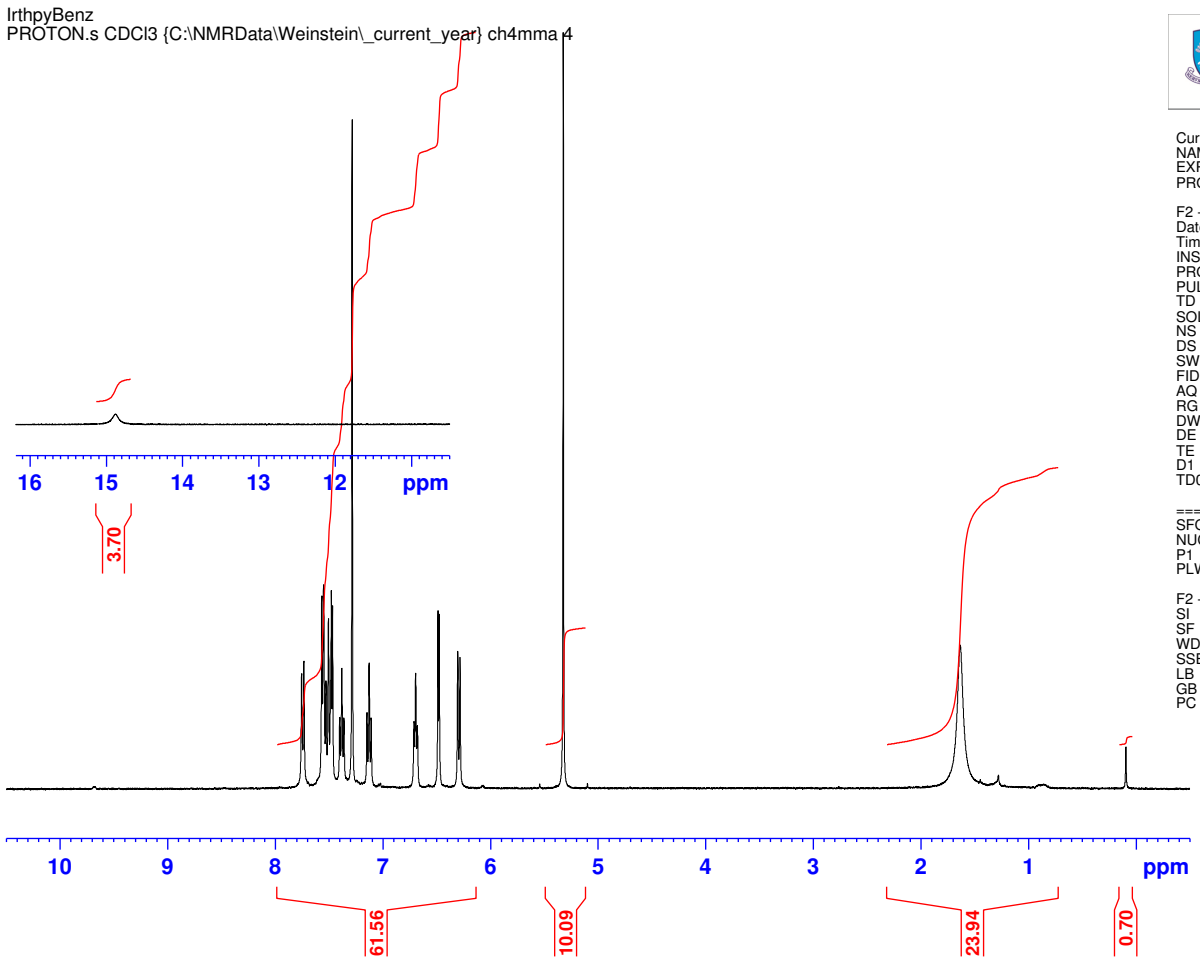

The University Of Sheffield.

Current Data Parameters
NAME Magnus_2019_06_13
EXPNO 1
PROCNO 1

F2 - Acquisition Parameters
Date_ 20190613
Time 21.10
INSTRUM AVIIIHD400
PROBHD 5 mm PABBO BB/
PULPROG zg30
TD 65536
SOLVENT CDCl3
NS 16
DS 2
SWH 8012.820 Hz
FIDRES 0.122266 Hz
AQ 4.0894465 sec
RG 195.75
DW 62.400 usec
DE 17.37 usec
TE 298.0 K
D1 0.50000000 sec
TD0 1

======== CHANNEL f1 ========
SFO1 400.2324716 MHz
NUC1 1H
P1 10.00 usec
PLW1 16.00000000 W

F2 - Processing parameters
SI 65536
SF 400.2300000 MHz
WDW EM
SSB 0
LB 0.30 Hz
GB 0
PC 1.00

Appendix 3 IrTHPyBenz ^{13}C NMR

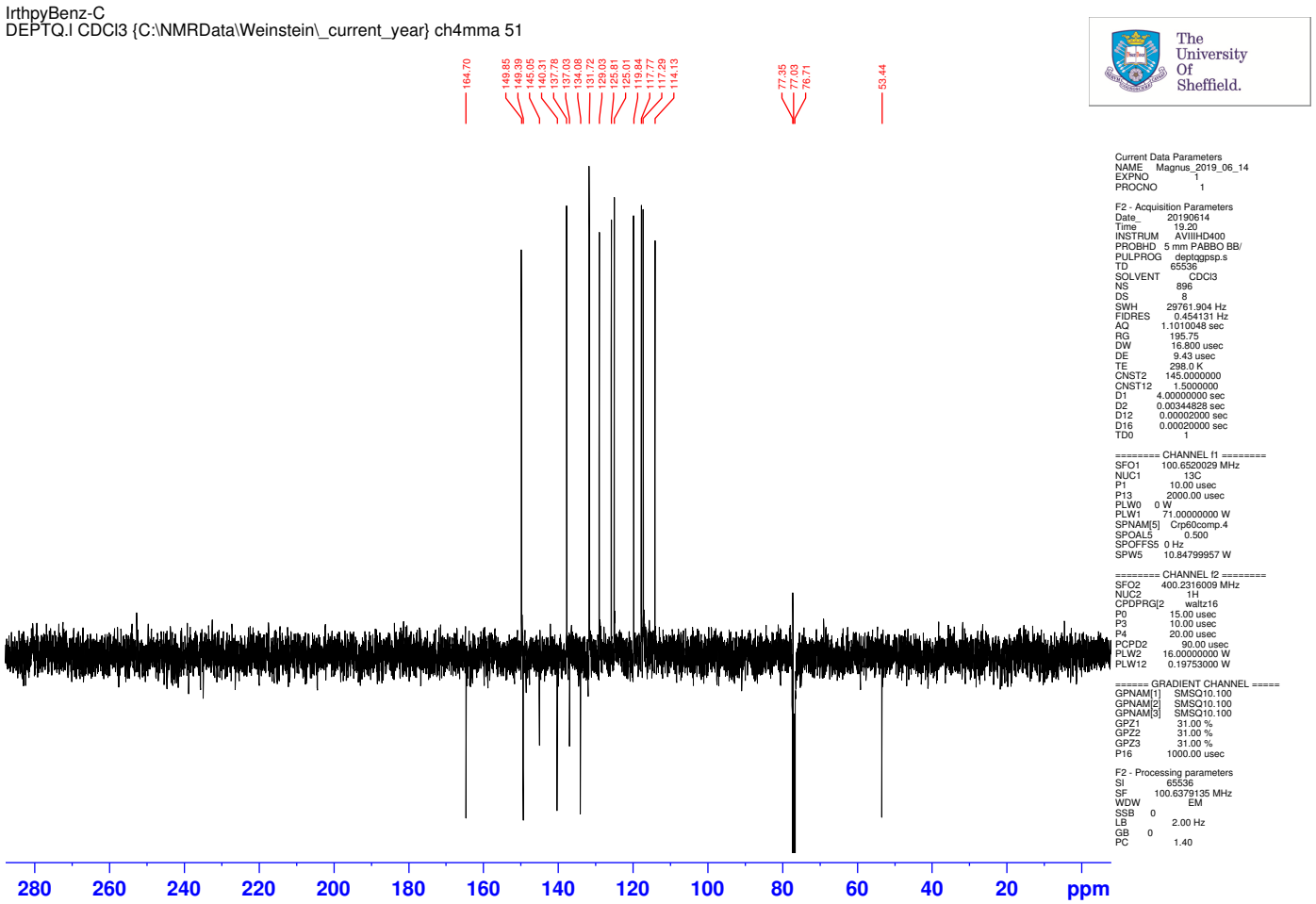

Appendix 4 IrTHPyBenz Mass Spectroscopy

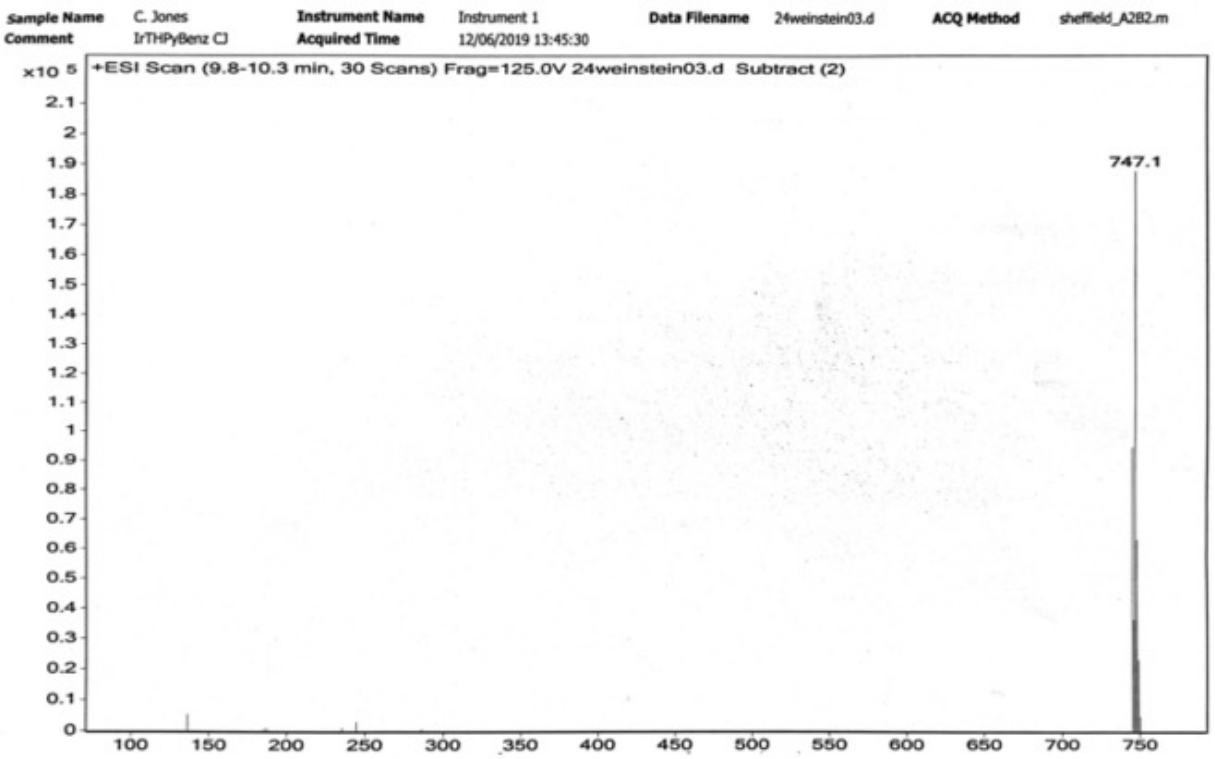

Appendix 5. IrNew Paper

ChemPubSoc Europe

DOI: 10.1002/chem.201604792

CHEMISTRY A European Journal Communication

Photoactive Complexes

Metal Complexes for Two-Photon Photodynamic Therapy: A Cyclometallated Iridium Complex Induces Two-Photon Photosensitization of Cancer Cells under Near-IR Light

Luke K. McKenzie,[a, b] Igor V. Sazanovich,[a, b, e] Elizabeth Baggaley,[b] Mickaële Bonneau,[c, d] Véronique Guerchais,[d] J. A. Gareth Williams,[c] Julia A. Weinstein,*[b] and Helen E. Bryant*[a]

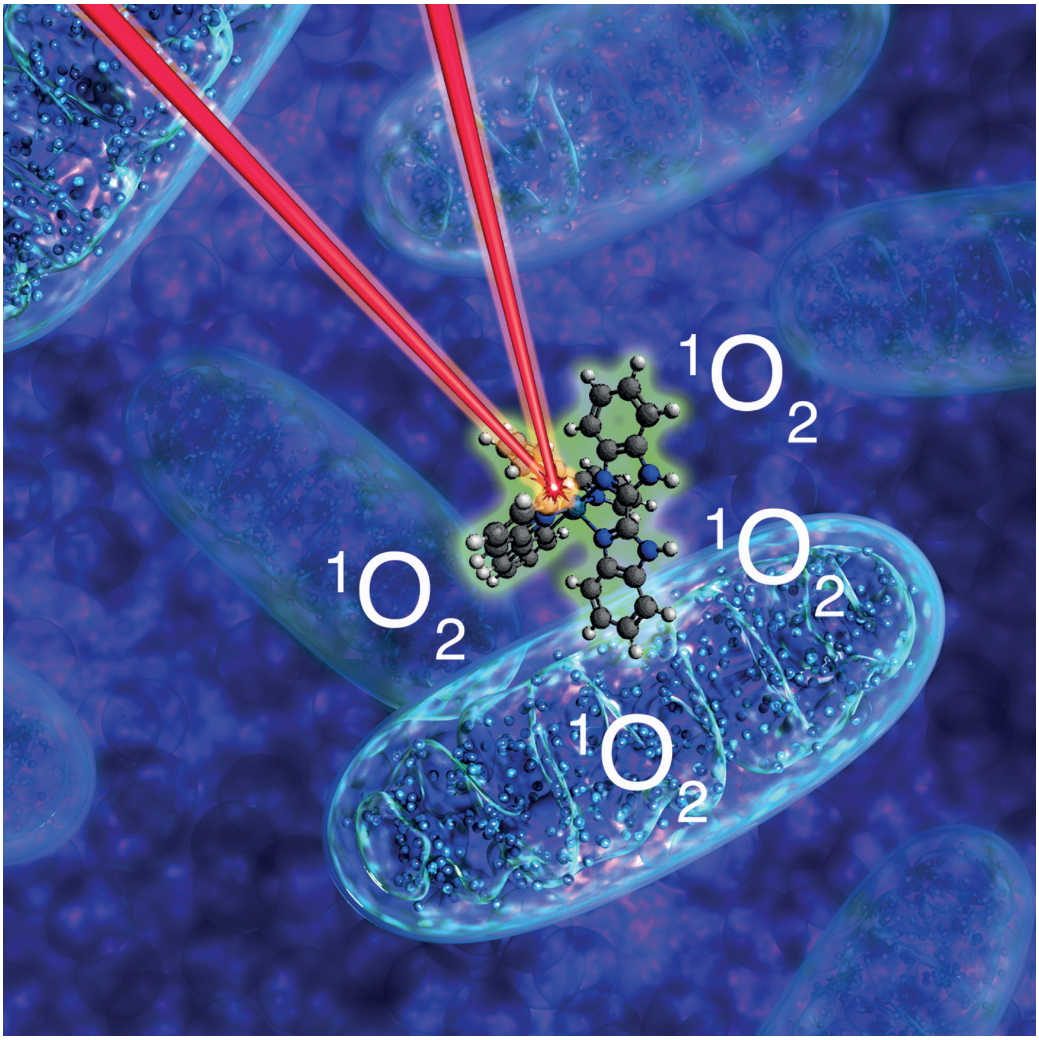

Abstract: Photodynamic therapy (PDT) uses photosensitizers (PS) which only become cytotoxic upon light-irradiation. Transition-metal complexes are highly promising PS due to long excited-state lifetimes, and high photo-stabilities. However, these complexes usually absorb higher-energy UV/Vis light, whereas the optimal tissue transparency is in the lower-energy NIR region. Two-photon excitation (TPE) can overcome this dichotomy, with simultaneous absorption of two lower-energy NIR-photons populating the same PS-active excited state as one higher-energy photon. We introduce two low-molecular weight, long-lived and photo-stable iridium complexes of the $[Ir(N^C)_2(N^N)]^+$ family with high TP-absorption, which localise to mitochondria and lysosomal structures in live cells. The compounds are efficient PS under 1-photon irradiation (405 nm) resulting in apoptotic cell death in diverse cancer cell lines at low light doses (3.6 $J\,cm^{-2}$), low concentrations, and photo-indexes greater than 555. Remarkably **1** also displays high PS activity killing cancer cells under NIR two-photon excitation (760 nm), which along with its photo-stability indicates potential future clinical application.

Photodynamic therapy (PDT) is a light-activated treatment offering reduced side effects compared to traditional therapy.[1] The PDT agent, a photosensitizer (PS), is only activated upon targeted irradiation by light of a PS-specific wavelength which promotes the PS to its excited, high-energy state (*PS).

In oxygen-dependent PDT, cellular oxygen and *PS interactions allow excited-state energy transfer, regenerating the ground state of the PS and producing reactive oxygen species (ROS) including singlet oxygen ($^1O_2$), with subsequent reactions with the intracellular components leading to cell death. Targeted intracellular localisation of the PS is important for maximum effect with organelles situated nearest to *PS being the most affected.[2]

[a] *L. K. McKenzie, Dr. I. V. Sazanovich, Dr. H. E. Bryant*
Department of Oncology and Metabolism
University of Sheffield, Sheffield S10 2RX (UK)
E-mail: h.bryant@sheffield.ac.uk

[b] *L. K. McKenzie, Dr. I. V. Sazanovich, Dr. E. Baggaley, Prof. J. A. Weinstein*
Department of Chemistry, University of Sheffield, Sheffield S3 7HF (UK)
E-mail: julia.weinstein@sheffield.ac.uk

[c] *Dr. M. Bonneau, Prof. J. A. G. Williams*
Department of chemistry, Durham University, Durham DH1 3LE (UK)

[d] *Dr. M. Bonneau, Dr. V. Guerchais*
UMR CNRS 6226, Université de Rennes 1
Institut des Sciences Chimiques de Rennes, Campus de Beaulieu
35042 Rennes (France)

[e] *Dr. I. V. Sazanovich*
Current address: Harwell Science Campus, OX11 0QX (UK)

Supporting information and ORCID from the author for this article are available on the WWW under http://dx.doi.org/10.1002/chem.201604792.

The photo-physical properties of many transition metal complexes make them ideal PS candidates. Their key advantage over organic molecules is the heavy atom effect which favours fast singlet to triplet intersystem crossing (ISC). The longer lifetimes, which result from ISC, lead to high yields of $^1O_2$ and/or other ROS. The ease of chemical modification and photo-stability adds to the appeal of these complexes. Accordingly, an increasing number of transition metal complexes have been investigated for use in PDT including those of Pt^{IV}, Pt^{II}, Ru^{II}, Re^{I},[3] and Ir^{III}.[4]

One limitation to the clinical use of metal complexes investigated for PDT has been their absorption of light in the UV/Vis region, as the optimal tissue penetration window is 700–900 nm. Two-photon excitation (TPE), or two-photon PDT (TP-PDT) can overcome this barrier. Compounds with high PDT activity under one-photon excitation at a particular wavelength in the UV/Vis region, should theoretically show PDT-activity under TPE in the low-energy NIR region, with the simultaneous advantages of the range of relative tissue transparency, increased potential depth of tissue penetration, and increased spatial targeting.[5] TP-PDT requires high two-photon absorption cross-section and exceptional photo-stability ruling out current clinical photosensitizers. A number transition metal complexes[3c,6] have been developed as two-photon agents, some of which have been shown to induce TPE cell killing in vitro using cell cultures.[3c,6a,7]

We present herein two low-molecular-weight, mitochondrial and lysosomal targeting, iridium complexes which display good PS activity under one-photon excitation in a number of cancer cell lines. Remarkably, one of the complexes is also an efficient PS inducing cell death under TPE, and thus displays highly promising results for TP-PDT.

The new iridium complexes **1** and **2** (Figure 1) are members of the $[Ir(N^C)_2(N^N)]^+$ family and closely related to the complex $[Ir(ppy)_2(pybzH)]^+$.[8] **1** and **2** feature bisbenzimidazole and its *N,N*-dimethylated derivative, respectively, as the N^N ligand (Figure 1). The complexes were prepared as their hexafluorophosphate salts from the chloro-bridged dimer $[Ir(ppy)_2(\mu\text{-}Cl)]_2$, by reaction with 2,2′-bisbenzimidazole or 1,1′-dimethyl-2,2′-bisbenzimidazole (for **1** and **2**, respectively), (Supporting Information, Figures S3–S5). The absorption spectra of **1** and **2** show moderately intense absorption bands in the visible region due to MLCT transitions (Supporting Information, Figure S2). The

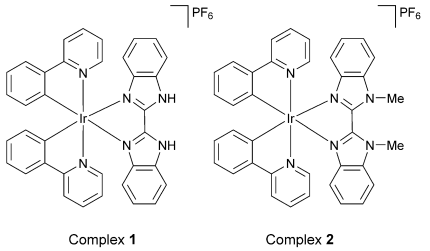

Complex **1** Complex **2**

Figure 1. Complexes **1** and **2**.

emission quantum yields are 0.33 and 0.24, respectively, Emission lifetimes of the order of a microsecond indicate the triplet nature of the emissive state. Importantly, the complexes phosphoresce intensely also under NIR TPE; and **1** has an appreciable two-photon cross-section of 112 GM at 760 nm (Supporting Information, Figure S2).

The TPE phosphorescence imaging of **1** and **2** demonstrate cellular uptake (Supporting Information, Figure S3) with cytoplasmic localisation, similar to that of the previously reported biscyclometallated iridium complexes.[4b,d] Co-localisation experiments with organelle-specific fluorescent dyes demonstrate mitochondrial and lysosomal localisation. Within 4 h of exposure, mitochondrial localisation is observed with a Pearson's correlation coefficient $r = 0.547$ (Figure 2 A and Supporting Information, Figure S4). Additionally, from 2 h increasing lysosomal staining occurs. By 24 h the lysosomal localisation of **1** becomes dominant with Pearson's correlation coefficients of $r = 0.387$ compared to 0.19 for the mitochondrial staining (Figure 2 B and Supporting Information, Figure S4).

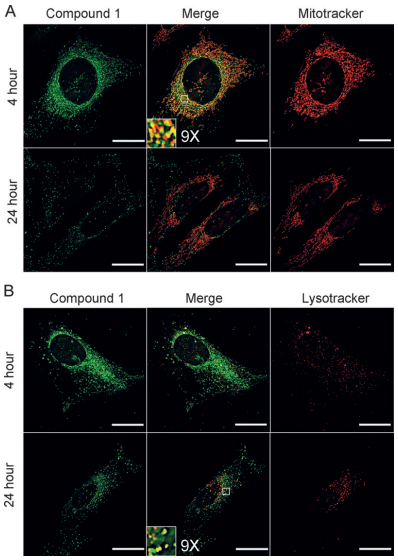

Figure 2. Subcellular localisation of **1**. U2OS cells following 4 or 24 hour incubation with **1** (green), co-localised with: A) Mitotracker orange (red), or B) Lysotracker (red). Zoomed sections are shown as insets. Scale bars = 20 μm.

Cellular uptake was not observed at 4 °C indicating that **1** is actively taken up rather than entering cells by passive diffusion (Supporting Information, Figure S5). A number of cellular uptake pathways were inhibited to determine the uptake route (Supporting Information, Figure S5). Only valinomycin, which is known to cause an increase in the membrane potential of cells, had an inhibitory effect on the uptake of **1** (Supporting Information, Figure S5). Thus uptake of **1** appears to largely occur via a cell membrane potential-dependent pathway which is consistent with it being a singly-charged cation.

Clonogenic survival assays in the cervical cancer cell line, HeLa demonstrate that **1** and **2** show high light cytotoxicity giving LD_{50} values of 0.3 and 0.5 μM respectively (405 nm, 3.6 J cm^{-2}; Figure 3 and Supporting Information, Figure S6).

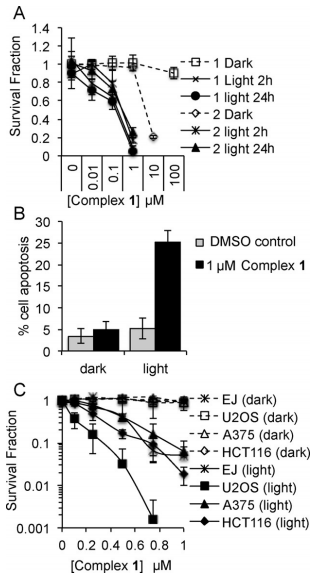

Figure 3. One-photon-induced PS activities of complexes **1** and **2**. A) Survival of HeLa cells pre-incubated for 2 or 24 h with complexes **1** or **2** +/− light. B) Anexin V staining in HeLa cells. C) Survival of bladder (EJ), osteosarcoma (U2OS), melanoma (A375) and colorectal (HCT116) cancer cells 1 +/− light treatment.

Complex **1** shows low dark cytotoxicity, with an LD_{50} of > 100 μM, whereas **2** shows a much higher dark cytotoxicity, $LD_{50} = 6.2$ μM. Comparative PDT activity of a compound can be estimated by the value of the photo-toxicity index (PI), $PI = LD_{50}^{dark}/LD_{50}^{light}$. The lowest estimated PI for **1** in HeLa cells is > 333, but only 12.4 for **2** due to its high dark cytotoxicity, hence **2** was not investigated further. The increased dark toxicity of **2** compared to **1** is likely due to the presence of N–Me groups, which would rule out H-bonding and profoundly affect intermolecular interactions within the cells. **1** also shows photosensitizing effects in a number of cancer cell lines (Supporting Information, Figure S6), demonstrating the potential broad applicability of **1** for PDT.

To evaluate the importance of oxygen in cell killing by **1** and **2**, the yield of singlet oxygen generation was measured. In air-equilibrated dichloromethane, high $\Phi(^1O_2)$ of 42% and 40% for **1** and **2** respectively were determined directly from the emission of the $^1\Delta_g$ state of O_2 in the NIR (λ_{em} 1275 nm) under 355 nm irradiation, demonstrating the ability of the complex

to generate singlet oxygen. In a cellular environment, singlet oxygen immediately reacts with the surroundings, from this point of view, the detection of ROS in cells is an important measurement as it confirms an increase of cellular ROS concentration in the presence of the complex. Here, an approximate 8-fold increase in ROS was detected in cells treated with **1** and light (405 nm) compared to cells treated with light alone (Supporting Information, Figure S7). Efficient intracellular ROS production and $^1O_2$ production in solution are suggestive of an oxygen dependant mechanism of cell killing.

The mechanism of cell death was determined to be apoptosis (Supporting Information, Figure S6). It is proposed that apoptotic cell death after light treatment is associated with localisation of photosensitizers to both the mitochondria and the lysosomes.[9] Here, similar photosensitizing efficacy is seen when the cells were exposed to light following a 2 h incubation—after which mainly mitochondrial localisation is seen, or a 24 h incubation—after which mainly lysosomal localisation is seen (Figure 3). We therefore suggest that light induced cell death by **1** may be due to disruption of one or both of these organelles, which can trigger apoptotic cell death.

The photosensitizing activity of **1** under TPE with 760 nm light was investigated in HeLa cells (Figure 4). The resulting images show apoptosis (green) and cell death (red) induced by TPE photosensitization. The **1**-exposed cells within the irradiated square clearly show apoptosis/cell death, whereas the surrounding non-irradiated cells do not. Little to no killing of cells is seen in the absence of **1** with light power as high as 25 mW

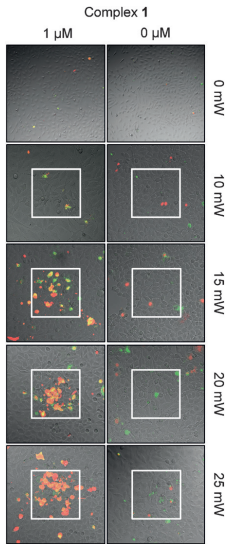

Figure 4. Two-photon-induced PS activity of **1**. HeLa cells treated with **1** or DMSO 2 h before irradiation of a central square with 760 nm multiphoton laser. After 24 h cells were stained with markers for apoptosis (Annexin V, red) and cell death (propidium iodide, green). All images are 450×450 μm except those in the 0 mW column which are 900×900 μm.

which under these conditions relates to a dose of 2720 J cm^{-2}, this is the lower end of light doses reported to date for two-photon photosensitizers.[7a–c] This result therefore demonstrates the potential of **1** as a specific two-photon-activated PS at low concentrations and at doses of light that, alone, are not harmful to cells.

In summary, we introduce two novel small-molecule Ir^{III} complexes, which are cell-permeable, easy to synthesize, possess long-lived triplet excited states, high linear absorption cross sections in the visible range, and high two-photon absorption cross sections in the NIR range of the spectrum. **1** has low dark toxicity and is rapidly and actively taken up into a diverse range of cancer cell types, in which localisation is primarily in the mitochondria and lysosomes. High PS activity of **1** has been demonstrated in a number of cancer cell lines under one-photon excitation with 405 nm light, with an impressive PI index of $>$333 and up to 555 depending on cell line (lower limit estimate). Remarkably, **1** is also active in photosensitizing cell death by apoptosis under NIR TPE (760 nm), at low concentrations and light doses.

Overall, the results demonstrate the exciting potential of **1** as a future two-photon PDT agent, and illuminate the potential of Ir^{III} complexes as TP-PDT agents.

Acknowledgements

This work was funded jointly by Yorkshire Cancer Research, Cancer Research UK, BBSRC, EPSRC KTA and MRC POC funds, University of Durham and CNRS (France). Microscopy was performed on equipment purchased by Welcome Trust grant WT093134AIA and MRC SHIMA award MR/K015753/1. The authors would like to thank Prof. Botchway, Dr. Grey, Mr. Shewring and Dr. Delor for help and advice, and Dr. Robinson for help in capturing images.

Keywords: cancer therapy · iridium · singlet oxygen · transition metals · two-photon photodynamic therapy

[1] A. E. O'Connor, W. M. Gallagher, A. T. Byrne, *Photochem. Photobiol.* **2009**, *85*, 1053 – 1074.
[2] A. P. Castano, T. N. Demidova, M. R. Hamblin, *Photodiagn. Photodyn. Therapy* **2005**, *2*, 1 – 23.
[3] a) F. S. Mackay, J. A. Woods, H. Moseley, J. Ferguson, A. Dawson, S. Parsons, P. J. Sadler, *Chem. Eur. J.* **2006**, *12*, 3155 – 3161; b) F. S. Mackay, J. A. Woods, P. Heringová, J. Kašpárková, A. M. Pizarro, S. A. Moggach, S. Parsons, V. Brabec, P. J. Sadler, *Proc. Natl. Acad. Sci. USA* **2007**, *104*, 20743 – 20748; c) S. C. Boca, M. Four, A. Bonne, B. Van Der Sanden, S. Astilean, P. L. Baldeck, G. Lemercier, *Chem. Commun.* **2009**, 4590 – 4592; d) A. Leonidova, V. Pierroz, R. Rubbiani, J. Heier, S. Ferrari, G. Gasser, *Dalton Trans.* **2014**, *43*, 4287 – 4294; e) K. Wähler, A. Ludewig, P. Szabo, K. Harms, E. Meggers, *Eur. J. Inorg. Chem.* **2014**, 807 – 811; f) A. Kastl, S. Dieckmann, K. Wähler, T. Völker, L. Kastl, A. L. Merkel, A. Vultur, B. Shannan, K. Harms, M. Ocker, *ChemMedChem* **2013**, *8*, 924 – 927; g) P. M. Antoni, A. Naik, I. Albert, R. Rubbiani, S. Gupta, P. Ruiz-Sanchez, P. Munikorn, J. M. Mateos, V. Luginbuehl, P. Thamyongkit, *Chem. Eur. J.* **2015**, *21*, 1179 – 1183; h) C. Mari, V. Pierroz, R. Rubbiani, M. Patra, J. Hess, B. Spingler, L. Oehninger, J. Schur, I. Ott, L. Salassa, *Chem. Eur. J.* **2014**, *20*, 14421 – 14436; i) A. Frei, R. Rubbiani, S. Tubafard, O. Blacque, P. Anstaett, A. Felgenträger, T. Maisch, L. Spiccia, G. Gasser, *J. Med. Chem.* **2014**, *57*, 7280 – 7292; j) A. Naik, R. Rubbiani, G. Gasser, B. Spingler, *Angew. Chem. Int. Ed.* **2014**, *53*, 6938 –

6941; *Angew. Chem.* **2014**, *126*, 7058 – 7061; k) T. Joshi, V. Pierroz, C. Mari, L. Gemperle, S. Ferrari, G. Gasser, *Angew. Chem. Int. Ed.* **2014**, *53*, 2960 – 2963; *Angew. Chem.* **2014**, *126*, 3004 – 3007; l) R. E. Doherty, I. V. Sazanovich, L. K. McKenzie, A. S. Stasheuski, R. Coyle, E. Baggaley, S. Bottomley, J. A. Weinstein, H. E. Bryant, *Sci. Rep.* **2016**, *6*, 22668; m) M. G. Walker, P. J. Jarman, M. R. Gill, X. Tian, H. Ahmad, P. A. Reddy, L. McKenzie, J. A. Weinstein, A. J. Meijer, G. Battaglia, *Chem. Eur. J.* **2016**, *22*, 5996 – 6000.

[4] a) X. Jiang, N. Zhu, D. Zhao, Y. Ma, *Sci. China: Chem.* **2016**, *59*, 40 – 52; b) Y. Li, C.-P. Tan, W. Zhang, L. He, L.-N. Ji, Z.-W. Mao, *Biomaterials* **2015**, *36*, 44; c) S. P.-Y. Li, C. T.-S. Lau, M.-W. Louie, Y.-W. Lam, S. H. Cheng, K. K.-W. Lo, *Biomaterials* **2013**, *34*, 7519 – 7532; d) L. He, Y. Li, C.-P. Tan, R.-R. Ye, M.-H. Chen, J.-J. Cao, L.-N. Ji, Z.-W. Mao, *Chem. Sci.* **2015**, *6*, 5409 – 5418; e) R.-R. Ye, C.-P. Tan, L. He, M.-H. Chen, L.-N. Ji, Z.-W. Mao, *Chem. Commun.* **2014**, *50*, 10945 – 10948; f) F. Xue, Y. Lu, Z. Zhou, M. Shi, Y. Yan, H. Yang, S. Yang, *Organometallics* **2014**, *33*, 73 – 77; g) D. Maggioni, M. Galli, L. D,ÄôAlfonso, D. Inverso, M. V. Dozzi, L. Sironi, M. Iannacone, M. Collini, P. Ferruti, E. Ranucci, *Inorg. Chem.* **2015**, *54*, 544 – 553.

[5] P. T. So, C. Y. Dong, B. R. Masters, K. M. Berland, *Annu. Rev. Biomed. Eng.* **2000**, *2*, 399 – 429.

[6] a) C.-T. Poon, P.-S. Chan, C. Man, F.-L. Jiang, R. N. S. Wong, N.-K. Mak, D. W. Kwong, S.-W. Tsao, W.-K. Wong, *J. Inorg. Biochem.* **2010**, *104*, 62 – 70; b) A. Colombo, C. Dragonetti, D. Roberto, A. Valore, C. Ferrante, I. Fortunati, A. L. Picone, F. Todescato, J. G. Williams, *Dalton Trans.* **2015**, *44*, 15712 – 15720; c) J. S. Nam, M.-G. Kang, J. Kang, S.-Y. Park, S. J. C. Lee, H.-T. Kim, J. K. Seo, O.-H. Kwon, M. H. Lim, H.-W. Rhee, T.-H. Kwon, *J. Am. Chem. Soc.* **2016**, *138*, 10968 – 10977.

[7] a) K. M. Scherer, R. H. Bisby, S. W. Botchway, J. A. Hadfield, A. W. Parker, *J. Biomed. Optics* **2014**, *20*, 051004 – 051004; b) E. Dahlstedt, H. A. Collins, M. Balaz, M. K. Kuimova, M. Khurana, B. C. Wilson, D. Phillips, H. L. Anderson, *Org. Biomol. Chem.* **2009**, *7*, 897 – 904; c) A. Karotki, M. Khurana, J. R. Lepock, B. C. Wilson, *Photochem. Photobiol.* **2006**, *82*, 443 – 452; d) J. Schmitt, V. Heitz, A. Sour, F. Bolze, P. Kessler, L. Flamigni, B. Ventura, C. S. Bonnet, É. Tóth, *Chem. Eur. J.* **2016**, *22*, 2775 – 2786; e) J. Schmitt, V. Heitz, A. Sour, F. Bolze, H. Ftouni, J. F. Nicoud, L. Flamigni, B. Ventura, *Angew. Chem. Int. Ed.* **2015**, *54*, 169 – 173; *Angew. Chem.* **2015**, *127*, 171 – 175; f) W. Yang, Q. Zou, Y. Zhou, Y. Zhao, N. Huang, Y. Gu, F. Wu, *J. Photochem. Photobiol. A* **2011**, *222*, 228 – 235; g) Y. Zhao, W. Wang, F. Wu, Y. Zhou, N. Huang, Y. Gu, Q. Zou, W. Yang, *Org. Biomol. Chem.* **2011**, *9*, 4168 – 4175; h) H. Huang, B. Yu, P. Zhang, J. Huang, Y. Chen, G. Gasser, L. Ji, H. Chao, *Angew. Chem. Int. Ed.* **2015**, *54*, 14049 – 14052; *Angew. Chem.* **2015**, *127*, 14255 – 14258; i) E. M. Boreham, L. Jones, A. N. Swinburne, M. Blanchard-Desce, V. Hugues, C. Terryn, F. Miomandre, G. Lemercier, L. S. Natrajan, *Dalton Trans.* **2015**, *44*, 16127 – 16135.

[8] L. Murphy, A. Congreve, L.-O. Pålsson, J. G. Williams, *Chem. Commun.* **2010**, *46*, 8743 – 8745.

[9] H. Abrahamse, M. R. Hamblin, *Biochem. J.* **2016**, *473*, 347 – 364.

Received: October 12, 2016
Published online on November 2, 2016

Appendix 6. PorphyrinPlus Unpublished Paper

A porphyrin platinum compound as a potential water soluble mitochondria-targeting photosensizer for photodynamic therapy

Luke K. McKenzie[§1,2], Harry Henson[§1], Atanu Jana[2,3], Julia A. Weinstein[2], Michael D. Ward[2] and Helen E. Bryant[1*]*

[1]Department of Oncology and Metabolism, University of Sheffield, Sheffield S10 2RX, UK

[2]Department of Chemistry, University of Sheffield, Sheffield S3 7HF, UK

[3]Atanu's current affiliation?

[§]Authors contributed equally to the work

CORRESPONDING AUTHORS INFORMATION

*Correspondence should be addressed to HB, tel. +44 (0)114 2759040, fax: +44 114 2795320, E-mail: h.bryant@sheffield.ac.uk or MW, tel:, fax: +44-(0)114-22-29346, E-mail:

ABSTRACT

Photodynamic therapy (PDT) is a modality using drugs which act as photosensitizers (PS) only causing cellular damage when activated by light.

We introduce a long-lived platinum/zinc metallo-porhpyrin compound that localises to mitochondria in live cells. The compound shows low cytotoxicity in the dark (LD_{50} = >500 μM) and highly efficient phototoxicity at 455 nm (LD_{50} = 1 μM, 3.6 J cm^{-2}). The compound shows high singlet oxygen yield of 0.83 and is shown to induce ROS production in cells upon irradiation.

INTRODUCTION

Photodynamic therapy (PDT) is an approved and relatively non-invasive treatment for many different diseases, both neoplastic and non-neoplastic[1]. PDT relies on photosensitizing compounds (PS) that are activated by certain wavelengths of light leading to formation of an excited photosensitizer (PS*) to elicit the production of reactive oxygen species (ROS) including singlet oxygen ($^1O_2$) and thus facilitate cell death.

A long-lived PS* is required to allow energy transfer to O_2 and thus molecules which readily enter the triplet state, through intersystem crossing, are sought after. The ideal PS is non-toxic in the dark, able to accumulate well within cells and at the tumour site, has a strong absorption of light at wavelengths with greatest tissue penetration and when activated produces a high quantum yield of $^1O_2$/ROS.

Many different porphyrin and porphyrin-based compounds have gained approval for their clinical application within PDT. Porphyrin structures have a great pedigree for use in PDT due to their excellent phototoxic properties in the presence of light[2]. Metalloporhyrin structures have also been explored as they have suitable photophysical properties. Zinc(II) based porphyrin structures are one type of metalloporphyrin that have been shown to undergo photosensitising activity[3], Zn(II) incorporation being shown to increase the lifetimes of their triplet states when compared to their metal-free counterparts [4]. Zn-porphyrin structures also carry an overall positive charge, making them more hydrophilic. This hydrophilicty and positive charge is a feature that all the most potent PS share, and means that the

structures are allowed to freely to diffuse across plasma membranes and accumulate within the cell[1].

We have previously reported a square planar platinum(II) complex, investigated as PS for PDT due to the attractive photophysical properties of transition metal complexes, though limited by relatively high dark toxicity[5]. Platinum porphyrin conjugates pose a potential new avenue for platinum in PDT, with tetra-platinated porphyrins being reported to be able to produce a high $^1O_2$ quantum yield when compared to porphyrin alone, and displaying high PI[6]. Whilst a series of soluble tetraarylporphyrin-platinum conjugates have shown synergistic effects between the cytotoxicity of the platinum compounds as in chemotherapy and the phototoxic effects of the porphyrin structure, taking advantage of the tumour 'homing' capabilities of porphyrin derived structures [7].

A previously reported compound, a Zn N-alkylpyridylporphyrin with similar Zn based porphyrin structure to that investigated here, showed free diffusion into the cell, with accumulation of the compound within the mitochondria, a property that is then associated with apoptosis upon production of $^1O_2$/ROS via activation by visible light [8, 9].

Here a novel water soluble Zn coordinated porphyrin with the addition of a platinum C^N^N group conjugate, compound **1**, is presented. Its cellular uptake, localisation and cytotoxicity are explored alongside its photosensitizing effect against the bladder cancer cell line EJ.

RESULTS AND DISCUSSION

Chemical properties

Compound **1** is a mono-platinated Zn(II) N-methylpyridylporphyrin, figure 2a. The positive charge present across the porphyrin structure is a common feature of Zn-based porphyrin structures[4], and makes the structure extremely hydrophilic. This hydrophilic nature and positive charge is theorised to allow for passive diffusion across cell membranes and for its accumulation within the cell; whilst the addition of the methyl groups have previously been shown to allow for accumulation of Zn-based

porphyrin structures at the mitochondria[8]. The effect of the addition of the single platinum group to the porphyrin structure is unknown, but tetra-platinated porphyrin structures have shown great efficacy in PDT in vitro[6]. It is hypothesised that addition of the platinum group will have a positive effect on the photosensitising properties of the compound when compared to the porphyrin structure alone. In addition we compared the platinum-porphyrin compound with a related platinum C^N^N complex, compound **2**, figure 2b.

Photophysical properties

The absorption spectra of compound **1** was recorded in a solution of purified H_2O ,figure x. The absorption spectrum shows a large peak at ~450 nm assigned to the porphyrin soret band. Q-bands with smaller absorptions are shown at ~560nm and ~600nm. Absorption between 200nm and 400nm is mostly attributed to the pendant platinum group with the peak at ~260 nm assigned to the π-π^* transition of the ligand whilst the peak at ~320 nm is assigned to .

The emission profile...

Localisation and uptake

The dose dependence and localisation of compound **1** was assessed by confocal microscopy, figure S2. In keeping with previously reported porphyrin complexes[9] staining appeared throughout the cytoplasm with no nuclear staining seen.

On closer inspection compound **1** is seen to colocalise with the mitochondrial stain Mitoview 633, figure 4, giving a Pearson's correlation coefficient (r) of 0.84, where an r of 1 means complete concurrence of stains and 0 means no correlation, thereby indicating mitochondrial staining. Compound **2** shows similar staining, figure S2b. Localisation of the PS at the intracellular level is important as this can determine the mechanism of cell death induced by the treatment. For instance mitochondrial-associated PS tend to cause photo-damage to the membrane of the mitochondria, thus releasing the caspase activator cytochrome-C which then, in turn, activates a caspase cascade culminating in the death of the cell through apoptosis[11].

Cellular uptake was not inhibited by incubation at 4 ºC indicating that compound **1** is enters cells by means of passive diffusion rather than active transport, figure S3.

Phototoxicity

The toxicity of compound **1**, alongside compound **2,** was assessed in the dark and post light treatment (455 nm, 3.6 J cm^{-2}) by clonogenic assay, figure 5a. LD_{50} values in the presence and absence of light were calculated to be 1 μM and >500 μM for compound **1** respectively giving a relatively high minimum photoindex (PI) of 500 where PI = LD_{50}dark/LD_{50}light at a very low light dose (3.6 J cm^{-2}). Compound **2** is somewhat more toxic in the dark with an LD_{50} ~70 μM and somewhat less toxic when irradiated at 455 nm (3.6 J cm^{-2}) with around two thirds of cells surviving with as high as 10 μM. The relatively high dark toxicity is consistent with previously reported platinum complexes for PDT[5]. Perhaps conjugation of the porphyrin in place of the relatively labile Cl group reduces binding possibilities of the Pt C^N^N complex thereby reducing toxicity.

This toxiciciy is shown using 455 nm light which corresponds with the porphyrin soret band. Many clinically approved porphyrin PS use activation of Q bands opening up the possibility of further investigating the red activation of the compound.

Cell death was confirmed by microscopy with cells exhibiting an appearance in keeping with apoptotic death following light exposure at low concentrations of compound **1**, figure 5c. At higher concentrations some cells appeared to have undergone necrosis, figure 5c, indicating the importance of drug concentrations in PDT.

Oxygen species

Both porphyrin and Pt(II) complexes are generally considered to induce photoactivated cell death by production of ROS. To support this mechanism the production of ROS and $^1O_2$ was explored. $^1O_2$ quantum yields (Φ) of compound **1** and compound **2** measured directly by $^1O_2$ phosphorescence (λ_{em} = 1275 nm) against the standard perinapthenone ($\Phi(^1O_2)$ = 95%[12]) in dichloromethane upon excitation with UV light (λ_{exc}= 355nm) . For compound **1** Φ = 0.83 +/- 0.044 and compound **2** Φ = 0.90 indicating highly efficient $^1O_2$ production.

After showing the generation of singlet oxygen in solution ROS production in cells was investigated using the commercial ROS detection kit, Oxyselect™ Intracellular

ROS Assay kit, where fluorescence of a probe increases upon reaction with ROS. Treatment with compound **1** (2 μM) and light is shown to be associative with a ~9.5 fold increase in ROS production, as measured by fluorescence of the probe, compared to light alone whereas 1 μM compound **1** is shown to be sufficient for a ~5.5 fold increase in ROS production.
These data indicate the likely dependence of cell death on the production of ROS/$^1O_2$.

CONCLUSION

Here we present a platinum C^N^N- Zn incorporated porphyrin conjugate soluble in aqueous media showing high PS in the bladder cancer cell line EJ when excited at 455 nm (3.6 J cm^{-2}) giving a PI of >500. The compound is seen to passively enter cells and localise to the mitochondria leading to apparent apoptotic cell death at low concentrations. A high singlet oxygen yield is shown (Φ = 0.83) and a ~9.5 fold increase in ROS production in cells compared to drug or light alone indicating the oxygen dependence of the compound. Incorporation of the porphyrin structure means the complex may benefit from the enhanced permeability and retention (EPR) effect demonstrated by porphyrin PS whereby porphyrin molecules accumulate well at tumour sites, and at a higher concentration that that of the surrounding tissue[13] further indicating the clinical potential of the compound.

EXPERIMENTAL

Materials

All chemicals were purchased from Sigma-Aldrich Company Ltd. Dorset, England unless otherwise stated. During biological experiments stock solutions of compound **1** were made up in deionized water and stored at −20°C protected from light, compound **2** was stored in stock solutions of DMSO and stored at −20°C before dilution in culture medium.

Synthesis of compounds

Mike/atanu

Synthetic scheme **fig 1,** spectra figure **s1**

Photophysical analysis

UV-visible absorption spectra in solution were recorded on [name] spectrometer in quartz cuvettes of 1 cm pathlength. Luminescence spectra were recorded in quartz cuvettes of the same dimensions. The excitation and emission spectra were obtained using a Fluoromax-2 spectrometer. Lifetimes were determined by time-correlated single photon counting using Edinburgh Instrument mini-tau following excitation with a pulsed laser diode at 405 nm, 75 ps.

Tissue Culture

The cell lines EJ (bladder carcinoma) and HeLa (cervical cancer) were cultured in DMEM (Dulbecco's modified Eagles Medium – obtained from Lonza, Cambridge, UK) containing 10% FCS (foetal calf serum – Lonza, Cambridge Uk). Cells were incubated at 37^{o}C and in an atmosphere of 5% CO_2. Cells were used within 20 passages of purchase from American type culture collection – LGC partnership (Teddington, UK) and were subject to routine checks for mycroplasma contamination.

Luminescence imaging

Glass cover slips (22 x 22 mm) were sterilised in industrial methylated spirits (IMS) and placed flat into six well plates. Cells were then seeded onto the coverslips at a seeding density of 1 x 10^5 cells per well, and left to incubate overnight in 2 ml of DMEM culture medium. Compounds were diluted from stock solutions in DMEM to the required concentration and administered to the cells for the required time period, before being removed. The coverslips were then exposed to 3 washes with PBS before being fixed in 4% paraformaldehyde for 20 mins. The paraformaldehyde solution was removed and the cells were washed 3 more times with PBS before the coverslips were mounted onto microscope slides using Immumount (Life

Technologies Ltd, Paisley, UK) mounting agent. Cells were then imaged using a Nickon A1 Confocal system (60x oil objective), with an excitation laser with a wavelength of 562 nm for compound **1** and 457 nm for compound **2**.

Co-localisation

Glass cover slips (22 x 22 mm) were sterilised in IMS and placed flat into 6-well plates. HeLa cells were then seeded onto the cover slips at a density of 1 x 10^5 cells per well and left to incubate overnight in DMEM media. Cells were incubated with compound **1** (10 μM in DMEM, 2 hours). After the two hours of incubation with compound **1** the media was removed and replaced with 100 nM MitoView™ 633 (Biotium Inc. Fremont, CA, USA, 100 nM in DMEM, 15 mins). Media was removed and the coverslips were washed three times with PBS before cells were treated with 4% paraformaldehyde solution for 20mins. Coverslips were then washed three more times with PBS before being mounted onto microscope slides using Immumount (Life Technologies Ltd, Paisley, UK) mounting agent. Cells were then imaged on a Nikon A1 confocal system (60x oil objective), using both 562 nm and 642 nm excitation lasers. Images were then merged using the open source image software FIJI, and co-localisation analysis was undertaken using the Coloc-2 tool with a bisection regression threshold to yield both a Pearson's R value and Manders' value.

Light toxicity Clonogenic Assay

6-well plates were seeded with cells at a density of 50,000 cells per well and incubated overnight. The wells were then treated with compound (0- 10 μm, 2 hours, controls DMEM or DMEM/DMSO for **1** & **2** respectively. Following incubation cells were washed 3 times with PBS before being trypsinised and cells suspended in media. Cells were pelleted and resuspended in clear media (w/o L-glutamine or phenol red, 2 ml). The solution containing the cells was then split equally between a glass vial (the cells to be irradiated with light) and a plastic eppendorf tube (control). Cells in the glass vial were then irradiated with 455nm light (20 mW cm^{-2}, 3 mins) the cells in the eppendorf were kept in the dark. Cells were plated onto 6 well plates at 200, 400, 800, 1000, and 5000 cells in DMEM media used for their incubation. After incubation for 5-7 days, when colonies were visible to the naked eye, culture media was removed and cells were stained with 4% methylene blue in 70% methanol for 20 mins. After

excess methylene blue was removed and plates were washed with water, and colonies could be counted. Each colony was considered as representing the survival of one cell.

Dark toxicity clonogenic assay

Cells were seeded at 200 and 400 cells per well in six well plates and incubated overnight. Wells were then treated with compound (varying concentrations, with required controls, 2 hrs) before culture media was replaced. Cells were then incubated for 5-7 days, until colonies were visible; cells were then stained and counted as with the light toxicity assay.

Cell uptake analysis

Glass coverslips (22 x 22 mm) were sterilised in IMS before being lay flat in 6-well plates. Cells were seeded onto the cover slips at 1 x 10^5 cells per well and incubated in culture media overnight. Prior to treatment with the compound one 6 well plate was refridgereated (4 ^oC, 20 mins) whilst the other was left in the incubator (37^oC, 5% CO_2). Media was then removed from the plates and replaced with either cold (4 ^oC) or warm DMEM media containing 10 μM compound **1**. The plates were then placed back in the refrigerator and incubator respectively for 2 hours. Subsequent to the completion of the treatment media was removed and the coverslips were subject to 3x washes with PBS, before being treated with 4% paraformaldehyde for 20 mins. The coverslips were then washed 3 more times with PBS before being mounted onto microscope slides (IMMU-MOUNTTM, Life Technologies Ltd, Paisley, UK). The slides were imaged on a Nikon A1 confocal system (40x oil objective, 562 nm laser), with the mean intensity over 100 cells being quantified by use of FIJI.

Reactive oxygen species detection

An Oxyselect^{TM} Intracellular ROS Assay kit (Cambridge Bioscience Ltd, Cambridge, UK) was used to detect the presence of intracellular reactive oxygen species. 6-well plates were seeded with cells the day before at a density of 200,000 cells per well and left in the incubator overnight. Cells were then treated with compound **1** (0 – 2 μM, 2

hours) before being washed (3x with PBS) and trypisinized and cell pellets obtained. Cells were then re-suspended in 200 µl 1 mM DCF-DA and placed back in the incubator for 30mins. Cells were then treated with light as in the light toxicity assay before cell pellets were collected from each condition. Flow cytometry was then used to detect the presence of ROS, with the cell pellets being re-suspended in 300 µl PBS. Flow cytometry detected the presence of the ROS probe using an excitation laser wavelength of 480nm with an emission wavelength read at 530nm (BD™ LSR II flow cytometer). Analysis of data was undertaken on FlowJo in order to plot the histogram gated for blue intensity vs side scatter of cells.

Singlet oxygen

Obtained as described previously[10]

ACKNOWLEDGEMENTS

1. A. P. Castano, T. N. Demidova and M. R. Hamblin, *Photodiagnosis and Photodynamic Therapy*, 2004, **1**, 279-293.
2. D. E. Dolmans, D. Fukumura and R. K. Jain, *Nature Reviews Cancer*, 2003, **3**, 380-387.
3. L. Benov, I. Batinić-Haberle, I. Spasojević and I. Fridovich, *Archives of biochemistry and biophysics*, 2002, **402**, 159-165.
4. K. Kalyanasundaram, *Inorganic Chemistry*, 1984, **23**, 2453-2459.
5. R. E. Doherty, I. V. Sazanovich, L. K. McKenzie, A. S. Stasheuski, R. Coyle, E. Baggaley, S. Bottomley, J. A. Weinstein and H. E. Bryant, *Scientific reports*, 2016, **6**.
6. A. Naik, R. Rubbiani, G. Gasser and B. Spingler, *Angewandte Chemie*, 2014, **126**, 7058-7061.
7. C. Lottner, K.-C. Bart, G. Bernhardt and H. Brunner, *Journal of medicinal chemistry*, 2002, **45**, 2079-2089.
8. L. Benov, J. Craik and I. Batinic-Haberle, *Anti-Cancer Agents in Medicinal Chemistry (Formerly Current Medicinal Chemistry-Anti-Cancer Agents)*, 2011, **11**, 233-241.
9. R. Ezzeddine, A. Al-Banaw, A. Tovmasyan, J. D. Craik, I. Batinic-Haberle and L. T. Benov, *Journal of Biological Chemistry*, 2013, **288**, 36579-36588.
10. P. A. Scattergood, M. Delor, I. V. Sazanovich, O. V. Bouganov, S. A. Tikhomirov, A. S. Stasheuski, A. W. Parker, G. M. Greetham, M. Towrie and E. S. Davies, *Dalton Transactions*, 2014, **43**, 17677-17693.
11. J. Reiners Jr, J. Caruso, P. Mathieu, B. Chelladurai, X.-M. Yin and D. Kessel, *Cell death and differentiation*, 2002, **9**, 934.
12. R. Schmidt, C. Tanielian, R. Dunsbach and C. Wolff, *Journal of Photochemistry and Photobiology A: Chemistry*, 1994, **79**, 11-17.

13. A. K. Iyer, K. Greish, T. Seki, S. Okazaki, J. Fang, K. Takeshita and H. Maeda, *Journal of drug targeting*, 2007, **15**, 496-506.

Figure 2

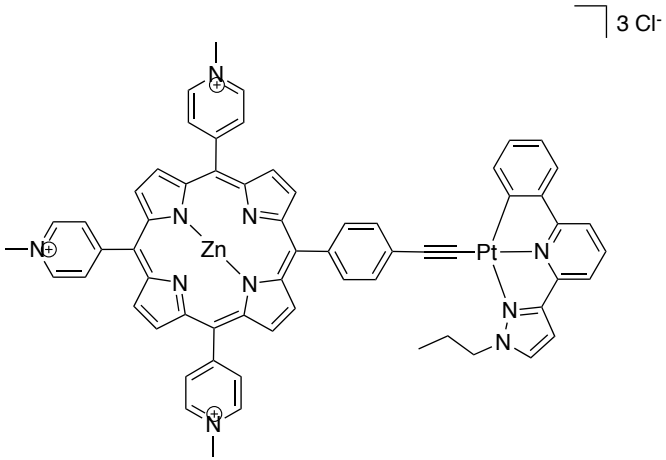

Compound **1**

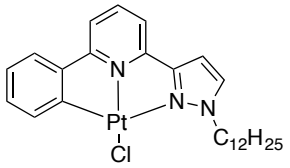

Compound **2**

Figure 3

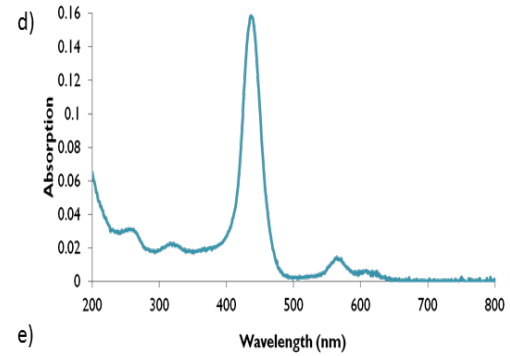

Photophysical data actual to be added and for platinum complex

Figure 4

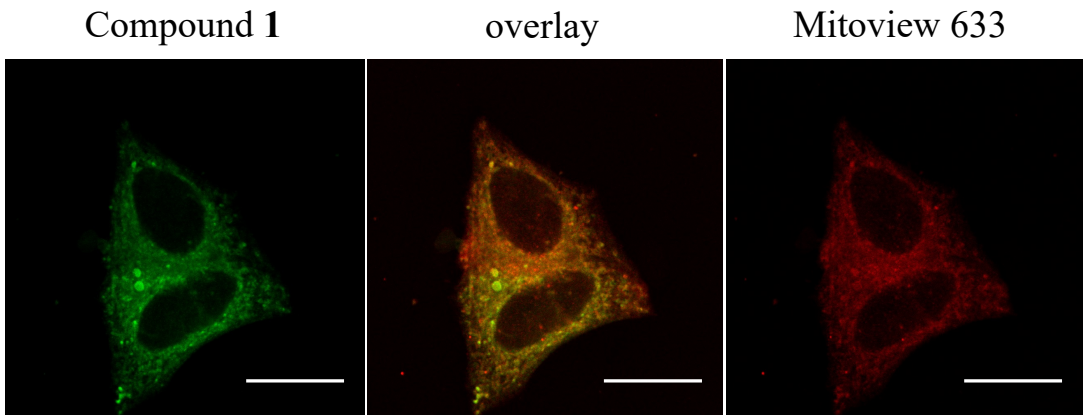

Figure 5

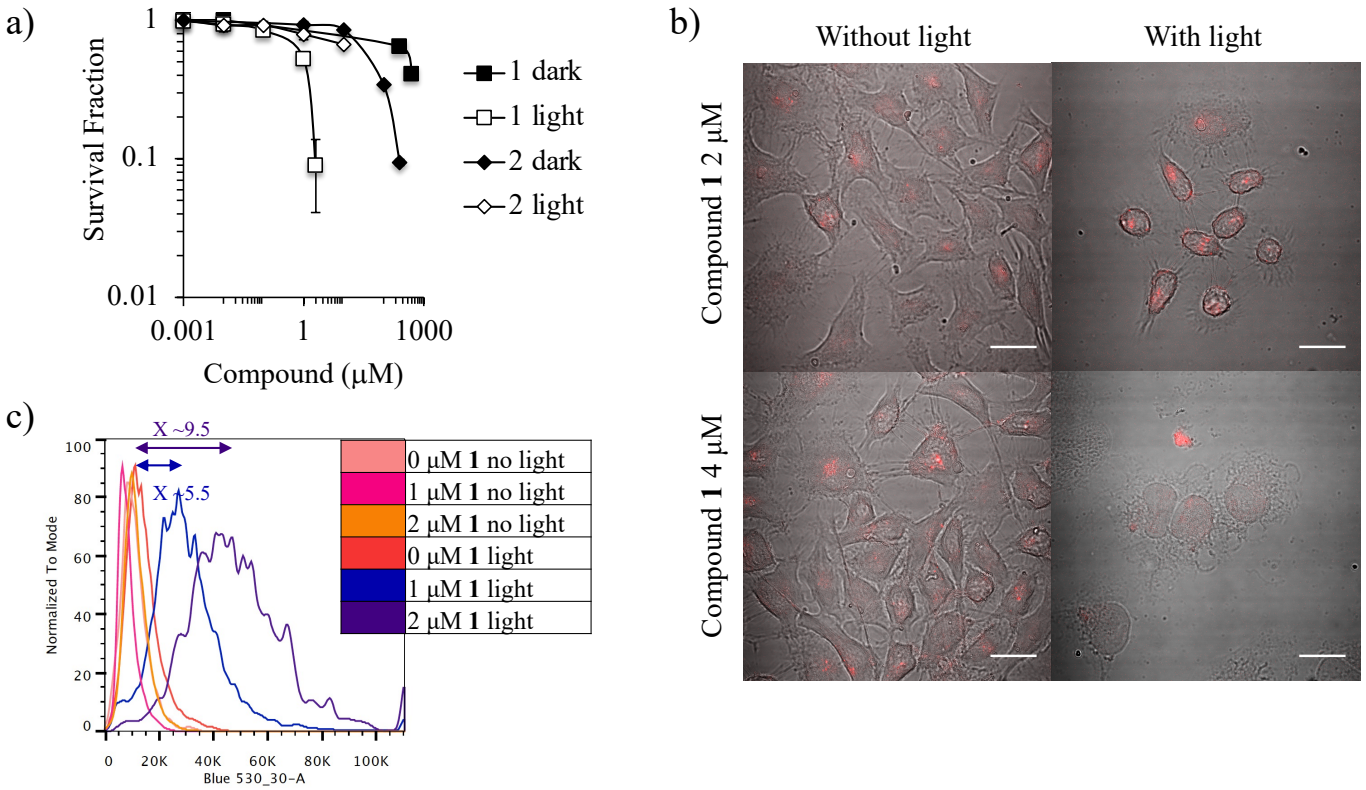
a)
Survival Fraction
1
0.1
0.01
0.001
1
1000
Compound (μM)
1 dark
1 light
2 dark
2 light
b)
Without light
With light
Compound 1 2 μM
Compound 1 4 μM
c)
X ~9.5
X ~5.5
Normalized To Mode
100
80
60
40
20
0
0
20K
40K
60K
80K
100K
Blue 530_30-A
0 μM 1 no light
1 μM 1 no light
2 μM 1 no light
0 μM 1 light
1 μM 1 light
2 μM 1 light